Transactions of the ASME

Transactions of the ASME, Journal of Fluids Engineering (ISSN 0098-2202) is published quarterly (Mar., June, Sept., Dec.) for $100 per year by The American Society of Mechanical Engineers, 345 East 47th Street, New York, NY 10017. Second class postage paid at New York, NY and additional mailing offices. POSTMASTER: Send address changes to Transactions of the ASME, Journal of Fluids Engineering, c/o THE AMERICAN SOCIETY OF MECHANICAL ENGINEERS, 22 Law Drive, Box 2300, Fairfield, NJ 07007-2300.
CHANGES OF ADDRESS must be received at Society headquarters seven weeks before they are to be effective. Please send old label and new address.
PRICES: To members, $29.00, annually; to nonmembers, $100. Add $15.00 for postage to countries outside the United States and Canada.
STATEMENT from By-Laws. The Society shall not be responsible for statements or opinions advanced in papers or . . . printed in its publications (B7.1, Par. 3).

INDEXED by Applied Mechanics Reviews and Engineering Information, Inc.

Journal of Fluids Engineering

Published Quarterly by The American Society of Mechanical Engineers

VOLUME 112 • NUMBER 2 • JUNE 1990

Journal of Fluids Engineering

Editorial

In this editorial I would like to share with the readership of JFE some of my ideas and thoughts, a few months before I start my five-year tenure as the Technical Editor. For some time this Journal has been an established and respected vehicle for communicating the results of fluid-mechanics research within the engineering community. It is supported by a very active division of ASME, the Division of Fluids Engineering, which has been striving to identify important emerging areas of research.

It might appear at first that all I would have to do to fulfill my responsibilities is to stay the course. But, I believe that the advances in modern technology may soon require some significant changes in our publishing practices. I suppose it is easy to introduce any topic today by reminding your audience of the spectacular progress technology has made recently. But, in the task of communicating technical information, the need to update our methods is real and urgent. After all, this is the age of communication explosion. And yet today scientific information is communicated by journals in much the same way as it was 100 or 200 years ago!!

I have been personally faced with the dilemma and the frustration of how to manage a few million pieces of experimental data. A few graphs that fit in the space of a journal article may convey the message but are totally inadequate for comparison with results of other methods of investigation. I always offer to supply to anyone interested all my numerical and experimental data on tape or disk, and I have had quite a few requests. But I am still not sure what and how an author should provide to the readers.

I believe that it is the responsibility of a scientific journal to organize, standardize, and document the exchange of scientific information. We may soon request that each article be accompanied by a file of data in a standardized form that will be available to the readers of the Journal. This type of information could be provided by the author at the time the paper is submitted and be available to the editors and reviewers. If the paper is accepted, the corresponding data file could be an integral part of the scientific contribution, available through the office of the Journal. In this way, all investigators who will later employ this information for comparison will use the same set of data. We are presently studying the details of a standardized method for electronic communication of the Journal audience with a Journal Bank. For the time being, authors are requested to offer voluntarily their data on disk.

During my tenure as a Technical Editor, I also plan to work on a few other topics. Most intriguing to me is the idea of trying to "return the Journal to the audience." Here is what I mean by that. Talking to many colleagues over the past 20 years, I came to understand that we all view a journal as a vehicle to publish our work. In case you are now wondering "well, what else is a journal for," you are proving my point, because, of course, communication of scientific information means that a journal is also meant to be read. Somehow, we all have come to understand that a journal serves the authors. I strongly believe that a journal should serve the readers. It is only a side effect that the author gets the benefit of becoming known or perhaps getting promoted because he had something nice to publish.

Here is how I propose to better serve this very important constituency of the Journal, the reader. We will do our best to ensure that every article has something important and useful to offer. And the terms "important" and "useful" are employed here in their broadest sense. In simpler terms, a paper fails to serve its purpose, if the reader can say after he has read it, "so what!" You may be thinking that this is nothing new. After all, criteria for acceptance for all scientific journals have always been such attributes as "originality," "significance" and "lasting contribution." And yet, I find that many papers published today simply discuss just another, perhaps smarter way of doing something. What the reader should be looking for and what I define as "useful" is the discussion of a new physical phenomenon, or a new interpretation of the physics of a known phenomenon, or the description of a new technique that the reader can use. The Editorial Board will make every effort to ensure that all submitted papers pass this criterion before they are accepted.

Another point that we should address is making the papers published in JFE more readable. Working as an associate editor for a few years, I found that there are areas which developed independently of others for a while. Investigators working in such areas tend to become isolated and thereby deprive themselves of the advantages of cross-fertilization. What concerns me is that their communications become more and more convoluted and their style and jargon incomprehensible to researchers in other areas. This can happen in every discipline, at every level. To improve the way papers are presented, I recommend that each paper be sent to one reviewer who is *not* a specialist in the area of the paper.

Our expectations from such a reviewer are, of course, different than those from one who has worked extensively in the area. At the same time, I urge the authors to think of a broader audience. You certainly need to reach the ones who work in the same area with you, but your paper will be more successful if people outside the area also actually read it.

I also plan to continue the traditions that Frank White and Bob Dean established for the Journal. I will try to have at least one review article of current interest in each issue. I will also welcome and on occasion invite authors to submit editorials.

When Dr. White took over as Technical Editor about 12 years ago, he made the observation that the Journal was becoming the territory of academicians. Fortunately, this trend did not continue. We all feel that one of our important constituencies is the industrial world. The mission of the Journal has always been to publish basic and original work in fluid mechanics. And yet, many of the problems discussed in these

pages are inspired by real engineering problems. Morever, quite often, our papers offer information that can find immediate application in practice or can be useful to the designer.

During Dr. White's tenure, the Journal led the way in establishing standards for experimental uncertainty and numerical accuracy. We will continue requiring that all papers uniformly abide by these rules.

We are working on a few more ideas which have not yet crystalized. This transition also coincides with some bold and promising plans of restructuring the activities of the ASME Division of Fluid Mechanics which are being introduced by its executive committee. I anticipate that more suggestions will result from these activities. The readers are also invited to share with the Editorial Board their opinion on the future of this Journal.

Demetri P. Telionis
Technical Editor-Elect

Errors Due to Turbidity in Particle Sizing Using Laser-Doppler Anemometry

Y. Kliafas
Research Assistant.

A. M. K. P. Taylor
Research Fellow.

J. H. Whitelaw
Professor of Convective Heat Transfer
Fluids Section.

Department of Mechanical Engineering,
Imperial College of Science and Technology,
London SW7 2BX, England

Flow turbidity, when introduced between the transmitting and receiving optics and the measuring volume of a laser-Doppler anemometer, changes the pedestal amplitude and visibility of the signal. The purpose of this work is to assess the effect on the accuracy of particle sizing, based on measurements of these two quantities, for depths of field of 5 and 10 cm, interrupting particle diameters between 14 to 212 μm in three discrete ranges and void fractions up to 0.1 percent. The turbidity introduces random fluctuations in visibility which increase with void fraction and the resulting rms errors in particle diameter for turbidity introduced on the receiving side of the optics are smaller than 10 percent at void fractions below 0.1 percent. For particles larger than about one third of the beam diameter, the influence of turbidity is largely due to the interruption of the incident beams over the 5 cm nearest to the measuring volume.

Introduction

The dispersion of solid and liquid particles in turbulent flow is important in a number of industrial applications, including coal-fired furnaces. Dispersion is a function of, among other things, the relative velocity between the particulate and air phases and of particle size. Velocity can be measured by the established technique of laser-Doppler anemometry and a number of publications have suggested methods to exploit characteristics of the Doppler signal to measure the corresponding particle size in the range from 1 to, say, 500 μm. These include inferring particle size from the magnitude of the "pedestal" amplitude (for example, by Levy and Lockwood, 1981; Mizutani, Kodama, and Miyasaku, 1982; Yule, Ereaut, and Ungut, 1983; Modarress and Tan, 1983; Allano, Gouesbet, Grehan, and Lisiecki, 1984; and Hess, 1985) or from the value of the signal "visibility" (for example, by Durst, 1973; Hong and Jones, 1976; Farmer, 1978; Bachalo, 1980; Negus and Drain, 1982; and Hadded, Bates and Yeoman, 1985). Combinations of both approaches have been suggested by Negus and Drain (1982) either to "calibrate" the relation between pedestal amplitude and particle diameter for diameters above which visibility is not single-valued or to provide a basis for rejecting signals with erroneous visibility.

In a companion paper (1987), we have shown that errors arise when a two-phase flowfield interrupts the laser beams between the transmitting optics and the measuring volume. The errors have random and systematic components, and the magnitude of these depends on the size and concentration of the particulate phase and on the "depth of field."

Purpose of Current Contribution. The purpose of this paper is to quantify the relative magnitudes of the errors in measuring particle size due to turbidity in the path of the transmission and receiving optics, respectively. Particle size was inferred from measurements of either the signal visibility or the amplitude of the pedestal component of the output of the photomultiplier. The fluctuations in the signal were generated by:

(1) introducing a two-phase flowfield between the measuring volume and the receiving optics, as a function of particle concentration, at one depth of field, with interrupting particle size as parameter; and
(2) introducing a two-phase flowfield simultaneously between the measuring volume and both the transmitting and the receiving optics.

A further purpose is to quantify the influence of the distance between the interrupting particles and the measuring volume in the transmission path. The results are also likely to be relevant to some single beam instruments (for example, those of Holve and Self, 1979; Wang and Tichenor, 1981; and Holve and Annen, 1984), as well as instruments based on laser-Doppler anemometers.

The following section describes the experimental technique and the results, and the discussion examines the implications of the results in the context of the attainable accuracy of particle sizing. The paper ends with a summary of the more important conclusions.

Experimental Method

The apparatus is illustrated in Fig. 1 and the principal characteristics of the anemometer are given in Table 1. A repetitive

Contributed by the Fluids Engineering Division of THE AMERICAN SOCIETY OF MECHANICAL ENGINEERS and presented at the AIAA/ASME 4th Fluid Mechanics Conference, Atlanta, Ga., May 11-14, 1986. Manuscript received by the Fluids Engineering Division Aug. 30, 1986.

Doppler signal was produced by rotating either an optical fiber (30 μm nominal diameter), which represented the smallest reproducible scattering center that could be attached to the rotating mount, or a 400 μm nominal diameter Plexiglass (acrylic) bead through the center of the measuring volume at constant angular velocity. Note that the use of a single scatterer implied that no more than one particle was present in the measuring volume at any one time, which is a necessary precondition for relating either measured quantity to particle size. Also, no special procedure, such as the use of a "pointer-volume," was necessary in this experiment to account for the nonuniform irradiance profile of the incident laser beams. In general, particles which traverse a nondiametral trajectory of the Gaussian light distribution produce signals with variations in amplitude or visibility which are unrelated to differences of size. In these experiments, however, the particle was constrained to traverse a *repetitive* trajectory which always passed through the center of the measuring volume of the laser-Doppler anemometer. The interrupting two-phase flowfields were established within transparent, plane-sided tanks of water which contained a known mass of particles of one of three size ranges (see Table 2); detailed size distributions for the largest and smallest ranges are given in our previous paper. Water tanks were chosen to provide a suspension of particles for experimental convenience. The range of particle diameters chosen is practically relevant to the use of the amplitude and visibility techniques for sizing and the lower limit of 14 μm was set by commercial availability. The particles were set in motion by the use of a paddle stirrer. Two tanks were used to provide depths of field corresponding to 5 and 10 cm. The figure shows the definitions of symbols D_1 and D_2, which are depths of field, and of L_1 and L_2, which are the distances from the measuring volume to the tanks.

The instruments for processing the output of the photomultiplier are shown in Fig. 2 and are identical to those used previously. The frequency counter incorporated amplitude and time-domain validation logic. The pedestal amplitude and visibility were calculated from the output of a 20 MHz, 8 bit transient recorder.

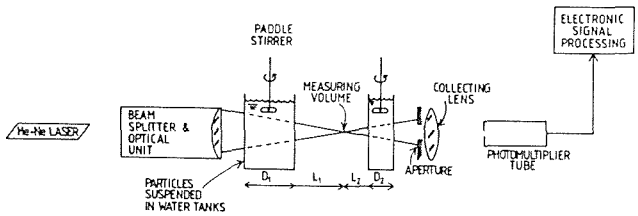

Fig. 1 Optical arrangement of laser-Doppler anemometer showing interruption on transmitting optics side by a dispersed two-phase flow. Doppler signal generated by rotation of a mounted scattering particle.

Results

In the absence of any interrupting particles in the water tanks, the pedestal amplitude and signal visibility were constant. The addition of particles to the tanks resulted in random variations in these two quantities and the probability distribution can be characterized by the changes in the mean and standard deviation. The following two subsections examine the influence of particle interruption between the measuring volume and the receiving optics only, and between the measuring volume and both transmitting and receiving optics simultaneously.

Particles Between the Measuring Volume and Receiving Optics. Figure 3 shows the attenuation of the pedestal amplitude due to introducing a water tank with D_2 = 10 cm between the measuring volume and the receiving optics. Measurements were made as a function of the void fraction, for three interrupting particle size ranges, and for Doppler signals generated by a Plexiglass sphere (400 μm diameter) and an optical fiber (30 μm diameter). The latter comparison shows that the variation of mean attenuation which results with increasing void fraction is the same (to within the experimental error) but that the spread of the random fluctuations is larger for the fiber by up to about one third. The results pertain to Doppler signals generated by the fiber and, although it is not certain whether the difference is due to the different shape or to the different diameter, the conclusions to be drawn are not affected by this difference. Comparison with previous results for the same conditions of interrupting particle size, concentration and depth of field, but placed between the transmission optics and the measuring volume, shows that the mean attenuation is the same

Table 1 Principal characteristics of the laser-Doppler anemometer

5 mW He-Ne laser wavelength	632.8	mm
Focal length of lenses:		
imaging lens	300	mm
light-collecting lens	150	mm
Beam diameter, at e^{-2} intensity, of laser	0.65	mm
Beam half-angle	5.74°	
Fringe separation (line pair spacing)	3.164	μm
Major and minor axes to e^{-2} intensity	3.72, 0.37	mm
Number of fringes	118	
Magnification ratios of receiving optics for:		
"small" tank (D_2 = 5 cm)	0.54	
"medium" tank (D_2 = 10 cm)	0.56	
"large" tank (D_2 = 14 cm)	0.57	
Collecting aperture for:		
400 μm bead (nominal)	61 × 2	mm
30 μm fiber (nominal)	60 × 10	mm
Pinhole diameter	0.48	mm

Table 2 Principal characteristics of scattering particles

Size range (μm)	Particle material	Density (kg/m^3)	Refractive index	Sizing method
14-40	Lead glass	2950	1.6	DIN silk test sieves
40-75	Plexiglass ("Diakon")*	1190	1.49	BS sieves
175-212	Plexiglass ("Diakon")*	1190	1.49	BS sieves

*Registered trademark, ICI.

Nomenclature

D = depth of field of water tank (see Fig. 1)
L = distance between measuring volume and water tank (see Fig. 1)

Subscripts

1 = pertaining to distances in transmission path
2 = pertaining to distances in receiving path

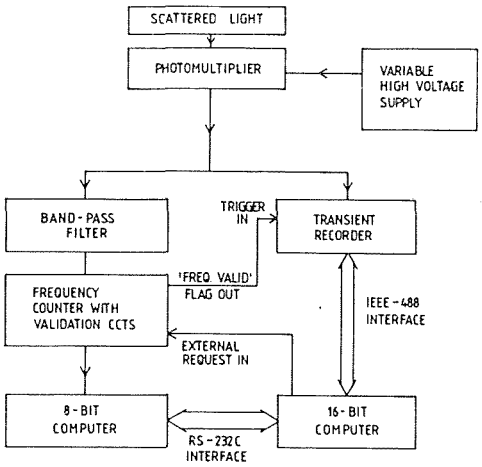

Fig. 2 Signal processing arrangement for velocity (counter) and maximum pedestal amplitude and visibility (transient recorder)

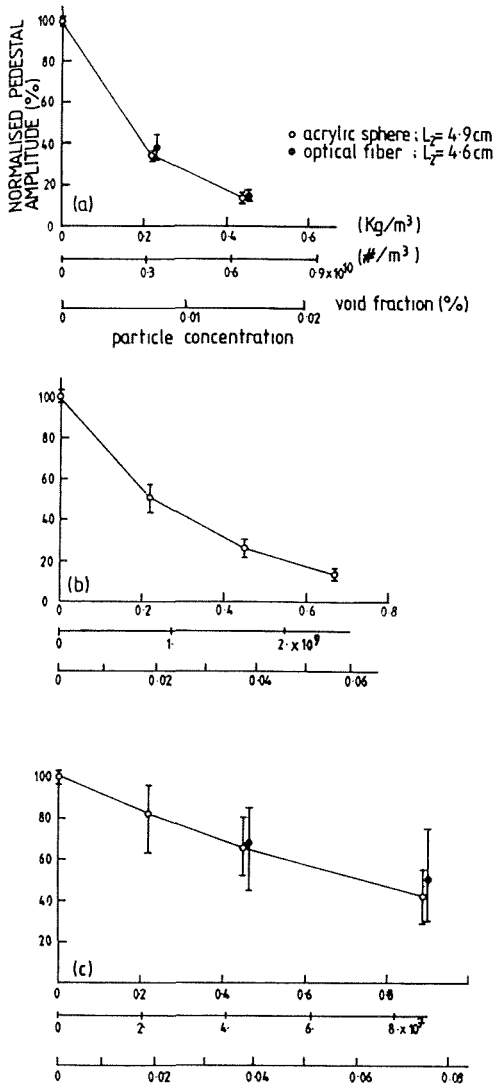

Fig. 3 Attenuation of pedestal amplitude by turbidity in receiving optics path for (*a*) 14-40 μm, (*b*) 40-75 μm, and (*c*) 175-212 μm particles. Depth of field, D_2 = 10 cm. See Fig. 1 for definition of L_2. Symbols are mean values: vertical bars show spread between the maximum and minimum values.

but that the spread of the random component of the attenuation is smaller here. This difference is because the sheet (from

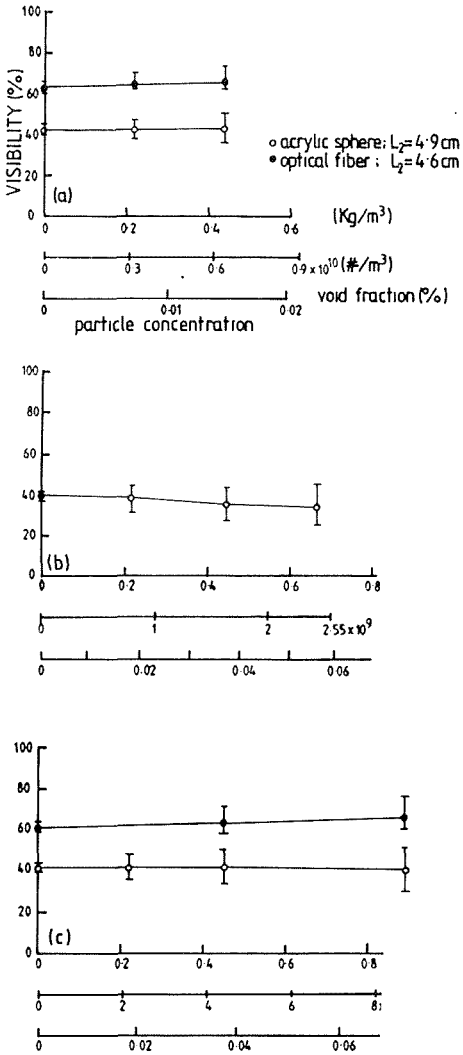

Fig. 4 Modification of visibility by turbidity in receiving optics path for (*a*) 14-40 μm, (*b*) 40-75 μm and (*c*) 175-212 μm particles. Depth of field, D_2 = 10 cm. See Fig. 1 for definition of L_2. Symbols are mean values: vertical bars show spread between the maximum and minimum values.

the fiber) or cone (from the sphere) of scattered light is interrupted by a larger number of particles than would interrupt the incident laser beams. The instantaneous number of particles is described by Poisson statistics and, since the mean number of interrupting particles is larger, the ratio of the standard deviation to the mean number is smaller.

Figure 4 allows comparison between the measurements of visibility for the sphere and the fiber, and the differences in visibility at zero void fraction are due to differences in the alignment of the aperture in the receiving optics. It is the change in the visibility relative to that recorded at zero void fraction that is of interest here. The results are similar for fiber and sphere and comparison with results for interruption of the incident laser beams shows that the magnitude of the random fluctuations here is smaller. The reader should note carefully that the random components of attenuation and visibility due to interruption in the transmission optics path increase as the diameter of the interrupting particles approaches the diameter of the incident laser beams: whereas these random components due to turbidity in the receiving optics path are not affected by this consideration. The incident beam diameter is approximately 400 μm (see Table 1) and a smaller diameter will result in larger random errors for the transmission path but will have no influence on the errors for the receiving path.

	D_1	D_2	L_1	L_2
○	5·0	10·0	16·5	3·5
●	–	10·0	–	4·9
△	5·0	–	16·5	–

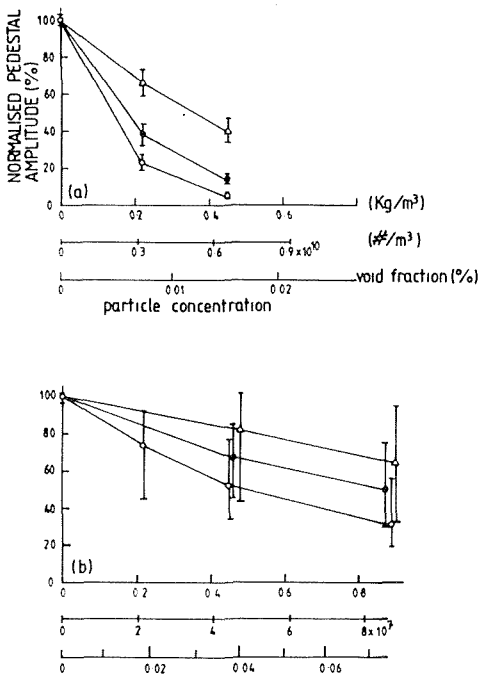

Fig. 5 Attenuation of pedestal amplitude by turbidity in transmission and receiving paths separately and simultaneously. (*a*) 14–40 μm, and (*b*) 175–212 μm particles. Lengths L and D (in cm) are defined in Fig. 1. Symbols are mean values: vertical bars show spread between the maximum and minimum values.

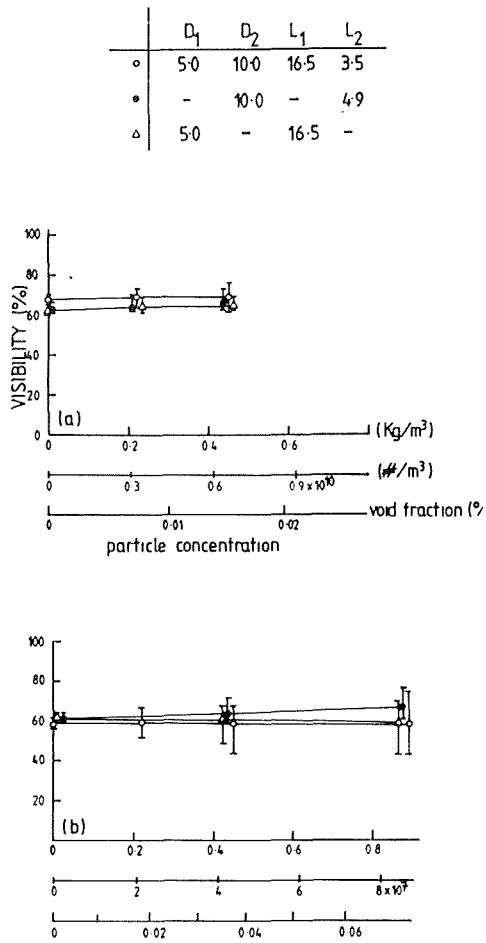

Fig. 6 Modification of visibility by turbidity in transmission and receiving paths separately and simultaneously. (*a*) 14–40 μm, and (*b*) 175–212 μm particles. Lengths L and D (in cm) are defined in Fig. 1. Symbols are mean values: vertical bars show spread between the maximum and minimum values.

Particles Simultaneously Present Between the Measuring Volume and the Transmitting and Receiving Optics. The simultaneous presence of turbidity on either side of the measuring volume has the expected effect (shown in Fig. 5) of lowering the mean value of the pedestal amplitude below that produced by interruption on either side separately. The results were obtained for depths of field of 5 and 10 cm on the transmitting and receiving sides, respectively, and for two particle size ranges. For comparison, the separate effects of interruption on either side are also included and this shows that the resultant mean attenuation for both tanks simultaneously present is equal to the product of the mean attenuation produced by each tank separately. The magnitude of the random component of attenuation is considered in the discussion below.

Figure 6 shows the corresponding effect on the signal visibility of simultaneous interruption of the light paths on both sides of the measuring volume. There is no large change in the mean visibility but the spread of the random variation of visibility is larger than is found with interruption on each side separately. The results may, however, be affected by the difference in the distance of the tank on the receiving optics side (i.e., L_2) from the measuring volume. This distance was 3.5 cm for simultaneous interruption and 4.9 cm for interruption on the receiving optics side only. The importance of this distance is described in the following subsection.

Separation Between Tank and Measuring Volume. Figures 7 and 8 show the effect on the pedestal amplitude and visibility of the separation between the tank (D_1 = 5 cm depth of field) containing the interrupting particles and the measuring volume on the transmitting optics side. Measurements were made for three separations (L_1 = 16.5, 10, and 3.5 cm) and two interrupting particle size ranges. Figure 7 shows that there is no dependence of the distribution of pedestal amplitudes on the separation. This is in contrast with the results for visibility (Fig. 8) which show that, for the larger particle size range (175–212 μm), the spread of the random component of visibility becomes wider the closer that the tank approaches the measuring volume. For the smaller size range (14–40 μm), there is no effect of the location of the tank.

Discussion

The implications of the results of the previous section are now considered for the application of laser-Doppler anemometry to the measurement of the size range of the particulate phase.

The spread of the visibility at any void fraction can be related to an error in the measurement of particle size by assuming a linear relationship between visibility (V) and particle diameter (d), which is a convenient approximation for $0.2 < V < 0.8$. The standard deviation (expressed as a percentage of the mean) in particle size due to turbidity in the path of the receiving optics is shown in Fig. 9 as a function of the void fraction (the conditions of Fig. 4 for the sphere). As would be expected, the error increases with increasing particle size and void fraction and the rms error is smaller than ±10 percent for interrupting particle diameters up to 212 μm and over the

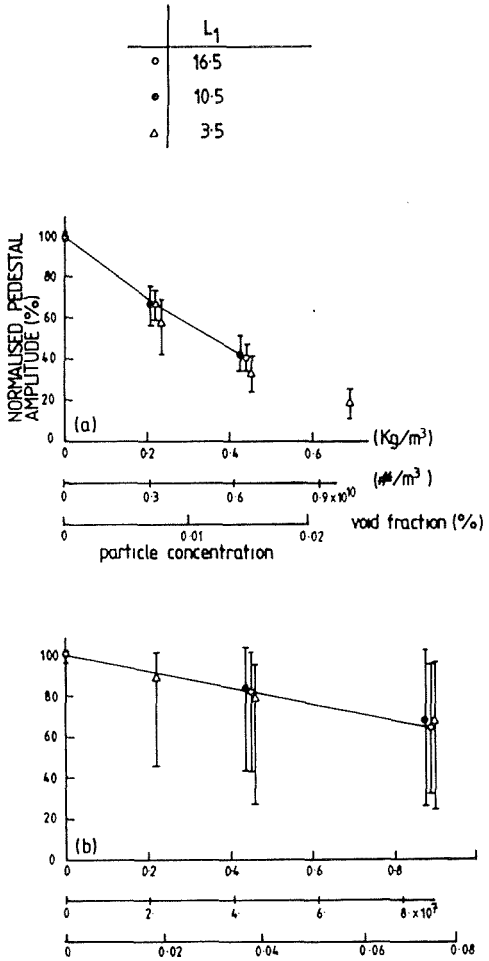

Fig. 7 Attenuation of pedestal amplitude by turbidity in transmission path for (*a*) 14-40 μm, and (*b*) 175-212 μm particles for three values of L_1 (in cm). Depth of field, D_1 = 5 cm.

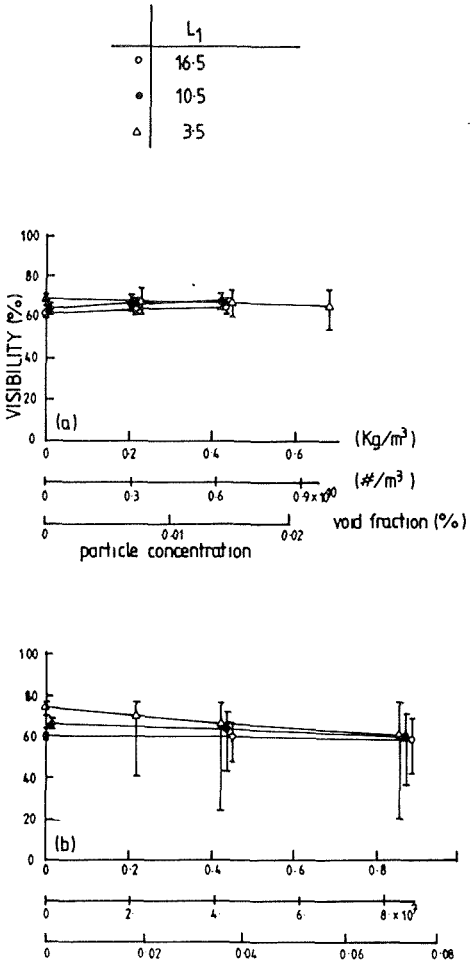

Fig. 8 Modification of visibility by turbidity in transmission path for (*a*) 14-40 μm, and (*b*) 175-212 μm particles for three values of L_1 (in cm). Depth of field, D_1 = 5 cm.

comparatively large depth of field of D_2 = 10 cm. For the conditions studied, there is no systematic influence of turbidity on the mean visibility. Figure 10 shows the same type of information for interruption of both the transmitting and receiving paths by particles in the 175–212 μm size range (the conditions of Fig. 6 for the fiber).

The figure shows that the error with interruption on both sides of the measuring volume is virtually indistinguishable from that which occurs due to turbidity in the transmitting path alone, where D_1 = 5 cm. The error due to turbidity in the receiving optics, where D_2 = 10 cm, is about half that caused by the turbidity in the transmitting path, even though the depth of field is twice as large. The error generated by a given turbidity between the transmitting optics and the measuring volume overshadows that due to the same turbidity between the volume and the receiving optics.

The results of Fig. 8 show that, for the larger size range, the random error in visibility (Fig. 11) generated by turbidity between the transmitting optics and the measuring volume becomes larger as the interrupting particles approach the measuring volume (i.e., as length L_1 decreases). The results suggest that "large" in this context refers to particles which are above one third of the diameter of the incident laser beams. This supports our observation (1987) that the spread of visibility becomes almost independent of depths of field greater than about 5 cm. The rapid increase in the spread of visibility as the interrupting particles approach the measuring volume suggests that the results underestimate the error because it was

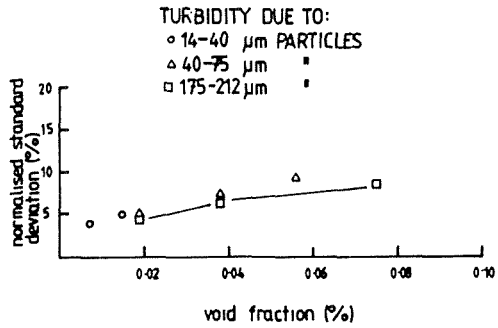

Fig. 9 Standard deviation in visibility due to turbidity in receiving path for three ranges of particle size. Depth of field, D_2 = 10 cm. Signal generated from Plexiglass (acrylic) sphere (400 μm nominal diameter).

not possible to make L_1 = 0, although the magnitude of the underestimation cannot be quantified from the available results. It is likely that a similar effect on the signal visibility occurs due to the distance of the tank on the receiving optics side (L_2) from the measuring volume. This has not been investigated but is certain to be a weaker influence than is L_1.

The relationship between particle diameter and visibility can be made single-valued for diameters up to about 60 μm but, above this size, the diameter must be inferred from an alternative measurement, such as the pedestal amplitude. Figures 3, 5, and 7 show that there is a systematic error due to the

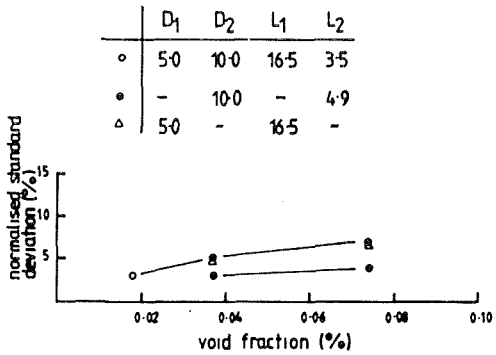

Fig. 10 Standard deviation in visibility due to turbidity in transmitting and receiving paths separately and simultaneously. Particle size: 175-212 μm. Lengths L and D (in cm) are defined in Fig. 1.

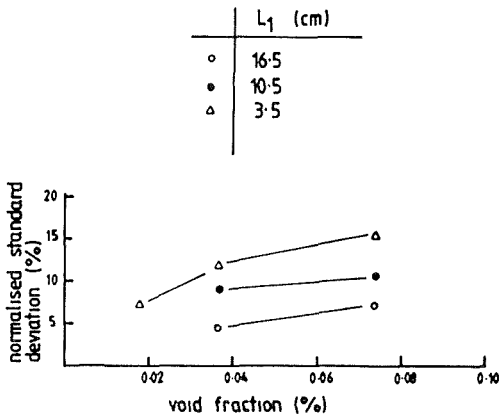

Fig. 11 Standard deviation in visibility due to turbidity in transmission path with L_1 as parameter. Depth of field, D_1 = 5 cm; particle size 175-212 μm.

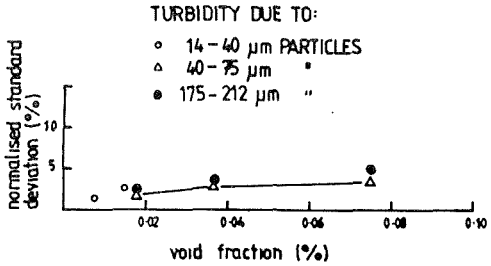

Fig. 12 Standard deviation in diameter inferred from pedestal amplitude due to turbidity in receiving path. Depth of field, D_2 = 10 cm.

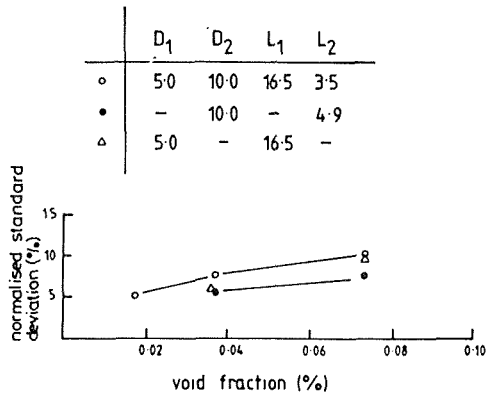

Fig. 13 Standard deviation inferred from pedestal amplitude due to turbidity in transmitting and receiving paths separately and simultaneously. Particle size: 175-212 μm. Lengths L and D (in cm) are defined in Fig. 1.

mean attenuation of this amplitude because of the turbidity on either side of the measuring volume. The magnitude of this error is found as $\epsilon = 1 - \sqrt{T}$, where T is the normalized pedestal amplitude, by assuming that the pedestal amplitude is proportional to the cross-sectional area of the particle (it is useful to note that the magnitude of the mean attenuation, and hence the mean error, can be estimated in any given flow by using the Lambert-Bouguer-Beer law for the purpose of assessing whether the error is unacceptably large). Negus and Drain (1982) have suggested that visibility and pedestal amplitude be used simultaneously to size particles smaller than 60 μm and this allows the determination of the constant of proportionality between amplitude and particle diameter for every point in the flow. With knowledge of this constant, it is argued that particles with diameter above 60 μm can be sized from the pedestal amplitude. In the absence of an independent local measurement of particle diameter, techniques which use the absolute intensity of the scattered light in either a laser-Doppler configuration or a single beam instrument must operate at particle concentrations which are sufficiently low that the resulting error is acceptable.

Although it is likely that the above procedure will account for the mean attenuation, it cannot remove the rms error due to the random variation about the mean. The standard deviation (again, expressed as a percentage of the mean) in particle size, inferred from the pedestal amplitude and due to turbidity in the path of the receiving optics, is shown in Fig. 12 for the conditions of Fig. 3. For interrupting particles with diameter smaller than 212 μm, the rms error is less than 5 percent over a 10 cm depth of field. The rms measurement error results in uncertainties in the calculated mean diameters of, for example, the size distribution of a spray. As an illustrative example, the consequences of a 10 percent rms error in measured visibility have been estimated for the size distribution of a kerosene spray measured by Hardalupas et al., 1990. The Sauter and volume mean diameters, which were measured by phase-Doppler anemometry and hence are unaffected the depth of field, were 57.9 and 44.7 μm, respectively, whereas the rms uncertainty would result in systematic shifts of about + 1 ½ and + ½ percent, respectively. The consequences of the rms measurement error will be more important when estimating the velocity of the carrier phase from that of the smallest particles in the flow, since the correlation between size and velocity will be broadened.

Measurements of particle size which are inferred from the pedestal amplitude are influenced by turbidity in both the transmitting and receiving paths. It has already been remarked that the overall mean attenuation is the product of the attenuations due to transmitting and receiving paths separately, which is expected. Figure 13 shows the same type of information but for interruption of both the transmitting and receiving paths by particles in the 175-212 μm range (the conditions of Fig. 5(b)). The rms error due to interruption in the path of the receiving optics is comparable to that due to interruption of the transmitting optics (contrast this with the result for visibility, Fig. 10), although the depth of field, D_2 (= 10 cm), is twice that in the transmitting path (D_1 = 5 cm). The rms error with interruption on both sides of the measuring volume is larger by between one and two percentage points than that due to interruption in the transmitting optics alone. Thus, although the larger contribution to the total rms error is likely to be due to the error caused by turbidity in the transmitting optics, the error generated in the path of the receiving optics may not be negligible and the magnitude of the latter should be assessed in each case. The overall variance due to turbidity on either side of the measuring volume is given, to accuracy sufficient for an error analysis, by the sum of the variances due to the turbidity on either side separately.

The information reported in this paper has two practical applications. It can guide the design of experiments by suggesting which combinations of particle and laser beam diameters, depth of field and void fraction should be avoided because of the ensuing low measurement accuracy. Second, it permits the estimation of the magnitude of systematic and rms errors, particularly when disadvantageous combinations of experimental conditions cannot be avoided.

Conclusions

1. Turbidity between the measuring volume and the receiving optics generates a spread of visibilities, corresponding to a tolerance on measured diameters, which increases with the void fraction of the interrupting particles. The tolerance caused by a given turbidity is larger for interruption between the measuring volume and the transmitting, rather than receiving, optics and, in practice, is likely to be the dominant source of uncertainty.
2. For particles larger than about one third of the incident beam diameter, the tolerance increases with decreasing distance between the interrupting particles and the measuring volume in the transmission path and the tolerance is generated mostly over the 5 cm nearest to the measuring volume. As a consequence, it is likely that the results underestimate the errors due to turbidity in the transmission path because L_1 was finite in the experiments.
3. The effect of turbidity on the pedestal amplitude can be separated into a mean attenuation and a spread about this mean, which correspond to mean and random errors in measured diameters. The mean attenuation caused by a given turbidity is the same for interruption on either side of the measuring volume and, for simultaneous interruption on either side, is the product of the attenuation on each side. The tolerance due to the mean component can be allowed for by simultaneous measurements of visibility, but the random error cannot be removed in this way and will increase with void fraction and diameter of the interrupting particles. The contribution of the turbidity in the path of the receiving optics to the total rms error is likely to be smaller that that due to interruption in the path of the transmitting optics.
4. In contrast to the results for visibility, the mean and random errors do not depend on the distance (L_1) between the interrupting particles and the measuring volume in the transmission path.

Acknowledgments

We are grateful to Dr. J. Gibb of CEGB Marchwood for useful technical discussions. This work is financed by the Science and Engineering Research Council and the Central Electricity Generating Board.

References

Allano, D., Gouesbet, G., Grehan, G., and Lisiecki, D., 1984, "Droplet Sizing Using a Top-Hat Laser Beam Technique," *J. Phys. D: Appl. Phys.*, Vol. 17, pp. 43–58.

Bachalo, W. D., 1980, "Method for Measuring the Size and Velocity of Spheres by Dual-Beam Light-Scatter Interferometry," *Applied Optics*, Vol. 19, pp. 363–370.

Durst, F., 1973, "Scattering Phenomena and Their Application in Optical Anemometry," *ZAMP*, Vol. 24, pp. 619–643.

Farmer, W. M., 1978, "Measurement of Particle Size and Concentrations Using LDV Techniques," *Proceedings, The Dynamic Flow Conference 1978 on Dynamic Measurements in Unsteady Flows* (eds. Kovasznay, L. S. G., Favre, A., Buchhave, P., and Fulachier, L.), Information Department, DANTEC Elektronic A/S, Skovlunde, pp. 373–395.

Hadded, O., Bates, C. J, and Yeoman, M. L., 1985, "Simultaneous Two-Phase Flow Measurement of Droplet Size and Velocity in a 32 mm Diameter Pipeline," *Second International Symposium on Laser Anemometry*, Miami, ASME FED, Vol. 33, pp. 103–109.

Hardalupas, Y., Taylor, A. M. K. P., and Whitelaw, J. H., 1990, "Velocity and Size Characteristics of Liquid-fuelled Flames Stabilised by a Swirl Burner," *Proceedings of the Royal Society of London*, Vol. A428, pp. 129–155.

Hess, C. F., 1985, "A Technique to Measure the Size of Particles in Laser-Doppler Velocimetry Applications," *Second International Symposium on Laser Anemometry*, Miami, ASME FED, Vol. 33, pp. 119–125.

Holve, D. J., and Self, S. A., 1979, "Optical Particle Sizing for in situ Measurements, Parts 1 and 2," *Applied Optics*, Vol. 18, pp. 1632–1652.

Holve, D. J., and Annen, K. D., 1984, "Optical Particle Counting, Sizing and Velocimetry Using Intensity Deconvolution," *Optical Engineering*, Vol. 23, pp. 591–603.

Hong, N. S., and Jones, A. R., 1976, "A Light Scattering Technique for Particle Sizing Based on Laser Fringe Anemometry," *J. Phys. D: Appl. Phys.*, Vol. 9, pp. 1839–1848.

Kliafas, Y., Taylor, A. M. K. P., and Whitelaw, J. H., 1987, "Errors in Particle Sizing by LDA Due to Turbidity in the Incident Laser Beams," *Experiments in Fluids*, Vol. 5, pp. 159–176.

Levy, Y., and Lockwood, F. C., 1981, "Velocity Measurements in a Particle Laden Turbulent Free Jet," *Comb. Flame*, Vol. 40, pp. 333–339.

Mizutani, Y., Kodama, H., and Miyasaku, K., 1982, "Doppler-Mie Combination Technique for Determination of Size-Velocity Correlation of Spray Droplets," *Comb. Flame*, Vol. 44, pp. 85–95.

Modarress, D., and Tan, H., 1983, "LDA Signal Discrimination in Two-Phase Flows," *Experiments in Fluids*, Vol. 1, pp. 129–134.

Negus, C. R., and Drain, L. E., 1982, "Mie Calculations of the Scattered Light from a Spherical Particle Traversing a Fringe Pattern by Two Intersecting Laser Beams," *J. Phys. D: Appl. Phys.*, Vol. 15, pp. 375–402.

Wang, J. C. F., and Tichenor, D. A., 1981, "Particle Size Measurements Using an Optical Variable-Frequency-Grid Technique," *Applied Optics*, Vol. 20, pp. 1367–1373.

Yule, A. J., Ereaut, P. R., and Ungut, A., 1983, "Droplet Sizes and Velocities in Vaporizing Sprays," *Comb. Flame*, Vol. 54, pp. 15–22.

Flow in a Rotating Straight Pipe, With a View on Coriolis Mass Flow Meters

F. Durst

H. Raszillier

Lehrstuhl für Strömungsmechanik,
Universität Erlangen-Nürnberg,
D-8520 Erlangen,
Federal Republic of Germany

The fully developed flow through a straight pipe, which rotates about an axis perpendicular to its own, is considered. The perturbation of the Hagen-Poiseuille flow, produced by the pipe rotation, is computed to second order and its features are described. The force of the fluid on the rotating pipe is correlated with other parameters of the flow, among them the mass flow rate Q. Possible relevance of the flow field and of the fluid forces in the rotating pipe for Coriolis flow meters are discussed.

1 Introduction

It is the aim of the present paper to look anew at the fluid flow through a rotating straight pipe (Barua, 1954; Benton, 1956; Jones and Walters, 1967). This kind of flow is interesting by itself, because it allows the investigation of nonlinear effects in the Navier-Stokes equation in a simple geometrical setting. It is, however, also of practical engineering relevance, because of the qualitative insight it offers into phenomena occurring in industrial devices, for instance in some flow rate measuring instruments. The simplest geometrical versions of these instruments pass the fluid through a straight pipe segment which is in planar vibration. The form of the vibration is influenced by the inertia of the fluid, mainly through the Coriolis effect; its analysis therefore furnishes a way to measure the mass flow rate of the fluid. For high precision measurements of one-phase mass flow and, especially, for the use of such instruments in particulate two-phase flow it is not enough to analyze only the vibration of the pipe and to take into account the fluid only by a mean velocity (Chen, 1987). A more detailed insight into the flow regime inside the oscillating pipe is certainly needed, as well as an understanding of its feedback on the behavior of the elastic pipe.

In this paper the secondary flow produced by rotation in a straight pipe is analyzed along the lines of Barua (1954), i.e., for laminar flow in which the effect of rotation is considered as a perturbation. His analytic results are extended here to the complete second order of perturbation. Higher orders can be obtained within a reasonable effort only by the use of computer algebra (Raszillier et al., 1988, 1990).

The features of the flow through the infinite rotating pipe provide elements for a qualitative understanding of the flow through the vibrating pipe segments of Coriolis mass flow meters. They also show to what degree global considerations are enough for the description of the reaction forces of the flowing fluid on the vibrating pipe segments and how these considerations can be refined.

Contributed by the Fluids Engineering Division for publication in the JOURNAL OF FLUIDS ENGINEERING. Manuscript received by the Fluids Engineering Division February 26, 1988.

The next section (2) of the paper presents the quantitative formulation of the problem to be discussed, defines the associated characteristic (Reynolds and Taylor) numbers, and formulates the strategy for the solution of the Navier-Stokes equations by a perturbation series. In Section 3 the two lowest orders of perturbation of the basic (Hagen-Poiseuille) flow, due to the rotation of the pipe, are presented and their qualitative properties are described. The reaction forces of the fluid against the imposed rotation of the pipe turn out (Section 4) to be independent of local details of the flow field, as long as the flow is fully developed. In particular, the force in the normal direction to the plane spanned by the pipe and rotation axes is precisely the Coriolis force, i.e., $2\dot{Q}\Omega$ when referred to the unit length of the pipe; here Ω denotes the angular velocity of the pipe and $\dot{Q}$ the mass flow rate. In the last section (5) the properties of the flow field and the fluid forces in the rotating straight pipe are used as a frame for an analysis of the phenomena which are expected to take place inside the vibrating pipe segment of the Coriolis flow meters. This analysis is qualitative, but it already shows the type of phenomena which have to be included in a detailed quantitative discussion of these flow meters. On the other hand, it shows how the fluid is expected to influence the particle trajectories in particulate two-phase flows. This could improve the understanding of the behavior of Coriolis flow meters in two-phase flow.

2 Equations Describing the Flow

A fixed (inertial) reference frame, with axes defined by the unit vectors $\mathbf{e}_1$, $\mathbf{e}_2$, $\mathbf{e}_2$ (Fig. 1) and a rotating coordinate frame rigidly attached to the pipe and characterized by the unit vectors $\mathbf{f}_1$, $\mathbf{f}_2$, $\mathbf{f}_3$ of the three axes will be considered. The common origin of both frames lies on the pipe axis and the vector $\mathbf{f}_3$ points along it. The $\mathbf{e}_1(=\mathbf{f}_1)$-axis is taken, following Barua (1954), as the axis of rotation of the pipe; the constant angular velocity is accordingly

$$\Omega = \Omega \mathbf{f}_1. \tag{2.1}$$

The geometry of the pipe suggests the use of cylinder coordinates (r, θ, z) in the frame attached to it (Fig. 2).

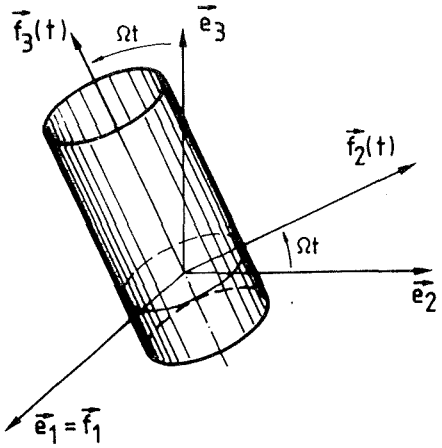

Fig. 1 Inertial and rotating frames of reference

There is only one geometrical length in this flow problem, the pipe radius a; together with the angular velocity Ω and the kinematic viscosity ν of the fluid it allows to form the dimensionless (Taylor) number

$$R = \frac{2\Omega a^2}{\nu}, \tag{2.2}$$

which characterizes the effect of rotation on the flow. In the fully developed flow the drop of the viscous pressure

$$\rho\chi(\mathbf{r}) = P(\mathbf{r}) - \frac{1}{2}\rho(\Omega \times \mathbf{r})^2, \quad \mathbf{r} = r\mathbf{f}_r + z\mathbf{f}_3, \tag{2.3}$$

(P = pressure, ρ = fluid density) in the direction of the pipe axis is a constant, say

$$-\frac{\partial \chi}{\partial z} = 4c\frac{\nu^2}{a^3}. \tag{2.4}$$

The dimensionless number c introduced here can be taken as an additional independent parameter characterizing the flow.[1] In the Hagen-Poiseuille flow ($R = 0$) c is precisely, with the normalization chosen here, the mean Reynolds number defined by $\frac{2\dot{Q}}{\pi\mu a}$ in terms of the mass flow rate $\dot{Q}$ and the dynamic viscosity $\mu = \rho\nu$. For the rotating pipe the ratio $\frac{2\dot{Q}}{\pi\mu a}\frac{1}{c}$ deviates from 1 and defines the resistance law of the flow.

The transverse part of the velocity field

$$\mathbf{V} = U\mathbf{f}_r + V\mathbf{f}_\theta + Wf_3 \tag{2.5}$$

in the rotating frame will be described, following Barua (1954), by a stream function $\Psi(r, \theta)$:

$$rU = -\frac{\partial \Psi}{\partial \theta}, \quad V = \frac{\partial \Psi}{\partial r}. \tag{2.6}$$

For the stream function Ψ and the axial velocity W one gets in a straightforward way two coupled partial differential equations. In terms of the dimensionless quantities ψ, w, x, defined by

$$\begin{aligned} r &= ax, \\ \Psi(r,\theta) &= \nu\psi(x,\theta), \\ W(r,\theta) &= \frac{\nu}{a}w(x,\theta) \end{aligned} \tag{2.7}$$

they are

$$x\nabla^4\psi = -R\left(x\cos\theta\frac{\partial w}{\partial x} - \sin\theta\frac{\partial w}{\partial \theta}\right) + \left(\frac{\partial \psi}{\partial x}\frac{\partial}{\partial \theta} - \frac{\partial \psi}{\partial \theta}\frac{\partial}{\partial x}\right)\nabla^2\psi, \tag{2.8}$$

[1] Barua's number with the same notation is in the present convention $-4c$.

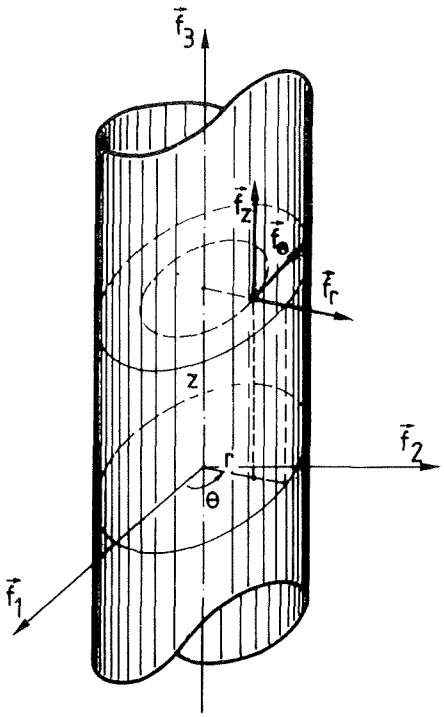

Fig. 2 Definition of cylinder coordinates

$$x\nabla^2 w = R\left(x\cos\theta\frac{\partial \psi}{\partial x} - \sin\theta\frac{\partial \psi}{\partial \theta}\right) + \left(\frac{\partial \psi}{\partial x}\frac{\partial}{\partial \theta} - \frac{\partial \psi}{\partial \theta}\frac{\partial}{\partial x}\right)w - 4cx. \tag{2.9}$$

One may look for a solution of these equations in the form of series expansions in the Taylor number R,

$$w(x,\theta) = \sum_{n=0}^{\infty} R^n w_n(x, \theta), \tag{2.10}$$

$$\psi(x, \theta) = \sum_{n=0}^{\infty} R^n \psi_n(x, \theta). \tag{2.11}$$

This solution represents a perturbation of the Hagen-Poiseuille flow $w_0(x, \theta) = c(1 - x^2)$, $\psi_0(x, \theta) = 0$, produced by the rotation of the pipe.

The nonlinear equations for w, ψ lead to an infinite system of equations for the various orders of perturbation w_n, ψ_n ($n = 1, 2, \ldots$):

$$x\nabla^4\psi_n = -\left(x\cos\theta\frac{\partial w_{n-1}}{\partial x} - \sin\theta\frac{\partial w_{n-1}}{\partial \theta}\right) + \sum_{k=1}^{n-1}\left(\frac{\partial \psi_k}{\partial x}\frac{\partial}{\partial \theta} - \frac{\partial \psi_k}{\partial \theta}\frac{\partial}{\partial x}\right)\nabla^2\psi_{n-k}, \tag{2.12}$$

$$x\nabla^2 w_n = 2cx\frac{\partial \psi_n}{\partial \theta} + \left(x\cos\theta\frac{\partial \psi_{n-1}}{\partial x} - \sin\theta\frac{\partial \psi_{n-1}}{\partial \theta}\right) + \sum_{k=1}^{n-1}\left(\frac{\partial \psi_k}{\partial x}\frac{\partial}{\partial \theta} - \frac{\partial \psi_k}{\partial \theta}\frac{\partial}{\partial x}\right)w_{n-k}, \tag{2.13}$$

which allows their stepwise computation starting from w_0 and ψ_0. Thereby first the transverse flow of order n (ψ_n) is computed from the axial flow of order $n-1$ (w_{n-1}) and from the mutal interferences of lower-order transverse flows. Then the axial flow of order n (w_n) is computed from the transverse flows of orders $n-1$ and n (ψ_{n-1} and ψ_n) and from interferences of the lower-order axial and transverse flows.

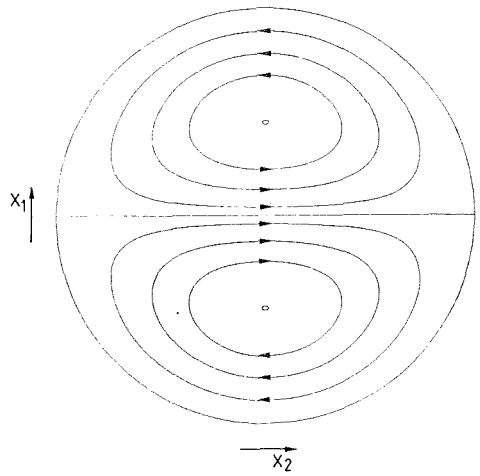

Fig. 3 Streamlines of the first order transverse flow, ψ_1

3 Approximate Solution and Interpretation

The system of equations (2.8), (2.9) can be interpreted qualitatively as follows. The linear terms on the right-hand side of equations (2.8), (2.9) have their origin in the Coriolis force. This force generates, according to equation (2.12), from the axial flow w_{n-1} a transverse flow ψ_n. The transverse flow ψ_{n-1} produces a Coriolis force which acts along the pipe axis and modifies, according to equation (2.13), the axial flow by w_n. Besides this feedback mechanism between axial and transverse flows to increasing orders of perturbation, which is reflected by the linear parts of equations (2.12), (2.13), there is an interference between different orders of perturbation, described by the nonlinear terms.

The lowest order contributions to the stream function, ψ_1, and to the perturbation of the axial velocity, w_1, have been computed by Barua (1954):

$$\psi_1(x, \theta) = \frac{c}{3 \cdot 2^5} x(1-x^2)^2 \cos\theta, \tag{3.1}$$

$$w_1(x, \theta) = \frac{c^2}{3^2 \cdot 2^8} x(1-x^2)(x^4 - 3x^2 + 3)\sin\theta. \tag{3.2}$$

From (2.13) it is seen that w_1 has no contribution from the Coriolis term; it is entirely produced by interference between w_0 and ψ_1.

The computation of the next order is already rather tedious: Barua (1954) has computed by hand ψ_2,

$$\psi_2(x, \theta) = \frac{c^2}{2^{15} \cdot 3^3 \cdot 5} x^2(1-x^2)^2(17 - 2x^2 - x^4)\sin 2\theta, \tag{3.3}$$

and part of w_2. The complete evaluation of w_2 gives

$$w_2(x, \theta) = g_1(x) + g_2(x)\cos 2\theta, \tag{3.4}$$

$$g_1(x) = \frac{c}{2^7 \cdot 3^2}(x^2-1)^3 + \frac{c^3}{2^{17} \cdot 3^4 \cdot 5}(x^2-1)^4(-10x^4 + 32x^2 - 37),$$

$$g_2(x) = \frac{c}{2^9 \cdot 3^2} x^2(x^2-1)(3x^2-5)$$

$$+ \frac{c^3}{2^{17} \cdot 3^4 \cdot 5^2 \cdot 7} x^2(x^2-1)(48x^8 - 302x^6 + 958x^4 - 1457x^2 + 923).$$

It is very time-consuming to do it by hand. Fortunately it turns out that equations (2.12), (2.13) can be brought to a form which is particularly suited for analytical calculation by computer (Raszillier et al., 1988). The calculation can then be extended to rather high orders of perturbation (Raszillier et al., 1990); the check of (3.1)-(3.4) by computer algebra is straightforward.

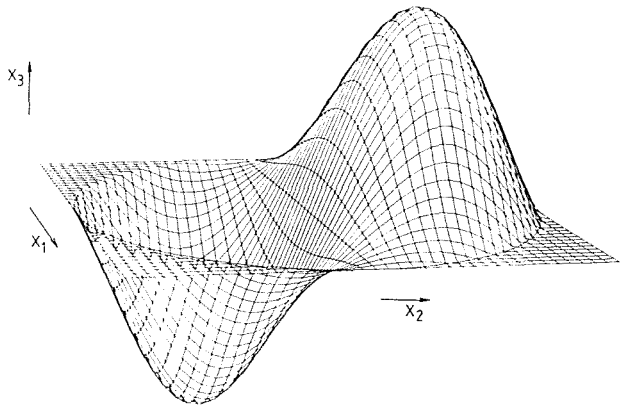

Fig. 4 First-order correction to the axial flow, w_1, in arbitrary units

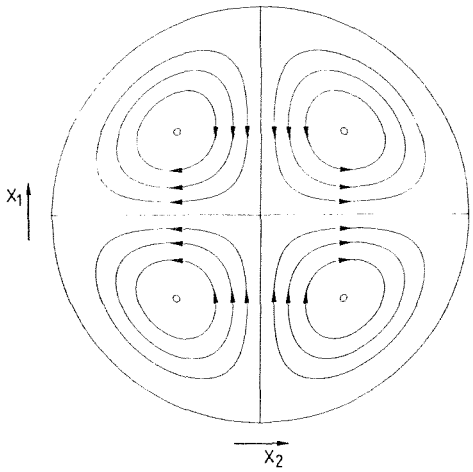

Fig. 5 Streamlines of the second-order transverse flow, ψ_2

The transverse flow has to lowest order two critical points, of vanishing velocity, at

$$x = \frac{1}{\sqrt{5}} = 0.447\ldots, \qquad \theta = 0, \pi, \tag{3.5}$$

which are the centers of two vortices (Fig. 3). The Coriolis force generated by these vortices is active only in w_2. The first-order perturbation, w_1, has its origin, as already mentioned, in the interference between w_0 and ψ_1; its effect is an increase of the axial velocity in the angular range $0 < \theta < \pi$ and a decrease in $-\pi < \theta < 0$ (Fig. 4). Thereby the velocity profile is perturbed, but the flow rate is not changed. This perturbation produces, therefore, as secondary axial flow driven by fluid inertia, an infinitely long vortex superposed over the Hagen-Poiseuille flow. Since Rw_1 is linear in R, but quadratic in c, this flow will reverse with the sense of rotation, but not with that of the main flow.

The second-order perturbation of the transverse flow, ψ_2, consists of four vortices (Fig. 5) which can be traced back, qualitatively, to the effect of the Coriolis force on the first-order perturbation, w_1, of the axial flow: there are two vortices in each half of the pipe cross section, where $w_1 > 0$ and $w_1 < 0$ respectively, which are like the two vortices of ψ_1, produced via the Coriolis term in (2.12) by w_0.

The axial flow of second order, w_2, leads through the term g_1 to a change (decrease) in the flow rate and through the term $g_2 \cos 2\theta$ to two infinitely long vortices (Fig. 6). These vortices can be interpreted for very low (Reynolds) numbers c (Fig. 6(a)), where the first term in g_2 dominates, in the same way

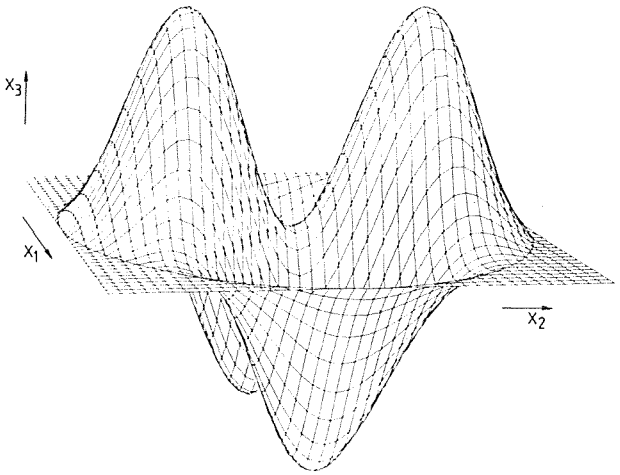

Fig. 6(*a*) For very small (Reynolds) numbers (*c*)

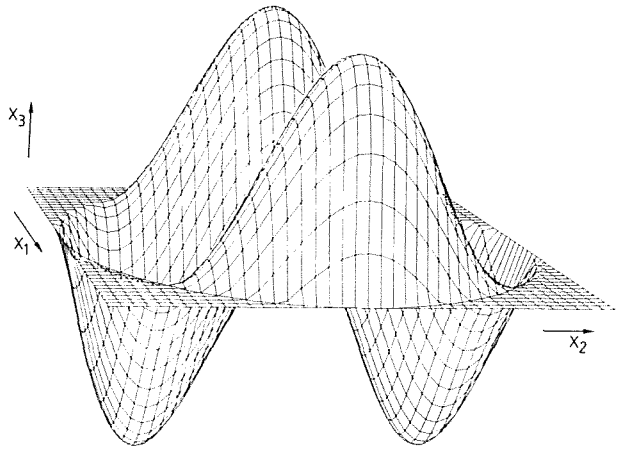

Fig. 6(*b*) For (Reynolds) numbers *c* around 80.

Fig. 6 Contribution $g_2 \cos 2\theta$ to the second-order correction of the axial flow, w_2, in arbitrary units

as the vortex of w_1: the transverse flow ψ_2 toward the pipe wall increases the axial velocity, that away from the wall decreases it: this determines the sense of the flow w_2. With increasing values of c (Fig. 6(*b*)) the second term in g_2 starts to dominate and the sense of the vortices changes.

4 Forces of the Fluid on the Pipe

When the velocity field of the flow is known, it is straightforward to compute the pressure distribution. Then one possesses all elements of the stress tensor σ_{ij}, which allows the computation of the forces and moments, by which the fluid acts on an element Σ_W of the inner pipe surface.

The force $\mathbf{F} = (F_1, F_2, F_3)$ is given by

$$F_i = -\int_{\Sigma W} \sigma_{ij}\, n_j\, dS, \tag{4.1}$$

where the normal vector unit $\mathbf{n} = (n_1, n_2, n_3)$ of Σ_W points from the fluid to the pipe. On the pipe surface the stress tensor is, up to a sign, equal to the tensor of momentum flux Π_{ij} (Landau and Lifshits, 1959),

$$\sigma_{ij} = -\Pi_{ij}. \tag{4.2}$$

Therefore one has the relation

$$F_i = \int_{\mathcal{V}} \frac{\partial \Pi_{ij}}{\partial X_j}\, d\mathcal{V} - \int_{\Sigma I} \Pi_{ij} n_j\, dS, \tag{4.3}$$

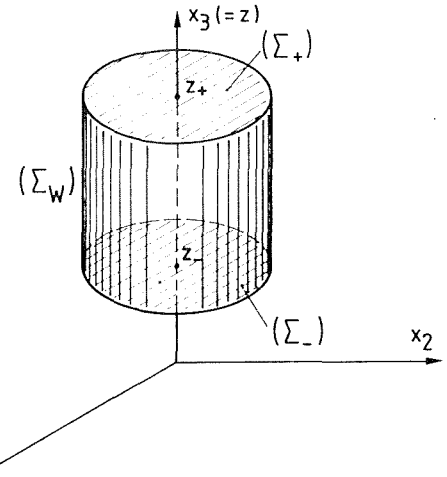

Fig. 7 Illustration to the computation of the fluid force

where the two surface elements Σ_W, Σ_I form together the whole boundary $\partial\mathcal{V} = \Sigma_W + \Sigma_I$ of the fluid volume $\mathcal{V}$. In (4.3) the volume integral of $\frac{\partial \Pi_{ij}}{\partial x_j}$ can be replaced with the help of the Navier-Stokes equation for an incompressible fluid by integrals of the densities

$$-\rho \frac{\partial V_i}{\partial t} + 2\rho(\mathbf{V} \times \Omega)_i + \frac{1}{2}\rho \left(\nabla (\Omega \times \mathbf{r})^2 \right)_i \tag{4.4}$$

of the inertial forces in the rotating frame. The resulting formula

$$F_i = -\frac{\partial}{\partial t}\int_{\mathcal{V}} \rho V_i\, d\mathcal{V} - 2\rho \left(\Omega \times \int_{\mathcal{V}} \mathbf{V}\, d\mathcal{V} \right)_i + \frac{1}{2}\rho \int_{\mathcal{V}} (\nabla (\Omega \times \mathbf{r})^2)_i d\mathcal{V} - \int_{\Sigma I} \Pi_{ij}\, n_j\, dS \tag{4.5}$$

follows exactly from the definition of the force and from the integral form of the momentum equation equation for the incompressible fluid (Pao, 1967). This formula is useful if the information available about the flow allows either to compute the force explicitly or to correlate it with global physical quantities which are directly accessible to measurement.

When the velocity field is fully developed, i.e., independent of the axial coordinate z, the interpretation of (4.5) becomes particularly transparent, if one considers as $\mathcal{V}$ the fluid volume between two cross sections $z = z_+$ and $z = z_-$ $(z_+ > z_-)$ of the pipe (Fig. 7). One gets for the force exerted by this fluid element on the pipe

$$F_1 = 0, \tag{4.6}$$

$$F_2 = 2\dot{Q}\Omega\Delta z, \tag{4.7}$$

$$F_3 = -\pi a^2 \rho (\bar{\chi}_+ - \bar{\chi}_-) - \Delta z \frac{d\dot{Q}}{dt}, \tag{4.8}$$

where $\rho\bar{\chi}_\pm$ is the average of the pressure $\rho\chi$ over the cross sections $\Sigma_\pm$,

$$\bar{\chi}_\pm = \frac{1}{\pi a^2} \int_{\Sigma_\pm} \chi r dr\, d\theta. \tag{4.9}$$

The transverse force of the fluid on the pipe is the Coriolis force, expressed through the mass flow rate

$$\dot{Q} = \rho \int_\Sigma W dS, \tag{4.10}$$

the longitudinal force F_3 (shear stress) is related to that part

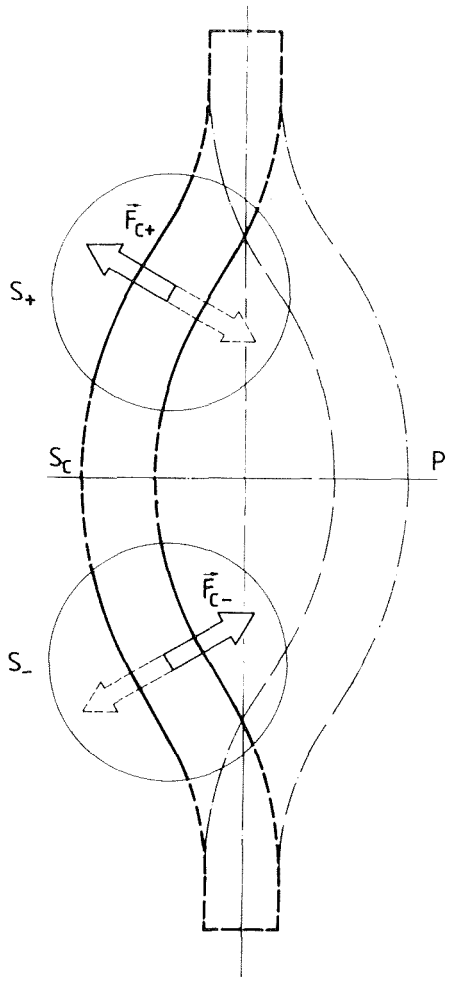

Fig. 8 Oscillating pipe segment, with the central section S_c in translation and the two oppositely rotating sections $S_\pm$

of the pressure drop, which is due to the fluid viscosity. When the magnitude of the angular velocity ($\Omega(t)$) is not constant in time, an additional inertial term, $\pi a^2 \Delta z \bar{z} \rho \dfrac{d\Omega(t)}{dt}$, with $\bar{z} = \dfrac{1}{2}(z_+ + z_-)$, appears in F_2.

Simple global correlations like those expressed by (4.7), (4.8), are no longer available, if the flow is geometrically or dynamically more complicated. One has then to come back to the solution of the local equations describing the fluid flow and to the computation of the tensor σ_{ij}, which gives the complete local information on the stresses produced by the fluid.

5 Relation to Coriolis Flow Meters

Mass flow rate measuring devices based on the Coriolis effect have in their simplest geometrical realization as fluid dynamical component a straight pipe, which performs planar oscillations (Fig. 8). The two segments ($S_\pm$) of this pipe, which are of particular interest here, are during the pipe oscillation essentially in a rotational motion; the motion of the segment (S_c) between them is essentially a translation. Therefore the considerations of the preceding Sections may be applied qualitatively to the segments $S_\pm$.

First, a few words on the limits of these considerations should be said. The considerations of local character, presented in Sections 2 and 3, are valid in a certain region of the (c, R)-plane, which can be reasonably estimated from the convergence properties of the flow rate Q as a function of c and R. For this one has to know a rather large number of terms of the expansions (2.10), (2.11) (Raszillier et al., 1990). In the limit $R \to 0$, $c \to \infty$, with a finite value of $\lim Rc = K$, this estimate has been given numerically by Mansour (1985), with the result that K should be smaller than a critical value $K_c = 413.3\ldots$. For qualitative purposes this result can be extrapolated beyond the infinitesimal region for which it was originally obtained. One arrives in this way at the estimate

$$c^2 R^2 < K_c^2 \tag{5.1}$$

for the region of validity of (2.10), (2.11). Outside this region one has to investigate the flow by other approaches. Yet numerical computations (Duck, 1983) suggest, that even for $c = 1500$ and $R = 10$ well outside (5.1) there are no significant departures of the transverse stream lines and the axial velocity from the picture given by the perturbation expansions. A complete picture of this flow, over the whole (c, R)-plane, is at present still missing. Therefore it seems natural to appeal to available pieces of local information from the series (2.10), (2.11) and to model independent global information, as that described in Section 4, in order to develop a qualitative picture of the rather more complicated flow in a Coriolis flow meter.

If one associates the two segments $S_\pm$ of the oscillating pipe with two oppositely rotating pipes, one expects the appearance of secondary flow in each of these segments. The relative orientation of these expected flows depends on the behavior of the axial velocity w and the stream function ψ under reversal of rotation ($\Omega \to -\Omega$). The flows in S_+ and S_- match only if w and ψ are insensitive to the sign of R: $w(r, \theta; -R) = w(r, \theta; -R)$, $\psi(r, \theta; -R) = \psi(r, \theta; -R)$. The pipe flow obeys the symmetry relations

$$w(r, \theta; -R) = w(r, -\theta; R), \tag{5.2}$$

$$\psi(r, \theta; -R) = -\psi(r, -\theta; R), \tag{5.3}$$

(Raszillier et al., 1988, 1990), which express the fact that the right and left parts of the velocity field in the rotating pipe exchange with the change of the rotation ($R \to -R$). For the matching condition of the flows in S_+ and S_- this symmetry implies that the axial velocity is left-right symmetric, $w(r, \theta; R) = w(r, -\theta, R)$, and the stream function is antisymmetric, $\psi(r, \theta; R) = -\psi(r, -\theta; R)$. Since the terms of the series expansions (2.10), (2.11) have the symmetry properties

$$w_n(r, -\theta) = (-1)^n w_n(r, \theta), \tag{5.4}$$

$$\psi_n(r, -\theta) = -(-1)^n \psi_n(r, \theta), \tag{5.5}$$

(Raszillier et al., 1988, 1990), which can be easily verified by the functions (3.1)–(3.4), one notices that there are obstructions to the matching, coming from the terms of odd order in the expansion of w and ψ. So one may expect in the sections S_+ and S_- of the oscillating pipe the same flow pattern, with a smooth matching over S_c, only when even orders dominate in these expansions. The odd orders tend to develop oppositely oriented flows in the two sections $S_\pm$. The actual flow pattern in the oscillating pipe is, therefore, expected to develop an asymmetry with respect to the geometric symmetry plane (P) of the pipe.

An asymmetry in the oscillation of the pipe is already produced by the main flow of the fluid in the pipe; it can be interpreted in terms of the Coriolis force (4.7) and, consequently, in terms of the mass flow rate $\dot{Q}$. Namely, since the Coriolis force changes sign with Ω, it acts oppositely in the sections $S_\pm$ of the oscillating pipe and produces in the oscillation an asymmetry with respect to the plane (P). This is the basic principle on which the Coriolis type of mass flow meter is based. An angular acceleration $\dfrac{d\Omega}{dt}$ produces, as discussed in Section 4, a force which acts in a symmetric way with respect

to the plane (P). One can view the asymmetry of the pipe oscillation in a first approximation as being produced by the moment of the Coriolis forces F_{c+} and F_{c-}. However, at the level of precision to which the instruments now tend, one is already faced with the need to go beyond the commonly used mean flow approximation in the analysis of the oscillations of the fluid conveying elastic pipe. The secondary flow in the pipe is possibly an additional source of asymmetry in the pipe oscillation of these instruments, with influence on their precision. There may be others too. Therefore more detailed answers concerning the fluid behavior in the pipe and its effect on the oscillation of the pipe will be needed. The present paper is a first attempt in this direction.

References

Barua, S. N., 1954, *Proc. Roy. Soc.*, (London), Series A227, p. 133.

Benton, G. S., 1956, ASME *Journal of Applied Mechanics*, Vol. 23, p. 123.

Jones, J. R., and Walters, T. S., 1967, *Z. Angew. Math. Phys.*, Vol. 18, p. 774.

Duck, P. W., 1983, *Phys. Fluids*, Vol. 26, p. 614.

Mansour, K., 1985, *J. Fluid Mech.*, Vol. 150, p. 1.

Chen, S.-S., *Flow-Induced Vibration of Circular Cylindrical Structures*, Hemisphere, Washington, 1987.

Raszillier, H., Guiasu, I., and Durst, F., 1988, University of Erlangen Report LSTM 234/T/88.

Raszillier, H., Guiasu, I., and Durst, F., 1990, *Symbolic Computation of Flow in a Rotating Pipe*, *Int. J. Numer. Methods Fluids*, Vol. 10, in print.

Landau, L. D., and Lifshits, E. M., 1959, *Fluid Mechanics*, Pergamon, London.

Pao, R. H. F., 1967, *Fluid Dynamics*, Merrill, Columbus, Ohio.

Charles C. S. Song
Professor,
St. Anthony Falls Hydraulic Laboratory,
Department of Civil and
Mineral Engineering,
University of Minnesota,
Minneapolis, MN 55414

Mingshun Yuan
Post Doctoral Fellow,
Department of Hydraulic Engineering,
Tsinghua University, Beijing
People's Republic of China

Simulation of Vortex-Shedding Flow About a Circular Cylinder at High Reynolds Numbers

Vortex shedding over a circular cylinder is modeled based on the weakly compressible flow equations with a simple subgrid scale turbulence model and a simple hybrid boundary condition. An explicit finite volume method is used. A subcritical and a supercritical case are computed. It is shown that the large-scale vortex-shedding phenomenon, the primary vortices, and the related oscillatory lift and drag can be calculated fairly well with a grid system coarser than the boundary layer thickness. The secondary vortices and the related higher frequency oscillations are also calculated by using somewhat finer grids.

Introduction

Understanding of the vortex-shedding flow behind a stationary circular cylinder is of great fundamental and practical importance. Numerous studies have been made for low Reynolds number cases ($Re < 1000$) by solving the Navier-Stokes equations for two-dimensional flow directly. A recent computational work of Braza et al. [1] showed the existence of secondary eddies previously observed experimentally by Bouard and Coutanceau [2], and elucidated the process of merging of two secondary eddies to form a primary eddy that is subsequently shed. Eaton's [3] analysis of streamlines and streaklines relating to the initiation of a shedding process confirmed the interpretation of Prandtl's movie by Perry et al. [4].

Direct calculation of vortex shedding flow is not practical at large Reynolds numbers because a very dense computational grid is needed to resolve the details of small-scale turbulence and thin boundary layers. The most common approach to solving large Reynolds number flows is to divide the flow field into the potential flow region and the boundary-layer region. The discrete vortex method for two-dimensional flows [5–7] and the vortex-lattice method [8–10] for three-dimensional flows are relatively recent developments which take into account the first order effect of vorticity shedding on the outer flow. It appears that the vortex method can fairly adequately simulate the vortex-shedding phenomenon because the viscous effect is relatively unimportant to large-scale eddies. However, the potential flow-boundary-layer approach cannot directly deal with the subjects of vortex diffusion and energy dissipation in the wake region.

The primitive equations of inviscid flow, such as Euler equations, support vorticity convection. If there is a proper numerical mechanism to produce vorticity on the cylinder surface, it should give a solution similar to that of the discrete vortex method. The advantage of using the equations of primitive variables is that they are easily extended to the viscous and turbulent flows and to the three-dimensional cases. The results obtained by the recent studies on inviscid separation are quite encouraging. Many researchers [11–14] showed that inviscid separation was caused by a singular boundary, such as a sharp corner, a smooth boundary with large curvature, or a shock. Although the full-slip condition is enforced at the rigid boundary when Euler equations are solved, the singular boundary could effectively create a vorticity source as the thin boundary layer does in the real flow. Quite often the analogy between the modeled result and the real flow is striking [11].

In the present study of vortex shedding flow, the full Navier-Stokes equations of large eddy motion are solved numerically. The primary boundary layers on the body are not actually resolved but are approximated by applying various degrees of partial-slip boundary conditions, ranging from full-slip to no-slip, depending on the relative magnitude of the boundary-layer thickness and the grid size chosen. The idea of using partial-slip boundary condition is similar to that of the wall function approach widely used in turbulent flow modeling. A more detailed description will be given later.

Governing Equations and Vorticity Dynamics

The weakly compressible flow is described in reference [15]. A brief explanation is given herein. For a barotropic process in which density is a function of pressure, the equation of continuity may be written as

$$\frac{\partial p}{\partial t} + \mathbf{u} \cdot \nabla p + \rho a^2 \nabla \cdot \mathbf{u} = 0 \tag{1}$$

where ρ, a, p, and $\mathbf{u}$ are fluid density, sound speed, pressure, and velocity vector, respectively. A weakly compressible flow refers to the flow with Mach number so small that ρ and a in equation (1) may be regarded as constants without causing significant error. By dimensional analysis, it can be shown

Contributed by the Fluids Engineering Division and presented at the Winter Annual Meeting, San Francisco, Calif., December 10-15, 1989 of THE AMERICAN SOCIETY OF MECHANICAL ENGINEERS. Manuscript received by the Fluids Engineering Division July 7, 1988. Paper No. 89-WA/FE-3.

that the second term in equation (1) is of order M^2 and can be neglected. The first term, however, should be retained if the flow is unsteady or the Strouhal number is very large.

The equation of motion of incompressible flow,

$$\frac{\partial \mathbf{u}}{\partial t} + \mathbf{u} \cdot \nabla \mathbf{u} + \frac{1}{\rho} \nabla p = \nu \nabla^2 \mathbf{u} \tag{2}$$

can be shown to be of the same order of accuracy as equation (1) if the Mach number is small. Thus, the weakly compressible flow may be defined as the flow with very small M such that equations (1) and (2) with ρ and a equal to constants may apply. It should also be noted that the weakly compressible flow is equivalent to multidimensional hydraulic transient flow.

For turbulent flow computations, the cell averaged large eddy simulation method [16, 17] has been adopted. In this case by taking the average of equation (2) over a finite volume, the equation of motion is written as

$$\frac{\partial \mathbf{u}}{\partial t} + \mathbf{u} \cdot \nabla \mathbf{u} + \frac{1}{\rho} \nabla p = \nu \nabla^2 \mathbf{u} - \overline{u_i' u_j'} \tag{2a}$$

A simple subgrid scale turbulence model proposed by Smagorinsky [18] and used by many others [19] with fairly good results is adopted. This model is based on the turbulent viscosity concept,

$$-\overline{u_i' u_j'} = \nu_T \, \overline{\partial u_i / \partial x_j} \tag{3}$$

where ν_T is the SGS diffusivity, being modeled by

$$\nu_T = (C\Delta)^2 (2 \bar{S}_{ij} \bar{S}_{ij})^{1/2} \tag{4}$$

In equation (4), $\bar{S}_{ij} = \frac{1}{2}(\partial \bar{u}_i / \partial x_j + \partial \bar{u}_j / \partial x_i)$ is the resolvable strain rate, Δ is the grid size, and C is the SGS coefficient to be determined by trial. In the present study of two-dimensional flows, $C = 0.5$ appears to give reasonable results.

For a special case of two-dimensional incompressible flows, by taking the curl of equation (2), we obtain the well-known vorticity transport equation,

$$\frac{\partial \omega}{\partial t} + \mathbf{u} \cdot \nabla \omega = \nu \nabla^2 \omega \tag{5}$$

in which ω is the vorticity. According to this equation, at least when the Mach number is very small, vorticity is conserved while it is transported by convection and diffusion. In other words vorticity production and destruction can take place only at the boundary but not in the flow field. Vorticity can be transported into or out of the flow field through the upstream end or the downstream end, mainly due to convection. It is usually produced at the solid boundary due to the adhesive force between fluid and solid (but not due to viscosity) which is mathematically represented by the no-slip or partial-slip boundary condition. The vorticity generated at the wall is transported away from the wall by viscous diffusion. It is important to note that viscosity, either real or numerical, has nothing to do with vorticity production or destruction, at least in the two-dimensional incompressible flow case.

Let us now consider the viscous flow about a flat plate placed parallel with an otherwise uniform flow of velocity U. At the leading edge, the velocity is suddenly brought to zero and a very large vorticity is produced there. The diffusion and convection mechanism start to transport the vorticity produced at the leading edge. At an arbitrary distance x downstream of the leading edge, the total vorticity flux across the boundary layer is, within the accuracy of boundary-layer approximation,

$$\frac{d\Gamma}{dt} = \int_0^\delta u \frac{\partial u}{\partial n} \, dn = \frac{1}{2} U^2 = \text{constant} \tag{6}$$

where Γ is the circulation and $d\Gamma/dt$ is the vorticity flux. Since vorticity flux is constant for all x, except at the leading edge, no vorticity is being generated or destroyed anywhere in the boundary layer, except at the leading edge. Moreover, the vorticity flux is determined only by the velocity in the outer region. For the flow about a circular cylinder to be analyzed, equation (6) still holds except that U is a variable representing the speed at the edge of the boundary layer. The concept described above is extremely important to the understanding of the work to follow.

It was pointed out by Song and Yuan (1988) that the weakly compressible flow approach becomes essentially equivalent to Chorin's (1967) artificial compressibility approach if the convective term in equation (1) is neglected and an artificial value is assigned to the speed of sound (a) to facilitate the speed of convergence. To enhance the convergence speed, this work uses a multicompressibility approach; start the computation with an artificially small sound speed (large M) and, as the solution approaches convergence, the speed of sound is raised to the real value in steps.

Numerical Approach

The well-known explicit finite volume method based on MacCormack's predictor-corrector scheme [20, 21] was used to integrate the governing equations of continuity and motion. Since the scheme is widely known, no detailed description will be given here. In short, for small Mach number flows, the convective term in equation (1) is neglected and the resulting equation together with equation (2*a*) is rewritten in conservative form. These equations are integrated over a finite volume and, by invoking the divergence theory, converted into a form of storage equations. The resulting equations are solved numerically for every finite volume with a second order accurate predictor-correcter alogrithm.

This algorithm requires a phantom point outside of the boundary for every boundary cell. All dependent variables (p,$\mathbf{u}$) on the phantom points must be assigned according to certain rules determined by the boundary conditions.

The two-dimensional flows around a circular cylinder placed between two fictitious parallel walls are computed. The purpose of the side walls is to limit the computational domain. They are assumed to be rigid but, in order to avoid the contamination of the flow field by the vorticity generated by these walls, the full-slip boundary condition is applied. This is equivalent to assuming that the fluid does not wet the boundary and should not be confused with the inviscid flow assumption.

On the upstream end located 2.5 diameter from the center of the cylinder, constant inflow velocity is assumed. The downstream end is taken as far away from the cylinder as necessary to allow full development of the vortex street. It is very important to select a good nonreflecting boundary condition at the downstream end to ensure good results. Pressure waves generated by the unsteady flow field that travel at the speed of sound and the large scale vortices that travel at near the convective speed should be allowed to pass the downstream end as freely as possible. It was found much better to allow the pressure at each grid point to vary with time and fix the average pressure rather than to simply fix the pressure. This condition is especially important to pass the vortices from the downstream boundary. The subject of nonreflecting boundary condition is still under investigation and will not be discussed in detail here.

The boundary condition on the cylinder surface which is responsible for vortex generation and flow separation is the most important part of the computational scheme. It is described in detail in the next section.

Boundary Conditions on Cylinder Surface

For a large Reynolds number flow of interest, a large portion of the boundary layer is too thin to be fully resolvable

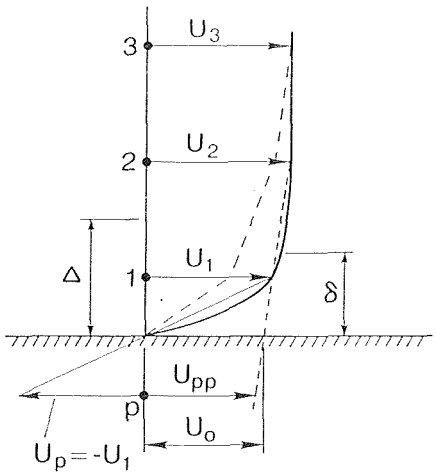

Fig. 1 Partial slip boundary condition

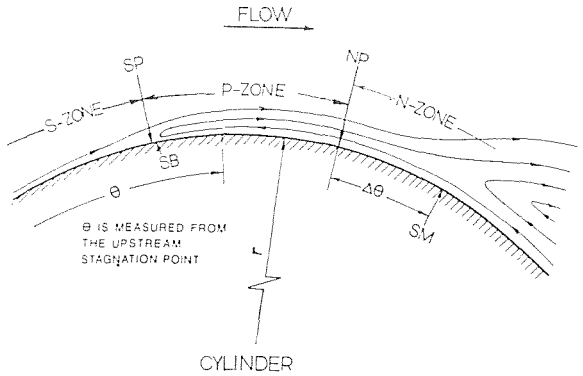

Fig. 2 Sketch of S-, P-, and N-zone, where slip, partial-slip, and no-slip conditions are applied, respectively

with our available computer resources. Two approximate approaches are commonly in use under this circumstance. The first approach is the well-known boundary layer-inviscid flow approach. The second approach is a simpler but rougher approach known as the wall function approach which largely ignores the detailed velocity distribution in the boundary layer, but considers the effect of boundary shear on the slope of the velocity profile of the outer flow near the boundary. For example, the log-law profile is often assumed to exist in the wall region of the turbulent flow, and the wall boundary condition is modified accordingly. For a developing boundary layer over a circular cylinder, however, it is rather difficult to develop a proper wall function.

Based on a concept similar to that of the wall function approach, a simpler partial-slip boundary condition approach is proposed. To fix the idea, consider a hypothetical velocity profile with large gradient near the wall as shown in Fig. 1. The boundary-layer thickness δ and the grid size Δ are shown to be of the same order of magnitude. The solid curve represents the actual velocity profile. Point 1 is the center of a boundary cell and point p is the corresponding phantom point. The no-slip boundary condition is equivalent to setting $U_p = -U_1$. Under this condition, a typical numerical solution will give a velocity profile represented by the broken line which tends to underestimate the velocity inside as well as outside of the boundary layer. On the other hand, if we assume that the velocity profile in the boundary layer is an extension of the velocity between the first two cell centers, points 1 and 2, then the velocity at the phantom point is U_{pp}. This condition is equivalent to assuming a partial-slip velocity U_0 or assuming a certain wall function. A typical computed velocity profile represented by a dotted line in this case tends to overestimate the velocity in the boundary layer but agrees with the outer flow very well. The full-slip boundary condition is given by $U_p = U_1$ and a partial-slip condition satisfies

$$-U_1 < U_{pp} < U_1 \tag{7}$$

It is interesting to note that the partial-slip boundary condition approaches the no-slip condition as $\Delta/\delta \to 0$ but approaches the full-slip condition as $\delta/\Delta \to 0$.

The cylinder surface is divided into three regions according to the relative magnitude of the boundary layer thickness δ and the grid size Δ, as shown in Fig. 2. In the front portion of the cylinder where $\delta \ll \Delta$, S-zone in Fig. 2, the effect of boundary layer is ignored and the fully slip boundary condition is imposed. In the rear part of the cylinder, which is always immersed under the large eddies and $\delta \gg \Delta$, N-zone in Fig. 2, the no-slip boundary condition is used. In the intermediate region, where δ is of the same order of magnitude as Δ, P-zone in Fig. 2, a partial slip condition is applied. The hybrid type of boundary conditions is applied in such a way that the P-zone smoothly connects with both the S- and N-zones.

The selection of the three zones and the points SP and NP must depend on the relative magnitude δ/Δ. For the present calculations, because of large Reynolds number and coarse grids, the boundary layer thickness before the boundary layer separation point SB is likely to be smaller than the grid size. For this reason, point SP is set to coincide with the laminar boundary layer separation point SB if the flow is subcritical. The laminar separation point is calculated at every time step using the formula of Curle and Skan [22]. Experience shows that the point SB moves appreciably due to vortex shedding. When the flow is supercritical, the turbulent boundary layer separation point is estimated using the Stratford formula [23]. Because the turbulent boundary layer separation was found to move very little during vortex shedding, the point SP was set at the average position of SB.

The point SM shown in Fig. 2, called the model separation point, is the point where the reverse flow is first detected at the boundary cells. In other words, it is the point where the velocity at the center of the boundary cells (V_1 in Fig. 1) becomes zero. Clearly, $\Delta \ll \delta$ and the no-slip condition is fully justified here. The model separation point SM moves by large amounts during the vortex shedding events and changes from one time step to another. We assumed, rather arbitrarily, that the point NP to be located at a constant distance $\Delta\theta$ upstream of SM in such a way that P-zone shrinks to zero when SM is at its extreme upstream point.

The full-slip, partial-slip, and no-slip zones are determined at every time step according to the method described above. The slip velocity varies smoothly from V_1 to zero all the time within the p-zone. According to the argument given previously, vorticity should be generated within the entire P-zone rather than at the leading edge as in the case of the flat plate. The total production rate, and hence the shedding rate, should be approximately equal to 0.5 U^2 where U is the maximum speed outside of NP. This fact is verified with the numerical results.

The computational scheme also requires the pressure at the phantom point to be specified. This additional boundary condition must be carefully selected so as not to conflict too much with the basic mechanics of the flow. The condition of zero pressure gradient normal to the wall is frequently used [20, 21]. This assumption is satisfactory when the grid size Δ is much smaller than the radius of curvature r of the bounding streamline. It will produce a significant error and even a premature flow separation if Δ is not much smaller than r because the centrifugal force is neglected. By considering the equation of motion in the direction normal to the streamline and retaining only the inertial and the pressure terms, a better boundary condition is obtained:

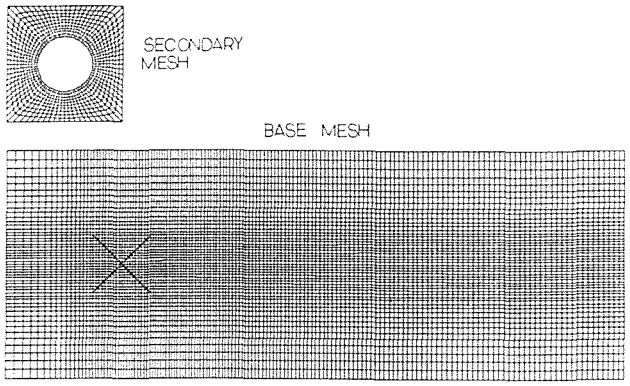

Fig. 3 Mesh system of a circular cylinder in a channel (coarse grids)

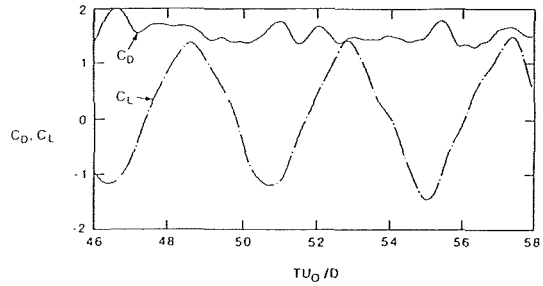

Fig. 4(*a*) Computed with fine grid system

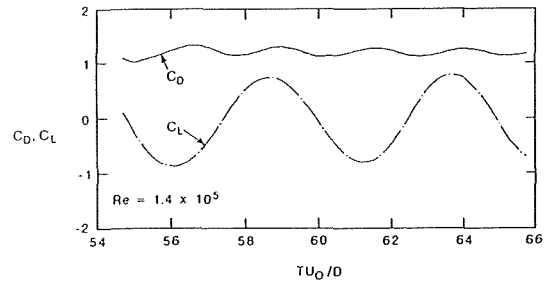

Fig. 4(*b*) Computed with coarse grid system

Fig. 4 Variation of drag and lift coefficients with time (Re = 1.4 x 10^5)

$$\frac{\partial p}{\partial n} = \rho (U_B^T)^2 / r \tag{8}$$

where r is the radius of the cylinder. The right-hand side of equation (8) represents the pressure gradient due to the centrifugal force, which is equal to zero when $U_B^T = 0$ or $r \to \infty$.

Results

For most of the computational results described herein the mesh system for a circular cylinder in a straight channel is shown in Fig. 3. The blockage ratio is $D/B = 0.125$, where B is the width of the channel. The smallest cells being centered at the cylinder surface have dimension $\Delta_n \cdot \Delta_\tau = .05\ D \cdot .04\ D$. Some computations were also carried out with a finer grid system obtained by subdividing each original cell into four smaller cells. The potential flow solution is used as the initial condition to simulate classical flow development experiments.

At first, a pair of symmetrical vortex will develop and grow. Then, instability will set in automatically and vortex shedding begins. The calculated flow fields after reaching the stationary periodic condition were analyzed and compared with experimental data. The symmetric steady flow field can be obtained by averaging the modeled unsteady field over a selected shedding period.

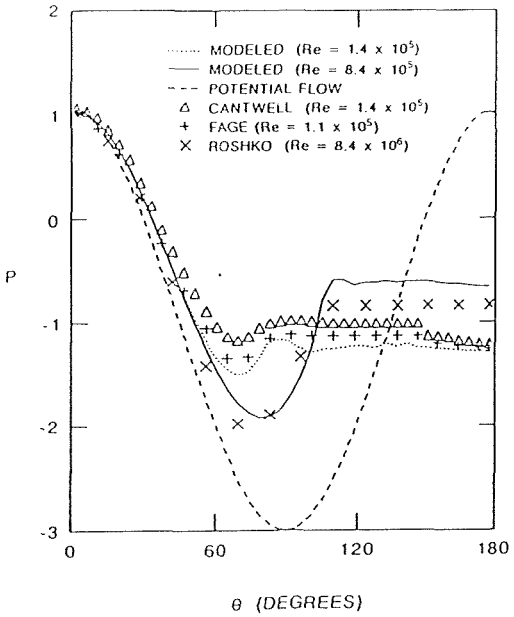

Fig. 5 Pressure distribution on the cylinder (Re = 1.4 x 10^5 and 8.4 x 10^6)

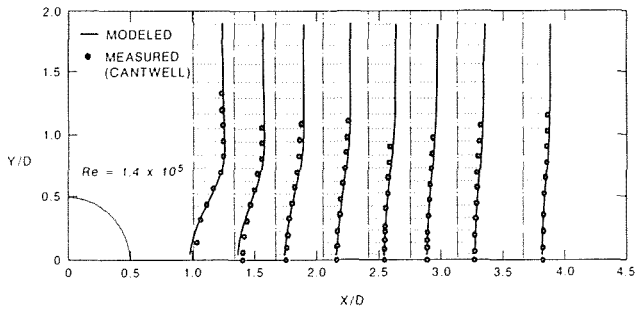

Fig. 6 Velocity distribution in the wake (Re = 1.4 x 10^5)

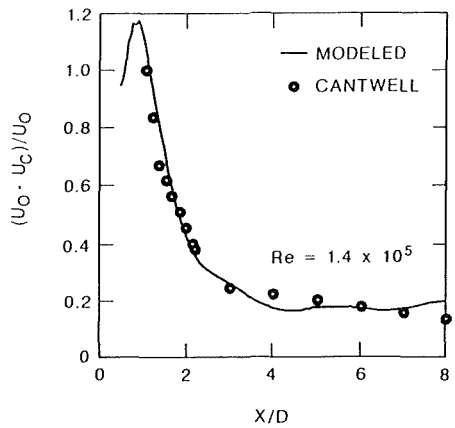

Fig. 7 Velocity defect (Re = 1.4 x 10^5)

A. Subcritical Regime. The modeled results for flow of $\mathrm{Re} = U_0 D/\nu = 1.4 \times 10^5$ (U_0 is the far field velocity) using a coarser grid system are shown in Figs. 4(*b*) to 9. The average drag coefficient $\bar{C}_D = 1.2$ and the amplitude of the lift coefficient $\Delta C_L = 0.75$, shown in Fig. 4(*b*), are both quite acceptable. The computed Strouhal number, 0.21, falls in the range of the measured values. Both C_D and C_L vary smoothly with time and the frequency of C_D is twice that of C_L, as expected. Figure 5 shows the comparison of the time-averaged pressure distribution on the cylinder surface with the measured data [24, 25]. Overall agreement is fairly good.

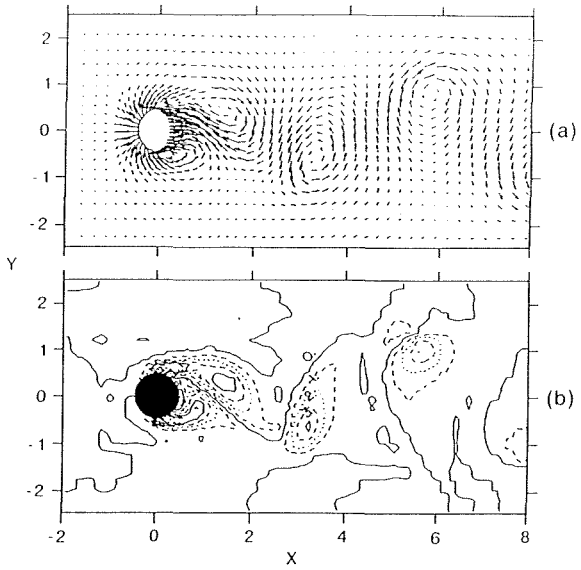

Fig. 8 Velocity vector and vorticity contour of modeled flow at $TU_0/D = 65.76$ ($Re = 1.4 \times 10^5$)

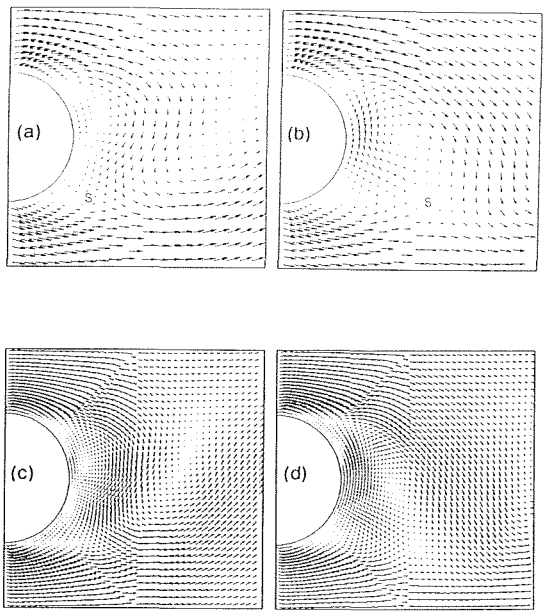

Fig. 9 Velocity vector calculated with coarse mesh (*a* and *b*) and fine mesh (*c* and *d*)

Figure 6 shows the comparison of the distribution of the time-averaged streamwise velocity in the near wake with the data obtained by Cantwell [24], using flying hotwire. The agreement is quite good, except in the region around the tail of the separation bubble. The modeled mean position of the bubble tail, defined as the point on the centerline where the velocity U_c is zero, which may be obtained from Fig. 7, is $x/D = 1.1$. This number agrees very well with measured value. It should be noted that the calculated velocity on the centerline failed to increase further after $x/D \approx 4.0$, as it should. This may be the result of the two-dimensional flow assumption, which fails to simulate the vortex stretching mechanism, and the lack of vorticity sink due to the shear stress on the end walls, which usually exist in any experimental setup.

A typical instantaneous flow field is shown by Fig. 8, where the velocity vectors were plotted as if viewed by an observer moving downstream at the speed U_0. The distance between the two rows of eddies is somewhat larger than the measured value by Cantwell [24]. Figure 9(a) shows the details of the instantaneous flow pattern near the body, where only one eddy occupies the bubble region at this moment and the newly generated eddy at the bottom side is just starting to grow. Figure 9(b) shows two counter-rotating eddies forming in the bubble region at a different phase of the shedding cycle. It should be mentioned that these two flow patterns have been conjectured by Cantwell [24]. The saddle region or the region around the interior stagnation, marked by S in Fig. 9, can also be seen in the experimental results.

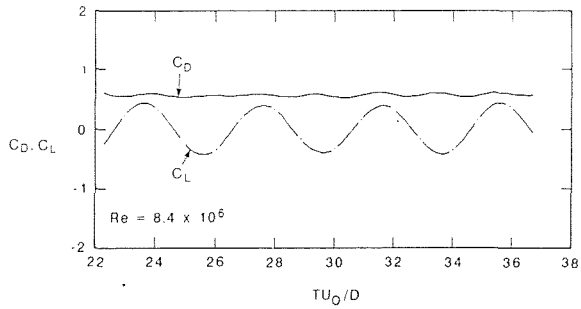

Fig. 10 Variation of drag and lift coefficients with time ($Re = 8.4 \times 10^6$)

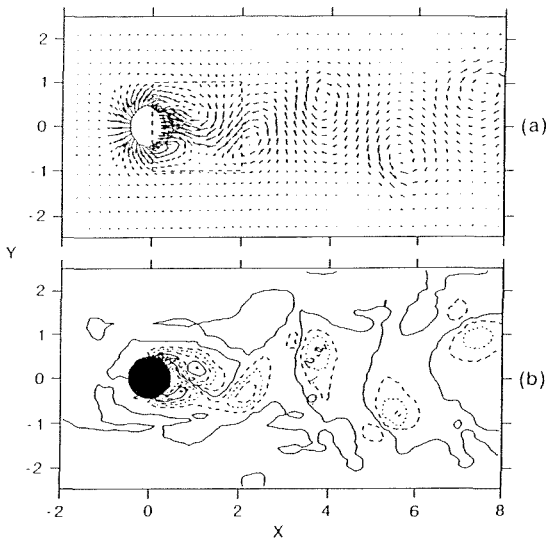

Fig. 11 Velocity vector and vorticity contour of modeled flow at $TU_0/D = 36.69$ ($Re = 8.4 \times 10^6$)

B. Supercritical Regime. Flow of $Re = 8.4 \times 10^6$ was calculated, and the results are shown in Figs. 5, 10, and 11. The average of the drag coefficient is $\bar{C}_D = 0.57$, which is quite reasonable if compared with the measured values, 0.61 ($Re = 4.3 \times 10^6$) by Achenbach [26] and 0.49 ($Re = 7.5 \times 10^6$) by Schewe [27]. The amplitude of C_L is 0.42 and the Strouhal number is 0.25 (Fig. 10), which are quite acceptable. Comparison of the time-averaged pressure distribution with Roshko's measurement [28], shows fairly good agreement (Fig. 5) except for the value of base pressure, C_{pb}. The calculated $C_{pb} = -0.64$, which is larger than $C_{pb} = -0.85$ by Roshko. However, the measured data themselves are quite scattered. For instance, $C_{pb} = -0.6$ for $Re = 4.3 \times 10^6$ and $C_{pb} = -0.68$ for $Re = 3.6 \times 10^6$ have been reported [26]. It should be noted that the flow is quite sensitive to other factors, such as surface roughness and free-stream turbulence intensity when it is in the supercritical regime.

The instantaneous flow field (Fig. 11) shows the calculated wake narrower than in the subcritical regime, due to the shift

of the location of the boundary-layer separation downstream. It can also be seen that the total amount of vorticity being carried by each eddy is smaller than in the subcritical regime.

C. Effect of Grid Size. As might be expected, use of finer mesh enables the resolution of finer eddy structures. As an example, an instantaneous velocity vector field in the near field calculated with two different mesh sizes for two comparable instants are compared in Fig. 9. Careful observation of Figs. 9(*c*) and 9(*d*) indicate that the finer grid system reveals the existence of primary and secondary eddies which merge and grow before being shed from the cylinder.

Also, as a consequence of secondary eddies, the computed drag coefficient based on finer grid systems contains at least three modes of vibrations with frequencies $2f_s$, $3f_s$, and $4f_s$, where f_s is the fundamental frequency of vortex shedding, as may be observed in Fig. 4(*a*). A problem related to the effect of grid sizes is the location of the resolvable primary separation point and the zone of partial-slip condition to be used. Based on the same boundary condition, a finer grid system will produce a resolvable separation point somewhat farther upstream than that calculated with a coarser grid system. Future research should be concentrated on the optimum use of the hybrid boundary condition in relationship with the value of Δ/δ.

Discussion

The method proposed above has been shown to be capable of simulating the large-scale structures of vortex-shedding flows. The calculated large scale feature is quite insensitive to the grid size chosen, as expected. Finer mesh systems produce finer structures and higher frequency fluctuations but have little effect on the time-averaged quantities. The agreement of the calculated flow quantities with measurements indicates that it is possible to approximate the viscous layer on the body by the simple hybrid type of boundary conditions proposed herein.

Since the full slip boundary condition is used on the two side walls, the side walls do not contribute to vorticity production. The full-slip boundary condition should also prevent the vorticity from diffusing out through the walls, thus serving as the vorticity insulator. This means all the vorticity produced in the two P-zones must be eventually transported through the downstream end. Numerical results indeed confirm that the absolute value of the vorticity (half positive and half negative) transported through any cross section downstream of the cylinder over a shedding period T is equal to the total production U^2T.

The maximum vorticity in an individual vortex does slowly decrease because of the diffusion mechanism, but its coherent structure is maintained as far as could be economically calculated. The results would be different if the no-slip condition was applied to the side walls to allow diffusion out of the region. It was also found that vortices can be made to decay as they travel downstream, if a shear stress term representing an end-wall effect (considering a finite span cylinder in a rectangular duct) is added to the two-dimensional flow equations of motion. However, not enough results are available on the subject of vortex decay in order for them to be presented in this paper. As shown by Song and Yuan [14], it is also well known that vorticity may also be produced by the enforcement of the Kutta-Joukowski condition in an inviscid flow calculation. Apparently, the large scale structure of the flow is largely determined by the total amount of vortex shedding and not sensitive to the detailed distribution of vorticity in the boundary layer. This is also a likely reason why various vortex methods can reproduce the overall flow pattern of large Reynolds number flows quite well. Smaller grids and a more accurate boundary layer computation would be needed if finer details of the flow are to be calculated.

Conclusions

The vortex shedding flow about a circular cylinder was modeled based on the weakly compressible flow equations with a simple subgrid scale turbulence model and a single full-slip, partial-slip, no-slip boundary condition. It is shown that the large-scale vortex shedding phenomenon, the primary vortices, and the associated oscillatory lift and drag, can be modeled fairly well with a grid system coarser than the boundary layer thickness. By refining the grid system it is also possible to model a small scale motion related to the secondary vortices and the second mode of oscillatory lift and drag. Detailed modeling of the boundary layer flow is apparently unnecessary for those relatively large-scale time dependent phenomena.

Acknowledgment

The authors are grateful to the Minnesota Supercomputer Institute for providing a supercomputer grant without which the work would not have been possible. The authors are also grateful to Prof. D. P. Telionis, whose detailed comments helped improve the paper.

References

1 Braza, M., Cchassaing, P., and Haminh, H., "Numerical Study and Physical Analysis of the Pressure and Velocity Fields in the Near Wake of a Circular Cylinder," *J. Fluid Mechanics*, Vol. 165, 1986, pp. 79-130.

2 Bouard, R., and Coutanceau, M., "The Early Stage of Development of the Wake Behind an Impulsively Started Cylinder for $40 < Re < 10^4$," *J. Fluid Mechanics*, Vol. 101, Part 3, 1980.

3 Eaton, B. E., "Analysis of Laminar Vortex Shedding Behind a Circular Cylinder by Computer-Aided Flow Visualization," *J. Fluid Mechanics*, Vol. 180, 1987, pp. 117-145.

4 Perry, A. E., Chong, M. S., and Lim, T. T., "The Vortex Shedding Process Behind Two-Dimensional Bluff Bodies," *J. Fluid Mechanics*, Vol. 116, 1982, pp. 77-99.

5 Sarpkaya, T., and Schoaff, R. L., "Inviscid Model of Two-Dimensional Vortex Shedding by a Circular Cylinder," *AIAA J.*, Vol. 17, No. 11, 1979, pp. 1193-1200.

6 Smith, P. A., and Stansby, P. K., "Generalized Discrete Vortex Method for Cylinders Without Sharp Edges," *AIAA J.*, Vol. 25, No. 2, 1987, pp. 199-200.

7 Stansby, P. K., "A Generalized Discrete-Vortex Method for Sharp-Edged Cylinders," *AIAA J.*, Vol. 23, No. 6, 1985, pp. 856-861.

8 Costis, C. E., and Telionis, D. P., "Vortical Wakes Over a Prolate Spheroid," *AIAA Journal*, Vol. 26, No. 10, Oct. 1988.

9 Levin, D., and Katz, J., "A Vortex-Lattice Method for the Calculation of Nonsteady Separated Flow Over Delta Wings," AIAA Paper 80-1803, 1980.

10 Thrasher, D. F., Mook, D. T., Kandil, D. A., and Nayfeh, A. H., "Application of the Vortex-Lattice Concept to General, Unsteady Lifting Surface Problems," AIAA Paper 77-1157, 1977.

11 Abbot, M. B., Larsen, J., and Tao, J., "Modelling Circulations in Depth-Integrated Flows. Part 1: The Accumulation of the Evidence," *J. Hydr. Research*, Vol. 23, No. 4, 1985, pp. 309-322.

12 Rizzi, A., "Damped Euler-Equation Method to Compute Transonic Flow Around Wing-Body Combinations," *AIAA J.*, Vol. 20, No. 10, 1982, pp. 1321-1328.

13 Salas, M. D., "Recent Developments in Transonic Euler Flow Over a Circular Cylinder," *Mathematics and Computers in Simulation*, Vol. XXV, 1983, pp. 232-236.

14 Song, C. C. S., and Yuan, M., "Modeling Large-Scale Vortices and Flow Separations," *XXII IAHR Congress*, Lausanne, Aug. 31-Sept. 4, 1987.

15 Song, C. C. S., and Yuan, M., "A Weakly-Compressible-Flow Model and Rapid Convergence Methods," ASME JOURNAL OF FLUIDS ENGINEERING, Vol. 110, No. 4, Dec. 1988.

16 Deardorff, J. W., "A Numerical Study of Three-Dimensional Channel Flow at Large Reynolds Numbers," *J. Fluid Mech.*, Vol. 41, Part 2, 1970, pp. 453-480.

17 Schumann, U., "Subgrid Scale Model for Finite Difference Simulations of Turbulent Flows in Plane Channels and Annuli," *J. Comp. Phys.*, Vol. 18, 1975, pp. 376-404.

18 Smagorinsky, J., "General Circulation Experiments with the Primitive Equations," *Mon. Weath. Rev.*, Vol. 91, No. 3, 1963, pp. 99-164.

19 Rogallo, R. S., and Moin, P., "Numerical Simulation of Turbulent Flows," *Ann. Rev. of Fluid Mech.*, Vol. 16, 1984, pp. 99-137.

20 Jacocks, J. L., and Kneile, K. R., "Computation of Three Dimensional

Time-Dependent Flow Using the Euler Equations," AEDC-TR-BO-49, July 1981.

21 Koenig, K., "Numerical Solution of the Three-Dimensional, Unsteady Euler Equations," Final Report, Contract No. F49620-82-C-0035, Air Force Armament Laboratory, Eglin, AFB, Aug. 1982.

22 Curle, N., and Skan, S. W., "Approximate Methods for Predicting Separation Properties of Laminar Boundary Layers," *Aeronaut. Quarter.*, Vol. 59, 1957, p. 257.

23 Stratford, B. S., "The Prediction of Separation of the Turbulent Boundary Layer," *J. Fluid Mech.*, Vol. 5, Part 1, 1959, pp. 1-16.

24 Cantwell, B. J., "A Flying Hotwire Study of the Turbulent Near Wake of a Circular Cylinder at a Reynolds Number of 140,000," Ph.D. thesis, California Inst. of Tech., 1976.

25 Fage, A., and Falkner, V. M., "The Flow Around a Circular Cylinder," Aero. Res. Counc., Lond., Rep. and Mem. No. 1369, 1931.

26 Achenbach, E., "Distribution of Local Pressure and Skin Friction Around a Circular Cylinder in Cross-Flow up to $Re = 5 \times 10^6$," *J. Fluid Mech.*, Vol. 34, Part 4, 1968, pp. 625-639.

27 Schewe, G., "Investigation of the Aerodynamic Forces on Bluff Bodies at High Reynolds Numbers," European Space Agency, ESA-TT-914, June 1985.

28 Roshko, A., "Experiments on the Flow Past a Circular Cylinder at Very High Reynolds Number," *J. Fluid Mech.*, Vol. 10, Part 3, 1961, pp. 345-356.

Time-Dependent Flow Using the Euler Equations," AEDC-TR-BO-49, July 1981.

21 Koenig, K., "Numerical Solution of the Three-Dimensional, Unsteady Euler Equations," Final Report, Contract No. F49620-82-C-0035, Air Force Armament Laboratory, Eglin, AFB, Aug. 1982.

22 Curle, N., and Skan, S. W., "Approximate Methods for Predicting Separation Properties of Laminar Boundary Layers," *Aeronaut. Quarter.*, Vol. 59, 1957, p. 257.

23 Stratford, B. S., "The Prediction of Separation of the Turbulent Boundary Layer," *J. Fluid Mech.*, Vol. 5, Part 1, 1959, pp. 1-16.

24 Cantwell, B. J., "A Flying Hotwire Study of the Turbulent Near Wake of a Circular Cylinder at a Reynolds Number of 140,000," Ph.D. thesis, California Inst. of Tech., 1976.

25 Fage, A., and Falkner, V. M., "The Flow Around a Circular Cylinder," Aero. Res. Counc., Lond., Rep. and Mem. No. 1369, 1931.

26 Achenbach, E., "Distribution of Local Pressure and Skin Friction Around a Circular Cylinder in Cross-Flow up to $Re = 5 \times 10^6$," *J. Fluid Mech.*, Vol. 34, Part 4, 1968, pp. 625-639.

27 Schewe, G., "Investigation of the Aerodynamic Forces on Bluff Bodies at High Reynolds Numbers," European Space Agency, ESA-TT-914, June 1985.

28 Roshko, A., "Experiments on the Flow Past a Circular Cylinder at Very High Reynolds Number," *J. Fluid Mech.*, Vol. 10, Part 3, 1961, pp. 345-356.

DISCUSSION

T. Sarpkaya[1]

Using "a grid system coarser than the boundary-layer thickness," approximating the primary boundary layers "by applying various degrees of partial-slip boundary conditions, ranging from full-slip to no-slip, depending on the relative magnitude of the boundary layer thickness and the grid size chosen," using "the weakly-compressible-flow solver," "a simple subgrid scale turbulence model proposed by Smagorinsky [18] . . . ," an SGS coefficient of $C = 0.5$ because it "appears to give reasonable results," calculating the laminar separation point at every time step "using the formula of Curle and Skan [22]," estimating the turbulent boundary layer separation point "using the Stratford formula [23]," assuming "rather arbitrarily, that the point NP (where the no-slip condition is applied) to be located at a constant distance $\Delta\theta$ upstream of SM (model separation point) in such a way that P-zone (partial-slip zone) shrinks to zero when SM is at its extreme upstream point," (see authors' Fig. 2), generating vorticity only within the two P-zones (partial-slip zones), and imposing "zero pressure gradient normal to the wall." Song and Yuan have arrived at the conclusion that "the large-scale vortex shedding phenomenon, the primary vortices, and the associated oscillatory lift and drag, can be modeled fairly well with a grid system coarser than the boundary layer thickness" and that "Detailed modeling of the boundary layer flow is apparently unnecessary for these relatively large-scale time-dependent phenomena." The authors have not carried out a sensitivity analysis to determine as to how did their results and conclusions depend on the numerous assumptions (some rather arbitrary) made by them. Why was not the vorticity generated along the entire periphery of the cylinder? How was the constant distance $\Delta\theta$ chosen? It seems that Song and Yuan's numerical experiments required numerous ad hoc assumptions to produce or reproduce the "best" or the "expected" solution with errors which are hard to estimate quantitatively and to minimize systematically.

The second point to be raised is the so-called "weakly-compressible-flow solver." It was Chorin (1967) who first introduced the "artificial compressibility" method. Song and Yuan should have referred to Chorin rather than to themselves (their reference [15]) regarding the genesis of the method. In the artificial compressibility formulation, a pseudotime derivative of pressure is added to the continuity equation [as in equation (1) of Song and Yuan], which directly couples the pressure and velocity. The equations are advanced in physical time by iterating until a divergent-free velocity field is obtained. Numerous versions of this method have been successfully used in computing time-accurate problems.

[1]Mechanical Engineering, Naval Postgraduate School, Monterey, CA 93943.

The last point to be raised concerns the various statements made by the authors regarding the generation and destruction of vorticity. Some of these are: "In other words vorticity production and destruction can take place only at the boundary but not in the flow field," "This may be the results of the two-dimensional flow assumption, and the lack of vorticity sink due to the shear stress on the end walls, which usually exist in any experimental setup," and others. As noted by this writer rather recently (Sarpkaya 1989), the generation of vorticity at rigid boundaries and its subsequent diffusion and decay have been the subject of much discussion. Lighthill (1963) invoked the existence of vorticity sources in a region of falling pressure along the boundary and vorticity sinks (at which vorticity is abstracted at the surface) in a following region of rising pressure. This is based on the fact that the tangential-vorticity source strength is related to the pressure gradient, at least for flow over a stationary plane surface ($y = 0$), by

$$-\nu \frac{\partial \omega_z}{\partial y} = \nu \frac{\partial}{\partial y}\left(\frac{\partial v}{\partial x} - \frac{\partial u}{\partial y}\right) = \nu \frac{\partial^2 u}{\partial y^2} = \frac{1}{\rho}\frac{\partial p}{\partial x} \qquad (9)$$

Batchelor (1967) also noted that "vorticity cannot be created or destroyed in the interior of a homogeneous fluid under normal conditions, and is produced only at the boundaries," implying that the mechanism whereby vorticity is lost is by diffusion to the boundaries. Morton (1984) has finally clarified all prior concepts regarding the generation and decay of vorticity. His conclusions will be summarized here since the understanding of where and how the vorticity is lost is of central importance in teaching fluid mechanics and in carrying out numerical experiments. According to Morton, "vorticity generation results from tangential acceleration of a boundary, from tangential initiation of boundary motion and from tangential pressure gradients acting along the boundary," "vorticity once generated cannot subsequently be lost by diffusion to boundaries," "reversal of the sense of acceleration or of the sense of pressure gradient results in reversal of the sense of vorticity generated" (which is interpreted by Lighthill as a vorticity sink), "walls play no direct role in the decay or loss of voriticity," and "vorticity decay results from cross-diffusion of two fluxes of opposite sense and takes place in the fluid interior." Lighthill (1986) subsequently noted, in connection with the discussion of the region of *retarded flow* around an elliptic cylinder and in agreement with the foregoing, that "there is necessarily new vorticity being generated at the solid surface with the *opposite* sense of rotation to that in the boundary layer" and made no mention of the vorticity sources and sinks. Suffice it to note that Song and Yuan's concepts of generation and destruction of vorticity need updating. Finally, it is the writer's opinion that Morton's contribution is a seminal one and must be read by every disciple of fluid mechanics.

Additional References

Batchelor, G. K., 1967, *An Introduction to Fluid Dynamics*, Cambridge University Press.

Chorin, A. J., 1967, "A Numerical Method for Solving Incompressible Viscous Flow Problems," *Journal of Computational Physics*, Vol. 2, pp. 12-26.

Lighthill, M. J., 1963, "Introduction: Boundary Layer Theory," Chapter 2 in *Laminar Boundary Layers*, Ed. L. Rosenhead, Oxford Univ. Press, pp. 72-82.
Morton, B. R., 1984, "The Generation and Decay of Vorticity," *Geophys. Astrophys. Fluid Dynamics*, Vol. 28, pp. 277-308, Gordon and Breach Science Publishers, Inc., England.
Sarpkaya, T., 1989, "Computational Methods with Vortices—The 1988 Freeman Scholar Lecture," ASME JOURNAL OF FLUIDS ENGINEERING, Vol. 111, No. 1, pp. 5-52.

C. Dalton[2]

There are two major concerns I have about this paper. First, there is a question concerning grid size and second is the issue concerning the nonphysical assumptions made by the authors to put the problem in perspective. First, let us consider the grid size question. The drag and lift coefficient results in Fig. 4 at a Reynolds number of 1.4×10^5 show considerable difference for the "fine" and "coarse" grid systems. One would reasonably expect the more accurate solution to be determined for the finer grid system. However, that doesn't appear to be the trend here. The drag coefficient for the fine grid seems to oscillate about a mean value of 1.5 to 1.6 with no apparent identifiable frequency of oscillation. The lift coefficient varies in a somewhat sinusoidal manner with peak values at about $C_L = \pm 1.3$. The trough to trough dimensionless time from the lift coefficient plot is 4.3 ($= U_o T/d$, where T is the elapsed time from the start of the calculations). The experimental drag coefficient is about 1.2 at this Reynolds number while the experimental lift coefficient has no clearly dominant value, but ± 1.3 is certainly consistent with the values reported in the literature. The coarse grid yields a drag coefficient value of about 1.2 which agrees quite well with the experimental value. This favorable comparison is surprising because one would expect the fine-grid solution to have converged because of the grid size; in this case, as the grid size became smaller, the solution deviates from the expected value. For the coarse grid, the lift coefficient oscillates with a very smooth sinusoidal behavior between peak values at about ± 0.7 to 0.8. The calculated lift coefficient range is somewhat less than the values one would expect based on experimental results. One would also not expect to see such a smooth behavior in the lift coefficient; the wake is very turbulent at this Reynolds number (just below the critical value where the boundary layer becomes turbulent) and the lift coefficient should be somewhat irregular. The drag coefficient oscillates at twice the lift coefficient frequency as expected, but, unexpectedly, there is a slight phase difference between the lift and drag coefficients. For the coarse grid, the dimensionless time between peaks is 5.1, which doesn't compare well to the fine grid value of 4.3. In addition, the two lift coefficient plots are considerably out of phase. This phase difference is another indication that something is amiss when the "coarse" and "fine" grid solutions are compared. Again, one would expect the more accurate solution to be obtained for the finer grid; this is not the case for these calculations. The converged solution should not be grid dependent. The authors calculated reasonable values of drag and lift coefficients at a supercritical Reynolds number of 8.4×10^6. The lift coefficient plot, shown in Fig. 4, is again remarkably smooth for a turbulent flow situation. However, the authors do not tell us if the supercritical case is for the "coarse" or "fine" grid, nor do they offer any comparison between values calculated for the two different grids.

[2]Department of Mechanical Engineering, University of Houston, Houston, Texas.

The second issue I have with this paper concerns the assumptions made by the authors. Regarding the concept of vorticity generation, I have a problem with Fig. 2. It is difficult for me to understand how the shed vorticity can be calculated due to effects that occur after the separation point. The authors state in the discussion concerning Fig. 2 that the no-slip boundary condition is not enforced in the region ahead of the separation point SB. All of the vorticity is assumed to be generated in the P region, i.e., after separation. (In effect, they are saying that the P region contains vorticity sources.) They do not discuss the size of the P zone; but by controlling its size, they should be able to produce whatever results they desire. This type of ad hoc assumption is not necessary to do meaningful calculations. I feel that, for a calculation procedure to be technologically acceptable, it must utilize assumptions that have a ring of reality. I do not think that this paper meets that criterion, nor does the grid size influence the results in the expected manner. Thus, it is difficult to have confidence in these results and to recommend use of the method.

Authors' Closure

Both Professors Sarpkaya and Dalton questioned the fundamental concept of vorticity production described in the paper and doubted the accuracy of the computation using the grid sizes larger than the boundary layer thickness upstream of the boundary layer separation point. Answers to these, and other questions, are listed below:

1. The concept of vorticity production and destruction described in the paper for the purpose of explaining why the computational results using fairly coarse grids can accurately represent the lower modes of vortex shedding flow is entirely consistent with that of Lighthill (1963), Batchelor (1967), and Morton (1984)—papers referred to by Professor Sarpkaya. Because the vorticity transport equation contains no source term, vorticity can be generated only at the boundary or transported to the flow domain of interest through the upstream end (which is also a boundary). The viscous term is responsible for the diffusion of vorticity and tends to make the vorticity distribution more uniform. If there are vorticities of different signs in the flow field, which is the case of flow around a circular cylinder, then the diffusion mechanism will act to cancel them out. However, the total vorticity in the flow field is conserved. In other words, the annihilation of positive and negative vortices in the flow field is a diffusion phenomenon and should not be confused with vorticity sink.
2. For a very thin boundary layer, the total vorticity flux is shown to be equal to

$$\frac{d\Gamma}{dt} = \frac{1}{2} U^2 \tag{1}$$

where U is the speed of flow at the outer edge of the boundary layer or the inner edge of the outer nonviscous flow. Because equation (1) contains no viscosity, the vorticity production is an inertia phenomenon. The production rate per unit length of the boundary is, by differentiating equation (1),

$$\frac{\partial^2 \Gamma}{\partial x \partial t} = U \frac{dU}{dx} \tag{2}$$

Lighthill, M. J., 1963, "Introduction: Boundary Layer Theory," Chapter 2 in *Laminar Boundary Layers*, Ed. L. Rosenhead, Oxford Univ. Press, pp. 72-82.
Morton, B. R., 1984, "The Generation and Decay of Vorticity," *Geophys. Astrophys. Fluid Dynamics*, Vol. 28, pp. 277-308, Gordon and Breach Science Publishers, Inc., England.
Sarpkaya, T., 1989, "Computational Methods with Vortices—The 1988 Freeman Scholar Lecture," ASME JOURNAL OF FLUIDS ENGINEERING, Vol. 111, No. 1, pp. 5-52.

C. Dalton[2]

There are two major concerns I have about this paper. First, there is a question concerning grid size and second is the issue concerning the nonphysical assumptions made by the authors to put the problem in perspective. First, let us consider the grid size question. The drag and lift coefficient results in Fig. 4 at a Reynolds number of 1.4×10^5 show considerable difference for the "fine" and "coarse" grid systems. One would reasonably expect the more accurate solution to be determined for the finer grid system. However, that doesn't appear to be the trend here. The drag coefficient for the fine grid seems to oscillate about a mean value of 1.5 to 1.6 with no apparent identifiable frequency of oscillation. The lift coefficient varies in a somewhat sinusoidal manner with peak values at about $C_L = \pm 1.3$. The trough to trough dimensionless time from the lift coefficient plot is 4.3 ($= U_o T/d$, where T is the elapsed time from the start of the calculations). The experimental drag coefficient is about 1.2 at this Reynolds number while the experimental lift coefficient has no clearly dominant value, but ± 1.3 is certainly consistent with the values reported in the literature. The coarse grid yields a drag coefficient value of about 1.2 which agrees quite well with the experimental value. This favorable comparison is surprising because one would expect the fine-grid solution to have converged because of the grid size; in this case, as the grid size became smaller, the solution deviates from the expected value. For the coarse grid, the lift coefficient oscillates with a very smooth sinusoidal behavior between peak values at about ± 0.7 to 0.8. The calculated lift coefficient range is somewhat less than the values one would expect based on experimental results. One would also not expect to see such a smooth behavior in the lift coefficient; the wake is very turbulent at this Reynolds number (just below the critical value where the boundary layer becomes turbulent) and the lift coefficient should be somewhat irregular. The drag coefficient oscillates at twice the lift coefficient frequency as expected, but, unexpectedly, there is a slight phase difference between the lift and drag coefficients. For the coarse grid, the dimensionless time between peaks is 5.1, which doesn't compare well to the fine grid value of 4.3. In addition, the two lift coefficient plots are considerably out of phase. This phase difference is another indication that something is amiss when the "coarse" and "fine" grid solutions are compared. Again, one would expect the more accurate solution to be obtained for the finer grid; this is not the case for these calculations. The converged solution should not be grid dependent. The authors calculated reasonable values of drag and lift coefficients at a supercritical Reynolds number of 8.4×10^6. The lift coefficient plot, shown in Fig. 4, is again remarkably smooth for a turbulent flow situation. However, the authors do not tell us if the supercritical case is for the "coarse" or "fine" grid, nor do they offer any comparison between values calculated for the two different grids.

[2]Department of Mechanical Engineering, University of Houston, Houston, Texas.

The second issue I have with this paper concerns the assumptions made by the authors. Regarding the concept of vorticity generation, I have a problem with Fig. 2. It is difficult for me to understand how the shed vorticity can be calculated due to effects that occur after the separation point. The authors state in the discussion concerning Fig. 2 that the no-slip boundary condition is not enforced in the region ahead of the separation point SB. All of the vorticity is assumed to be generated in the P region, i.e., after separation. (In effect, they are saying that the P region contains vorticity sources.) They do not discuss the size of the P zone; but by controlling its size, they should be able to produce whatever results they desire. This type of ad hoc assumption is not necessary to do meaningful calculations. I feel that, for a calculation procedure to be technologically acceptable, it must utilize assumptions that have a ring of reality. I do not think that this paper meets that criterion, nor does the grid size influence the results in the expected manner. Thus, it is difficult to have confidence in these results and to recommend use of the method.

Authors' Closure

Both Professors Sarpkaya and Dalton questioned the fundamental concept of vorticity production described in the paper and doubted the accuracy of the computation using the grid sizes larger than the boundary layer thickness upstream of the boundary layer separation point. Answers to these, and other questions, are listed below:

1. The concept of vorticity production and destruction described in the paper for the purpose of explaining why the computational results using fairly coarse grids can accurately represent the lower modes of vortex shedding flow is entirely consistent with that of Lighthill (1963), Batchelor (1967), and Morton (1984)—papers referred to by Professor Sarpkaya. Because the vorticity transport equation contains no source term, vorticity can be generated only at the boundary or transported to the flow domain of interest through the upstream end (which is also a boundary). The viscous term is responsible for the diffusion of vorticity and tends to make the vorticity distribution more uniform. If there are vorticities of different signs in the flow field, which is the case of flow around a circular cylinder, then the diffusion mechanism will act to cancel them out. However, the total vorticity in the flow field is conserved. In other words, the annihilation of positive and negative vortices in the flow field is a diffusion phenomenon and should not be confused with vorticity sink.
2. For a very thin boundary layer, the total vorticity flux is shown to be equal to

$$\frac{d\Gamma}{dt} = \frac{1}{2} U^2 \tag{1}$$

where U is the speed of flow at the outer edge of the boundary layer or the inner edge of the outer nonviscous flow. Because equation (1) contains no viscosity, the vorticity production is an inertia phenomenon. The production rate per unit length of the boundary is, by differentiating equation (1),

$$\frac{\partial^2 \Gamma}{\partial x \partial t} = U \frac{dU}{dx} \tag{2}$$

Streak Characteristics and Behavior Near Wall and Interface in Open Channel Flows

M. Rashidi

S. Banerjee

Department of Chemical and Nuclear Engineering, University of California, Santa Barbara, CA 93106

Turbulent structures near the boundaries (solid wall and gas-liquid interface) have been studied in open channel flows. Experiments with no shear, countercurrent shear, and cocurrent shear at the gas-liquid interfaces were conducted. Results indicate that near the sheared interfaces, the mean nondimensional spanwise streak-spacing, λ^+, appears to be essentially invariant with shear Reynolds number, exhibiting consistent values of $\lambda^+ \approx 100$ at $y_I^+ = 5$, while increasing with distance from the interface. Observation of the streaks near the interface indicates that the process of streak merging is active even for $y_I^+ < 5$. Further studies show that the low-speed streaks frequently occur as regions between longitudinal vortices separated by $\Delta z^+ \approx 50$ near the boundaries. These vortices generally originate from the boundaries at an angle of about 20–25 deg (for $y^+ < 20$), then lift up or eject chaotically at an angle of about 40–50 deg (for $y^+ > 20$). Based on these observations, a conceptual mechanism of streak breakdown near the sheared boundaries has been provided.

Introduction

One of the most significant findings in turbulence has been the discovery of the organized or coherent structures, namely the existence of an ordered structure within a turbulent boundary layer. The investigation of ordered structures dates back to the experiments of Fage and Townend (1932) who used an ultramicroscope to examine fluid motion near a solid boundary for turbulent flow in a square tube and a circular pipe. They found that the region very close to the wall ($0 \le y_w^+ \le 4$) did not behave like a laminar liquid film but was periodically disturbed by fluctuations. Later, the measurements of Laufer (1954) and Klebanoff (1954) near the wall both showed that the rate of production of turbulent energy peaks at the outer edge of the viscous sublayer ($y_w^+ = 11.5$) as does the dissipation of this energy. Their results illustrated the importance of the region very close to the wall ($5 \le y_w^+ \le 20$) which was the primary motivation for the early work of Kline and Runstadler (1959) and later Kline et al. (1967).

Kline et al. (1967) did the first systematic investigation and quantification of the low-speed/high-speed phenomenon. They found through a series of flow visualization experiments using hydrogen bubbles that even at $y_w^+ = 2.7$ the bubbles did not follow straight trajectories and they accumulated into an alternating array of high-speed and low-speed regions called "streaks." They observed that these structures periodically lifted off, oscillated, then became unstable and broke up chaotically. The repeating cycle of events ended with an insweep or inrush of fresh fluid to replace the ejected fluid in the wall region. Kim et al. (1971) showed that virtually all of the net production of turbulent energy for the range, $0 < y_w^+ < 100$ occurs during the lifting and breakdown of these streaks. Both ejection and insweep events were later shown by many authors to be extremely important and contributing to as much as 60–80 percent of the production of Reynolds stresses (Grass, 1971; Willmarth and Lu, 1972; Nakagawa and Nezu,1977). Experiments of Grass (1971) also showed that the ejection and the insweep events were present irrespective of the surface roughness.

Blackwelder and Eckelmann (1979) were able to make a rather detailed study of the structure of wall streaks using a combination of hot-film sensors and flush-mounted wall elements. They identified the low-speed streaks observed by Kline et al. and others as the regions between pairs of counter-rotating streamwise vortices. They found the streamwise vortices to be separated by $\Delta z^+ \approx 50$ and their length to be $\Delta x^+ \approx 1000$. Their findings were in essence later confirmed in probe-correlation studies by Kreplin and Eckelmann (1979). The point that the low-speed streaks may be the regions between counter-rotating streamwise vortices is fascinating because it brings up the conjecture (suggested earlier by Kline et al., 1967; Hinze, 1975; Smith 1983; among others) that the streamwise vortices at the wall may actually be the upstream legs of horseshoe vortices seen by Head and Bandyopadhyay (1981). Head and Bandyopadhyay studied the turbulent boundary-layer structures using smoke visualization of the wall region. They illuminated the flow with sheets of lights entering

Contributed by the Fluids Engineering Division of THE AMERICAN SOCIETY OF MECHANICAL ENGINEERS and presented at the Joint ASCE/ASME Applied Mechanics, Biomechanics, and Fluids Engineering Conference, San Diego, Calif., July 9–12, 1989. Manuscript received at the Fluids Engineering Division January 26, 1989.

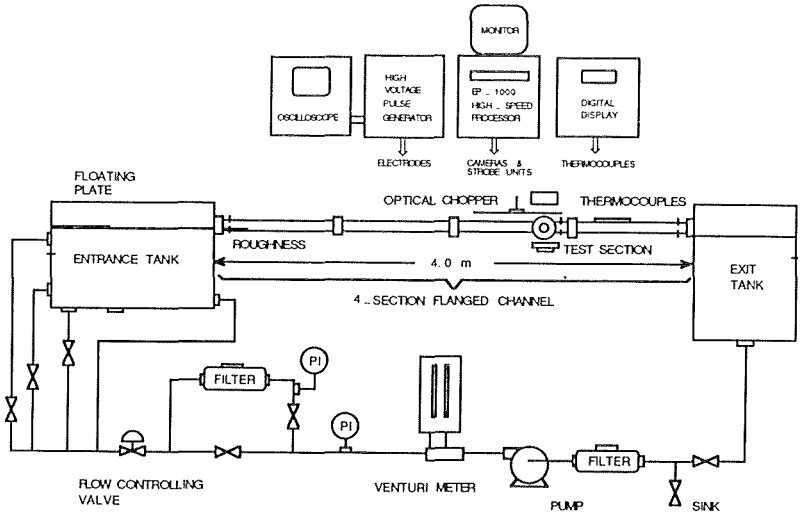

Fig. 1 Experimental facilities

through the bottom of their channel at two different angles. When the sheet was inclined in the flow direction, they observed an eddy-like structure lay on that plane. However, when the sheet was angled against the flow direction, they observed two roughly circular spots in the plane of illumination. These experiments showed that horseshoe or hairpin shape structures existed in the log layer region but no direct connection was made between these and the low-speed/high-speed streaks at the wall.

More recently, Nakagawa and Nezu (1981), Smith and Metzler (1983), Moin and Kim (1985), Luchik and Tiederman (1987), Kim et al. (1987), and Lam and Banerjee (1988), among others, have been able to confirm some characteristics of the streaks and the vortices discussed above, however, there are still many unanswered questions in the way of our understanding of the phenomena.

In view of the significance of this problem, in particular its relevance to the understanding of turbulent transport processes at the gas-liquid interface, an extensive program has begun in our laboratory. The present work is part of a continuing investigation of turbulence structure and transport mechanisms in liquid layers bounded by a solid wall and a gas-liquid interface. The first paper in this series, Rashidi and Banerjee (1988), was concerned with the dominant large-scale structures in the flow arising from lift up and breakdown of the low-speed streaks, i.e., "bursts," in the wall region, when no shear was imposed on the interface. The "bursts" were observed to originate from the near wall region, reach the gas-liquid interface, roll off, and mix into the flow leading to characteristic rotational structures. Furthermore, the burst brought fresh fluid to the interface giving rise to patches of "renewed surface" that are of importance in interfacial heat and mass transfer. In the second paper, Rashidi and Banerjee (1990), shear was imposed at the gas-liquid interface by countercurrent and cocurrent gas flows. These experiments showed for the first time the formation and breakdown of low-speed/high-speed streaks near the sheared interfaces and provided some characteristics of these structures. In particular, it was shown that there was a critical shear rate at which the streaks began to form at the interface. The critical point of appearance of the streaks was expressed in terms of the dimensional shear rate (du/dy) to be in the range of about 8 to 10 s^{-1}.

The present paper reports on some characteristics of the interface and the wall streaks, in an attempt to relate the streak formation and breakdown near the boundaries to the horseshoe or hairpin vortices observed in the log layer (Head and Banyopadhyay, 1981).

Experimental Facilities and Procedures

The equipment used for the present study was a plexiglas rectangular channel with gas and liquid cocurrent and countercurrent facilities (shown in Fig. 1). The channel itself was made up of four equal sections and had dimensions of 4.0 m long, 0.20 m wide, and 0.15 m deep. Measurements were taken at a location of the channel sufficiently downstream from the entrance to ensure that the flow was fully-developed turbulent with regard to the mean velocity profile (Schlichting, 1979). Both fluids, air and water, were filtered before entering the channel. In the case of water, the circulating flow was filtered continuously to remove solids greater than 5 μm. The liquid flow rate was provided by a Jacobs centrifugal pump and was continuously measured using an Aeroquip Venturi meter. The gas flow rate was maintained through the use of two Dayton shaded pole blowers in series. In order to measure gas flow rate accurately, a rotary precision gas meter (7M125) was used

Nomenclature

Fr = Froude number, $\mathbf{u}_M/(gh)^{1/2}$
h = flow depth
Re = Reynolds number, $\mathbf{u}_M h/\nu$
Re* = friction Reynolds number, $u_* h/\nu$
$\mathbf{u}_M$ = mean streamwise velocity
u_* = friction velocity, $(\tau/\rho)^{1/2}$
x, y, z = streamwise, vertical, and spanwise coordinates
x^+ = nondimensional streamwise distance, $u_* x/\nu$
y^+ = nondimensional vertical distance, $u_* y/\nu$
z^+ = nondimensional spanwise distance, $u_* z/\nu$
α = growth angle between longitudinal vortices and boundary
β = ejection angle between longitudinal vortices and boundary
λ = mean spanwise streak-spacing
λ^+ = mean nondimensional spanwise streak-spacing, $u_* \lambda/\nu$
ν = kinematic viscosity
ρ = density
τ = shear stress at boundary

Subscripts

G = gas
I = gas-liquid interface
L = liquid
W = wall

Table 1 No gas flows

Run	Liquid Flow Depth h (cm)	Liquid Mean Velocity U_M (cm/sec)	Wall Friction Velocity u_{*w} (cm/sec)	Liquid Kinematic Viscosity ν (cm²/sec) x 100	Shear Reynolds Number Re_{*w} $(u_{*w}h/\nu)$	Liquid Froude Number Fr $(U_M/\sqrt{gh})$	Liquid Reynolds Number Re $(U_M h/\nu)$
1a	3.65±0.05	23.9±2-3%	1.26	0.858	536	0.40	10,000
2a	2.75	23.6	1.29	0.848	418	0.46	7,500
3a	2.75	15.6	0.90	0.839	245	0.30	5,000
4a	2.75	11.0	0.66	0.830	219	0.21	3,500
5a	2.70	7.8	0.49	0.821	161	0.15	2,500

Table 2 Countercurrent gas flows

Run	Liquid Flow Depth h (cm)	Liquid Mean Velocity U_M (cm/sec)	Liquid Kinematic Viscosity ν (cm²/sec) x 100	Shear Reynolds Number Re_{*_I} $(u_{*_I}h/\nu)$	Liquid Froude Number Fr $(U_M/\sqrt{gh})$	Liquid Reynolds Number Re $(U_M h/\nu)$	Gas Reynolds Number Re_G $(U_{MG}h_G/\nu_G)$
1b	2.85±0.05	7.4±2-3%	0.839	156	0.14	2,500	16,600
2b	2.85	7.4	0.839	136	0.14	2,500	14,000
3b	2.85	7.4	0.839	98	0.14	2,500	10,200
4b	2.85	7.4	0.839	78	0.14	2,500	7,700

Table 3 Cocurrent gas flows

Run	Liquid Flow Depth h (cm)	Liquid Mean Velocity U_M (cm/sec)	Liquid Kinematic Viscosity ν (cm²/sec) x 100	Shear Reynolds Number Re_{*_I} $(u_{*_I}h/\nu)$	Liquid Froude Number Fr $(U_M/\sqrt{gh})$	Liquid Reynolds Number Re $(U_M h/\nu)$	Gas Reynolds Number Re_G $(U_{MG}h_G/\nu_G)$
1c	2.85±0.05	7.4±2-3%	0.839	153	0.14	2,500	16,600
2c	2.85	7.4	0.839	132	0.14	2,500	14,000
3c	2.85	7.4	0.839	95	0.14	2,500	10,100
4c	2.85	7.4	0.839	71	0.14	2,500	7,100

to monitor the flow during each run. Temperature measurements were taken at entrance, exit, and test section of the channel using thermocouples placed both in gas and liquid. These measurements were also simultaneously checked with precision mercury thermometers placed at these locations.

Measurements were primarily made in the liquid stream by a variety of techniques. The first was through the use of very small (~ 20 μm) oxygen bubbles (Rashidi and Banerjee, 1988) that were photographed using a high-speed video analyzer (Kodak Ekta Pro 1000) and two strobe units. Alternatively, some photographs were also taken with a 35 mm camera and mechanically chopped flashes. This resulted in well-spaced traces of bubbles in a film frame from which velocities were found by image processing. In addition, local velocity measurements were also taken with a 3D laser Doppler anemometer with a focal volume of 30 μm × 30 μm × 30 μm. In this paper, the results obtained using the first technique, namely the oxygen bubbles and high-speed video photography will be discussed.

The bubbles could be generated from two platinum wires 25 μm in diameter. One wire was held vertically across the channel, while the other wire was strung horizontally parallel to the bottom of the channel and aligned in the spanwise direction. The horizontal wire was 0.18 m in length and was uniquely designed so that it could be moved up and down. This allowed the distance between the wall and the wire or between the interface and the wire to be varied. The bubbles were produced by pulsing a high voltage generator capable of providing high voltage pulses of up to 300 V at very short durations. This gave rise to a series of marker lines that could be used to visualize and photograph the fluid motion.

The video viewing and recording system was a two-camera Kodak EP-1000 high-speed motion analyzer with conventional and fiber-optic synchronized-strobe units. The system had a maximum full screen capability of 1000 frames/sec and a maximum split-screen capability of 6000 frames/s. The split-screen capability allowed two different fields of view to be simultaneously displayed on the monitor and recorded on the tape. The recorded data could be played back in flicker-free slow motion (30 frames/s), as well as single frames (1, 2, 3, and 4 frames/s) for detailed data analysis. One camera was used to record the flow structures in the vertical plane, while the other captured the structures in the horizontal plane.

Experimental Conditions

The details of the experimental conditions are summarized in Tables 1, 2, and 3. The subscripts: W, I, L, and G are throughout this paper in reference to the wall, interface, liquid, and gas, respectively. However, since most measurements are with respect to the liquid streams, the subscript L is generally omitted in the results for simplicity. The three cases studied were (i) no gas flows, (ii) countercurrent gas flows, and (iii) cocurrent gas flows. As discussed earlier, it was possible to impose a shear on the gas-liquid interface by flowing gas either cocurrent or countercurrent to the direction of liquid flow. For the first case, no gas flows, experiments were conducted at five different liquid Reynolds (and Froude) numbers. The values of wall friction velocity for these runs were evaluated from the measured mean velocity profiles. On the other hand, the countercurrent flow and cocurrent flow cases were done at one liquid Reynolds (and Froude) number, while varying the gas Reynolds number to achieve different levels of shear at the gas-liquid interface. The value of Reynolds numbers reported here are based on the flow depth. Reynolds numbers based on hydraulic diameter are about three times greater than what is reported here. The interfacial friction velocities listed in Tables 2 and 3 were computed from the mean velocity gradients near the interface.

Results

A. Streak Formation. The low-speed/high-speed streaks were studied in detail near the wall and sheared interfaces. Figure 2 illustrates the low-speed/high-speed streaks that form near the wall and near the interfaces of countercurrent and cocurrent flows. It is clear that the wall streaks have similar characteristics to those observed by many others. On the other hand, the streaks found at the interfaces are seen to be more pronounced (with respect to the differential velocities between the adjacent high-speed and low-speed regions) than the wall streaks. In the case of cocurrent flows, since the gas-liquid interface is moving faster than the mean flow, the streaky structure is reversed compared to that at the wall or the countercurrent flow case. This means that since the direction of interfacial shear rate has been reversed in these cocurrent flow runs, the low-speed regions of the two previous cases now appear as the regions with higher velocities (relative to the mean interfacial velocity).

Characteristics of the streaks, mainly their mean spacings were determined from the video sequences obtained using the high-speed video system discussed before. For each run, a video sequence of at least 22,000 frames (~ 3 min) was recorded. From this sequence, 60–80 frames were analyzed. This corresponded to at least 200 counts of the streaks. The streak counts were done based on a set of systematic rules. The streaks were counted from individual still pictures with each picture about 100 frames apart. This was done twice independently. The counting of streaks were performed when the upstream end of the streaks were still within $\Delta x^+ \approx 50$ downstream of the wire. It was also required that the differential velocities between the adjacent high and low-speed regions to be at least 1.5 to 1. If it appeared that the two adjacent low-speed regions had no well-defined high-speed region (i.e., had merged), they would be counted as one. Figure 3 shows the variation of the mean non-dimensional spanwise streak-spacing, λ^+, as a function of shear Reynolds number for the interface streaks. It is

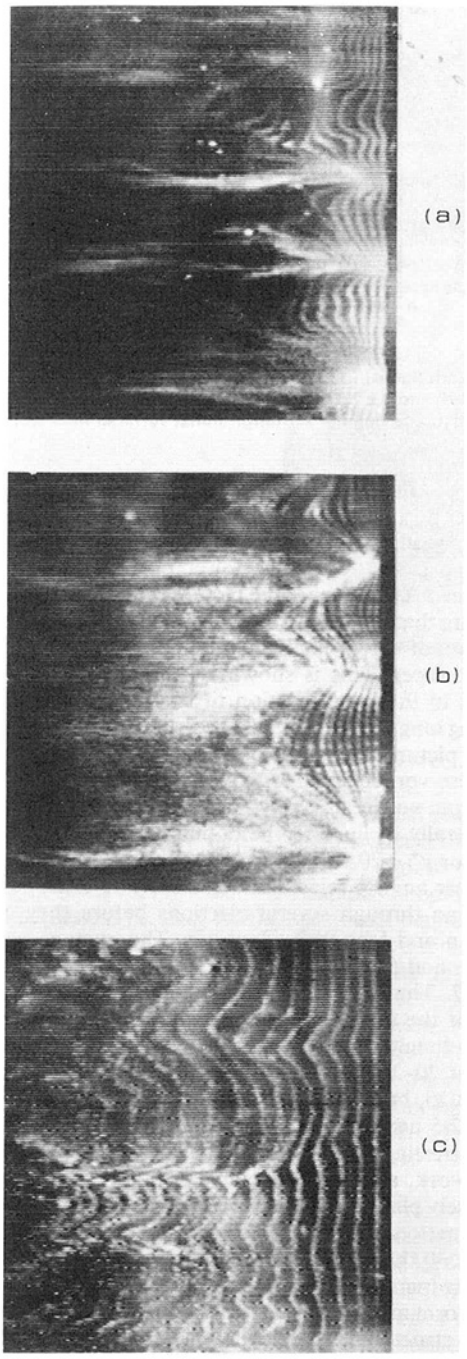

Fig. 2 Low-speed/high-speed streaks visualized by means of oxygen bubbles in horizontal plane at $y^+ 5 \pm 1$ (*a*) near wall: no gas flow, Run 3a; (*b*) near interface: countercurrent gas flow, Run 1b; (*c*) near interface; cocurrent gas flow, Run 1c.

clear that the mean spacing of the streaks non-dimensionalized with the interfacial shear velocity (u_{*I}) and kinematic viscosity (ν), changes very little with the shear Reynolds number and exhibits consistent values of $\lambda^+ \approx 100 \pm 7$ percent (95 percent confidence level) at $y_I^+ = 5 \pm 1$. The variation of streak-spacing near the wall was also shown to be independent of Reynolds number by Rashidi and Banerjee (1990). This is an important finding, since the boundary conditions are quite different at the wall and at the interface. Rashidi and Banerjee (1990) studied the effect of boundary conditions and shear rate on the streak formation and breakdown. They concluded that the shear rate has the main influence on the phenomena and the effect of boundary conditions is much less important.

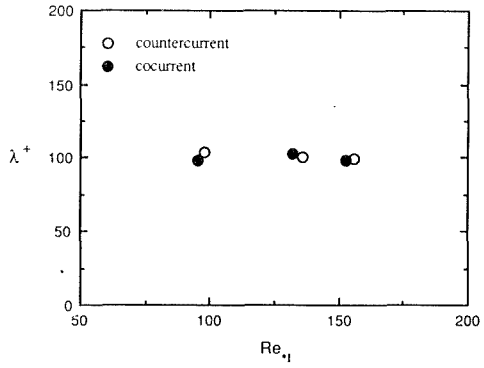

Fig. 3 Mean nondimensional spanwise streak-spacing $\lambda^+ \pm 7$ percent (95 percent confidence level), as a function of shear Reynolds number at $y_I^+ = 5 \pm 1$. ○, interface streaks: countercurrent gas flow; ●, interface streaks: cocurrent gas flows

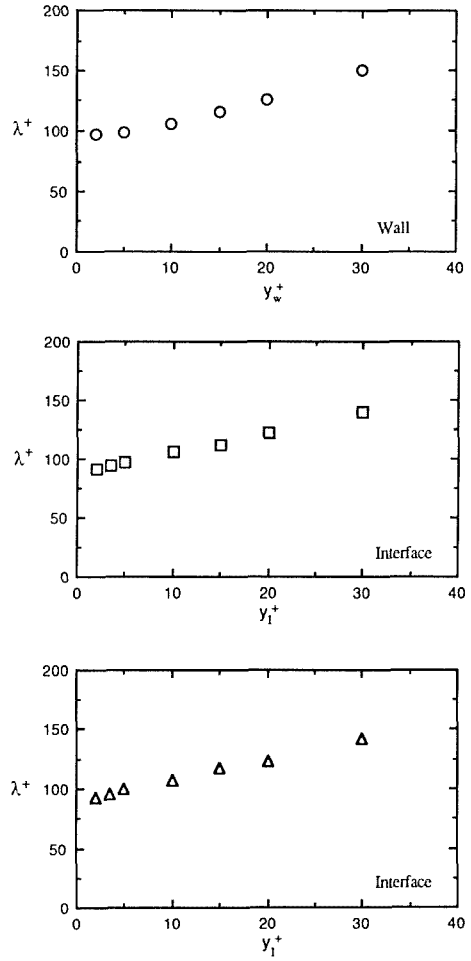

Fig. 4 Variation of mean nondimensional spanwise streak-spacing $\lambda^+ \pm 7$ percent (95 percent confidence level), with nondimensional distance $y_I^+ \pm 1$ from the boundaries, ○, wall streaks: no gas flow, Run 3a; □, interface streaks: countercurrent gas flow, Run 1b; △, interface streaks: cocurrent gas flow, Run 1c

Measurements of the mean non-dimensional spanwise streak-spacing, λ^+, as a function of the non-dimensional distance, y^+, were also obtained near the sheared interfaces. Beyond $y^+ = 30$ the streaks were not sufficiently well defined to obtain accurate streak counts. Figure 4 shows comparison of the results near the wall (Rashidi and Banerjee, 1990) and near the sheared interfaces. It appears that the value of λ^+ increases with increased distance from either boundaries. This increase

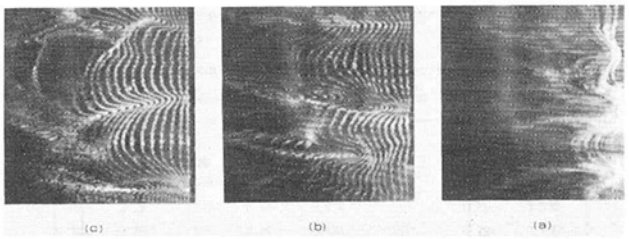

Fig. 5 Interfacial streaks at various distances from interface ($y_i^+ \pm 1$) for countercurrent gas flow, Run 1b, (*a*) $y_i^+ = 2$; (*b*) $y_i^+ = 10$; (*c*) $y_i^+ = 20$.

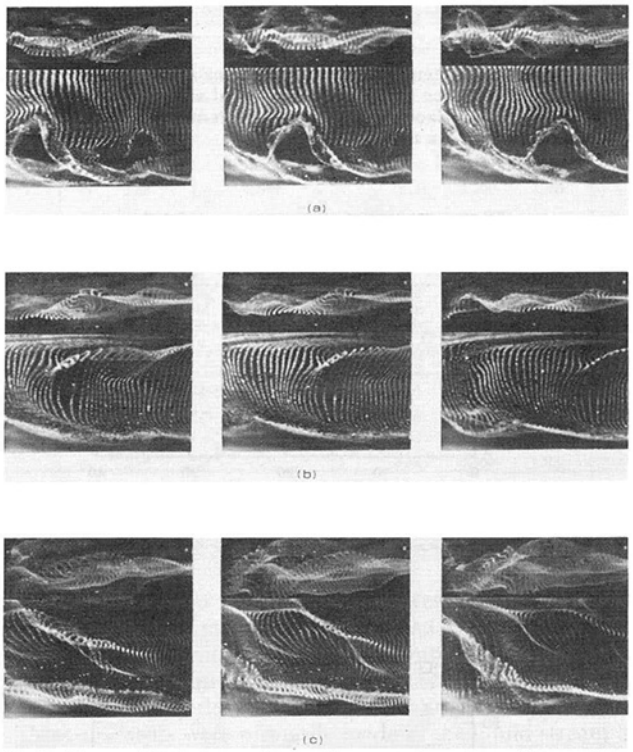

Fig. 6 Sequential pictures of formation, growth, and breakdown of longitudinal vortices. (*a*) near wall: no gas flow, Run 3a; (*b*) near interface: countercurrent gas flow, Run 1b; (*c*) near interface: cocurrent gas flow, Run 1c. Time intervals between photographs are 0.08, 0.16, and 0.16 sec for Runs 3a, 1b, and 1c, respectively.

has been seen from our video sequences to be caused by the two effects of fluttering and merging or coalescence of the low-speed streaks. Observations of the streaks near the wall show that the merging of the low-speed streaks begins at about $y_w^+ \approx 5$ and continues to be dominant for $10 \le y_w^+ \le 30$. However, similar observations near the interface show that the process of streak merging or coalescence begins to occur at $y_i^+ < 5$ and continues to be dominant up to $y_i^+ \approx 30$. These examinations seem to agree with the variation of the streak-spacing reported above, namely that near the wall ($y_w^+ \le 5$) the streak-spacing appears to be approximately constant (Oldaker and Tiederman, 1977) and increases (monotonically) for $5 \le y_w^+ \le 30$, whereas near the interface the streak-spacing increases monotonically throughout for $2 \le y_i^+ \le 30$. Figure 5 illustrates the interfacial streaks at various distances from the interface for countercurrent gas flow case.

B. Streak Breakdown. In order to study the detail of streak formation and breakdown near the two boundaries, the high-speed video system and the two cameras were used to view simultaneously the streaky structure in the horizontal plane and the lift-up and breakdown of the streaks in the vertical plane. Figure 6 illustrates the sequence of pictures obtained this way for the three cases: no gas flows, counter-

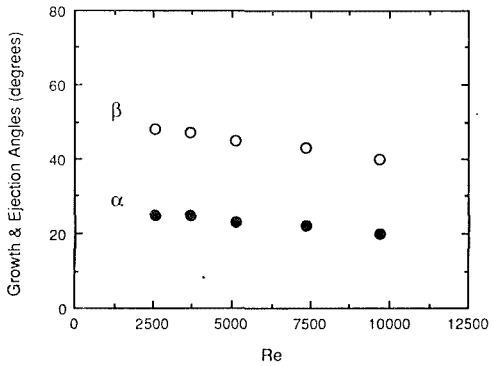

Fig. 7 Variation of inclination angles $\alpha \pm 5$ percent (95 percent confidence level) and $\beta \pm 2.5$ percent (95 percent confidence level), as a function of Reynolds number for longitudinal vortices near wall

current gas flows, and cocurrent gas flows. In each picture, the upper portion provides the horizontal view of the structure (near the wall for the first case and near the interface for the other two cases), while the lower portion gives the vertical plane view. As seen from the pictures and the video sequences, it appears that the breakdown of the streaks is associated with formation of vortex-like structures near both boundaries (wall and interface). This is shown by the folding of the bubble markers in the lower portion of each picture and the corresponding longitudinal vortex-like structure in the upper portion of each picture. Observation of the video sequences indicates that these vortices (which may be conjectured as the legs of the hairpin vortices seen by Head and Bandyopadhyay, 1981) are generally inclined to the boundary at an angle α (growth angle) for $y^+ < 20$ and go through a chaotic lift-up or ejection at a larger angle β (ejection angle) for $y^+ > 20$. These vortices usually go through several ejections before they completely break up and lose their identities. The average variation of angles α and β as a function of Reynolds number are shown in Fig. 7. The data in this figure correspond to 200 measurements of the angles for each run. It appears on the average that the longitudinal vortices form near the wall at an angle of about 20–25 deg $\pm$ 5 percent (95 percent confidence level) for $y_w^+ < 20$, but lift up chaotically at an angle of about 40–50 deg $\pm$ 2.5 percent (95 percent confidence level) for $y_w^+ > 20$. It is interesting to mention that Heidrick et al. (1971) in an earlier work, also found inclined structures to the wall using two closely placed hot film velocity sensors. They showed that the inclination angle increased with distance from the wall, i.e. for $y_w^+ < 30$ the inclination angle was seen to be less than 45 deg while increasing to 45 deg for $y_w^+ \approx 30$. However, they did not perform any conditional averaging to isolate the dynamics of these structures and relate them to the vortices observed in the present work (Moin and Kim, 1985 and Gad-el-Hak and Hussain, 1986 provide good reviews of the various angles of the near wall vortices observed by others).

It is also worth noting that an increase in Reynolds number causes a decrease in these angles as seen from Fig. 7. Head and Bandyopadhyay (1981) observed a similar effect near the wall, namely that an increase in Reynolds number resulted in a decrease in the inclination angle of the hairpin vortices i.e., as Reynolds number increases, (due to the increase in the shear rate) the longitudinal vortex loops are pulled closer to the wall and their spacing is decreased. In addition to the wall region, the values of angles α and β were measured near the sheared interfaces. These values near the interfaces of countercurrent and cocurrent gas flows (Runs 1b and 1c) reveal similar ranges of 20–25 deg and 45–50 deg for the two angles, respectively.

In order to investigate further the association of longitudinal vortices with the low-speed streaks near the boundaries, both vertical and horizontal wires were employed to generate oxygen bubble tracers in the flow. In this way, the streaky structure

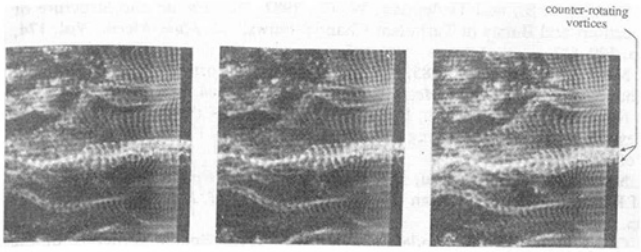

Fig. 8 Sequential pictures (from right to left) of low-speed streaks and longitudinal vortices near wall (Run 3a). Time interval between photographs is 0.020 s.

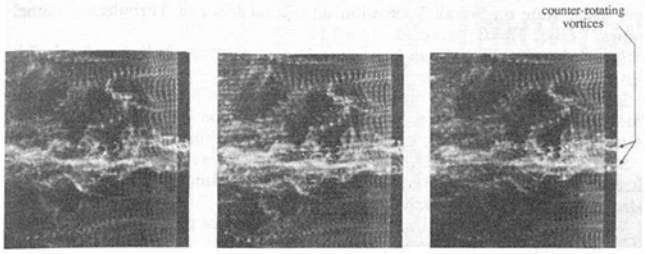

Fig. 9 Sequential pictures (from right to left) of low-speed streaks and longitudinal vortices near wall (Run 3a). Time interval between photographs is 0.020 s.

and the orientation of the longitudinal vortices were viewed in the horizontal plane with one camera, while the lift up and breakdown of the vortices were seen in the vertical plane with the other camera. Observation of the video sequences revealed that the low-speed streaks frequently occur as regions between pairs of longitudinal vortices near the boundary. Figures 8 and 9 illustrate sequential pictures (in the horizontal plane) of formation of these vortices adjacent to a low-speed streak near the wall. It appears from these pictures and many others that the bubbles generated from the vertical wire break up into two vortex-like structures along the streamwise direction. The vortices visualized this way generally form on either side of the low-speed streaks. From the video sequences of the events, it appears as if these vortices are the counter-rotating legs of the elongated loops in the flow direction. Furthermore, the spanwise distance between these vortices seems to be about $0.5\ \lambda^+ (\Delta z^+ \approx 50)$.

These results reinforce our earlier conjecture that the longitudinal counter-rotating vortices seen by Blackwelder and Eckelmann (1979) (among others) are perhaps the legs of hairpin or horseshoe vortices observed by Head and Bandyopadhyay (1981). Blackwelder and Eckelmann suggested that the observed inclined vortices could perhaps be the results of the instabilities caused by a high-speed sweep interacting with a low-speed streak while forming a localized free shear layer. However, the sequences of video films obtained here show that the longitudinal vortices seldom locate themselves in the regions of the low-speed streaks. They generally form in pairs with each vortex on either side of a low-speed streak.

C. Conceptual Mechanism of Streak Breakdown. The general picture arising from the present experiments and observations of previous investigators can perhaps be best illustrated by Fig. 10. This illustration is similar to the ones suggested by some other investigators (Kline et al., 1967; Blackwelder and Eckelmann, 1979; Hinze, 1975). It appears that the low-speed streaks observed near either the wall or the sheared interfaces are perhaps formed between the pairs of the longitudinal counter-rotating vortices (Head and Bandyopadhyay, 1981). These vortices are elongated in the direction of flow and are separated in the spanwise direction by $\Delta z^+ \approx 50$. The legs of these vortices are inclined at an angle of about 20–25 deg to the boundary for $y^+ < 20$. As they grow above $y^+ \approx 20$, they begin to flutter up and down and sideways, till they go through several ejections and lose their identity. The ejection process transports low momentum fluid away from the boundary causing the rolling of the eddies that move with the mean flow (Rashidi and Banerjee, 1988).

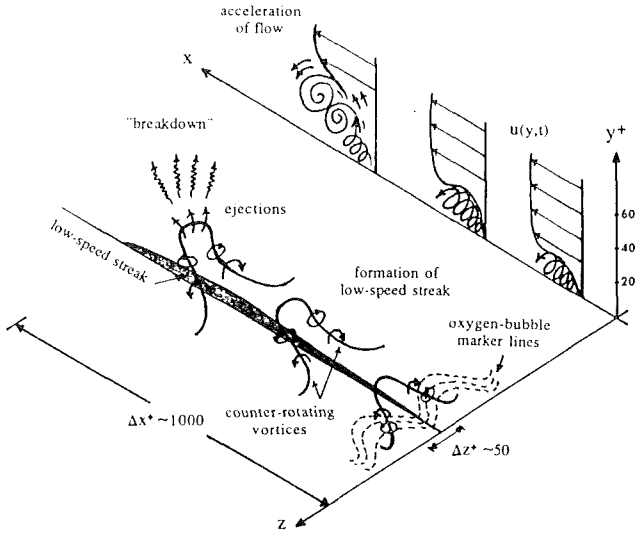

Fig. 10 Conceptual mechanism of streak breakdown near the boundary

Although the present experiments provide some convincing results to support the mechanism discussed above, many important questions remain to be answered. In particular, it is not yet clear as to why the flow primarily organizes itself in this manner near the sheared boundaries.

Conclusions

The results of the present visualization study indicate that near the sheared interfaces, the mean non-dimensional spanwise streak-spacing, λ^+, appears to be essentially invariant with shear Reynolds number, giving consistent values of $\lambda^+ \approx 100$ at $y_i^+ = 5$, while increasing with distance from the interface. The increase in λ^+ appears to be the results of both a merging or coalescence of the streaks (seen to occur even at $y_i^+ < 5$, as opposed to the wall region) and an intermittency effect due to fluttering in the upper extent of the low-speed streaks.

The simultaneous observation of streak formation (in the horizontal plane) and the streak breakdown (in the vertical plane) indicates that the low-speed streaks frequently occur as regions between the longitudinal vortices near the boundaries. Examination of these vortices shows that they originate from the boundaries at an angle of about 20–25 deg (for $y^+ < 20$) and begin to lift up or eject chaotically at a larger angle of about 40–50 deg (for $y^+ > 20$). Based on the present experiments and observations of previous investigators, a conceptual mechanism of streak breakdown near the sheared boundaries has been illustrated (Fig. 10).

Acknowledgment

We would like to express our gratitude to the U.S. Department of Energy, Basic Energy Sciences Program, for support of this project through Contract No. DE-FG03-85ER13314.

References

Blackwelder, R. F., and Eckelmann, H., 1979, "Streamwise Vortices Associated with the Bursting Phenomenon," *J. Fluid Mech.*, Vol. 94, pp. 577–594.

Fage, A., and Townend, H. C. H., 1932, "An Examination of Turbulent Flow with an Ultramicroscope," *Proc. Roy. Soc.*, Series A, Vol. 135, pp. 656–677.

Grass, A. J., 1971, "Structural Features of Turbulent Flow Over Smooth and Rough Boundaries," *J. Fluid Mech.*, Vol. 50, pp. 233-255.

Head, M. R., and Bandyopadhyay, P., 1981, "New Aspect of Turbulent Boundary-Layer Structure," *J. Fluid Mech.*, Vol. 107, pp. 297-338.

Heidrick, T. R., Banerjee, S., and Azad, R. S., 1971, "Speed and Inclination of Eddies in Wall Turbulence," *Nat. Phys. Sci.*, Vol. 234, pp. 136-138.

Hinze, J. O., 1975, *Turbulence*, McGraw-Hill, New York, 2nd edition.

Kim, H. T., Kline, S. J., and Reynolds, W., 1971, "The Production of Turbulence Near a Smooth Wall in a Turbulent Boundary Layer," *J. Fluid. Mech.*, Vol. 50, pp. 133-160.

Kim, J., Moin, P., and Moser, R., 1987, "Turbulence Statistics in Fully Developed Channel Flow at Low Reynolds Number," *J. Fluid Mech.*, Vol. 177, pp. 133-166.

Klebanoff, P. S., 1954, "Characteristics of Turbulence in a Boundary Layer with Zero Pressure Gradient," NACA Tech. Note No. 3178.

Kline, S. J., and Runstadler, P. W., 1959, "Some Preliminary Results of Visual Studies of the Flow Model of the Wall Layers of the Turbulent Boundary Layer," ASME *Journal of Applied Mechanics*, Vol. 2, pp. 166-170.

Kline, S. J., Reynolds, W. C., Schraub, F. A., and Runstadler, P. W., 1967, "The Structure of Turbulent Boundary Layers," *J. Fluid Mech.*, Vol. 30, pp. 741-773.

Kreplin, H. P., and Eckelmann, H., 1979, "Propagation of Perturbations in the Viscous Sublayer and Adjacent Wall Region," *J. Fluid Mech.*, Vol. 95, pp. 305-322.

Lam, K., and Banerjee, S., 1988, "Investigation of Turbulent Flow Bounded By a Wall and a Free Surface," *Fundamentals of Gas-Liquid Flows* ASME-FEd, ed. E. Michaelides and M. Sharma, pp. 29-38.

Laufer, J., 1954, "The Structure of Turbulence in Fully Developed Pipe Flow," NACA Tech. Note, No. 2954.

Luchik, T. S., and Tiederman, W. G., 1987, "Timescale and Structure of Ejections and Bursts in Turbulent Channel Flows," *J. Fluid Mech.*, Vol. 174, pp. 529-552.

Moin, P., and Kim, J., 1985, "The Structure of the Vorticity Field in Turbulent Channel Flow," *J. Fluid Mech.*, Vol. 155, pp. 441-464.

Nakagawa, H., and Nezu, I., 1977, "Predication of the Contribution to the Reynolds Stress from Bursting Events in Open-Channel Flows," *J. Fluid Mech.*, Vol. 80, pp. 99-128.

Nakagawa, H., and Nezu, I., 1981, "Structure of Space-Time Correlations of Bursting Phenomena in an Open-Channel Flow," *J. Fluid Mech.*, Vol. 104, pp. 1-43.

Oldaker, D. K., and Tiederman, W. G., 1977, "Spatial Structure of the Viscous Sublayer in Drag-Reducing Channel Flows," *Phys. Fluids*, Vol. 20, pp. S133-S144.

Rashidi, M., and Banerjee, S., 1988, "Turbulence Structure in Free-Surface Channel Flow," *Phys. Fluids*, Vol. 31, pp. 2491-2503.

Rashidi, M., and Banerjee, S., 1990, "The Effect of Boundary Conditions and Shear Rate on Streak Formation and Breakdown in Turbulent Channel Flows," *Phys. Fluids*, accepted.

Schlichting, H., 1979, *Boundary Layer Theory*, McGraw-Hill, New York, 7th edition.

Smith, C. R., 1983, "A Synthesized Model of the Near-Wall Behavior in Turbulent Boundary Layers," *Proc. of 8th Symp. on Turbulence* (ed. G.K. Patterson and J. L. Zakin), University of Missouri-Rolla.

Smith, C. R., and Metzler, S. P., 1983, "The Characteristics of Low-Speed Streaks in the Near-Wall Region of a Turbulent Boundary Layer," *J. Fluid Mech.*, Vol. 129, pp. 27-54.

Willmarth, W. W., and Lu, S. S., 1972, "Structure of the Reynolds Stress Near the Wall," *J. Fluid Mech.*, Vol. 55, pp. 65-92.

The Three-Dimensional Jet-Jet Impingement Flow in a Closed-End Cylindrical Duct

T.-M. Liou
Professor.
Mem. ASME

Y.-H. Hwang
Graduate Student.

S.-M. Wu
Graduate Student.

Department of Power Mechanical Engineering,
National Tsing Hua University,
Hsin-Chu, Taiwan 30043

Experimental and theoretical studies are reported on the three-dimensional jet-jet impingement flow in a closed-end cylindrical duct with two 60-deg side inlets. The measurements were made using the laser-Doppler velocimeter. The Reynolds number based on the air density, duct diameter, and bulk velocity was 2.6×10^4. The governing partial differential equations were solved numerically with the $k-\epsilon$ turbulence model. The flow field was characterized in terms of the mean velocity and turbulence intensity components, the swirl intensity, the stagnation points, and the mass flow bifurcated into the head region and was found to be weakly dependent on the head height. Simple geometrical expressions were deduced and were found to effectively estimate the stagnation points and the optimal head height. Furthermore, the dependence of the mass flow into the head region on the head height was found to parallel the dependence of the combustion efficiency and flame stability on the head height.

Introduction

The flow field in a closed-end cylindrical duct with two or more jets introduced through ports in the duct periphery (Figs. 1-2) is very complicated since it is characterized by a synthesis of a number of diverse flow modulus. These flow modulus are the inlet jets, the jet-jet head-on collision, the jet-wall impingement, the recirculating flow in the separated region, and the developing duct flow far downstream of the inlet ports. Such a flow field has several practical applications; for example, it is one of the flow fields involved in internal biofluid-dynamics (Lighthill, 1975). Additionally, the impingement of jets provides one of the most effective ways to mix the fluids, and is an important feature of the flow field in utility boiler furnaces and in side-dump ramjet combustors. Therefore, a better understanding of such a flow field is highly desirable. Especially, the role of the head height (L_d^*), which denotes the distance between the closed end (i.e., head plate) and the upstream edge of the inlet ports, deserves the special interest since the vortices generated in the head height region can serve as a flame stabilizer such that there is no need to place the physical flame holder in the combustor.

Shahaf et al. (1980) first conducted an investigation on the two-dimensional (2-D) mean flow field in a square cross-sectional channel with two side inlets both analytically and experimentally. Large discrepancies between the measured and calculated axial mean velocity profiles were found along the channel axis and in the recirculation region. No measurements were made in the head region and no information relevant to the influence of the head height on the jet-jet impingement flow field was reported. Choudhury (1982) experimentally tested the combustor performance of a gas generator ramjet with four side inlets and concluded that the system of vortices in the head region is crucial to the stable operation of the combustor. They also concluded that the inlet flow angle does not have any influence on the vortex system in the head region of their combustor. More importantly, they found an optimal head height for the best flame blowoff performance; however, they did not provide detailed physical explanation to the ex-

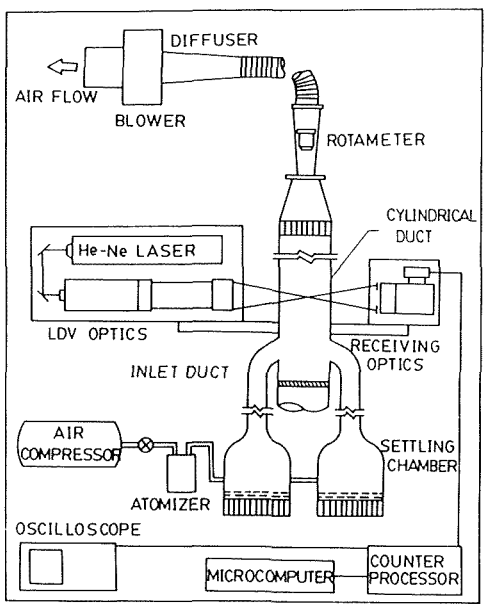

Fig. 1 Schematic drawing of overall experimental system

Contributed by the Fluids Engineering Division for publication in the JOURNAL OF FLUIDS ENGINEERING. Manuscript received by the Fluids Engineering Division February 23, 1989.

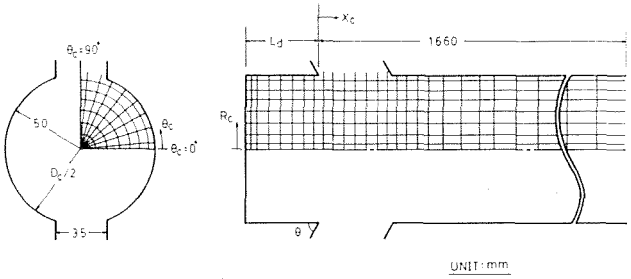

Fig. 2 Sketch of configuration, coordinate system and dimensions of a dual-inlet closed-end cylindrical duct (Uncertainty in X_c position: less than ±0.3 mm, in R_c position: less than ±0.3 mm, in θ_c: less than ±1.5 deg, in D_c: less than ±0.3 mm, in L_d: less than ±0.5 mm)

istence of such an optimal head height. Vanka et al. (1983) calculated the three-dimensional mean flow field in a cylinder combustor with two side inlets separated by an azimuthal angle of 90 deg. Two head heights were studied. They observed the main effects of the smaller head height are to compress the head recirculation region and to alter its shape by making the eddy form near the central region. Their calculations, however, did not predict a vortex pattern in the head region in the $\theta_c = 180$ deg plane shown by flow visualization (Stull et al., 1985). Vanka et al. (1985) further performed calculations of the three-dimensional reacting flow in the same combustor. They also found an optimal head height for the best combustion efficiency. Nonetheless, as pointed by Vanka et al., there are no experimental data to validate the turbulence and combustion models used in their calculations. In view of the lack of quantitative experimental data, particularly the turbulence data, with which to compare numerical predictions, Liou and Wu performed detailed mean velocity and turbulence intensity measurements in curved 60-deg inlet ducts (Liou and Wu, 1986) and in a three-dimensional side-dump cylindrical combustor (Liou and Wu, 1988) using Laser-Doppler velocimetry (LDV); nevertheless, their measurements were carried out only at a single head height.

The brief literature survey made above clearly suggests that a further study on the effects of the head height on the jet-jet impingement flow field in a closed-end cylindrical duct both experimentally and analytically would be worthwhile. Accordingly, this paper presents both LDV measured and numerically calculated results for the flow in such a configuration with L_d^* varied in the range of 0 to 4. The measurements were made using LDV since the flow reversal in the head recirculation region and the large turbulence fluctuations generated by the jet-jet impingement make the use of hot-wire technique impractical. Furthermore, the flow field will be characterized in terms of both the mean velocity and the turbulence intensity since the foregoing literature survey indicates that the turbulence information is lacking. In addition to the numerical computations, simple geometrical relations will also be derived to aid in understanding the flow characteristics. It is hoped that the results presented in this study will provide useful information to the researchers in this area.

In the following sections of this paper, the experimental system and the theoretical treatment are stated first. The computed mean flow patterns are subsequently discussed and compared with LDV measured results. Then, the measured mean velocity and the turbulence intensity at various streamwise cross sections are presented in detail. Finally, simple geometrical expressions are used to estimate the locations of some critical stagnation points and the optimal head height.

Experimental Apparatus and Conditions

Experimental System. The closed-end cylindrical duct with two side inlets and LDV experimental set-up is shown in schematic form in Fig. 1. Air was drawn into the curved side inlets and a 10:1 contraction by a turbo blower (3500 rpm/3 phase/10 hp) at the downstream end. The air then flowed into the curved side inlets, the cylindrical duct, a flow straightener, a rotameter, a bellows; and was exhausted by the blower which was driven by a dc motor.

The LDV optics were set up in a dual-beam forward or off-axis scattering configuration. A linearly polarized 15-mW helium-neon laser (632.8 nm wavelength) provided the coherent light source. This beam was split into two parallel beams of equal intensity by a beamsplitter. A Bragg cell was used to cause a 40 MH_Z frequency shift on one of the beams. A frequency shift is used to eliminate the directional ambiguity, which is essential if there is flow reversal as is expected in a

Nomenclature

C_1, C_2, C_μ = constants in $k-\epsilon$ turbulence models
D_c = duct diameter
k = turbulent kinetic energy
L_d = head height of circular duct
L_d^* = nondimensional head height $L_d^* = L_d/(D_c/2)$
L_{do}^* = optimal nondimensional head height for $(\dot{m}_{ri}/\dot{m}_{in})_{max}$
$\dot{m}_{in}$ = inlet mass flow rate
$\dot{m}_{ri}$ = mass flow rate transported into the head region
R_c = radial coordinate
R_c^* = nondimensional radial coordinate $R_c^* = R_c/(D_c/2)$
Re_c = Reynolds number $Re_c = \rho U_{ref} D_c/\mu_l$
SI = swirl intensity
U = axial mean velocity
U_{ref} = bulk mean velocity
u' = axial turbulence intensity
X^* = alternative nondimensional axial coordinate $X^* = X_c/(D_c/2)$
X_c = axial coordinate
X_c^* = nondimensional axial coordinate $X_c \le 0$; $X_c^* = X_c/L_d$ $X_c \ge 0$; $X_c^* = X_c/D_c$
X_i = axial coordinate at impingement stagnation point
X_i^* = nondimensional axial coordinate at impingement point
X_r = axial coordinate at reversal stagnation point
X_r^* = nondimensional axial coordinate at stagnation point
θ = angle of side-inlet jets
θ_c = azimuthal coordinate
ϵ = dissipation rate of turbulent kinetic energy
ρ = air density
μ_l = molecular dynamic viscosity
μ_t = turbulent dynamic viscosity
σ_k, σ_ϵ = turbulent Prandtl number of k and ϵ, respectively

closed-end cylindrical duct with two side inlets. The resulting pair of beams was then passed through a 120- or 250-mm focal-length lens. The focused beams entered the cylindrical duct through the transparent plexiglas wall, intersected inside the duct giving a probe volume with dimensions of 0.52 mm by 0.097 mm (120 mm focal-length lens, forward scattering) or 0.57 mm by 0.18 mm (250 mm focal-length, off-axis scattering), and then passed through another side wall into the beam traps. The entire LDV system was mounted on a milling machine with four vibration isolation mounts. The light scattered from the seeding particles was collected by a receiving optical package to reflect the collected light into a photomultiplier. The detected signal was electrically downmixed to the appropriate frequency shift (2 to 10 MH_z in the present work). Then a counter processor with 2 ns resolution was used to process the Doppler signal. The Doppler signal was monitored on an oscilloscope and the digital output of the counter processor was fed directly to a micro-computer for storage and analysis. The seeding particles were introduced into the air stream by eight atomizers symmetrically located on the four walls of two settling chambers. The atomizers were operated by filtered compressed air and salt water and produced particles in the size range of 0.5–5 μm. The salt solution was mixed to give a nominal 0.8 μm particle after the droplet dried. The seeding flow rate was 74.7 (liters/min), and the seeding concentration was 1×10^6 (particles/cm^3).

The configuration of the dual-inlet closed-end cyclindrical duct model, coordinate system and dimensions are sketched in Fig. 2. The model consisted of two curved rectangular inlet ducts (Fig. 1) and a circular chamber.

The two rectangular inlet ducts intersect the chamber at an inlet angle of 60 deg. The centerlines of both inlet ducts intersect the chamber at the same axial station and are located radially at 180 deg to each other. The internal dimensions of the inlet ducts are 35 mm $\times$ 47 mm. The upstream edge of the inlet ports is taken as the chamber longitudinal zero reference point, and, thus, the longitudinal coordinate downstream of the zero reference point is positive.

The chamber model was made of a 5-mm plexiglas. It has a flat head plate which is adjustable, i.e., can be positioned axially from zero reference point to 200 mm forward of the inlet ducts. The diameter of the chamber is 100 mm and measures 650 mm in length from the axial zero reference point to the exit.

Experimental Conditions. The velocity measurements were made in 9 planes ($R_c^*-\theta_c$ planes) normal to the longitudinal axis. These data planes were located at $X_c^*=-0.8$, -0.6, 0.0, 0.25, 0.5, 1.0, 2.5, 4.0, and 6.5, respectively. In each data plane the velocity measurements were made along two orthogonal diameter. That is, for diameter $\theta_c=0$ deg both axial and tangential velocity components were measured at 16 to 17 locations and for diameter $\theta_c=90$ deg both axial and radial velocity components were measured at 10 to 17 locations. Within a given data plane, the probe volume was brought as near as 3 mm to 10 mm, depending on the existence of the dead zone or region masked by the inlet flanges, from the wall for measurements. The chamber bulk velocity 4.15 m/s was used as a reference to normalize the experimental results. This velocity corresponds to a Reynolds number (Re_c) of 2.6×10^4 indicating the flow to be turbulent.

Theoretical Treatment

The computations were performed by numerically solving the fully elliptic 3-D Navier-Stokes equations. To simplify the problem, the flow was considered to be isothermal, incompressible, and steady-state in the mean.

The Mean Flow Equations. The time averaged equations for conservation of mass and momentum can be expressed in the tensor notation as

$$\frac{\partial U_i}{\partial X_i}=0 \tag{1}$$

$$\frac{\partial}{\partial X_j}(\rho U_i U_j)=-\frac{\partial P}{\partial X_i}+\frac{\partial}{\partial X_j}\left[\mu_l\left(\frac{\partial U_i}{\partial X_j}+\frac{\partial U_j}{\partial X_i}\right)-\rho\overline{u_i u_j}\right] \tag{2}$$

Note that the turbulence correlation $\overline{u_i u_j}$ is the time-average $u_i u_j$ and stands for the Reynolds stresses which must be modeled to close the above set of equations.

The Turbulence Model. In the present calculation, the $k-\epsilon$ two-equation turbulence model (Launder and Spalding, 1974) which adopts the generalized Boussinesq eddy viscosity concept (Hinze, 1959) is expressed as

$$-\rho\overline{u_i u_j}=\mu_t\left(\frac{\partial U_i}{\partial X_j}+\frac{\partial U_j}{\partial X_i}\right)-\frac{2}{3}\delta_{ij}\rho k \tag{3}$$

where δ_{ij} is the Kronecker-Delta function and μ_t is the turbulent viscosity that may be related to the kinetic energy of turbulence, k, and its dissipation rate, ϵ, by dimensional analysis

$$\mu_t=C_\mu\rho k^2/\epsilon \tag{4}$$

where $C_\mu=0.09$ (Launder and Spalding, 1974) is a constant of the model. The differential equations for k and ϵ are

$$\frac{\partial}{\partial X_j}(\rho U_j k)=\frac{\partial}{\partial X_j}\left[(\mu_l+\mu_t/\sigma_k)\frac{\partial k}{\partial X_j}\right]-\rho\overline{u_i u_j}\frac{\partial U_i}{\partial X_j}-\rho\epsilon \tag{5}$$

$$\frac{\partial}{\partial X_j}(\rho U_j\epsilon)=\frac{\partial}{\partial X_j}\left[(\mu_l+\mu_t/\sigma_\epsilon)\frac{\partial\epsilon}{\partial X_j}\right]-C_1\frac{\epsilon}{k}\rho\overline{u_i u_j}\frac{\partial U_i}{\partial X_j}-C_2\rho\epsilon^2/k \tag{6}$$

where $C_1=1.44$ and $C_2=1.92$ are further constants in this model. Furthermore, $\sigma_k=1.0$ and $\sigma_\epsilon=1.217$ are turbulent Prandtl numbers for k and ϵ, respectively. Equations (3) and (4) can be substituted into equations (2), (5), and (6) to form a set of equations which have the same number of equations and unknowns. The system of 6 equations for 6 unknowns U_i, P, k, and ϵ with prescribed laminar viscosity and density completes the closure problem for the turbulent flow investigated.

Boundary Conditions. The above set of three-dimensional ($R_c^*-\theta_c-X_c^*$ and $V-W-U$), elliptic partial differential equations has to be solved with the following boundary conditions (see Figs. 1 and 2):

(i) Symmetric planes ($\theta_c=0$ deg and $\theta_c=90$ deg)

$$\frac{\partial U}{\partial\theta_c}=\frac{\partial V}{\partial\theta_c}=\frac{\partial k}{\partial\theta_c}=\frac{\partial\epsilon}{\partial\theta_c}=0;\ W=0$$

(ii) Central axis ($R_c=0$)

$$\frac{\partial U}{\partial R_c}=\frac{\partial k}{\partial R_c}=\frac{\partial\epsilon}{\partial R_c}=0;\ V=W=0$$

(iii) Exit

$$\frac{\partial U}{\partial X_c}=\frac{\partial k}{\partial X_c}=\frac{\partial\epsilon}{\partial X_c}=0;\ V=W=0$$

In this study, the location of the computational downstream boundary was determined from the measured results or from the computational test. In fact, the computational test showed that there is no noticeable change in the flow field as long as the location of the exit plane was far enough to allow the flow to become unidirectional.

(iv) Inlet (Liou and Wu, 1986)

U = measured U_{in}; V = measured V_{in};
W = measured W_{in}
k = measured k_{in}; $\epsilon = \epsilon_{in} = k_{in}^{3/2}/(B \cdot \lambda)$
where B = inlet-duct width $= D_c/2$ and $\lambda = 0.005$

(v) Walls

$$U = 0;\ V = 0;\ W = 0$$

Since the $k-\epsilon$ model is valid only in those regions that are strongly turbulent, that is, in regions where the eddy diffusivity overwhelms the molecular diffusivity, it is not applicable in the viscous sublayer. In the other way, the steep change of flow properties in the wall region needs an extremely fine grid arrangement and makes the computational efforts unpractical. Therefore, in this study, the near-wall region was simulated by a semi-empirical two-zone model, i.e., viscous sublayer and fully turbulent zone, and wall-function (Launder and Spalding, 1974) was used to bridge the viscous sublayer.

Numerical Scheme. The solution of the above partial differential equations along with the boundary conditions is obtained by using the iterative finite difference scheme based on the SIMPLE (Semi-Implicit Pressure-linked Equations) algorithm of Patankar and Spalding (1980). The partial differential equations are integrated over small discrete control volumes which are formed by the grid system and are converted to a set of nonlinear algebraic equations. A staggered grid system is employed. Figure 2 shows the grid arrangement for all scalar variables. The nodes of the velocity grid are located midway between the scalar grid nodes to represent the true convective quantities across the boundary of such control volumes. To formulate the total fluxes, including convective and diffusive terms, across the faces of the control volumes, the power-law scheme (Patankar, 1980) is applied.

The solution procedure is initiated with guesses for the velocity and pressure fields and then proceeds with line by line iteration. After each sweep over the solution domain, adjustments for the pressure field are made to satisfy the continuity along each line of cells. These adjustments in turn destroy the compliance of the velocities and pressure fields with the momentum equations. Further iterations are thus needed until the continuity and momentum equations are simultaneously satisfied to the requisite degree of accuracy. The tolerance of the normalized mass and momentum residuals are typically from 0.005 to 0.001. k and ϵ are also solved line by line simultaneously with the mean velocity distribution. To prevent numerical instability, successive changes of the flow variables are underrelaxed with their old values. The under relaxation factors are 0.5 for U, V, W, k, ϵ, μ_t, and 0.3 for P.

The calculations were made using a $9 \times 10 \times 40$ grid (Fig. 2) in the radial, azimuthal, and axial directions, respectively, for the typical case of $L_d^* = 1.0$. A large number of grid points were placed in the areas where steep variations in velocities were revealed from the previous experimental results. To ensure the grid independence, solutions were calculated using different grid sizes. The tested grid sizes were $6 \times 8 \times 28$, $9 \times 10 \times 40$, and $16 \times 14 \times 54$. Less than 5 percent differences in the computed results were found between grid sizes of $9 \times 10 \times 40$ and $16 \times 14 \times 54$. Consequently, the grid size $9 \times 10 \times 40$ was chosen for $L_d^* = 1.0$ in the present work. The grid systems for other head heights were arranged at the same grid density as that for $L_d^* = 1.0$. Typically, convergence required 400 iterations, and the corresponding CPU time on a CDC-CYBER 180/840 computer system was about 3/4 hours.

Uncertainty Estimates

Representative values of uncertainty estimates are noted in figure captions. More detailed uncertainty estimates such as velocity bias, refraction at cylindrical walls, and statistical error associated with finite number of measurements (typically 2000–4000) at each measuring location are included in Liou and Wu (1988).

Results and Discussion

General Flow Pattern. The general flow pattern for the case of $L_d^* = 1.0$ was measured and reported in detail in Liou and Wu (1988), and can be summarized as follows. It is found that the helical flows with their axis parallel to the central axis are mainly generated in the impinging region of the two inlet jets and decay rapidly toward both the head and downstream regions. They further degenerate into unidirectional flow at about four duct diameters downstream. The flow field in the head region is mainly composed of recirculating flows with their vortex axes perpendicular to the $X_c^* - R_c^*$ planes. Moreover, the aforementioned recirculating flows in planes of constant azimuthal angles $\theta_c = 0$ deg and $\theta_c = 90$ deg are counterrotating. The recirculating flows in the $\theta_c = 90$ deg plane (i.e., the inlet-jet plane) are driven by the upstream bifurcating flow of the jets impinging upon one another and by the shear of the inlet jets.

The effects of the head height on the flow characteristics described above have been investigated both experimentally and computationally in the present study and will be discussed in the following.

Swirl Intensity. The circumferential motion associated with the streamwise vortices mentioned in the previous section has the function of enhancing mixing and, therefore, greatly affects the combustion characteristics for the case of a side-inlet combustor. It was found that the swirl intensity (SI), defined as the ratio of the axial flux of the swirling mean kinetic energy at a given X_c^* to the flux of the total mean kinetic energy at the inlet, can be used to quantitatively characterize the circumferential motion (Hwang, 1989). Figure 3 depicts the swirl intensity distribution for various head heights. As one can see the calculated results for $0 \le L_d^* \le 4$ all fall into the shaded region and, therefore, the swirl intensity is rather insensitive to the variation of the head height. The weak dependence of SI on L_d^* is because the streamwise vortices are generated in the region where the two inlet jets impinge on one another and that the resulting swirling motion is mainly confined within the range of $0 \le X_c^* \le 2$ with a peak intensity at $X_c^* = 0.5$, as shown in Fig. 3.

Flow Patterns in the Azimuthal Planes. Figure 4(*a*) through 4(*c*) indicate the calculated flow patterns in the $\theta_c = 90$ deg plane for $L_d^* = 0.0$, 1.0 and 2.0, respectively. The flow patterns downstream of the inlet port are found to be similar. The differences among the velocity vectors shown in

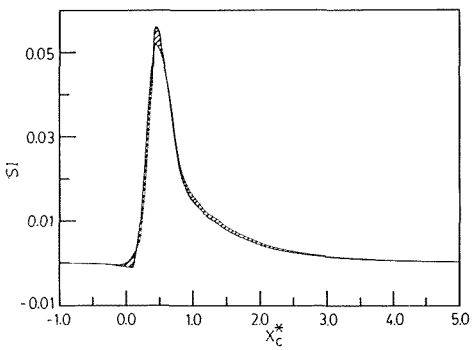

Fig. 3 Calculated swirl intensity distribution for various head heights ($0 \le L_d^* \le 4$)

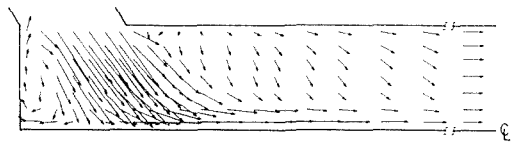

Fig. 4(a)

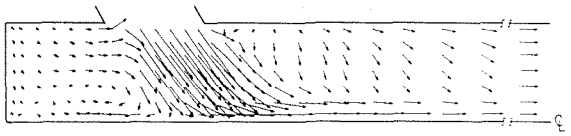

Fig. 4(b)

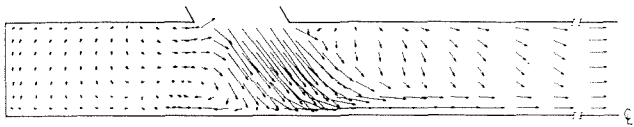

Fig. 4(c)

Fig. 4 Calculated flow pattern in the $\theta_c = 90$ deg for (a) $L_d^* = 0.0$, (b) $L_d^* = 1.0$, (c) $L_d^* = 2.0$

Figs. 4(a)-(c) are less than 5 percent of U_{ref} as $X_c^* \geq 0.5$. On the other hand, the recirculating flow pattern in the head region is compressed as the head height becomes smaller and has a triangular shape as $L_d^* = 0$. As mentioned earlier in the literature survey, a similar observation was also reported by Vanka et al. (1983). For $L_d^* = 0$ (Fig. 4(a)), the upstream bifurcating flow of the jet-jet impingement directly impinges upon the head plate. Thus relatively large impinging force will act on the head plate as the head height reduced to zero. As L_d^* is increased to 1.0 (Fig. 4(b)), however, there exists additional low-speed flow region adjacent to the head plate. This low speed flow region behaves like a source for the flow in the $\theta_c = 90$ deg plane since it supplies fluids from the other azimuthal planes. Thus instead of impinging upon the head plate, the aforementioned upstream bifurcating flow collides with part of these low speed fluids at about $X_c^* = -0.66$ (referred to as reversal stagnation point in this study) and near the central axis. The similar behavior, but more pronounced, is also found for the case of $L_d^* = 2.0$, as depicted in Fig. 4(c).

A further comparison of Fig. 4(b) with Fig. 4(c) reveals that the clockwise recirculation flow patterns, located between the reversal stagnation point and the jet impingement stagnation point ($X_c^* = 0.35$ for L_d^* studied), are quite similar for $L_d^* = 1.0$ and 2.0. Also the positions of the two stagnation points remain approximately invariant for $L_d^* \geq 1.0$, as will be shown later. Furthermore, the mean velocity in the low-speed flow region mentioned above is typically below 10 percent of U_{ref}. These low speed fluids, especially those adjacent to the head plate, play the role of a nearly stagnant wall to the upstream bifurcating flow of the jet-jet impingement. All the above observations tend to suggest that there may also exist similar characteristics for the flow field upstream of the inlet port provided the head height is large enough to allow the appearance of a reversal stagnation point in the head region.

Comparison Between Computations and Measurements. Figure 5 shows the calculated and measured mean axial velocity profiles at various axial stations in the $\theta_c = 90$ deg plane for the case of $L_d^* = 2.0$. As one can see, the calculated results are in general agreement with the measured data. Discrepancies between calculated and measured mean velocity profiles decrease toward the head region and toward the region far downstream. For $0 \leq X_c^* \leq 1.0$, a maximum discrepancy of less than 20 percent of U_{ref} is found. The large discrepancy in the region of $0 \leq X_c^* \leq 1.0$ is partly because that the asymmetrical flow pattern shown by the measured data is not considered in the computations.

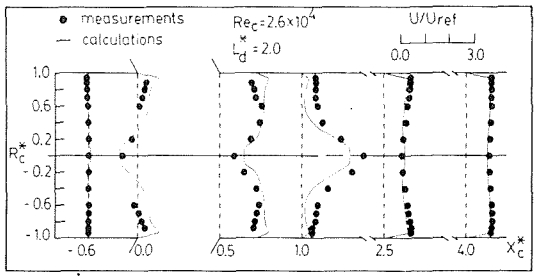

Fig. 5 Calculated and measured profiles of mean axial velocities at various X_c^* for $\theta_c = 90$ deg (Uncertainty in U/U_{ref}: less than ± 2.5 percent, in R_c^*: less than ± 0.6 percent)

Measured Mean Velocity and Turbulence Intensity. The effects of L_d^* on the jet-on-jet impingement flow field can also be characterized using the measured axial mean velocity and turbulence intensity profiles, as shown in Figs. 6(a) through 6(d). For the flow regions downstream of the inlet port ($X_c^* > 0.5$), Fig. 6(a) depicts that both the mean velocity and the turbulence intensity at $X_c^* = 1.0$ have similar profile as L_d^* varies from 0 to 4. The jet-like mean velocity profile near the central axis indicates the bifurcating flow immediately downstream of the jet-on-jet impingement. The associated steep mean velocity gradient is the source of the turbulence generation and illustrates the high turbulence level shown in Fig. 6(a) where the two u' peaks corresponding to the steepest mean velocity gradient at $R_c^* = \pm 0.2$ have values comparable to U_{ref}. As the flow proceeds downstream, Fig. 6(b) shows that all the curves representing different L_d^* at $X_c^* = 2.5$ tend to collapse into one curve with a variance less than 5 percent of U_{ref}. The smaller variance for the curves at $X_c^* = 2.5$, compared with that at $X_c^* = 1.0$, is partly due to the lower turbulence level at $X_c^* = 2.5$ which is approximately half of u' at $X_c^* = 1.0$. Also note that the peak mean axial velocity has been helically convected downstream from the central axis at $X_c^* = 1.0$ to the wall region at $X_c^* = 2.5$. Thus the mean velocity profile at $X_c^* = 2.5$ is more uniform than that at $X_c^* = 1.0$ and is still not fully developed. However, even in the developing state, the influence of upstream variance of L_d^* on the flow characteristics at $X_c^* = 2.5$ is already very weak. It is worth mentioning here that the above experimental observations (Figs. 6(a) and 6(b)) for the flow downstream of the inlet port is in general agreement with the previous observations based on the computational predictions (Figs. 3 and 4).

For the flow region immediately upstream of the inlet port, that is, at $X_c^* = 0.0$, Fig. 6(c) shows that both the measured axial mean velocity and turbulence intensity profiles are very similar independently of L_d^*. This trend suggests that the bifurcating flow immediately upstream of the jet-jet impingement is mainly controlled by the inlet jet and not by the head height. At $X_c^* = -0.6$ (Fig. 6(d)), that is, in the head region, the axial mean velocity is positive near the wall and negative around the centerline for the case of $L_d^* = 1.0$, whereas this trend is completely reversed for the case of $L_d^* = 2.0$ and 4.0. In addition, the corresponding turbulence intensity shown in Fig. 6(d) monotonically decreases with increased L_d^*. Thus both the measured axial mean velocity and turbulence intensity in the head region display nonsimilar profiles to the variation of L_d^* under the coordinate X_c^* which is normalized by the head height for $X_c < 0$ (Fig. 2) such that the coordinate at the head plate is always -1.0 irrespective of L_d^*. However, as discussed previously, the measured results at $X_c^* = 0$ suggest that the bifurcating flow immediately upstream of the jet-jet impingement is majorly controlled by the inlet jets. Hence, the physical distance between any cross-section plane in the head region and the plane passing through the upstream edge of the inlet port ($X_c = 0$) would be an important length scale to

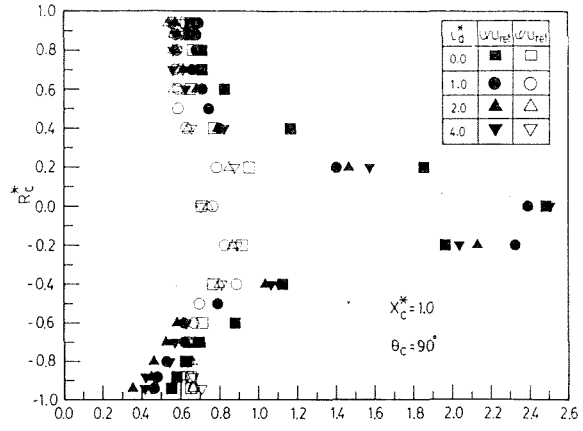

Fig. 6(a)

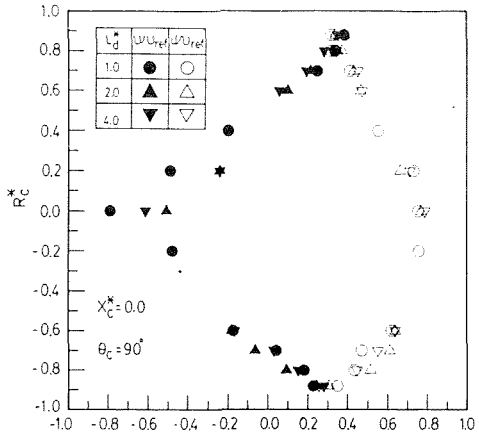

Fig. 6(c)

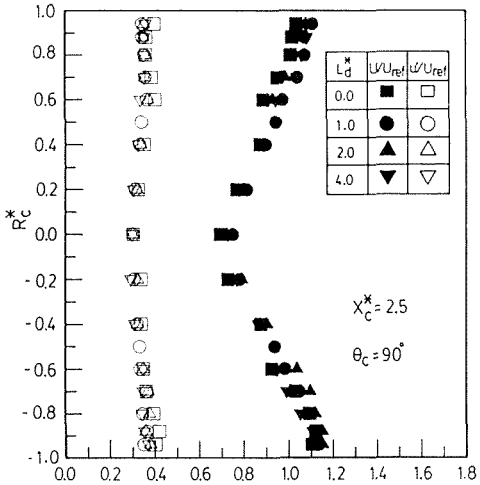

Fig. 6(b)

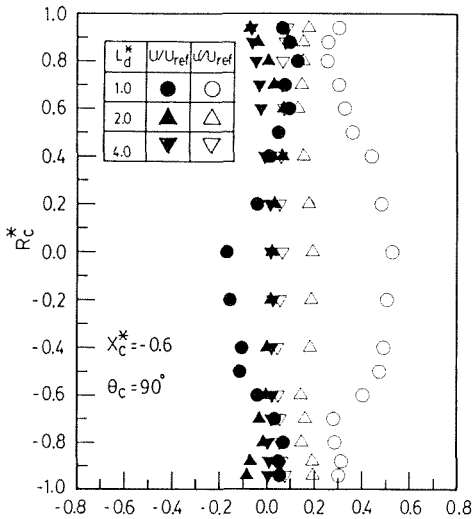

Fig. 6(d)

Fig. 6 Measured axial mean velocity and turbulence intensity profiles for various L_d^* at (a) $X_c^* = 1.0$, (b) $X_c^* = 2.5$, (c) $X_c^* = 0.0$, (d) $X_c^* = -0.6$ (Uncertainty in U/U_{ref}: less than ±2.5 percent, in u'/U_{ref}: less than ±3.1 percent, in R_c^*: less than ±0.6 percent)

characterize the flow field in the head region. Figure 7 is a plot of the measured centerline mean velocity and turbulence intensity versus the new coordinate $X^* = X_c/(D_c/2)$ for various L_d^*. As one can see, rather similar profiles are found for both U/U_{ref} and u'/U_{ref} as $L_d^* > 1.0$. The variance is less than 10 and 5 percent of U_{ref} for the U/U_{ref} and u'/U_{ref} curves, respectively. It is also worthwhile to note that both U/U_{ref} and u'/U_{ref} almost vanish, that is, the fluid is nearly stagnant, between the head plate and $X^* = -1.0$ as $L_d^* > 1.0$. This fact suggests that the position of the head plate is effectively moved to $X^* = -1.0$ as $L_d^* > 1.0$.

Stagnation Points. The feature of similar flow patterns in the head region for $L_d^* > 1.0$ can be further interpreted by studying the positions of aforementioned two stagnation points as a function of L_d^*. Figure 8 is such a plot. The dotted line represents the position of the head height which, strictly speaking, is another stagnation point according to the no-slip condition. Several observations can be made from Fig. 8. First, topologically, the existence of the two stagnation points as shown by the solid squares and circles delimits three flow region according to the flow direction along the centerline. Second, the experimentally measured and numerically computed positions of the two stagnation points are in good agreement. Third, the impingement stagnation point is found to be relatively insensitive to the changes in the head height. This is

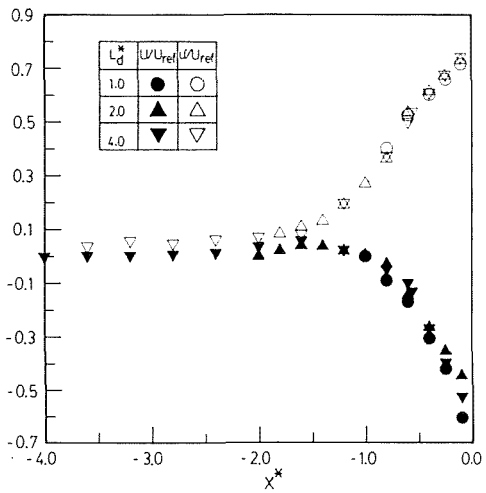

Fig. 7 Measured centerline mean velocity and turbulence intensity profiles versus X^* for various L_d^* (Uncertainty in U/U_{ref}: less than ±2.5 percent, in u'/U_{ref}: less than ±3.1 percent, in X^*: less than ±0.6 percent)

a further justification of the previously made statement, that is, the flow field near the jet-jet impingement is mainly affected by the jet itself. In fact, a simple geometrical relation

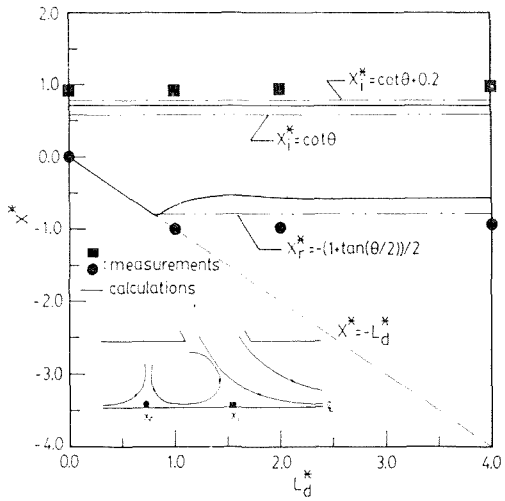

Fig. 8 The positions of jet impingement stagnation point and reversal stagnation point as a function of head height (Uncertainty in L_d^*: less than ±1 percent, in X^*: less than ±0.6 percent)

can be proposed for predicting the impingement stagnation point if one considers the two inlet jets impinge on each other in a straight manner. The derivation is done in the Appendix and the expression obtained is

$$X_i^* = \cot\theta \tag{7}$$

In this work, the inlet flow angle θ is 60 deg which gives $X_i^* = 0.577$. This estimated value is lower than both measured and computed ones. The reason is due to the existence of a separation bubble near $X_c^* = 0.0$ in the curved inlet duct (Liou and Wu, 1986) which pushes the inlet jet toward the downstream edge ($X_c^* = 0.5$) of the inlet port. The jet impingement point is therefore shifted downstream. To account for this shift, expression (7) can be modified as

$$X_i^* = \cot\theta + 0.2 \tag{7'}$$

since the separation bubble has a thickness of 1.0 D_c. The modified expression gives $X_i^* = 0.777$ which is between the calculated and the measured values. Fourth, Fig. 8 shows that the reversed stagnation point will occur if L_d^* is increased beyond 1.0. In addition, once the reversed stagnation point appears its position will remain invariant for $L_d^* > 1.0$. This feature further implies that the distance between the jet impingement stagnation and the reversal stagnation point will remain constant and, therefore, the recirculating zone (Fig. 4) between these two stagnation points will approximately have the same size for $L_d^* > 1.0$. This fact reinforces the observations made previously in Figs. 4 and 7 and the similarity of the flow field with respect to L_d^* is further justified. Furthermore, as has been done for the location of the jet impingement point, one may also estimate the location of the reversed stagnation point from the geometrical consideration. The derivation is given in the Appendix and is based on the assumption that the vortex located between the two stagnation points can be most easily driven by the inlet jet if it forms a smooth circle. The deduced expression is

$$X_r^* = -(1+\tan(\theta/2))/2 \tag{8}$$

which gives a value of -0.789 for $\theta = 60$ deg. This value lies between the computed and measured results, as shown in Fig. 8. Moreover, equation (8) tells us that the reversal stagnation point will appear and the flow pattern in the head region will become similar if $L_d^* > (1+\tan(\theta/2))/2$.

Mass Flow Rate Transported Into the Head Region. Since the fraction of the inlet mass flow rate which is transported into the head region ($\dot{m}_{ri}/\dot{m}_{in}$) may have an important effect on

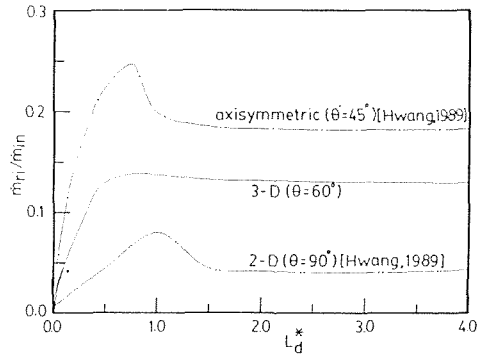

Fig. 9 Numerically computed fraction of inlet mass flow rate transported into the head region as a function of head height

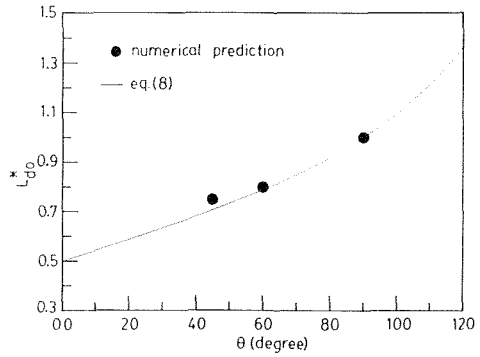

Fig. 10 Numerically predicted and geometrically estimated positions of $(\dot{m}_{ri}/\dot{m}_{in})_{max}$ versus inlet angle

the fluid mixing and the flame stability inside a combustor (Shahaf, 1980; Kennedy, 1974), three-dimensional numerical calculations of $\dot{m}_{ri}/\dot{m}_{in}$ as a function of nondimensionalized head height were performed, and the results are shown in Fig. 9 (solid line). Note that the results obtained from the axisymmetric and the two-dimensional computations (Hwang, 1989) are also included in Fig. 9 for comparison purpose. As one can see, for each case in Fig. 9 as the head height is increased from 0, $\dot{m}_{ri}/\dot{m}_{in}$ first increases to a peak value, subsequently decreases, and then remains approximately constant. The initial increase of $\dot{m}_{ri}/\dot{m}_{in}$ is because that the size of head region is increased as the head height increases. The nearly constant $\dot{m}_{ri}/\dot{m}_{in}$ for large L_d^* is because that a further increase of L_d^* from a certain large L_d^* is actually increasing the amount of stagnant fluids between the recirculation zone and the head plate and not increasing $\dot{m}_{ri}$. The presence of a peak $\dot{m}_{ri}/\dot{m}_{in}$ is due to the fact that only for a certain optimal head height (denoted as L_{do}^*) the head vortex tends to form a smooth circle which can be most easily driven by the inlet jet. Thus L_{do}^* correlates with the geometrical shape of the head vortex and therefore can be estimated by equation (8). Figure 10 is a plot of θ dependence of numerically predicted L_{do}^* for the three cases of Fig. 9 together with geometrically deduced equation (8). It is seen that both methods predict the same trend, that is, the optimal head height increases with increasing inlet angle. The discrepancy between the L_{do}^* predicted by the two methods is less than 5 percent.

There are several more aspects of Fig. 9 that are worthy of discussion. The existence of an optimal head height for the maximum $\dot{m}_{ri}/\dot{m}_{in}$ shown by the present cold-flow study parallels the existence of an optimal head height for the best flame blowoff performance found experimentally by Choudhury (1982) and for the best combustion efficiency predicted computationally by Vanka et al. (1985), respectively. This observation suggests the presence of correlations

among the $\dot{m}_{ri}/\dot{m}_{in}$, the flame stability, and the combustion efficiency. As shown in Fig. 9, the difference between the peak $\dot{m}_{ri}/\dot{m}_{in}$ at L^*_{do} and the constant $\dot{m}_{ri}/\dot{m}_{in}$ at large L^*_d is quite modest for the three-dimensional case, compared with those for the two-dimensional and the axisymmetric cases. The reason is that, in addition to flow upstream and downstream in the two-dimensional and the axisymmetric cases, the inlet jets can flow in two opposite azimuthal directions for the three-dimensional case. Furthermore, the modest difference between $\dot{m}_{ri}/\dot{m}_{in}$ at L^*_{do} and at large L^*_d is consistent with that found for the reactng flow investigated by Vanka et al. (1985) in a similar combustor configuration with the same number of side inlets, although the azimuthal angle between the two side inlets is different between the two works. The calculations of Vanka et al. showed that $L^*_{do}=0.76$ offers the best combustion efficiency compared with $L^*_d=0.$, 0.34, and 1.52 and that the combustion efficiency for $L^*_d=1.52$ is slightly lower than that for L^*_{do}.

Summary and Conclusions

The paper presents the results of an investigation of the head-height effects on the three-dimensional jet-jet impingement flow in a closed-end cylindrical duct. Reasonable agreement between LDV measured and analytically computed mean velocity profiles has been obtained. The presented swirl intensity, mean velocity, and turbulence intensity profiles, positions of both the jet impingement and the reversal stagnation points, and $\dot{m}_{ri}/\dot{m}_{in}$ all tend to suggest that the flow field downstream of the inlet ports is insensitive to the variation of the head height and that the flow field flow in the head region is similar for $L^*_d>1.0$ provided an appropriate axial coordinate is used.

The geometrical expressions deduced from considering the straight collision of two inlet jets and the shape of the recirculating flow in the head region provide a simple convenient way to effectively estimate the locations of both the jet impingement and the reversal stagnation points and the optimal head height for the maximum $\dot{m}_{ri}/\dot{m}_{in}$. In addition to aid useful illustrations to the flow feature in the head region, these geometrical expressions provide a criterion to the appearance of the reversal stagnation point which implies similar flow patterns in the head region irrespective of the head height.

Furthermore, the effect of the head height on $\dot{m}_{ri}/\dot{m}_{in}$ presented in this cold-flow study is found to parallel the effect of the head height on the combustion efficiency and on the flame stability investigated by the previous researchers for the reacting flows in the similar geometrical configurations. Consequently, the presented results and discussion in the present work will aid in understanding the combustion performance of the corresponding reacting flow from the fluid dynamical point of view.

Acknowledgment

Support for this work was partially provided by the National Science Council of the Republic of China under contract NSC-74-0401-E007-11.

References

Choudhury, P. R., 1982, "Characterization of a Side Dump Gas Generator Ramjet," AIAA Paper 82-1258.

Hwang, Y. H., 1989, "Theoretical Analysis of Flow Fields and Combustion Performances in Side-Inlet Dump Combustors," Ph.D. thesis, Dept. of Power Mechanical Engineering, National Tsing Hua University, Hsin-Chu, Taiwan.

Kennedy, J. B., 1974, "Ramburner Flow Visualization Studies," *Proceedings of 11th JANNAF Combustion Meeting*, Vol. II, Publication 261, Chemical Propulsion Information Agency, pp. 415-440.

Launder, B. E., and Spalding, D. B., 1974, "The Numerical Computation of Turbulent Flows," *Computer Methods in Applied Mechanics and Engineering*, Vol. 3, pp. 269-289.

Lighthill, J., 1975, "Mathematical Biofluiddynamics," Published by *SIAM*.

Liou, T. M., and Wu, S. M., 1986, "Application of Laser Velocimetry to the Curved Inlet Duct of a Side Dump Combustor," *Third International Symposium on Application of Laser-Doppler Anemometry to Fluid Mechanics*, Ladon-Instituto Superior Tecnico, pp. 9.3.1-9.3.6.

Liou, T. M., and Wu, S. M., 1988, "Flow Field in a Dual-Inlet Side-Dump Combustor," *Journal of Propulsion and Power*, Vol. 4, No. 1, pp. 53-60.

Patankar, S. V., 1980, *Numerical Heat Transfer and Fluid Flow*, Hemisphere Publishing Co., New York.

Shahaf, M., Goldman, Y., and Greenberg, J. B., 1980, "An Investigation of Impinging Jets in Flow with Sudden Expansion," *Proceedings of the 22nd Israel Annual Conference on Aviation and Astronautics*, Israel Ministry of Transport, pp. 100-106.

Stull, F. D., Craig, R. R., Wtreby, G. D., and Vanka, S. P., 1985, "Investigation of Dual Inlet Side Dump Combustor Using Liquid Injection," *Journal of Propulsion and Power*, Vol. 1, No. 1, pp. 83-86.

Vanka, S. P., Craig, R. R., and Stull, F. D., 1985, "Mixing, Chemical Reaction and Flow Field Development in Ducted Rockets," AIAA paper 85-1271.

Vanka, S. P., Stull, F. D., and Craig, R. R., 1983, "Analytical Characterization of Flow Field in Side Inlet Dump Combustor," AIAA paper 83-1399.

APPENDIX

As shown in the following figure, the locations of stagnation points can be derived as:

$$X_i=(D_c/2)\cot\theta \text{ and } X_r=-(D_c/2)(1/2+\tan(\theta/2)/2)$$

therefore

$$X^*_i=\cot\theta \tag{A1}$$

and

$$X^*_r=-(1+\tan(\theta/2))/2 \tag{A2}$$

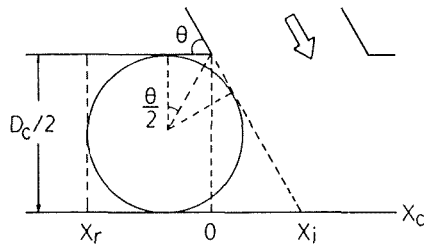

Impingement of Under-Expanded Jets on a Flat Plate

J. Iwamoto
Department of Mechanical Engineering,
Tokyo Denki University,
Tokyo 101, Japan
Mem. ASME

When an under-expanded sonic jet impinges on a perpendicular flat plate, a shock wave forms just in front of the plate and some interesting phenomena can occur in the flow field between the shock and the plate. In this paper, experimental and numerical results on the flow pattern of this impinging jet are presented. In the experiments the flow field was visualized using shadow-photography and Mach-Zehnder interferometry. In the numerical calculations, the two-step Lax-Wendroff scheme was applied, assuming inviscid, axially symmetric flow. Some of the pressure distributions on the plate show that the maximum pressure does not occur at the center of the plate and that a region of reversed flow exists near the center of the plate.

1 Introduction

It is well known that when air is expanded through a convergent nozzle into the atmosphere, with its stagnation pressure higher than the critical pressure ($p_0 > ((\kappa+1)/2)^{\kappa/(\kappa-1)} p_a$, where p_0 is the stagnation pressure of the air jet, p_a the atmospheric pressure, and κ the ratio of specific heats), an under-expanded sonic jet is obtained. Such a jet can be found in many industrial applications, for example, downstream of the throat or the valve in a duct or a pipe involving high pressure gases, in the exhausts from rocket engines and from certain aircraft engines, and so on. The study of the structure of this type of jet has been conducted for many years by many researchers (Donaldson and Snedeker, 1971; Sinha et al., 1971; and Chang and Chow, 1974). But the explanation on the mechanism of the occurrence of Mach disk in the jet has not been satisfactorily given yet and the problems on the interaction of the acoustic wave with the jet have not been fully solved. The topic is still under investigation.

When solid objects such as wedges, flat plates, cavities etc. are placed downstream of the under-expanded jets, some interesting phenomena can occur, as shown by Lamont and Hunt (1976), Kalghatgi (1975) and Iwamoto (1986). The Hartmann whistle and Hartmann-Sprenger tube have been studied by some researchers (Iwamoto, 1986), but the mechanism of the self-excited oscillation of flow in the tube has not been well established.

It is known that, under certain conditions, when the underexpanded jet impinges upon a flat plate, the flow in the neighborhood of the plate is excited into an oscillation (Moerch, 1964). In this paper, however, the steady flow pattern is examined using the experimental and numerical results when the jet with relatively low degree of underexpansion impinges on a flat plate, because even in steady flow some interesting phenomena are involved. And it is hoped that the present results will form the basis for the analysis of the oscillatory flow in the neighborhood of the plate.

2 Experimental Apparatus

The apparatus used in the experiment is shown schematically in Fig. 1. Dry air was supplied to the plenum chamber in the

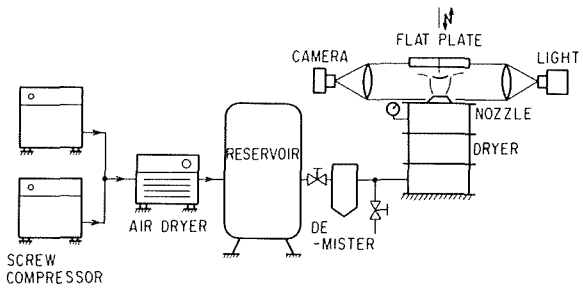

(a) EXPERIMENTAL ARRANGEMENT

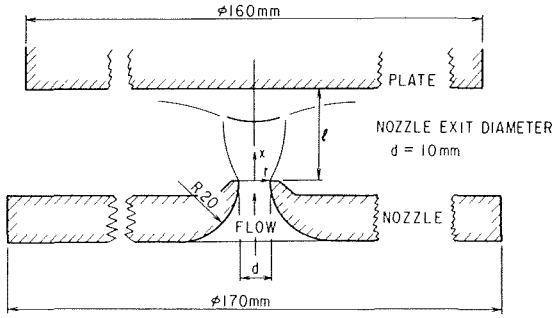

(b) NOZZLE AND PLATE

Fig. 1 Experimental apparatus

Contributed by the Fluids Engineering Division and presented at the Winter Annual Meeting. San Francisco, Calif., December 10-15, 1989 of THE AMERICAN SOCIETY OF MECHANICAL ENGINEERS. Manuscript received by the Fluids Engineering Division July 1989. Paper No. 89-WA/FE-2.

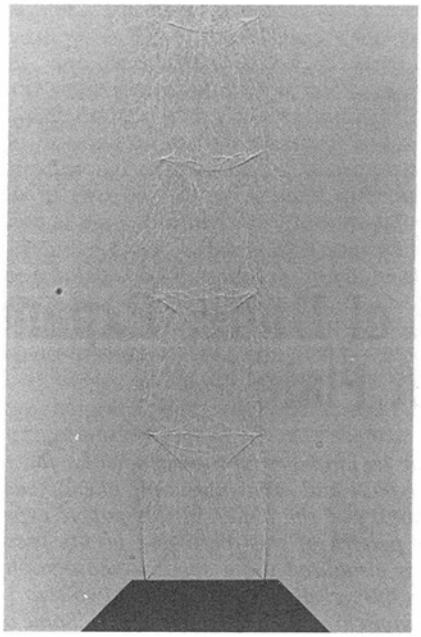

Fig. 2(*a*) Shadowgraph picture for free jet (p_0/p_a = 3.0)

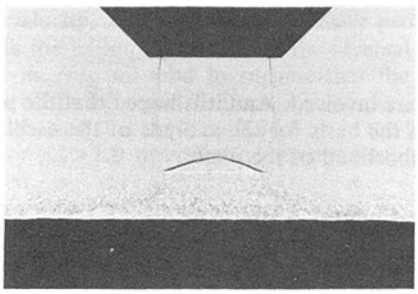

Fig. 2(*b*) Shadowgraph picture for impinging jet (p_0/p_a = 3.0, l/d = 1.5)

side of which a convergent nozzle was fitted. The throat diameter (d) of the convergent nozzle was 10mm and the internal surface of the nozzle was well finished.The diameter of the nozzle plate was 170mm. The nozzle-to-plate distance (l) was easily adjusted with the feed screw mechanisms.

The impingement plate, 160mm in diameter, was mounted on the cross-slide and could, therefore, be traversed in a plane parallel to the nozzle exit plane. The plate had five pressure taps (0.3mm in diameter) along its diameter with the one centrally placed. The distances between the taps were 15mm. Plate pressures were measured by traversing the plate.

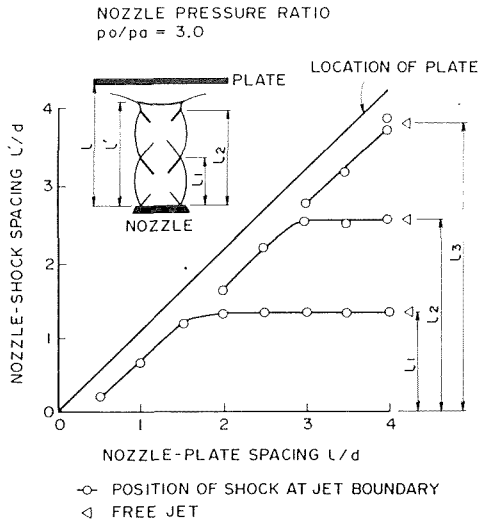

Fig. 3 Positions of the shock waves at the jet boundary (p_0/p_a = 3.0)

The flow in the space between the nozzle and the plate was visualized by shadow-photography. The light from the light source becomes parallel after passing through the convex lens and goes through the flow field of interest. In order to take shadowgraph pictures of the flow field, the camera was focused on a position approximately 50mm from the lens measured from the axis of symmetry of the jet. The Mach-Zehnder interferometry was also used to obtain the density distributions of the flow field.

3 Experimental Results

Figure 2 shows the shadowgraph pictures of a free jet and a jet impinging on a plate for the nozzle pressure ratio p_0/p_a = 3.0. In the free jet shown in Fig. 2(*a*) Mach disk is not formed since the degree of underexpansion of the jet is not high enough. The cellular structure of the jet is apparent.

Figure 2(*b*) shows the shadowgraph picture of a jet when a plate is located normally to it at a distance of 15mm (l/d = 1.5) measured from the nozzle exit plane. The bow shock can be seen in front of the plate. The flow pattern upstream of the bow shock is similar to that of the free jet.

Figure 3 is a plot of shock wave locations in the jet against the varying nozzle-to-plate distances, which are measured on the shadowgraph pictures. The locations of the shocks at the

Nomenclature

c = speed of sound
d = nozzle exit diameter
e = total energy per unit volume of gas
F = (see equation (1))
G = (see equation (1))
l = nozzle-to-plate distance
l' = distance between nozzle exit plane and the position of shock at the jet boundary
$l_1, l_2 \ldots$ = distance between nozzle exit plane and the position of shock at the jet boundary in the free jet
p = pressure
r = radial coordinate
t = time
T = temperature
u = velocity component in x-direction
U = (see equation (1))
v = velocity component in r-direction
W = (see equation (1))
x = axial coordinate
Δr = radial increment
Δt = time increment
Δx = axial increment
κ = ratio of specific heats
ρ = density

Subscripts

0 = stagnation state
a = atmospheric state

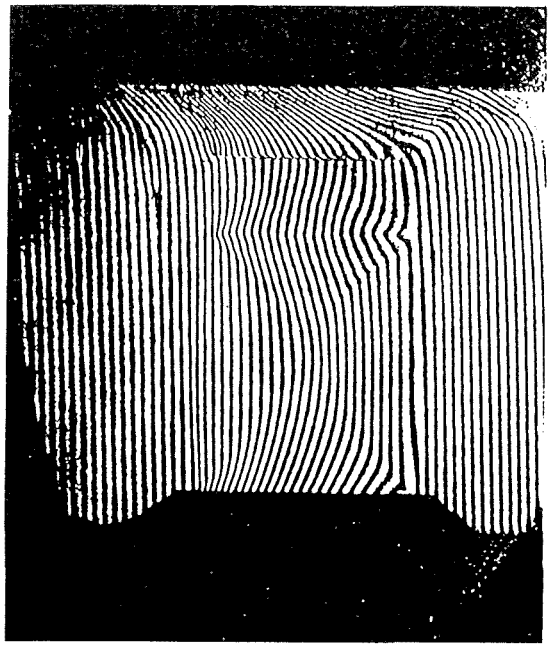

Fig. 4 Interferogram (p_0/p_a = 3.0, l/d = 2.0)

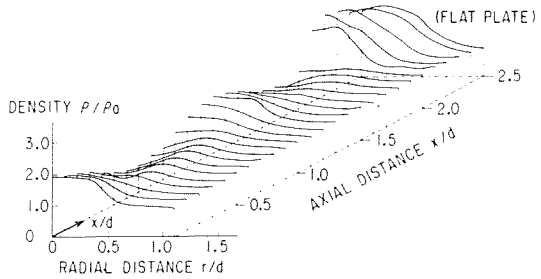

Fig. 5(*a*) Density distributions (p_0/p_a = 3.0, l/d = 2.5)

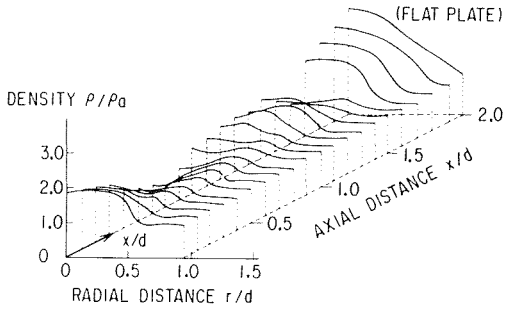

Fig. 5(*b*) Density distributions (p_0/p_a = 3.0, l/d = 2.0)

jet boundary in the free jet are indicated by l_1, l_2, etc., in the same figure. When the nozzle-to-plate distance 1/d is less than 1.5, a single shock stands in front of the plate (see Fig. 2(*b*)) and the distance between the plate and the shock ($l-l'$) is almost independent of the nozzle-to-plate distance. When the plate is moved further from the nozzle ($l/d > 1.5$), the shock moves together with the plate. When its position coincides with that in the free jet ($l' = l_1$), it remains at this position and, downstream of it another shock appears ($2.0 < l/d < 3.0$), the distance between this shock and the plate being almost constant. The shock wave located closer to the plate is almost normal or slightly bow-shaped.

In order to obtain the flow field of the impinging jet in detail, the interferograms were taken using Mach-Zehnder interferometry. Density distributions were thus obtained. Figure 4 is an example of the interferogram for p_0/p_a = 3.0, l/d = 2.0. Figures 5(*a*) and 5(*b*) show the density distributions obtained from the interferograms for l/d = 2.5 and 2.0, respectively. Density distributions in only one half of the flow field are shown in Figs. 5(*a*) and 5(*b*), because the flow is assumed to be axially symmetric.

Figure 5(*a*) shows that the density decrease from the high value at the nozzle exit plane to its minimum at x/d = 0.6 (for notation, see Fig. 1) and, due to the occurrence of the oblique shock waves crossing on the axis, the maximum density is obtained at x/d = 1.3 downstream of the position of minimum density. As shown in Fig. 3 the oblique shock wave reaches the jet boundary at l'/d = 1.3 ($=l_1/d$) and the expansion wave is reflected. So, the density becomes on the axis near x/d = 1.9. The strong shock wave is located in front of the plate at x/d = 2.1 and, downstream of this location, density decreases slightly towards the plate. Qualitatively the same thing can be said of the density distributions for l/d = 2.0 in Fig. 5(*b*) except that the shock stands at x/d = 1.6.

4 Numerical Results

In order to obtain the flow properties in the impinging flow field in further detail, the numerical method known as two-step Lax-Wendroff scheme (Sinha et al., 1971 and Aki, 1970) was applied assuming inviscid, axially symmetric flow. The governing equations are,

where

$$U_t + F_x + G_r + W = 0 \tag{1}$$

$$U = \begin{bmatrix} \rho \\ \rho u \\ \rho v \\ e \end{bmatrix} \quad F = \begin{bmatrix} \rho u \\ \rho u^2 + p \\ \rho uv \\ u(e+p) \end{bmatrix}$$

$$G = \begin{bmatrix} \rho v \\ \rho uv \\ \rho v^2 + p \\ v(e+p) \end{bmatrix} \quad W = \begin{bmatrix} \rho v/r \\ \rho uv/r \\ \rho v^2/r \\ v(e+p)/r \end{bmatrix}$$

where r is the radial coordinate, p the density and, u and v are the velocity components for x and r directions, respectively. The total energy per unit volume of the gas(e) is expressed by,

$$e = \rho\left(\frac{T}{\kappa - 1} + \frac{u^2 + v^2}{2}\right)$$

where T is the temperature. Equation (1) was solved numerically using a two-step Lax-Wendroff scheme as follows;

$$U^{(p)}(x,r,t+\Delta t/2) = \tilde{U}(x,r,t) - \frac{\Delta t}{2}\left[F_x(x,r,t)G_r(x,r,t) + W\right]$$

$$U(x,r,t+\Delta t) = U(x,r,t) - \Delta t[F_x^{(p)}(x,r,t+\Delta t/2) + G_r^{(p)}(x,r,t+\Delta t/2) + W^{(p)}(x,r,t+\Delta t/2)] \tag{2}$$

where Δt is the time step, and the superscript (p) denotes the provisional values and ˜ the average value, which are given by,

$$F_x^{(p)} = F_x(U^{(p)}),\ G_r^{(p)} = G_r(U^{(p)})$$

$$\tilde{U}(x,r,t) = \frac{1}{4}\left[U(x+\Delta x,r,t) + U(x-\Delta x,r,t) + U(x,r+\Delta r,t) + U(x,r-\Delta r,t)\right]$$

where Δx and Δr are the increments in x and r directions, respectively. The artificial viscosity terms were introduced in

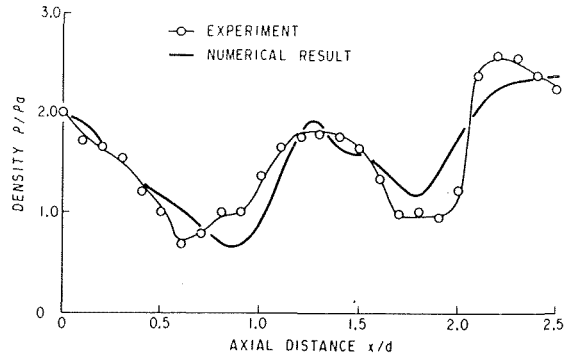

Fig. 6(*a*) Comparison between density distributions obtained experimentally and numerically (p_0/p_a = 3.0, l/d = 2.5)

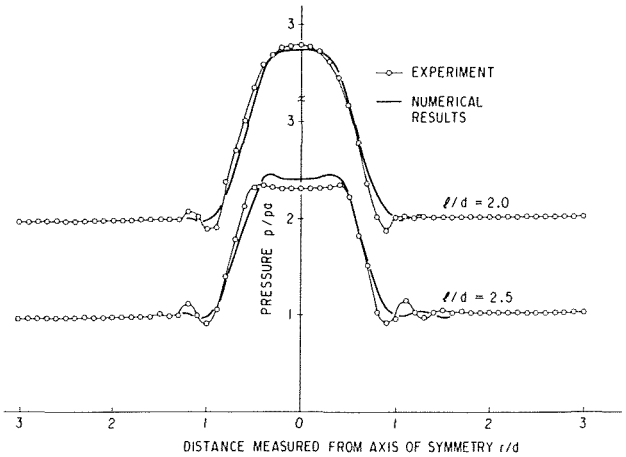

Fig. 6(*b*) Comparison between pressure distributions obtained experimentally and numerically (p_0/p_a = 3.0)

the equations to enhance the stability properties of the numerical calculation, and so it is difficult to locate the shock wave accurately by numerical results.

The reflective boundary was employed at the flat plate and the axis symmetry, and the continuous boundary elsewhere except at the nozzle exit plane. It is known that the sonic line does not coincide with the nozzle exit plane and the flow velocity on the nozzle exit plane is subsonic near the axis of symmetry and supersonic near the nozzle wall. Therefore, the flow properties in the neighborhood of the nozzle exit were obtained using Hall's theory (1964), and these flow properties were given at the nozzle exit plane as boundary conditions.

5 Comparison Between Experimental and Numerical Results and Discussions

Figure 6 shows the comparison between the experimental and numerical results for p_0/p_a = 3.0. Figure 6(*a*) shows the density distributions along the axis of symmetry obtained from the interferograms and along the line 0.5mm away from the axis of symmetry obtained from the numerical calculation for l/d = 2.5. Figure 6(*b*) shows the pressure distributions on the flat plate obtained from the pressure measurements and on the plane 0.5mm upstream of the plate obtained from the numerical calculation for l/d = 2.0 and 2.5. Since the numerical calculations give the flow variables at the center of each cell into which the flow field is divided and since the surfaces of the plate and the axis of symmetry coincide with the cell boundaries, the nearest position where the solutions are found is one half the length of the cell side away from the boundary.

The experimental and numerical results are relatively in good agreement. As can be seen in Fig. 6(*a*), the numerical results

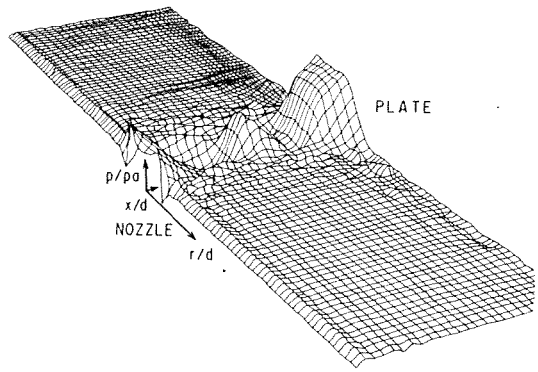

Fig. 7 Calculated pressure distributions for p_0/p_a = 3.0 and l/d = 2.5

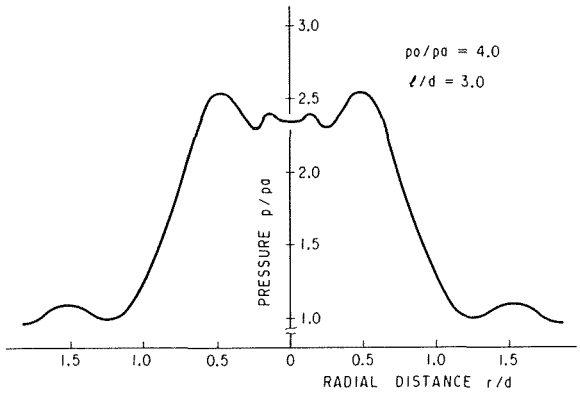

Fig. 8(*a*) Calculated pressure distributions on the plate for p_0/p_a = 4.0 and l/d = 3.0

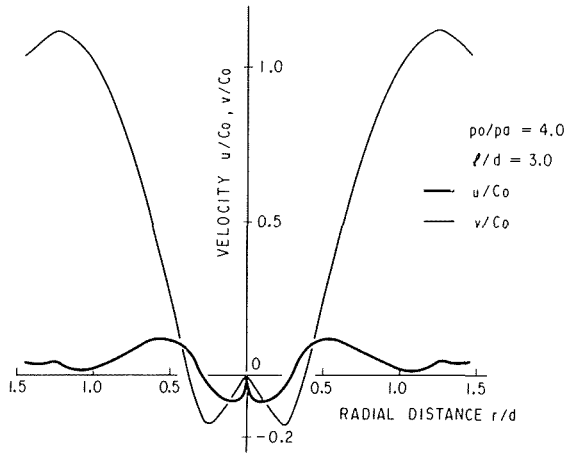

Fig. 8(*b*) Calculated velocity distributions on the plate for p_0/p_a = 4.0 and l/d = 3.0

show that the density along the axis of symmetry of the jet drops from the value at nozzle exit plane to its minimum value at x/d = 0.9 and reaches its maximum at x/d = 1.3 in the area downstream of the oblique shock wave. The density decreases again and reaches its minimum at x/d = 1.8 upstream of the shock (x/d = 2.1) standing in front of the flat plate. Downstream of the shock at x/d = 2.1 the experimental curve shows the decrease towards the plate, while numerical results show the monotonic increase toward the plate.

Figure 7 shows pressure distribution of the entire flow field in the space between the nozzle and the plate obtained numerically for p_0/p_a = 3.0 and l/d = 2.5. The jet expands from the high pressure at the nozzle exit plane to the lowest pressure at the position where the oblique shock waves cross on the jet axis. And then through the oblique shocks there is pressure

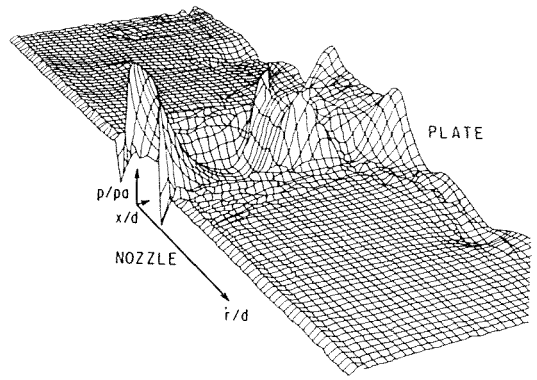

Fig. 9(*a*) Calculated pressure distributions for p_0/p_a = 6.0 and l/d = 3.0

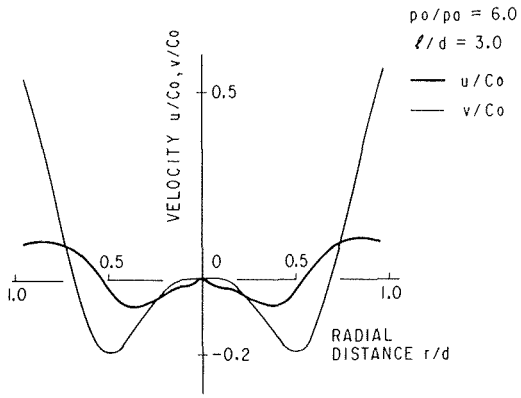

Fig. 9(*b*) Calculated velocity distributions on the plate for p_0/p_a = 6.0 and l/d = 3.0

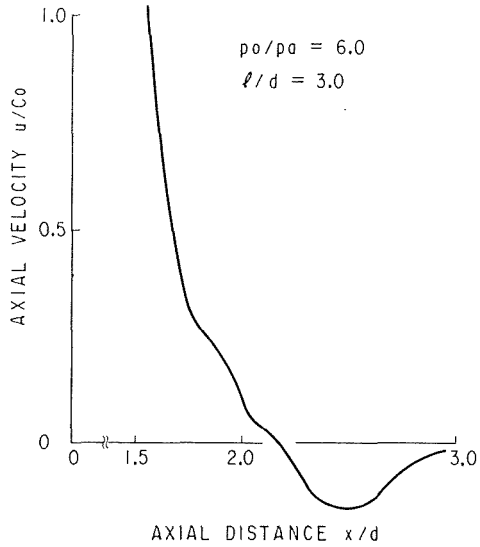

Fig. 9(*c*) Calculated velocity distributions along the axis of symmetry for p_0/p_a = 6.0 and l/d = 3.0

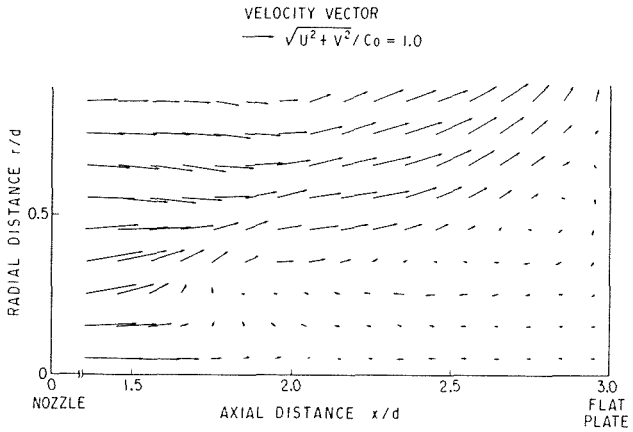

Fig. 9(*d*) Calculated velocity vectors in the flow field near the axis of symmetry and the plate for p_0/p_a = 6.0 and l/d = 3.0

increase, which is followed by the decrease in pressure due to the expansion waves reflected from the jet boundary as a result of the interaction of the oblique shocks with the jet boundary. Then the pressure increases again across the shock wave just in front of the plate.

In Fig. 6(*b*) the maximum pressure on the plate for l/d = 2.0 is at the center of the plate and downstream of r/d = 1.0 there are slight variations of pressure. In contrast, the curve for l/d = 2.5 shows that the maximum pressure does not occur at the center of the plate but at a certain distance away from the center. In Fig. 8(*a*) which shows the pressure distribution calculated numerically for p_0/p_a = 4.0 and l/d = 3.0 even larger decrease in pressure at the center is noticed.

For the uniform supersonic jet issueing from the Laval nozzle, Kalghatgi and Hunt (1976) found that lower pressure can be obtained near the axis of symmetry on the flat plate. They showed that the decrease in the pressure in the central area of the plate was due to the occurrence of a shear layer along the slip surface in the impinging jet. The shear layer originated at the point of interaction (triple point) of the shock in front of the plate with the weak shocks which were produced by small imperfections in the nozzle wall or by slight inaccuracies in the design/production of the nozzle contour. The stagnation pressure of the fluid which goes through the oblique shock of smaller shock wave angle is higher and this higher stagnation pressure is obtained in the outer layer of the jet. The same can be said of the density. Therefore, it is possible that the outer fluid with high stagnation pressure reverses towards the center on the plate. The existence of the region of this reversed flow has been confirmed by observing the flow direction with the Pitot probe when the jet impinges upon a flat plate through the Laval nozzle (Gubanova et al., 1973). Since in the present study the nozzle-to-plate distance is larger than that in the study by Kalghatgi and Hunt (1976), their theory can not wholly by applied to our flow field. However, the stagnation pressure in the outer flow behind the shock may be higher than that in the central flow on the flat plate, so that there can be inward flow radially, towards the center of the plate.

In Fig. 8(*b*) the distributions of the velocity are shown. These were obtained from the numerical calculation for p_0/p_a = 4.0 and l/d = 3.0. As can be seen in the figure, both u and v are negative near the axis of symmetry, which indicates that the flow is reversed in the central region on the plate.

This phenomenon can occur more conspicuously when the nozzle pressure ratio is higher. Figure 9(*a*) shows the pressure distribution in the whole flow field between the nozzle and the plate obtained numerically for p_0/p_a = 6.0 and l/d = 3.0. As can be seen in the figure, the maximum pressure is not at the center on the plate. Figure 9(*b*) and 9(*c*) show the corresponding distributions of the velocity components. As seen in these figures, in the region of the flow field between x/d = 2.2 and 3.0 along the axis of symmetry and between r/d = 0 and r/d = 0.7, the flow is reversed. Figure 9(*d*) shows the velocity vectors of the flow in the field near the axis of symmetry and the plate.

6 Conclusions

The flow pattern in the flow field of the impinging jet upon a perpendicular flat plate is examined using experimental and

numerical results. The numerical results, obtained using two-step Lax-Wendroff scheme under the assumption of inviscid, axially-symmetric flow, are found to be in good agreement with the experimental results. The numerical results show that, under certain conditions, the maximum density or pressure on the flat plate does not occur at the center and that there is a region of reversed flow near the central area on the plate.

Experimental Uncertainty

The maximum uncertainty in the measured density obtained from the interferogram is about 4 percent of the maximum density on the plate which occurs at the jet axis on the plate in Figs. 5 and 6(*a*). The maximum uncertainty in measured values of the shock wave locations in Fig. 3 is less than 2.5 percent of the maximum nozzle-to-plate distance. The pressure data in Fig. 6(*b*) have a maximum uncertainty of about 1.5 percent of the stagnation pressure of the jet.

References

Aki, T., 1970, "Numerical Tests on Lax-Wendroff Difference Scheme with Artificial Viscosity and its Variations by the Two-Step Method," Technical Report of National Aerospace Laboratory TR-217.

Chang, I. S., and Chow, W. L., 1974, "Mach Disk from Underexpanded Axisymmetric Nozzle Flow," *AIAA J.*, Vol. 12, No. 8, pp. 1079–1082.

Donaldson, C. D. and Snedeker, R. S., 1971, "A Study of Free Jet Impingement," *J. Fluid Mechanics*, Vol. 45, pp. 281–319.

Gubanova, O. I., Lunev, V. V., and Plastinina, L. N., 1973, "The Central Breakaway Zone with Interaction Between a Supersonics Underexpanded Jet and a Barrier," *Fluid Dynamics*, Vol 6, pp. 298–301.

Hall, I. M., 1964, "Transonic Flow in Two-Dimensional and Axially-Symmetric Nozzles," *Quart. Journ. Mech. and Applied Math.*, Vol. XV, Part 4, pp. 487–508.

Iwamoto, J., 1986, "Unsteady Flow and the Thermal Effect in a Tapered H-S Tube," *Trans. JSME*, Vol. 52, No. 482, pp. 3422–3427.

Kalghatgi, G. T., 1975, "Some Aspects of Supersonic Jet Impingement on Plane Perpendicular Surfaces," Ph.D. thesis, University of Bristol.

Kalghatgi, G. T. , and Hunt, B. L., 1976, "The Occurrence of Stagnation Bubbles in Supersonic Jet Impingement Flows," *Aeronautical Quarterly*, Aug., pp. 169–185.

Lamont, P. J., and Hunt, B. L., 1976, "The Impingement of Underexpanded Axisymmetric Jets on Wedges," *J. Fluid Mechanics*, Vol. 76, Part 2, pp. 307–336.

Moerch, K. A., 1964, "A Theory for the Mode of Operation of the Hartmann Air Jet Generator," *J. Fluid Mechanics*, Vol. 20, Part 1, pp. 141–159.

Sinha, R., Zakkay, V., and Erdos, J., 1971, "Flowfield Analysis of Plumes of Two-Dimensional Underexpanded Jets by a Time-Dependent Method," *AIAA J.*, Vol. 9, No. 12, pp. 2362–2370.

Viscous Damping of Stationary Wave Formed Near an Obstacle in a Channel

K. Katoh
Research Associate,
Department of Mechanical Engineering.

H. Fujita
Professor,
Department of Mechanical Engineering.

Nagoya University,
Nagoya 464, Japan

The purpose of this study is to investigate surface wave damping due to viscosity. The stationary wave formed near an obstacle in a horizontal channel is chosen as the subject of this analysis because gravitational and surface tension waves appear separately before and behind the obstacle, and, hence, the effect of viscosity on two typical kinds of waves can be analyzed. The linearized differential equation for the stream function is solved analytically to obtain the waveform. The calculated damping rate of wave amplitude does not agree well with that of Stokes' approximate estimation. This shows that the Stokes' estimation is not sufficient, and that an exact analysis as presented here is necessary when the Reynolds number is as low as $Re \leq 1000$. As an application of this analysis, the waveform is calculated for the stationary wave formed by an obstacle in falling liquid film flow.

1 Introduction

The effect of the viscosity on a surface wave motion is an important topic in industry, for example, in dealing with the range which is under the influence of wave motion or the damping of wave power. However, only a few reports have provided an exact analysis of wave damping due to viscosity, and no report has considered systematically the surface tension and gravitational force on viscous damping (Hunt, 1964; Keulegan, 1948; Lamb, 1932; and Leblond and Mainardi, 1987). In an old example, Stokes calculated the wave damping rate using a solution for a potential flow (Lighthill, 1978a). He noticed that the solution of the stream function for the nonviscous Laplace equation could also satisfy the exact equation with viscous terms except for boundary conditions. Stokes considered that the effect of viscosity may be estimated by the discrepancy of the boundary conditions when the approximate nonviscous stream function was applied to the exact equation. Under these hypotheses, the damping rate of the wave energy by the bottom friction and the internal friction was calculated separately. This analysis, however, is not exact, although the calculation reflects a creative approach.

The purpose of the present study is to analyze exactly the viscous damping of the surface wave motion. In order to clarify the effect of surface tension and gravitational force on the viscous damping, we investigate the damping rate of the wave amplitude for various Reynolds, Weber, and Froude numbers. The stationary wave near an obstacle in a horizontal channel is chosen as the subject of the analysis. The wave is generated by a disturbance, that is, an abrupt pressure increase caused by the obstacle. It is known that two kinds of stationary waves, namely, the surface tension and the gravitational waves, are formed before and behind the obstacle (Lighthill, 1978b). This flow system makes the analysis simpler and efficient because the phenomena are steady and the viscous effect on the two typical kinds of waves mentioned above can be investigated simultaneously.

In this report, we first obtain both viscous and nonviscous solutions for the stationary wave in a horizontal channel. The viscous effect on wavelength and amplitude is considered. Viscous damping rates are calculated for both surface tension and gravitational waves, and both results are discussed. Based on these results, the physical mechanism of viscous action on both kinds of waves is considered. Next, a stationary wave near an obstacle such as a step in a falling liquid film flow (Fujita et al., 1986) is analyzed as an application of the above theory.

2 Analysis of Stationary Wave Formed in Horizontal Channel Flow

2.1 Basic Equations and Boundary Conditions. It is considered that the stationary waves appearing before and behind the obstacle are formed due to an abrupt pressure increase caused by an obstacle. Although the wave propagation velocities are equal to the stream velocity, a surface tension and a gravitational wave appear before and behind the obstacle, respectively, because of the difference in their group velocities (Lighthill, 1978b).

Forbes (1983) analyzed the stationary wave generated in a horizontal flow where a cylindrical obstacle was settled on the bottom surface under an assumption of potential flow. Although analysis of each flow with an obstacle of a definite shape seems useful from a practical viewpoint, it is quite difficult because of the complicated boundary conditions. Since our aim is only to clarify the effect of the fluid viscosity on the wave motion, a simple flow system was chosen as the

Contributed by the Fluids Engineering Division for publication in the JOURNAL OF FLUIDS ENGINEERING. Manuscript received by the Fluids Engineering Division November 22, 1988.

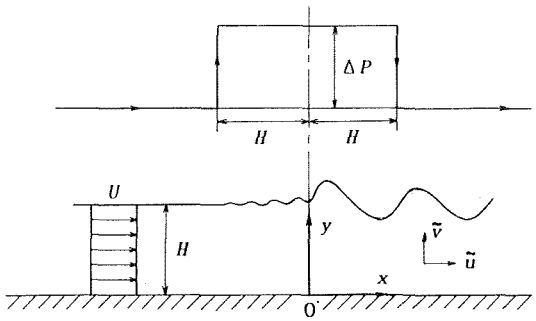

Fig. 1 Coordinate system

subject of analysis as shown in Fig. 1, where a stationary wave is generated by a pressure increase which is described by a step function within a certain region in a channel. Therefore, the obstacle effects are represented solely by the pressure increase in this report. As shown in Fig. 1, the x an y indicate the flow direction and the vertical direction to the bottom wall, respectively.

Viscous Flow Model. The nondimensional Navier-Stokes equations for the two-dimensional flow and steady-state condition can be written as follows.

$$\bar{u}\frac{\partial \bar{u}}{\partial \bar{x}} + \bar{v}\frac{\partial \bar{u}}{\partial \bar{y}} = -\frac{\partial \bar{P}}{\partial \bar{x}} + \frac{1}{\mathrm{Re}}\left(\frac{\partial^2 \bar{u}}{\partial \bar{x}^2} + \frac{\partial^2 \bar{u}}{\partial \bar{y}^2}\right) \tag{1}$$

$$\bar{u}\frac{\partial \bar{v}}{\partial \bar{x}} + \bar{v}\frac{\partial \bar{v}}{\partial \bar{y}} = -\frac{\partial \bar{P}}{\partial \bar{y}} + \frac{1}{\mathrm{Fr}} + \frac{1}{\mathrm{Re}}\left(\frac{\partial^2 \bar{v}}{\partial \bar{x}^2} + \frac{\partial^2 \bar{v}}{\partial \bar{y}^2}\right) \tag{2}$$

$$\bar{x} = \frac{x}{H},\ \bar{y} = \frac{y}{H},\ \bar{u} = 1 + \frac{\tilde{u}}{U},\ \bar{v} = \frac{\tilde{v}}{U},\ \bar{P} = \frac{P}{\rho U^2} \tag{3}$$

where H is the liquid depth, $\tilde{u}$ and $\tilde{v}$ are the x and y components of the fluctuation velocity caused by the pressure disturbance, P is the pressure and ρ is the liquid density. U is the mean stream velocity. Because the wavelength is not so long compared with the liquid depth, the waves in this study can be considered a deep-sea wave. In which case the stream velocity can be assumed to be uniform in the cross section of flow because the effect of the bottom friction may be ignored. It is necessary, however, to take into account the velocity distribution when the liquid depth is exceedingly shallow, a case which will be discussed in section 4.

In equations (1) and (2), Re and Fr denote the Reynolds and Froude numbers which are defined as

$$\mathrm{Re} = \frac{UH}{\nu} \tag{4}$$

$$\mathrm{Fr} = \frac{U^2}{gH} \tag{5}$$

where ν is the kinematic viscosity and g is the gravitational acceleration.

If the stream function for the fluctuation $\bar{\Psi}_\alpha$ is defined by the following equation (6) for each wave number component $\bar{\alpha}$ non-dimensionalized by the liquid depth H, the fluctuation velocity components $\tilde{u}$ and $\tilde{v}$ can be written as equation (7).

$$\bar{\Psi}_\alpha = \bar{\psi}_\alpha(\bar{y})e^{i\bar{\alpha}\bar{x}} \tag{6}$$

$$\tilde{u} = \frac{\tilde{u}}{U} = \bar{\psi}_\alpha',\ e^{i\bar{\alpha}\bar{x}}$$

$$\tilde{v} = \frac{\tilde{v}}{U} = -i\bar{\alpha}\,\bar{\psi}_\alpha e^{i\bar{\alpha}\bar{x}} \tag{7}$$

where i is the imaginary unit and a prime indicates the differentiation with respect to $\bar{y}$. An equation without the pressure term can be obtained by combining equations (1) and (2). Inserting equation (7) into this equation, the following linearised differential equation (8) can be obtained for the stream function of each wave number component $\bar{\psi}_\alpha$ by ignoring the quadratic terms of the fluctuation.

$$\bar{\psi}_\alpha'''' - (2\bar{\alpha}^2 + i\bar{\alpha}\mathrm{Re})\bar{\psi}_\alpha'' + (\bar{\alpha}^4 + i\bar{\alpha}^3\mathrm{Re})\bar{\psi}_\alpha = 0 \tag{8}$$

As for the boundary conditions, at the wall ($\bar{y} = 0$),

$$\bar{\psi}_\alpha = 0 \tag{9}$$

$$\bar{\psi}_\alpha' = 0 \tag{10}$$

since the velocities are zero there. At the liquid surface ($\bar{y} = 1$) the force balance in the y-direction can be written as

$$\bar{P} - \bar{P}_a = \frac{\bar{h}}{\mathrm{Fr}} - \frac{1}{\mathrm{We}}\frac{d^2\bar{h}}{d\bar{x}^2} + \frac{2}{\mathrm{Re}}\frac{\partial \bar{v}}{\partial \bar{y}} + \Delta\bar{P}\{S(\bar{x}+1) - S(\bar{x}-1)\} \tag{11}$$

where $\bar{P}_a$ is the atmospheric pressure and We is the Weber number defined by

$$\mathrm{We} = \frac{\rho U^2 H}{\sigma} \tag{12}$$

where σ is the surface tension. $\bar{h}(\bar{x})$ in equation (11) denotes the liquid surface profile, and can be written as follows by integrating each wave number component of the amplitude $\bar{\Phi}(\bar{\alpha})$.

$$\bar{h}(\bar{x}) = \int_{-\infty}^{\infty} \bar{\Phi}(\bar{\alpha})\, e^{i\bar{\alpha}\bar{x}} d\bar{\alpha} \tag{13}$$

On the right-hand side of equation (11) the 4th term shows the pressure increase caused by the disturbance, where $\Delta\bar{P}$ is the nondimensional magnitude of the pressure increase and $S(\bar{x})$ is an unit step function. The pressure increase is distributed between $x = -H$ and H ($-1 \leqq \bar{x} \leqq 1$) like a step function on both sides of $\bar{x} = 0$ as shown in Fig. 1. Differentiation of equation (11) with respect to $\bar{x}$ gives

$$\frac{\partial \bar{P}}{\partial x} = \int_{-\infty}^{\infty}\left\{\frac{1}{\mathrm{Fr}} i\bar{\alpha}\,\bar{\Phi}(\bar{\alpha}) + \frac{i\bar{\alpha}^3}{\mathrm{We}}\bar{\Phi}(\bar{\alpha}) + \frac{2\bar{\alpha}^2}{\mathrm{Re}}\bar{\psi}_\alpha'\right\} e^{i\bar{\alpha}\bar{x}} d\bar{\alpha} + \Delta\bar{P}\{\delta(\bar{x}+1) - \delta(\bar{x}-1)\} \tag{14}$$

Nomenclature

Fr = Froude number ($= U^2/gH$)
g = gravitational acceleration
H = liquid depth
$h(x)$ = liquid surface profile
i = imaginary unit
P = pressure
P_a = atmospheric pressure
Re = Reynolds number ($= UH/\nu$)
U = liquid velocity
u and v = x and y velocity components
We = Weber number ($= \rho U^2 H/\sigma$)
x and y = orthogonal coordinates (defined as Fig. 1)
α = wave number
$\delta(x)$ = Dirac's delta function
η = damping rate of wave amplitude
ν = kinematic viscosity
ρ = density
σ = surface tension
$\Phi(\alpha)$ = amplitude component of each wave number
ψ_α = stream function component of each wave number
$\bar{\ }$ = nondimensional quantity

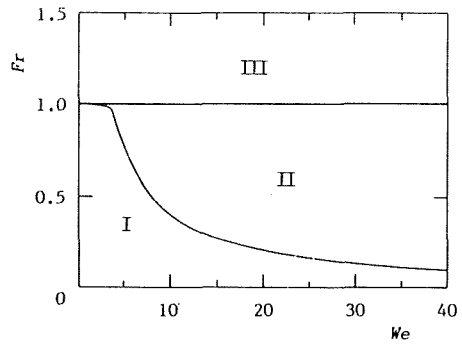

Fig. 2 Classification of flow pattern

where $\delta(\bar{x})$ is the Dirac's delta function. Noting the relation (Hino, 1977)

$$\delta(\bar{x}) = \frac{1}{2\pi}\int_{-\infty}^{\infty} e^{i\bar{\alpha}\bar{x}}d\bar{\alpha}$$

and substituting equation (14) into equation (1), the following equation can be obtained for each wave number component.

$$\bar{\psi}_\alpha''' - (3\bar{\alpha}^2 + i\bar{\alpha}\mathrm{Re})\bar{\psi}_\alpha' - \mathrm{Re}\left(\frac{i\bar{\alpha}}{\mathrm{Fr}} + \frac{i\bar{\alpha}^3}{\mathrm{We}}\right)\bar{\Phi}(\bar{\alpha}) = \frac{i}{\pi}\Delta\bar{P}\mathrm{Re}\sin\bar{\alpha} \quad (15)$$

The kinematic condition of the velocity at the liquid surface $\bar{y}=1$ gives

$$\bar{u}\frac{d\bar{h}}{d\bar{x}} = \bar{v} \quad (16)$$

Substituting equations (7) and (13) into equation (16), we have

$$\bar{\Phi}(\bar{\alpha}) = -\bar{\psi}_\alpha \quad (17)$$

Then substituting this into equation (15), the boundary condition at the liquid surface is eventually obtained as

$$\bar{\psi}_\alpha''' - (3\bar{\alpha}^2 + i\bar{\alpha}\mathrm{Re})\bar{\psi}_\alpha' + \mathrm{Re}\left(\frac{i\bar{\alpha}}{\mathrm{Fr}} + \frac{i\bar{\alpha}^3}{\mathrm{We}}\right)\bar{\psi}_\alpha = \frac{i}{\pi}\Delta\bar{P}\mathrm{Re}\sin\bar{\alpha} \quad (18)$$

The boundary condition that the shear force is equal to zero at the liquid surface gives the other equation,

$$\bar{\psi}_\alpha'' + \bar{\alpha}^2\bar{\psi}_\alpha = 0 \quad (19)$$

Nonviscous Flow Model. Since the Laplace equation holds for the stream function of the nonviscous flow, the following equation can be obtained for each wave number component.

$$\bar{\psi}_\alpha'' - \bar{\alpha}^2\bar{\psi}_\alpha = 0 \quad (20)$$

The boundary condition by which the y component velocity is equal to zero at the wall ($\bar{y}=0$) gives

$$\bar{\psi}_\alpha = 0 \quad (21)$$

At the liquid surface ($\bar{y}=1$), the following equation is obtained by excluding the viscous terms in equation (18).

$$\bar{\alpha}\bar{\psi}_\alpha' - \left(\frac{\bar{\alpha}}{\mathrm{Fr}} + \frac{\bar{\alpha}^3}{\mathrm{We}}\right)\bar{\psi}_\alpha = -\frac{1}{\pi}\Delta\bar{P}\sin\bar{\alpha} \quad (22)$$

2.2 Solution

Viscous Solution. Equation (8) can be solved analytically as

$$\bar{\psi}_\alpha = Ae^{\bar{\alpha}\bar{y}} + Be^{-\bar{\alpha}\bar{y}} + Ce^{(p+qi)\bar{y}} + De^{(-p-qi)\bar{y}}$$

where

$$p = \sqrt{(\bar{\alpha}^2 + \bar{\alpha}\sqrt{\bar{\alpha}^2 + \mathrm{Re}^2})/2},$$

$$q = \sqrt{(-\bar{\alpha}^2 + \bar{\alpha}\sqrt{\bar{\alpha}^2 + \mathrm{Re}^2})/2} \quad (23)$$

Therefore the stream function for the fluctuation $\bar{\psi}_\alpha$ can be obtained by determining constants A, B, C, and D based on the conditions of equations (9), (10), (18), and (19). Using equation (17), each wave number component of the amplitude $\bar{\Phi}(\bar{\alpha})$ is calculated by equation (23). The liquid surface profile is obtained by substituting $\bar{\Phi}(\bar{\alpha})$ into equation (13) and by integrating equation (13) by means of numerical calculation.

Nonviscous Solution. Solving equation (20) under the boundary conditions of equations (21) and (22) and using equation (17), the liquid surface profile of the nonviscous flow can be obtained.

$$\bar{h}(\bar{x}) = \int_{-\infty}^{\infty} \frac{2\Delta\bar{P}\sin\bar{\alpha}\tanh\bar{\alpha}e^{i\bar{\alpha}\bar{x}}}{\bar{\alpha}\{\bar{\alpha} - (1/\mathrm{Fr} + \bar{\alpha}^2/\mathrm{We})\tanh\bar{\alpha}\}}d\bar{\alpha} \quad (24)$$

The integration of equation (24) may be performed by Cauchy's integration theorem. The wave number of the liquid surface profile is determined by the following equation.

$$\bar{\alpha} = \left(\frac{1}{\mathrm{Fr}} + \frac{\bar{\alpha}^2}{\mathrm{We}}\right)\tanh\bar{\alpha} \quad (25)$$

2.3 Comparison of Present Analysis With Crapper's Results.

In order to confirm the validity of our analysis, we compared the results in this study with those of Crapper waves (Crapper, 1957). Crapper treated the case of nonlinear waves for nonviscous flow and infinite liquid depth and did not consider the gravitational force. Hence, the wave number for nonviscous flow determined by equation (25) was compared with that for Crapper wave with the condition of infinite liquid depth and without the gravitational force.

Crapper's result of nondimensional wave number for a linear wave is

$$\bar{\alpha} = \mathrm{We} \quad (26)$$

When the gravitational force is neglected ($\mathrm{Fr}\to\infty$) and the liquid depth approaches infinity ($\bar{\alpha}\to\infty$), equation (25) agrees with equation (26) of Crapper wave, from which the validity of the present results is confirmed.

3 Results and Discussion

3.1 Profile of Liquid Surface. When an obstacle is installed in a horizontal channel flow, the following three kinds of flow patterns are observed on the liquid surface as Forbes (1983) showed for the potential flow: (I) no stationary wave appears; (II) both surface tension and gravitational waves appear before and behind the obstacle, respectively; (III) only the surface tension wave appears before the obstacle and the gravitational wave does not.

These three patterns can be classified by the number of wave number solutions $\bar{\alpha}$ determined by equation (25) for nonviscous flow; that is, (I), (II), and (III) correspond to the case of (*a*) no solutions, (*b*) two solutions, and (*c*) one solution, respectively. Equation (25), by which the flow patterns are classified, is the same form as Forbes obtained. As noted from equation (25), the above flow regimes are classified by Weber and Froude numbers. The results are shown in Fig. 2. The results for the viscous solution are independent of the Reynolds number and agree completely with those for the nonviscous flow.

The typical surface profiles calculated by the viscous solutions are shown in Fig. 3. Figures 3(*a*), (*b*), and (*c*) correspond to (I), (II), and (III) described above. Although each surface profile is obtained for the condition that the pressure increase is distributed within the region $-1 \leqq \bar{x} \leqq 1$, the results for $-2 \leqq \bar{x} \leqq 2$ are also shown in Fig. 3 for the purpose of comparison. Note that the disturbance region does not influence the significant characteristics of the stationary wave, such as the wave damping rate or the wavelength, although it does

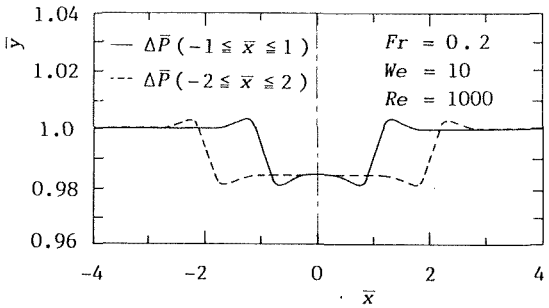

Fig. 3(*a*) Example for regime (I)

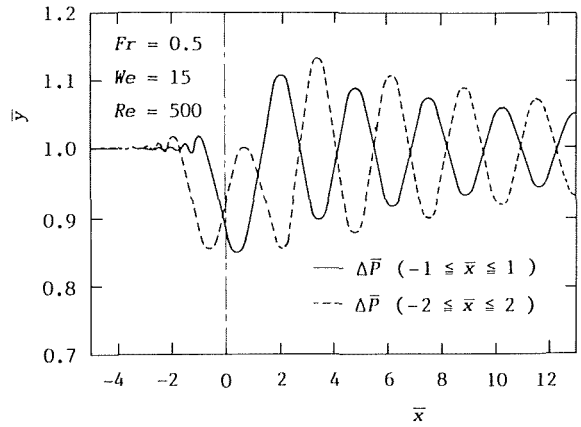

Fig. 3(*b*) Example for regime (II)

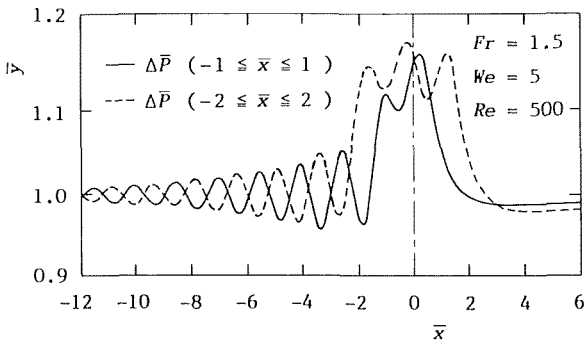

Fig. 3(*c*) Example for regime (III)

Fig. 3 Liquid surface profile

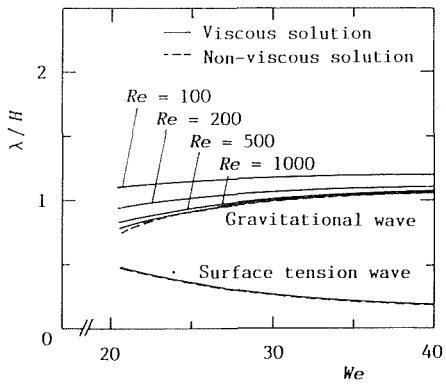

Fig. 4(*a*) Fr = 0.2

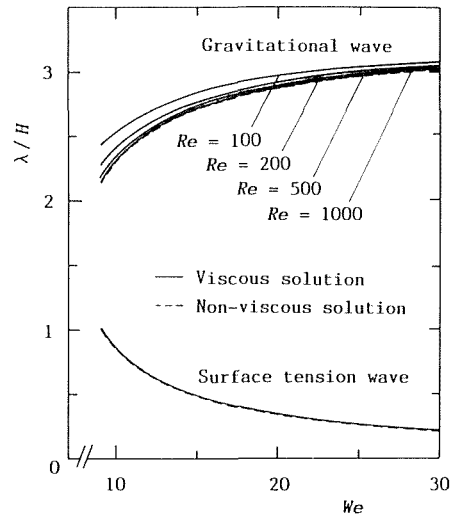

Fig. 4(*b*) Fr = 0.5

Fig. 4 Wavelength change with Weber number

influence the starting point of the wave as seen in Fig. 3. The surface profiles shown in this report were calculated for $\Delta\bar{P} / \pi = 0.02$ in equation (18). The magnitude of $\Delta\bar{P}$ influences only the amplitude of the wave as is obvious from the boundary conditions of equations (9), (10), (18), and (19).

3.2 Wavelength. The calculated wavelength which is nondimensionalised by the liquid depth H is shown in Fig. 4. The results of the nonviscous solution determined by equation (25) are also shown by dotted lines in the figure. Each curve in the figures starts at the Weber numbers at which the waves appear as stated in section 3.1. It is shown that the wavelength of the surface tension wave agrees with that of nonviscous solution irrespective of the Reynolds number. Therefore, the effect of the viscosity on the wavelength is not recognized. On the other hand, the wavelength of the gravitational waves decrease and approach those of the nonviscous solution as Re increases. As seen from Figs. 4(*a*) and 4(*b*), the effect of Re, namely, the viscous effect on the wavelength, becomes weak as Fr increases. The ratio of the gravitational force to the viscous one reduces as Fr increases for a fixed Re. Thus, for the gravitational wave, the effect of the viscosity becomes weaker as the wave driving force decreases.

The waves considered here belong to the deep-sea waves, since λ/H in Fig. 4 is on the order of unity. Therefore it is reasonable to assume that the stream velocity is constant in the flow cross section, because the effect of the bottom friction on the wave damping can be neglected. In Section 4, we discuss the case in which the liquid depth is too shallow to assume an uniform velocity distribution.

3.3 Wave Damping by Viscosity. The wave damping rates are shown in Fig. 5 for the regimes (II) and (III) in Fig. 2. The ordinate, η, is the damping rate of the amplitude per wavelength. Thus, if the ratio of the wave amplitude of adjacent two waves is $a(<1)$, η is defined by $1-a$. The present analysis shows that η remains constant for every two adjacent waves. Each curve in the figures starts at the Weber numbers at which the waves appear, as well as in Fig. 4. Figure 5(*a*) shows the results for (II), in which both the surface tension and the gravitational waves appear. Figure 5(*b*) corresponds to the regime (III) in which only the surface tension waves appear. In the case of Re = 100 and 200 for Fr = 0.2 shown in Fig. 5(*a*), the surface tension waves cannot be recognized, since viscosity is so strong that the waves disappear within the first wave length ($\eta = 1$). The critical Reynolds numbers at which η becomes unity will be discussed later.

As shown in Fig. 5, η (i.e., the effect of the viscosity on the wave motion) becomes weaker as Re increases in each case. In general, the damping rates of the surface tension waves are

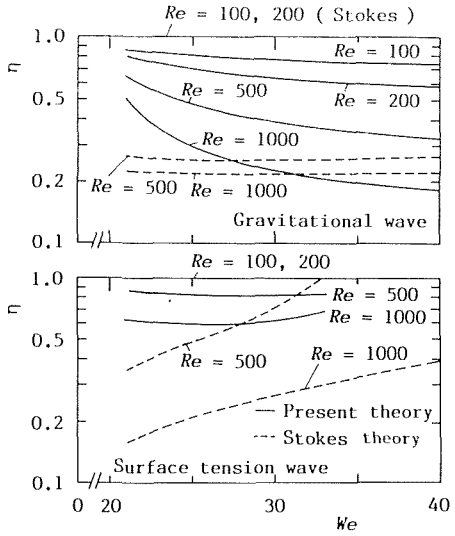

Fig. 5(*a*) Fr = 0.2

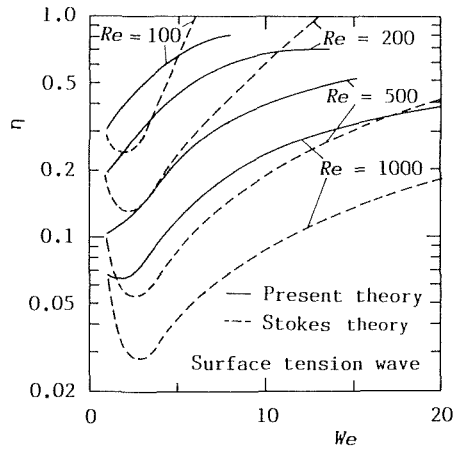

Fig. 5(*b*) Fr = 0.5

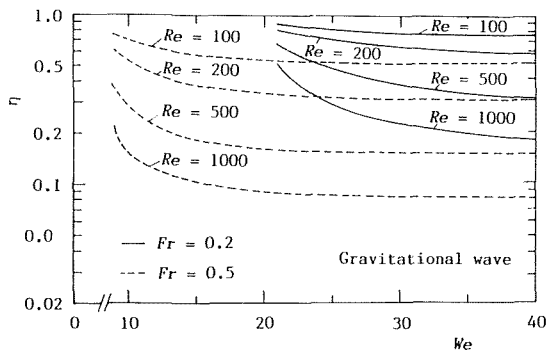

Fig. 5(*c*) Comparison of Fr = 0.2 and Fr = 0.5

Fig. 5 Change of wave damping rate with Weber number

larger than those of the gravitational ones. For the gravitational waves, η decreases in the range of small Weber numbers and then approaches a certain value. On the other hand, η for the surface tension waves gradually increases as We increases as shown in both Figs. 5(*a*) and 5(*b*). The increasing rate of η is more remarkable in Fig. 5(*b*) for the case in which only the surface tension waves appear before the obstacle. The surface tension becomes small compared with the viscous force as We increase keeping Re a constant, while the viscous damping becomes more remarkable as the wave driving force (the surface tension) relatively decreases.

The results of η calculated for various Re's and Fr's are compared with each other in Fig. 5(*c*). Although η of the surface tension wave increases as We increases, that of the gravitational wave decreases as Fr increases (cf. Section 3.2). With gravitational wave the viscous damping is proportional to the wave driving force, the opposite of the case for the surface tension wave. Since the gravitational force and the surface tension act on the wave motion in different ways, it is considered that the action of the viscosity is also different on both kinds of waves.

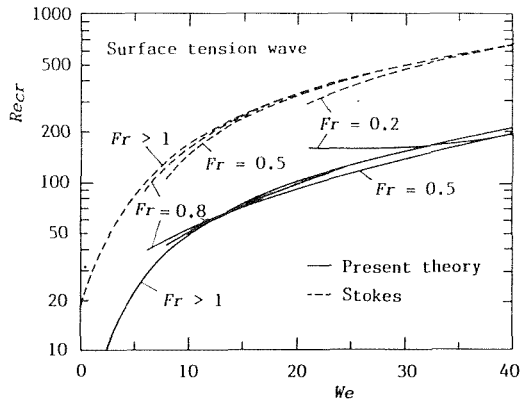

Fig. 6 Re_{cr} for surface tension waves

In Figs. 5(*a*) and (*b*), the results obtained by the Stokes' theory (Lighthill, 1978a) are also shown for the purpose of comparison. The Stokes' theory makes $\eta = 1$ for Re = 100 and 200 in Fig. 5(*a*). The results of η obtained by the present analysis and those by Stokes' theory generally do not agree with each other, although the present results tend to approach those by Stokes as Re increases, as seen from the results of the gravitational waves shown above in Fig. 5(*a*). In the case of small Reynolds number, especially, both results are quite different. Stokes' results show $\eta = 1$, which means that the waves disappear within the first wavelength as stated before, contrary to the results of the present study, $\eta \neq 1$. This is attributed to the fact that the Stokes' theory is based on the solution for nonviscous flow. An exact analysis as in our study is needed for a relatively small Reynolds number range such as $Re \leqq 1000$.

Figure 6 shows the results of the critical Reynolds numbers Re_{cr} at which the waves disappear within the first wavelength. Each curve starts at the Weber numbers at which the waves appear as stated in Section 3.1. In Fig. 6, which shows the results for the surface tension waves, Re_{cr} increases with We as expected from the preceding results for the damping rate η. The results for each Fr agree well with one another except in the small Weber number region in which the waves begin to appear. This is due to the fact that the Froude number does not influence substantially the behavior of the surface tension waves. The broken lines indicating the results by Stokes' theory are almost parallel to those by the present theory, although Stokes' curves are larger in all the cases. For gravitational waves, the effect of the Weber number on Re_{cr} was not recognized, and the Froude number also did not have a significant influence, contrary to the case of the damping rate η.

4 Stationary Waves on Falling Liquid Film Flow

4.1 Basic Equations and Their Solution. When the liquid film flows down the vertical wall which has an obstacle such as a protuberance or a step, various flow patterns are observed near the obstacle (Fujita, 1986). In particular, when the Reynolds number is on the order of 100, the stationary waves due to the surface tension appear above the obstacle as shown in Fig. 7. The gravitational waves, however, do not appear, because the gravitational force does not act in the normal di-

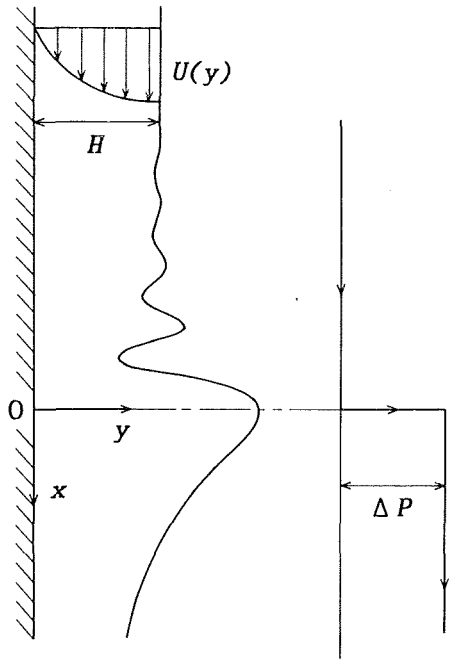

Fig. 7 Coordinate system for falling liquid film flow

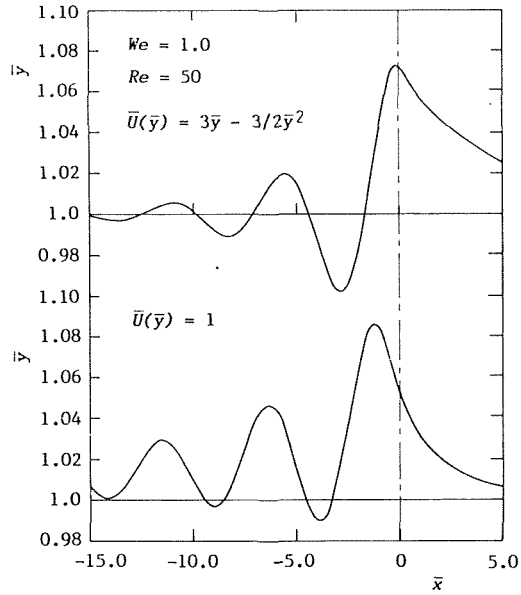

Fig. 8(a) We = 1.0, Re = 50

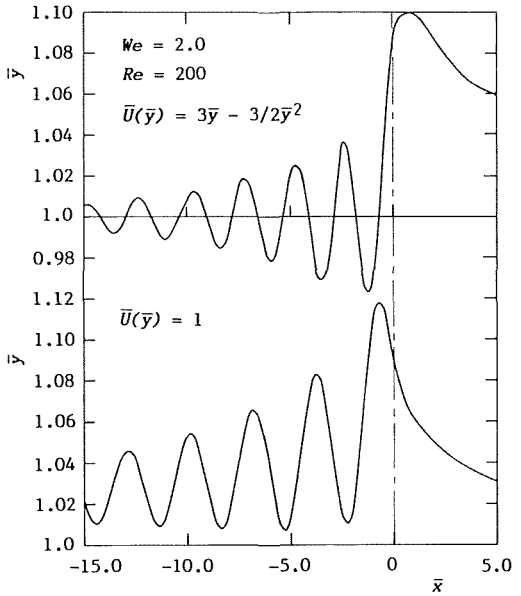

Fig. 8(b) We = 2.0, Re = 200

Fig. 8 Stationary wave profile of falling liquid film flow

rection to the flow. This corresponds to the infinite Froude number. As an application of the preceding analysis, the waveform of this flow is obtained here.

Since the falling liquid films are generally very thin (i.e., on the order of 0.1 to 1 mm), the assumption of the uniform velocity distribution as used in Section 3 is not applicable. Hence, we use the following Nusselt's velocity distribution for laminar falling liquid film flow (Re < 600) (Nusselt, 1923).

$$\bar{U}(\bar{y}) = 3\bar{y} - \frac{3}{2}\bar{y}^2 \tag{27}$$

As a result, the following equation for the stream function can be obtained in the same manner as derived in Section 2.

$$\bar{\psi}_\alpha'''' - \left\{2\bar{\alpha}^2 + i\bar{\alpha}\mathrm{Re}\left(3\bar{y} - \frac{3}{2}\bar{y}^2\right)\right\}\bar{\psi}_\alpha'' + \left\{-3i\bar{\alpha}\mathrm{Re} + \bar{\alpha}^4 + i\bar{\alpha}^3\mathrm{Re}\left(3\bar{y} - \frac{3}{2}\bar{y}^2\right)\right\}\bar{\psi}_\alpha = 0 \tag{28}$$

The boundary conditions of equations (9), (10), and (19) can be also used for the falling film flow, except for those of equation (18) which must be rewritten by neglecting the gravitational term as a result of $\mathrm{Fr} \to \infty$. Since no waves appear downstream of the obstacle, only the upstream side is significant. Therefore, assuming that the pressure increase occurs only in the region $\bar{x} \geqq 0$, the following relation can be obtained for the boundary condition at the liquid surface $\bar{y} = 1$ instead of equation (18).

$$\bar{\psi}_\alpha''' - \left(3\bar{\alpha}^2 + \frac{3}{2}i\bar{\alpha}\mathrm{Re}\right)\bar{\psi}_\alpha' + \frac{2}{3}\frac{i\bar{\alpha}^3\mathrm{Re}}{\mathrm{We}}\bar{\psi}_\alpha = \frac{1}{2\pi}\Delta\bar{P}\mathrm{Re} \tag{29}$$

4.2 Calculated Results. Since equation (28) cannot be solved analytically, the solution is obtained by the numerical calculation. A subroutine for the initial value problem of the ordinary differential equation is generally prepared in the computer system. However, since the differential equation treated in this study, equation (28), has the boundary conditions at two places, namely, the wall ($\bar{y} = 0$) and the liquid surface ($\bar{y} = 1$), the subroutine cannot be applied directly. Therefore, in the present calculation the boundary conditions at the liquid surface ($\bar{y} = 1$) were transformed into those at the wall ($\bar{y} = 0$) by considering that equation (28) is linear.

Calculated waveforms for the falling water film flow are shown in Fig. 8. The results assuming the uniform velocity distribution are also shown in the figure for the purpose of comparison. Although the wavelength for both results agree roughly with each other, the damping rate is somewhat larger for the results assuming Nusselt's velocity distribution. This is considered due to the friction at the bottom wall. On the other hand, the wave amplitude and the displacement from the average film thickness are larger for the uniform velocity distribution. From these results, it is noted that the effect of the viscosity on the stream tends to suppress the deviation of the surface profile from the profile in the nondisturbed flow and to damp the wave motion.

5 Conclusions

The effect of the viscosity on the surface wave motion was theoretically investigated for the stationary waves generated by the disturbance arranged in the flow. The results are summarized as follows.

1 Expressing the disturbance in the flow by the pressure increase, the liquid surface profiles can be obtained exactly by linear analysis involving viscous effects.

2 The effect of the viscosity on the wave motion becomes stronger as the Weber number increases for the surface tension waves and becomes weaker as the Froude number increases for gravitational waves.

3 The exact analysis prepared in this report is needed for the small Reynolds number range (at least for $Re \leqq 1000$ treated in this study), in which Stokes' theory based on the non-viscous solution cannot be applied.

4 Applying the present analysis, the waveforms are obtained for falling liquid film flow with Nusselt's velocity distribution. Results show that the damping rate is somewhat larger and the wave amplitude smaller than for flow with a uniform velocity distribution.

References

Crapper, G. D., 1957, "An Exact Solution for Progressive Capillary Waves of Arbitrary Amplitude," *Journal of Fluid Mechanics*, Vol. 2, pp. 532–540.

Forbes, L. K., 1983, "Free-surface Flow over a Semicircular Obstruction, Including the Influence of Gravity and Surface Tension," *Journal of Fluid Mechanics*, Vol. 127, pp. 283–297.

Fujita, H., Katoh, K., and Takahama, H., 1986, "Falling Water Films on a Vertical Cylinder with a Downward Step," *International Journal of Engineering Science*, Vol. 24, pp. 1405–1418.

Hino, M., 1977, *Spectrum Analysis*, Asakura-Shoten, Tokyo, pp. 70–73 (in Japanese).

Hunt, J. N., 1964, "The Viscous Damping of Gravity Waves in Shallow Water," *La Houille Branche*, Vol. 19, pp. 685–691.

Keulegan, G. H., 1948, "Gradual Damping of Solitary Waves," *Journal of Research of the National Bureau of Standards*, Vol. 40, pp. 487–498.

Lamb, H., 1932, *Hydrodynamics, 6th Edition*, Cambridge University Press, Cambridge, pp. 625–628.

Leblond, P. H., and Mainardi, F., 1987, "The Viscous Damping of Capillary-Gravity Waves," *Acta Mechanica*, Vol. 68, pp. 203–222.

Lighthill, J., 1978a, *Waves in Fluids*, Cambridge University Press, Cambridge, pp. 229–237.

Lighthill, J., 1978b, *Waves in Fluids*, Cambridge University Press, Cambridge, pp. 260–269.

Nusselt, W., 1923, "Der Wärmeaustäusch am Berieselungskühler," *Zeitschrift des Vereines deutscher Ingenieure*, Vol. 67, pp. 206–210.

An Analytical Study of the Standard k-ϵ Model

N. Takemitsu
Associate Professor,
Institute of Industrial Science,
University of Tokyo,
Tokyo 106, Japan

An asymptotic solution of the standard k-ϵ model for two-dimensional turbulent channel flow is found. Using this solution, five model constants in the model are all determined reasonably with the aid of experimental data. If an asymptotic solution with the logarithmic law as the leading term is sought for, the standard k-ϵ model is shown to be ill-posed since the second-order solution has divergent terms.

Introduction

Flows appearing in engineering and natural sciences are almost always turbulent. Their direct simulation with no turbulence models cannot be performed at high Reynolds number even by existing largest computers since such flows contain a number of scales. In fact, a direct numerical simulation is confined to a low Reynolds number [1]. Therefore, some turbulence models are indispensable for numerical simulation of flows at high Reynolds numbers.

As representative of higher order turbulence models, there are large eddy simulation (LES) models [2, 3], and the stress and k-ϵ models [4-8]. Among them, the k-ϵ models, especially the k-ϵ model by Jones and Launder [7], have become popular, mainly owing to short computing times as well as the simplicity of model. In fact, many flows such as wall flows, jets, wakes, reacting flows, and flows with buoyancy effects have been successfully calculated with the k-ϵ models [6, 8]. Recently, the models have been improved to treat flows in the vicinity of solid walls by using wall damping functions [7, 9-10]. These modified k-ϵ models account for the effects of anisotropy due to the existence of walls. Unfortunately, this treatment of anisotropy lacks for universality because such modifications cannot be applied to general three-dimensional flows, and the constants of damping function need to be adjusted for different Reynolds number and flows. These facts are unavoidable difficulties of the k-ϵ models.

Recently, Yoshizawa [11] has derived an anisotropic expression for the Reynolds stress statistically. This work extended widely the range of application of the k-ϵ models since the expression is applicable to three-dimensional flows. In fact, Nisizima and Yoshizawa [12] used the expression to predict the anisotropy of turbulent intensities in wall turbulence.

The k-ϵ models are complex nonlinear systems of equations. Because of this nonlinearity, the detailed mathematical structure of the k-ϵ model has hardly been investigated. In this paper, we shall discuss an asymptotic solution of the standard k-ϵ model and investigate the intrinsic property of the model.

On the basis of the above investigation, we are led to the following important conclusion. Namely, the standard k-ϵ model [7] is mathematically ill-posed if an asymptotic solution with the logarithmic velocity law taken as the leading terms is sought for.

Standard k-ϵ Model

In this paper, the ensemble mean parts of the velocity and the pressure are denoted by $\bar{U}_i$ and $\bar{p}$, respectively, and the fluctuation of velocity is denoted by $\bar{u}_i$ (the variables with overbar are dimensional). Then, the mean equations for three-dimensional incompressible flows neglecting viscous effects are given by

$$\frac{D\bar{U}_\alpha}{D\bar{t}} \equiv \left(\frac{\partial}{\partial \bar{t}} + \bar{U}_a \frac{\partial}{\partial \bar{x}_a}\right) \bar{U}_\alpha = -\frac{1}{\bar{\rho}} \frac{\partial \bar{p}}{\partial \bar{x}_\alpha} + \frac{\partial \bar{R}_{\alpha a}}{\partial \bar{x}_a}, \tag{1}$$

$$\frac{\partial \bar{U}_a}{\partial \bar{x}_a} = 0. \tag{2}$$

Here, $\bar{\rho}$ is the density of fluid, the Reynolds stress $\bar{R}_{\alpha\beta}$ is defined as

$$\bar{R}_{\alpha\beta} = -\langle \bar{u}_\alpha \bar{u}_\beta \rangle, \tag{3}$$

by using the ensemble mean $\langle\ \rangle$, and repeated subscripts are summed from 1 to 3 (for clarity, Greek letters are used for noncontracted subscripts).

In the standard k-ϵ model, $\bar{R}_{\alpha\beta}$ is approximated by using the eddy viscosity $\bar{\nu}_e$ as

$$\bar{R}_{\alpha\beta} = -\frac{2}{3}\bar{k}\delta_{\alpha\beta} + \bar{\nu}_e \bar{e}_{\alpha\beta}. \tag{4}$$

Here $\delta_{\alpha\beta}$ is the Kronecker delta symbol, the turbulent kinetic energy $\bar{k}$ is defined by

$$\bar{k} = \langle \bar{u}_a \bar{u}_a \rangle / 2, \tag{5}$$

$\bar{\nu}_e$ is the eddy viscosity, and $\bar{e}_{\alpha\beta}$ is the velocity strain defined by

$$\bar{e}_{\alpha\beta} = \frac{\partial \bar{U}_\alpha}{\partial \bar{x}_\beta} + \frac{\partial \bar{U}_\beta}{\partial \bar{x}_\alpha}. \tag{6}$$

Moreover, $\bar{\epsilon}$ (the dissipation rate of turbulent kinetic energy) is introduced as

$$\bar{\epsilon} = \bar{\nu} \left\langle \frac{\partial \bar{u}_a}{\partial \bar{x}_b} \frac{\partial \bar{u}_a}{\partial \bar{x}_b} \right\rangle, \tag{7}$$

Present address: Toyama Prefectural University, Faculty of Engineering, Department of Mechanical Sytems Engineering, Imisu-gun, Toyama 939-03, Japan.

Contributed by the Fluids Engineering Division for publication in the JOURNAL OF FLUIDS ENGINEERING. Manuscript received by the Fluids Engineering Division February 26, 1987.

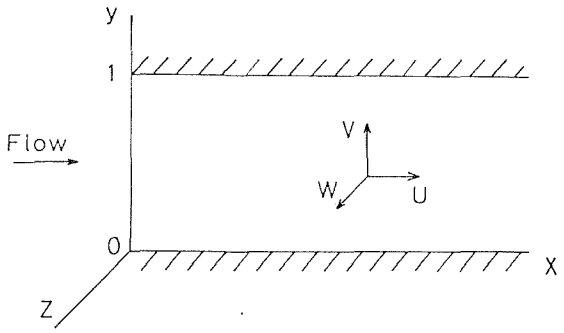

Fig. 1 Coordinate system

where $\bar{\nu}$ is the kinematic viscosity. In the k-ϵ model, from dimensional analysis $\bar{\nu}_e$ is modeled as

$$\bar{\nu}_e = C_\nu \frac{\bar{k}^2}{\bar{\epsilon}}, \tag{8}$$

in terms of $\bar{k}$ and $\bar{\epsilon}$ (C_ν is a model constant). The governing equations $\bar{k}$ and $\bar{\epsilon}$ are also modeled in the form that

$$\frac{D\bar{k}}{D\bar{t}} = \bar{P} - \bar{\epsilon} + \frac{\partial}{\partial \bar{x}_a}\left(C_{k1}\bar{\nu}_e \frac{\partial \bar{k}}{\partial \bar{x}_a}\right), \tag{9}$$

$$\frac{D\bar{\epsilon}}{D\bar{t}} = \frac{\partial}{\partial \bar{x}_a}\left(C_{\epsilon 1}\bar{\nu}_e \frac{\partial \bar{\epsilon}}{\partial \bar{x}_a}\right) + C_{\epsilon 2}\frac{\bar{\epsilon}}{\bar{k}}\bar{P} - C_{\epsilon 3}\frac{\bar{\epsilon}^2}{\bar{k}}, \tag{10}$$

$$\bar{P} = \bar{\nu}_e \frac{\partial \bar{U}_a}{\partial \bar{x}_a}\left(\frac{\partial \bar{U}_a}{\partial \bar{x}_b} + \frac{\partial \bar{U}_b}{\partial \bar{x}_a}\right) \tag{11}$$

(C_{k1}, $C_{\epsilon l}$, etc, are model constants). Thus, (1)-(2), (4), and (8)-(11) constitute a closed system of equations. The model constants are usually chosen as [6]

$$C_\nu = 0.09,\ C_{k1} = 1.0,\ C_{\epsilon 1} = 1/1.3,\ C_{\epsilon 2} = 1.45,\ C_{\epsilon 3} = 1.9. \tag{12}$$

An Asymptotic Solution for Two-Dimensional Channel Flow

Let us consider a fully developed turbulent channel flow (see Fig. 1). In this simple case, the standard k-ϵ model also retains all five model constants C_ν, C_{k1}, $C_{\epsilon n}$ ($n = 1,2,3$), and becomes

$$\frac{\partial}{\partial \bar{y}}\left(\bar{\nu}_e \frac{\partial \bar{U}}{\partial \bar{y}}\right) = \frac{1}{\bar{\rho}}\frac{\partial \bar{p}}{\partial \bar{x}}, \tag{13}$$

$$\frac{\partial}{\partial \bar{y}}\left(C_{k1}\bar{\nu}_e \frac{\partial \bar{k}}{\partial \bar{y}}\right) + \bar{\nu}_e\left(\frac{\partial \bar{U}}{\partial \bar{y}}\right)^2 - \bar{\epsilon} = 0, \tag{14}$$

$$\frac{\partial}{\partial \bar{y}}\left(C_{\epsilon 1}\bar{\nu}_e \frac{\partial \bar{\epsilon}}{\partial \bar{y}}\right) + C_{\epsilon 2}\bar{\nu}_e\frac{\bar{\epsilon}}{\bar{k}}\left(\frac{\partial \bar{U}}{\partial \bar{y}}\right)^2 - C_{\epsilon 3}\frac{\bar{\epsilon}^2}{\bar{k}} = 0 \tag{15}$$

$$\bar{\nu}_e = C_\nu \frac{\bar{k}^2}{\bar{\epsilon}}, \tag{16}$$

$$\bar{R}_{12} = \bar{\nu}_e\left(\frac{\partial \bar{U}}{\partial \bar{y}}\right). \tag{17}$$

Equations (13)-(17) are nondimensionalized using

$$\bar{x}_i = Lx_i,\ \bar{U}_i = VU_i,\ \bar{p} = \rho V^2 p,\ \bar{\nu}_e = \nu\nu_e,$$

$$\bar{k} = V^2 k,\ \bar{\epsilon} = (V^3/L)\epsilon,\ \bar{R}_{12} = V^2 R_{12}, \tag{18}$$

where L and V are the characteristic length and the velocity of the flow field, respectively. As a result, we obtain

$$\frac{\partial}{\partial y}\left(\nu_e \frac{\partial U}{\partial y}\right) = \mathrm{R_e}\frac{\partial p}{\partial x}, \tag{19}$$

$$\frac{\partial}{\partial y}\left(C_{k1}\nu_e \frac{\partial k}{\partial y}\right) + \nu_e\left(\frac{\partial U}{\partial y}\right)^2 - \mathrm{R_e}\epsilon = 0, \tag{20}$$

$$\frac{\partial}{\partial y}\left(C_{\epsilon 1}\nu_e \frac{\partial \epsilon}{\partial y}\right) + C_{\epsilon 2}\frac{\epsilon}{k}\nu_e\left(\frac{\partial U}{\partial y}\right)^2 - C_{\epsilon 3}\mathrm{R_e}\frac{\epsilon^2}{k} = 0, \tag{21}$$

$$\nu_e = C_\nu \mathrm{R_e}\frac{k^2}{\epsilon}, \tag{22}$$

$$R_{12} = \nu_e\left(\frac{\partial U}{\partial y}\right)/\mathrm{R_e}, \tag{23}$$

where $\mathrm{R_e}$ is the Reynolds number defined by

$$\mathrm{R_e} = VL/\nu. \tag{24}$$

If the molecular viscosity effect is recovered in equation (19), then it is replaced by

$$\frac{\partial}{\partial y}(1 + \nu_e)\frac{\partial U}{\partial y} = \mathrm{R_e}\frac{\partial p}{\partial x}. \tag{25}$$

Integration of (25) yields

$$(1 + \nu_e)\frac{\partial U}{\partial y} = \mathrm{R_e}\frac{\partial p}{\partial x}y + \text{const}. \tag{26}$$

Nomenclature

x_a = position vector, Cartesian components are x, y, z
t = time
D/Dt = Lagrangian derivative
U_i = mean part of velocity, Cartesian components are U, V, W
u_i = fluctuation of velocity, Cartesian components are u, v, w
p = mean part of the pressure
p' = fluctuation of pressure
ρ = density of the fluid
ν = kinematic viscosity
$\mathrm{R_e}$ = Reynolds number defined based on the centerline velocity and the channel width
u_τ = friction velocity
y = distance from the wall
y^+ = distance from the wall in wall units ($= \mathrm{R_e}u_\tau y$)
$\langle\ \rangle$ = notation for ensemble mean
$R_{\alpha\beta}$ = Reynolds stress
P = production term
$\delta_{\alpha\beta}$ = Kronecker delta symbol
ν_e = eddy viscosity
k = turbulent kinetic energy
ϵ = dissipation rate of turbulent kinetic energy
κ = Karman constant
A = constant in the logarithmic velocity law
C_ν = model constant
C_{k1} = model constant used in k equation
$C_{\epsilon n}(n = 1,2,3)$ = model constants used in ϵ equation
a_n, b_n, $c_n(n = 1,2,3)$ = coefficients of expanded solution
$\alpha = \kappa^2/\sqrt{C_\nu}$
$\beta = C_{\epsilon 1}/C_{\epsilon 2}$
$\gamma = C_{\epsilon 3}/C_{\epsilon 2}$

Since $\partial U/\partial y = 0$ at $y = 1/2$, we have

$$(1+\nu_e)\frac{\partial U}{\partial y} = \mathrm{R_e}\frac{\partial p}{\partial x}\,(y-1/2). \tag{27}$$

In the limit of $y \to 0$ and $\nu_e \to 0$, (27) becomes

$$\left(\frac{\partial U}{\partial y}\right)_{wall} = -\frac{1}{2}\,\mathrm{R_e}\frac{\partial p}{\partial x}. \tag{28}$$

Combining the friction velocity u_τ in the nondimensional form

$$u_\tau = \sqrt{\frac{1}{\mathrm{R_e}}\left(\frac{\partial U}{\partial y}\right)_{wall}}, \quad \left(\frac{\partial U}{\partial y}\right)_{wall} = \mathrm{R_e}u_\tau^2, \tag{29}$$

with (28), the pressure gradient is written in terms of the friction velocity as

$$-\frac{\partial p}{\partial x} = 2u_\tau^2. \tag{30}$$

From (27) and (30), we have

$$(1+\nu_e)\frac{\partial U}{\partial y} = \mathrm{R_e}u_\tau^2(1-2y). \tag{31}$$

This equation is integrated to give

$$U = \mathrm{R_e}u_\tau^2 y - \mathrm{R_e}u_\tau^2 y^2 + \mathrm{O}(y^3), \quad \text{or} \quad U/u_\tau = y^+(1-y) + \mathrm{O}(y^3), \tag{32}$$

where y^+ $(= \mathrm{R_e}u_\tau y)$ is the distance from the wall in wall units. In obtaining (32), we have used the fact that ν_e in the immediate vicinity of the wall should be of $\mathrm{O}(y^3)$ because $u \propto y$, $v \propto y^2$ [13], and the Taylor expansion formula

$$\frac{1}{1+x} = 1 - x + x^2 - x^3 + \ldots, \quad |x| \ll 1 \tag{33}$$

has been used.

In (32), it should be noted that the leading term of (32) corresponds to the so-called wall law in the viscous sublayer, and the second term comes from the effect of the pressure gradient. Moreover, we should note that this expression does not depend on the modeling of ν_e since ν_e is of $\mathrm{O}(y^3)$. Hence it is concluded that the modified k-ϵ models with the effect of a wall incorporated can predict (32) correctly regardless of the values of model constants or the form of damping functions.

In the case of high Reynolds numbers ($\nu_e \gg 1$), (19) becomes

$$\frac{\partial}{\partial y}\left(\nu_e\frac{\partial U}{\partial y}\right) = -2\mathrm{R_e}u_\tau^2 \tag{34}$$

using (30). For the purpose of obtaining a solution in a universal form, we introduce the transformations

$$U = (u_\tau/\kappa)U^*,\ k = (u_\tau^2/\sqrt{C_\nu})k^*,\ \epsilon = (u_\tau^3/\kappa)\epsilon^*,$$
$$\nu_e = \mathrm{R_e}\kappa u_\tau \nu_e^*,\ R_{12} = u_\tau^2 R_{12}, \tag{35}$$

where κ is the Karman constant referred to later.

As a result, (34) and (20)-(23) take the form

$$\frac{\partial}{\partial y}\left(\nu_e^*\frac{\partial U^*}{\partial y}\right) = -2, \tag{36}$$

$$\alpha C_{k1}\frac{\partial}{\partial y}\left(\nu_e^*\frac{\partial k^*}{\partial y}\right) + \nu_e^*\left(\frac{\partial U^*}{\partial y}\right)^2 - \epsilon^* = 0, \tag{37}$$

$$\alpha\beta\frac{\partial}{\partial y}\left(\nu_e^*\frac{\partial \epsilon^*}{\partial y}\right) + \nu_e^*\frac{\epsilon^*}{k^*}\left(\frac{\partial U^*}{\partial y}\right)^2 - \gamma\frac{\epsilon^{*2}}{k^*} = 0, \tag{38}$$

$$\nu_e^* = \frac{k^{*2}}{\epsilon^*}, \tag{39}$$

$$R_{12}^* = \nu_e^*\left(\frac{\partial U^*}{\partial y}\right), \tag{40}$$

$$\alpha = \kappa^2/\sqrt{C_\nu}, \quad \beta = C_{\epsilon 1}/C_{\epsilon 2}, \quad \gamma = C_{\epsilon_3}c_{\epsilon_2}. \tag{41}$$

In what follows, we seek for a solution of the standard k-ϵ model with the logarithmic velocity law as the leading terms. The logarithmic law has been established experimentally and can be derived numerically from the standard k-ϵ model. This law also has been used as a kind of wall boundary condition in the numerical simulation of various k-ϵ models not imposing the noslip velocity condition. Hence, it is very interesting and important to obtain the solution of the k-ϵ model for small y (near the end of so-called buffer layer) with the logarithmic law as the leading terms. If the k-ϵ model does not permit such an analytic solution, use of the logarithmic law as a substitute boundary condition is not justified mathematically. For, any numerical schemes are based on analyticity of solution including the vicinity of boundaries.

We consider flows at very high Reynolds number. In such a flow, y becomes smaller and smaller for fixed $y^+ (= \mathrm{R_e}u_\tau y)$ as the Reynolds number becomes large, and the following assumption becomes more valid. Let us assume

$$\nu_e^* = y(1 + a_1 y + a_2 y^2 + a_3 y^3) + \mathrm{O}(y^5), \tag{42}$$

$$k^* = 1 + b_1 y + b_2 y^2 + b_3 y^3 + \mathrm{O}(y^4), \tag{43}$$

$$\epsilon^* = (1 + c_1 y + c_2 y^2 + c_3 y^3 + \mathrm{O}(y^4))/y, \tag{44}$$

where each leading term corresponds to the familiar logarithmic law.

Substituting (42)-(44) into (36)-(39), we have U^*, a_n, b_n, and c_n $(n = 1,2,3)$ as

$$U^* = \ln y^+ + \text{const.} - (a_1+2)y + \frac{1}{2}\{-a_2 + a_1(a_1+2)\}y^2$$
$$+\frac{1}{3}\{-a_3 + 2a_2(a_1+1) - a_1^2(a_1+2)\}y^3 + \mathrm{O}(y^4), \tag{45}$$

$$a_1 = -\frac{2\{3(\gamma-1)+\alpha C_{k1}\}}{(\gamma-1)(2-\alpha C_{k1})}, \qquad b_1 = -\frac{4}{2-\alpha C_{k1}},$$
$$c_1 = \frac{2(\alpha C_{k1} - \gamma + 1)}{(\gamma-1)(2-\alpha C_{k1})}, \tag{46a, b, c}$$

$$a_2 = f_1 + 2b_2 - c_2, \qquad b_2 = \frac{f_1+f_2}{2(2\alpha C_{k1}-1)}, \tag{47a, b}$$

$$c_2 = \frac{1}{2(\alpha\beta+1-\gamma)}\left\{(\alpha\beta+1)f_1 + f_3 + \frac{(f_1+f_2)(2\alpha\beta-\gamma+3)}{2(2\alpha C_{k1}-1)}\right\}, \tag{47c}$$

$$f_1 = (b_1-c_1)^2, \quad f_2 = -(a_1+2)^2 - 2\alpha C_{k1}a_1 b_1,$$
$$f_3 = -(a_1+2)^2 - (b_1-c_1)\{a_1+b_1+4-\gamma(b_1-c_1)\}, \tag{48a-c}$$

$$a_3 = g_1 + 2b_3 - c_3, \quad b_3 = \frac{g_1+g_2}{(9\alpha c_{k1}-2)}, \tag{49a, b}$$

$$c_3 = \frac{1}{2(3\alpha\beta-\gamma+1)}\left\{(2\alpha\beta+1)g_1 + g_3 + \frac{(g_1+g_2)(4\alpha\beta-\gamma+3)}{9\alpha C_{k1}-2}\right\}, \tag{49c}$$

$$g_1 = (b_1-c_1)\{2(b_2-c_2) - c_1(b_1-c_1)\}, \tag{50a}$$

$$g_2 = -(a_1+2)\{2a_2 - a_1(a_1+2)\} - 3\alpha C_{k1}(2a_1b_2 + a_2b_1), \tag{50b}$$

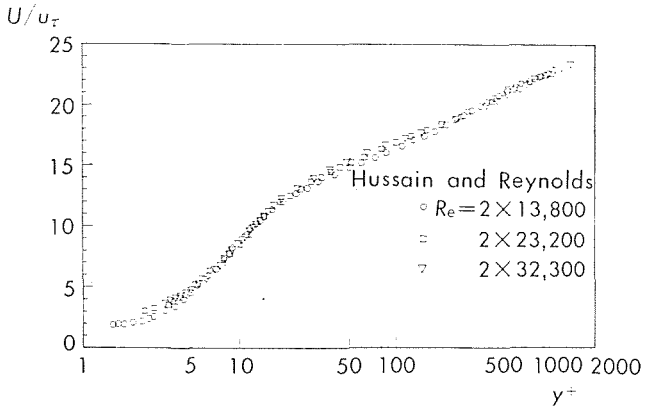

Fig. 2 Mean velocity profile due to Hussain and Reynolds [12]

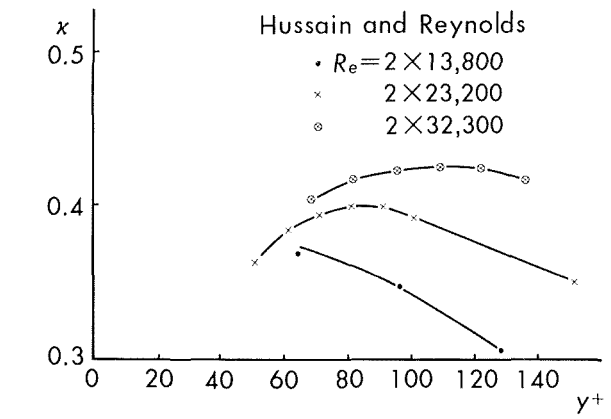

Fig. 3 Distribution of κ, which is calculated from experimental data of Hussain and Reynolds [12]

$$g_3 = -(a_1+2)\{2a_2 - a_1(a_1+2)\}$$
$$-(b_2-c_2)(a_1+b_1+4) - 2\alpha\beta a_1 c_2$$
$$-(b_1-c_1)\{a_2 - (2\gamma-1)b_2 + 2\gamma c_2$$
$$-(a_1+2)^2 - b_1(a_1+b_1+4) + \gamma b_1(b_1-c_1)\}. \quad (50c)$$

Here, the expansion (33) has been used.

Comparing solutions (42)-(45) with (32), we can see that the solution (42)-(45) is an asymptotic solution for small y after taking the limit $\nu \to 0$. The occurrence of y^+ and the constant in (45) signifies that this type of solution is completed by the matching with the solution in the sublayer.

Zeroth-Order Solution. The zeroth-order solution of the standard k-ϵ model is well known as the wall function or the logarithmic law, which is usually used as the boundary conditions for the standard k-ϵ model, as has already been noted. From (42)-(45), it is given by

$$U/u_\tau = (1/\kappa)\ln y^+ + A, \quad (51)$$

$$\nu_e/\mathrm{R_e}u_\tau = \kappa y, \quad (52)$$

$$k/u_\tau^2 = 1/\sqrt{C_\nu}, \quad (53)$$

$$\epsilon/u_\tau^3 = 1/(\kappa y), \quad (54)$$

where A is a constant. This zeroth-order solution leads to the balance of production and dissipation terms in the k equation. This solution, however, does not satisfy (36)-(40) exactly because of pressure term (i.e., -2 in (36)). This means that the influence of the pressure gradient is small for the unidirectional flow and the pressure term gives the higher order effects. Hence, the zeroth-order solution coincides with that of zero-pressure gradient.

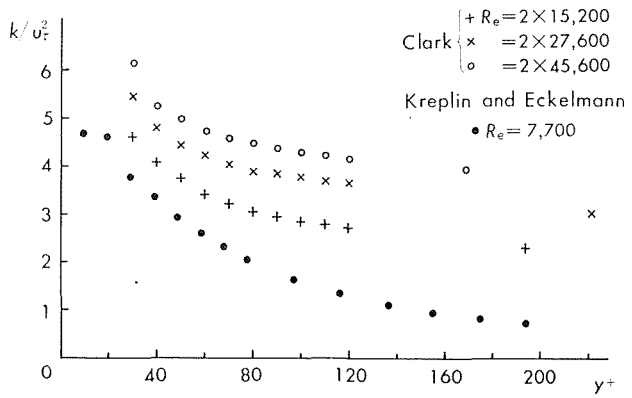

Fig. 4 Distribution of turbulent energy due to Clark [14] and Kreplin and Eckelmann [15]

From the results, we can conclude as follows:

1. U^* determines κ and A.
2. ν_e^* determines κ.
3. k^* determines C_ν.
4. ϵ^* determines κ.

The constants κ and C_ν can be determined using experimental data. From the mean velocity profile of Hussain and Reynolds [14] (see Fig. 2), the values of κ and A in (51) are determined as

$$\kappa = 0.4088 \pm 0.0063, \quad (55a)$$

$$A = 5.4042 \pm 0.5003 \quad (55b)$$

where use has been made of the experimental data at $y^+ = 60$ and 100. Here, we should note that our $\mathrm{R_e}$ is defined on the basis of the centerline velocity and the channel width and is twice the Reynolds number defined in cited experiments. From Laufer's data [15] at $y^+ = 60$ and 100, we have

$$\kappa = 0.3380 \pm 0.0083, \quad (56a)$$

$$A = 5.0787 \pm 0.5547. \quad (56b)$$

The value of (56a) is rather small compared with the commonly accepted value [6]

$$\kappa \fallingdotseq 0.41. \quad (57)$$

In this paper, we adopt the values of (55a, b) since they contain (57). The value of κ obtained from the experimental data about the eddy viscosity [14] is shown in Fig. 3. This figure clearly shows that the value of κ depends not only on y^+ but also on $\mathrm{R_e}$. This fact seems to indicate that the asymptotic expansions for U^*, k^*, ϵ^*, and ν_e^* do not satisfy (36)-(39) with the same degree of accuracy at a location. The value of κ between $y^+ = 70$ and 90, however, is nearly equal to 0.4, as seen in Fig. 3. Hence we assume that all of U^*, k^*, ϵ^*, and ν_e^* can be approximated by the wall function at $y^+ \fallingdotseq 80$.

The turbulent energy k measured by Clark [16] and Kreplin and Eckelmann [17] is shown in Fig. 4. From the data of Clark [16] of $\mathrm{R_e} = 2\times 15200$ and 2×27600 at $y^+ = 80$, C_ν is estimated as

$$C_\nu = 0.08654 \pm 0.02074. \quad (58)$$

From the data of $\mathrm{R_e} = 2\times 45600$, C_ν is given as 0.04948. From the data of Kreplin and Eckelmann [17] at $y^+ \fallingdotseq 80$, C_ν is estimated as 0.2371, but their Reynolds number ($\mathrm{R_e} = 7700$) is rather low. From the data of Laufer [15] at $y^+ \fallingdotseq 80$ and $\mathrm{R_e} = 2\times 30800$, C_ν is estimated at 0.1164. As can be seen from the above comparison of various data, the values of C_ν considerably scatter compared with the value of κ. The spatial

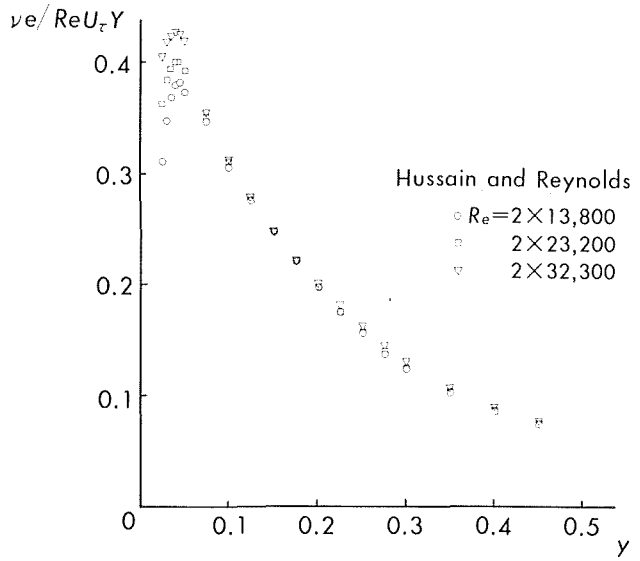

Fig. 5 Distribution of eddy viscosity due to Hussain and Reynolds [12]

variation of C_ν also has been pointed out by Rodi [18] in channel flow. In this paper, let us adopt the value (58) as C_ν. Figures 3 and 4 imply a possibility that the values of κ and C_ν depend on R_e and y^+, although they are commonly considered constant.

Experimental data of ϵ are obtained using the assumption [13]

$$\langle(\partial w/\partial y)^2\rangle = \langle(\partial u/\partial y)^2\rangle, \quad \text{etc.} \tag{59}$$

Therefore, the reliability of such data is low compared with those of U^*, k^* and ν_e^*, and we do not estimate κ from ϵ.

First-Order Solution. The first-order solution is

$$U^* = ly^+ + A - (a_1+2)y, \tag{60}$$

$$\nu_e^* = y(1+a_1 y), \tag{61}$$

$$k^* = 1 + b_1 y, \tag{62}$$

$$\epsilon^* = (1+c_1 y)/y. \tag{63}$$

The importance of the first term in (60) is very high, compared with that of the counterparts in ν_e^* and k^*. This fact comes from that in the limit $\nu \to 0$ ($R_e \to \infty$) with y^+ fixed, y tends to zero and that part of U^*, which depends on y^+, becomes dominant. This is the reason why the logarithmic velocity profile has a wide range of applicability. The influence of the third term of (60) can be detected only for large y^+. This term makes the observed velocity for $y^+ \gtrsim 500$ larger than the logarithmic velocity profile (see Fig. 2) since $a_1 + 2 < 0$ (see (70)).

Using (46*b*), C_{k1} in (37) is calculated as

$$C_{k1} = (2 + 4/b_1)/\alpha, \tag{64}$$

which can be estimated with the aid of b_1 estimated from (62). At this time, α ($=\kappa^2/\sqrt{C_\nu}$) can be estimated from the zeroth-order solution. Using (46*a*), γ and β are calculated as

$$\gamma = 1 - \frac{2\alpha C_{k1}}{6 + a_1(2 - \alpha C_{k1})}, \tag{65}$$

$$\alpha\beta + 1 - \gamma = 0, \text{ or } \beta = (\gamma - 1)/\alpha. \tag{66}$$

The relation (66) is well known [10] and can be obtained by substituting the zeroth-order solution into the ϵ equation (38). If the constant $C_{\epsilon 3}$ ($\fallingdotseq 2$) is determined from the data about the decay of grid turbulence, all of the five constants C_ν, C_{k1}, $C_{\epsilon 1}$, $C_{\epsilon 2}$, and $C_{\epsilon 3}$ are determined. Hence, it is concluded that the asymptotic solution of the standard k-ϵ model can be constructed up to the first order without any mathematical difficulty.

From the data of Laufer [15] of $R_e = 2 \times 12300$ at $y^+ = 78$ and 130, k is estimated as

$$k/u_\tau^2 = 3.2083 - 8.4861y. \tag{67}$$

Since $C_{\nu\max} = 0.10728$ and $C_{\nu\min} = 0.06580$, b_1 is estimated as

$$-2.7795 \leqq b_1 \leqq -2.1768. \tag{68}$$

From the data of Hussain and Reynolds [14] (see Fig. 5) at $y = 0.075$ and 0.1, ν_e is approximated as

$$\nu_e/R_e u_\tau y = 0.4725 - 1.660y \quad (R_e = 2 \times 13800), \tag{69a}$$

$$\nu_e/R_e u_\tau y = 0.4698 - 1.572y \quad (R_e = 2 \times 23200), \tag{69b}$$

$$\nu_e/R_e u_\tau y = 0.4834 - 1.700y \quad (R_e = 2 \times 32300). \tag{69c}$$

Using $\kappa_{\max} = 0.4151$ and $\kappa_{\min} = 0.4025$, α_1 is estimated as

$$-4.2236 \leqq a_1 \leqq -3.7870. \tag{70}$$

From (64) and (68), C_{k1} is estimated as

$$0.5745 \leqq C_{k1} \leqq 0.7802, \tag{71}$$

where 0.6717 and 0.4946 have been adopted as the maximum and minimum values of α in (41), respectively. In estimating γ of (65), we need some caution. When we use (70) and (71) to estimate (65), we encounter vanishing of the denominator in (65). In order to avoid it, we adopt the mean value of (68) or -2.4782. Consequently, αC_{k1} is estimated as 0.3859 from (64), and we have

$$-6.8173 \leqq a_1(2 - \alpha C_{k1}) \leqq -6.1126. \tag{72}$$

Combining (65) and (66) with (72), we obtain

$$1.9443 \leqq \gamma \leqq 7.8544, \quad 1.4059 \leqq \beta \leqq 13.8585. \tag{73}$$

As a result, the choice of $C_{\epsilon 3} = 2$ leads to

$$0.3579 \leqq C_{\epsilon 1} \leqq 14.2549, \quad 0.2546 \leqq C_{\epsilon 2} \leqq 1.0286. \tag{74a, b}$$

On comparing (58), (71), (74), and $C_{\epsilon 3}(=2)$ with (12), we can see that the usually adopted constants (12) are really not so far from the values estimated above.

Let us study the channel flow at $R_e = 2 \times 13800$ and $u_\tau = 0.0464$ using both the present asymptotic solution and the numerical integration of (36)-(39) based on the author's numerical method [19]. In the latter numerical integration, the boundary conditions are given at $y = 0.05$ and $y = 0.95$ ($y^+ \fallingdotseq 64$), and the constants (12) are used, and uniform mesh size 1/100 is taken. Figures 6*a-d* show the numerical and asymptotic solutions (60)-(63). The numerically calculated mean velocity and turbulent energy show good agreement with experimental results. The numerically calculated eddy viscosity, however, does not coincide with the experimental results near the central region. This point has not so far been pointed out clearly. The reason is that the eddy viscosity has been considered as a secondary quantity of turbulence since the Reynolds stress R_{12} is determined almost by the imposed pressure gradient. The asymptotic solution shows good agreement with the numerical solution for $y \leqq 0.1$.

The reasons why the range of applicability of our asymptotic solution is narrow compared with the numerical solution can be stated as follows. The terms which exert the largest influence in the k and ϵ equations are different in the order of y near the wall.

Second-Order Solution. The second-order solution is similarly obtained as

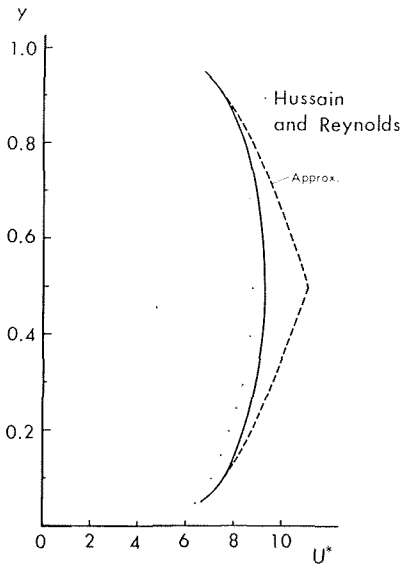

Fig. 6(*a*) Distribution of mean velocity

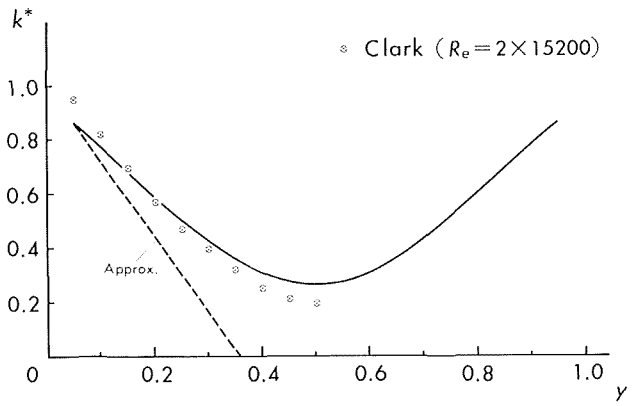

Fig. 6(*b*) Distribution of turbulent energy

$$U^* = \ln y^+ + A - (a_1+2)y + \frac{1}{2}\{-a_2 + a_1(a_1+2)\}y^2, \quad (75)$$

$$\nu_e^* = y(1 + a_1 y + a_2 y^2), \quad (76)$$

$$k^* = 1 + b_1 y + b_2 y^2, \quad (77)$$

$$\epsilon^* = (1 + c_1 y + c_2 y^2)/y. \quad (78)$$

This solution has

$$\alpha\beta + 1 - \gamma \quad (79)$$

in the denominators of a_2 and c_2 of (47). The first-order solution, however, requires that (79) should vanish, as can be seen from (66). Similarly, the third-order solution (42)-(45) has divergent terms. That is, the standard k-ϵ model is mathematically ill-posed if an asymptotic solution with the logarithmic velocity law as the leading terms is sought for or an asymptotic solution is sought for in the limit of $\nu \to 0$ with y^+ fixed (its lowest-order solution has been used as a substitute boundary condition of the k-ϵ model not imposing the noslip velocity condition).

Then, how has this difficulty been avoided in the standard k-ϵ model? In the model, we do not impose complete vanishing of (79) to use

$$\alpha\beta + 1 - \gamma \doteqdot 0 \quad (80)$$

and estimate $C_{\epsilon 2}$ [5]. As a result, such a solution does not satisfy the logarithmic velocity law in a strict sense.

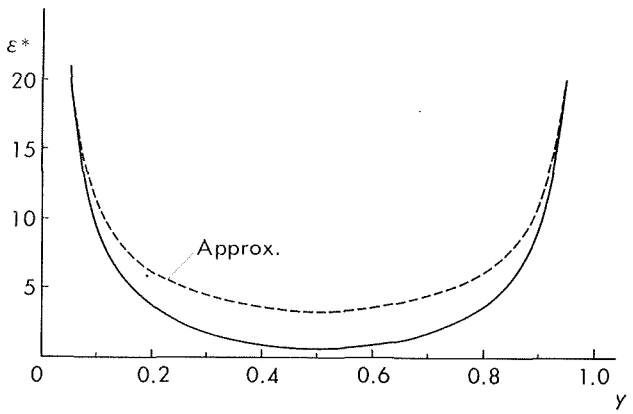

Fig. 6(*c*) Distribution of dissipation rate of turbulent energy

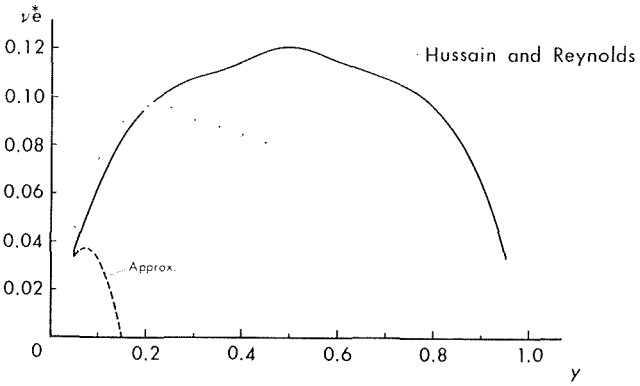

Fig. 6(*d*) Distribution of eddy viscosity

Fig. 6 Numerical and asymptotic solution of the standard k-ϵ model —— Numerical solution, ···· Asymptotic solution

Conclusion

In this paper, an asymptotic solution of the standard k-ϵ model with the logarithmic velocity law as leading terms is found, and a method to estimate the model constants is given. The most important property of the standard k-ϵ model is the dominance of energy production and dissipation effects. This property is supplemented by the addition of the diffusion effect from k and ϵ itself in the k and ϵ equations, respectively.

The present asymptotic solution, whose leading terms are called the wall law, is shown to have divergent terms. This mathematical ill-posedness of the standard k-ϵ model is usually avoided through the delicate adjustment of model constants. This point is closely related to the stiffness of the model constants in the k-ϵ model.

In order to overcome this deficiency of the standard k-ϵ model, a revised k-ϵ model, that is mathematically well-posed, will be reported in a future paper.

Acknowledgments

The author is grateful to Professors Shuzo Murakami, Toshio Kobayashi, Akira Yoshizawa, and the other members of NST (Numerical Simulation for Turbulence) at IIS (Institute of Industrial Science) for their kind support and valuable discussion.

References

1 Kim, J., Moin, P., and Moser, R., "Turbulent Statistics in Fully Developed Channel Flow at Low Reynolds Number," *Journal of Fluid Mechanics*, Vol. 177, 1987, pp. 133-166.

2 Moin, P., and Kim, J., "Numerical Investigation of Turbulent Channel Flow," *Journal of Fluid Mechanics*, Vol. 118, 1982, pp. 341-377.

3 Horiuti, K., "Comparison of Conservative and Rotational Forms in Large Eddy Simulation of Turbulent Channel Flow," *Journal of Computational Physics*, Vol. 71, 1987, pp. 343-370.

4 Hanjalic, K., and Launder, B. E., "A Reynolds Stress Model of Turbulence and Its Application to Thin Shear Flows," *Journal of Fluid Mechanics*, Vol. 52, 1972, pp. 609-638.

5 Launder, B. E. and Spalding, D. B., *Lectures in Mathematical Models of Turbulence*, Academic Press, London and New York, 1972.

6 Bradshaw, P., Cebeci, T., and Whitelaw, J. H., *Engineering Calculation Methods for Turbulent Flow*, Academic Press, 1981.

7 Jones, W. P., and Launder, B. E., "The Prediction of Laminarization with a Two-Equation Model of Turbulence," *International Journal of Heat and Mass Transfer*, Vol. 15, 1972, pp. 301-314.

8 Rodi, W., "Turbulence Models and their Application in Hydraulics—A State of Review," International Association of Hydraulic Research, Monograph, Delft, the Netherland, 1980.

9 Lam, C. K. G., and Bremhorst, K., "A Modified Form of k-ϵ Model for Predicting Wall Turbulence," ASME JOURNAL OF FLUIDS ENGINEERING, Vol. 103,1981, pp. 456-460.

10 Patel, V. C., Rodi, W., and Scheuerer, G., "Turbulence Models for Near-Wall and Low Reynolds Number Flows, A Review," *AIAA Journal*, Vol. 23, 1985, pp. 1308-1319.

11 Yoshizawa, A., "Statistical Analysis of the Deviation of the Reynolds Stress from Its Eddy-Viscosity Representation," *The Physics of Fluids*, Vol. 27, 1984, pp. 1377-1387.

12 Nisizima, S., and Yoshizawa, A., "Turbulent Channel and Couette Flows Using Anisotropic k-ϵ Model," *AIAA Journal*, Vol. 25, 1987, pp. 414-420.

13 Hinze, J. O., *Turbulence*, McGraw-Hill, New York, 1975.

14 Hussain, A. K. M. F., and Reynolds, W. C., "Measurement in Fully Developed Turbulent Channel Flow," ASME JOURNAL OF FLUIDS ENGINEERING, Vol. 97, 1975, pp. 568-580.

15 Laufer, J., "Investigation of Turbulent Flow in a Two-Dimensional Channel," NACA Rept. 1053, 1951.

16 Clark, J. A., "A Study of Incompressible Turbulent Boundary Layers in Channel Flow," ASME *Journal of Basic Engineering*, Vol. 90, 1968, pp. 455-468.

17 Kreplin, H., and Eckelmann, M., "Behavior of the Three Fluctuating Velocity Components in the Wall Region of Turbulent Channel Flow," *The Physics of Fluids*, Vol. 22, 1979, pp. 1233-1239.

18 Rodi, W., "A Note on the Empirical Constant in the Kolmogorov-Prandtl Eddy-Viscosity Expression," ASME JOURNAL OF FLUIDS ENGINEERING, Vol. 90, 1975, pp. 386-389.

19 Takemitsu, N., "On a Finite-Difference Approximation for the Steady-State Navier-Stokes Equations," *Journal of Computational Physics*, Vol. 36, No. 2, 1980, pp. 236-248.

T. C. Vu
Dominion Engineering Works, GE Canada
Lachine, Québec, Canada H8S 2S8

W. Shyy
University of Florida,
Department of Aerospace Engineering,
Mechanics and Engineering Science,
Gainesville, FL 32611

Navier-Stokes Flow Analysis for Hydraulic Turbine Draft Tubes

Three-dimensional turbulent viscous flow analyses for hydraulic turbine elbow draft tubes are performed by solving Reynolds averaged Navier-Stokes equations closed with a two-equation turbulence model. The predicted pressure recovery factor and flow behavior in the draft tube with a wide range of swirling flows at the inlet agree well with experimental data. During the validation of the Navier-Stokes flow analysis, particular attention was paid to the effect of grid size on the accuracy of the numerical result and the importance of accurately specifying the inlet flow condition.

1 Introduction

The role of the draft tube is to decelerate the velocity of the water leaving the turbine runner, thereby converting the excess kinetic energy of the outlet stream into a rise in static pressure.

For a number of reasons, the proper design of an elbow draft tube is a difficult task. The geometry of a typical elbow draft tube is illustrated in Fig. 1(*a*). It consists essentially of a short conical diffuser followed by a 90 deg elbow of varying cross section and then a rectangular diffuser section. The shape of the cross section changes from being circular at the inlet end through elliptical within the elbow to rectangular at the exit. At the same time, the cross-sectional area of the draft tube mostly increases from inlet to outlet.

Recently, intensive efforts have been devoted to develop a suitable numerical algorithm for computing the general Navier-Stokes flows bounded by complex geometries [1,2,4]. The algorithm has been applied to solve two and three-dimensional flow problems in different hydraulic turbine components [3,4,7], and has proven to be an excellent analytical tool for the hydraulic designer when they are well validated.

The most important parameter characterizing the draft tube performance is the pressure recovery factor, or pressure-rise coefficient [3,8], which is defined as:

$$C_{pr} = \frac{P_2 - P_1}{\textit{Massflow weighted averaged kinetic energy at inlet}}$$

where P_1 is the massflow-weighted averaged static pressure at the inlet and P_2 is the massflow-weighted averaged static pressure at the outlet.

The strength of the swirling flow at the draft tube inlet can be quantified as the swirl intensity, which is defined as the ratio of the angular momentum flux to the axial momentum flux. In the present paper, we use this definition of swirl intensity to characterize the swirling inlet flow. This definition is different from the solid-body swirl ratio which is defined as the ratio of the maximum tangential velocity to the bulk axial velocity at the inlet.

Experimental work has also been carried out to study the flow behavior in hydraulic turbine draft tubes in order to validate the numerical algorithm. Both wind tunnel and water test stand were used for the investigation. A series of tests with the wind tunnel was done to study the efficiency and flow behavior of a low head elbow draft tube with a wide range of swirling flow conditions at the inlet. Measured velocity vector field and evolution of total pressure loss, of static and dynamic pressures along the main flow direction are compared with computer prediction. Also, in a water model test stand, the pressure recovery factor of a medium head elbow draft tube operating with Francis runners was selected for the study.

During the validation of the Navier-Stokes flow analysis, particular attention was paid to the effect of grid size on the accuracy of the numerical result and the importance of accurately specifying the inlet flow condition. Also, the effect of the Reynolds number on the draft tube efficiency was investigated.

2 Numerical Analysis

2.1 Formulation and Numerical Algorithm. The three-dimensional draft tube flow analysis is based on the full Reynolds-averaged Navier-Stokes equations. The $k - \epsilon$ two equation turbulence model [6] is adopted here as closure form. The numerical formulation comprises a linearized, semi-implicit, conservative finite volume algorithm implemented in a general curvilinear coordinate system. The detail of the governing equations, curvilinear coordinate system, algorithm of treating pressure-velocity coupling, and solution method can be found in [1,2,4] and will not be repeated here.

As to the finite difference operators, the standard 2^{nd}-order central difference approximation is applied to all the derivatives except the convection terms. For the convection terms, both the commonly used hybrid scheme, i.e., combination of the 1^{st}-order upwind and 2^{nd}-order central differencing scheme, and the 2^{nd}-order upwind scheme are used for discretisation [5]. The system of finite difference equations are solved using the successive line overrelaxation method. Here a combined use of the Cartesian velocity components and contravariant velocity components is devised. In the momentum equation, the Cartesian components are treated as the primary variables,

Contributed by the Fluids Engineering Division for publication in the JOURNAL OF FLUIDS ENGINEERING. Manuscript received by the Fluids Engineering Division June 17, 1988.

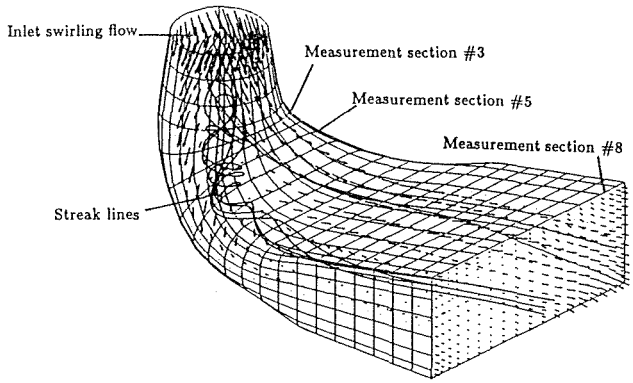

Fig. 1(*a*) Three-dimensional view of the flow behavior in a low head elbow draft tube

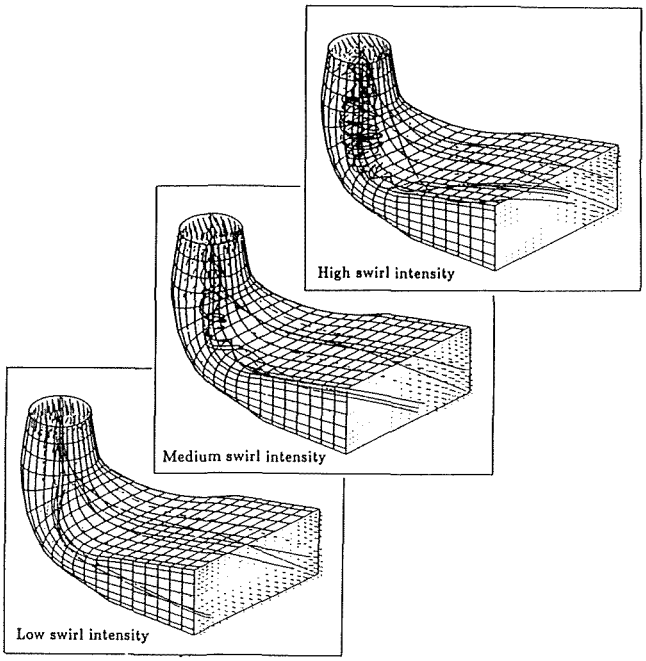

Fig. 1(*b*) Three-dimensional view of the flow behavior with three different inlet swirl conditions

while in the continuity equation the contravariant velocity components are first updated directly to satisfy the continuity equation. Then the so-called D'Yakonov iteration [2] is used to yield the corresponding values between the contravariant and Cartesian components in an efficient manner. The body-fitted grid system is generated using the combined elliptic generation method and local interpolation procedures [9].

2.2 Boundary Conditions. Figure 1(*a*) illustrates the flow domain of an elbow draft tube. No-slip conditions are applied to all the nodes at solid walls. At the nodal position next to the solid wall, the so-called wall function treatment [6] is used. At the inlet of the flow domain, the velocity profiles are imposed by the turbine exit flow. At the exit, a zero 1^{st}-order derivative along the streamwise direction is adopted for all the dependent variables, except for the static pressure which does not require numerical boundary conditions due to the nature of the staggered grid system. As demonstrated in [10], this practice works very well for the general flow computation.

3 Experimental Investigation

Experimental work has been carried out to study the flow behavior in hydraulic turbine draft tubes in order to validate the numerical algorithm. Detail flow behavior investigation was performed in the wind tunnel. Also, realistic inlet flow profiles from Francis runner model in water test stand were used for the validation.

3.1 Wind Tunnel Test Results. A low head elbow draft tube (see Fig. 1(*a*) was selected for the experimental investigation in the wind tunnel. The inlet swirling flow was generated by means of an axial distributor which is an annular cascade of 18 NACA0012 profile blades. The swirl intensity at the inlet varies from 0 to 44.6 percent when the blades are oriented from 0 to 30 deg. Typical inlet flow profile generated by the axial distributor is shown at the top of Fig. 5(*a*). The axial component, represented by solid line, is decelerated at the center of the inlet region due to the presence of the hub. The tangential component, shown in dotted line, is a combination of a solid body swirl and a free vortex flow. As the flow at the draft tube inlet is assumed to be axisymmetrical, only one pitot traverse along the diameter is required to obtain the inlet flow condition. For each diametrical traverse, 13 points of reading were taken. The distance from the wall to the nearest reading point is 0.5 in. The diameter at the inlet section is 16.3 ins.

The first series of test was to determine the inlet swirling flow which provides the optimal pressure recovery of the draft tube. The second series of tests with the wind tunnel is to investigate the flow behavior of the same elbow draft tube with and without swirling flow at the inlet. First, the draft tube was tested with the optimal swirling flow by setting the distributor blade orientation at 15 deg. Then, the axial distributor was removed in order to obtain a uniform flow condition at the draft tube inlet. From the inlet to the outlet of the draft tube, 8 measurement cross sections were selected for the flow behavior investigation. For each cross section, as many as 6 traverses, spaced side wall to side wall, were made. For each pitot traverse, 7 readings were taken. Exception was made for the first two sections, located in the cone region where the flow is assumed to be axisymmetrical, only one diametrical traverse was required to obtain the flow characteristics. During the flow investigation with inlet uniform flow, difficulties were encountered with the pressure reading due to large flow separation occurring inside the draft tube. Also, the assumed axisymmetrical flow condition at the inlet was not always respected, especially for low swirl and uniform inlet flow. In such cases, the average profile is obtained between the two halves of the diametrical pitot measurement.

3.2 Water Model Test Stand Result. An elbow draft tube of medium head was selected for the flow investigation in the water model test stand. The inlet flow profile, obtained from various Francis runners at different operating conditions, varies from a solid body swirl to a free vortex. The pressure recovery of the draft tube was measured for each inlet condition and compared with the computer prediction.

4 Validation With Experimental Data

The aim of the present study is to verify if the Navier-Stokes flow analysis could predict correctely the pressure recovery and the flow behavior in an elbow draft tube for a wide range of inlet flow conditions. Also, a parametric study is carried out in order to evaluate the influence of some important parameters on the accuracy of the numerical solution.

Hybrid and second order upwind schemes were used during the validation process. In general, both numerical schemes predict similar flow behaviors. The hybrid scheme always predicts a higher pressure recovery factor by about 3 percent. But for all the cases, the second upwind scheme predicts better the evolution of the static and dynamic pressures along the main flow direction, as shown in Figs. 5(*a*), 5(*b*), 8(*a*), and 8(*b*). The second upwind scheme gives us the most satisfactory re-

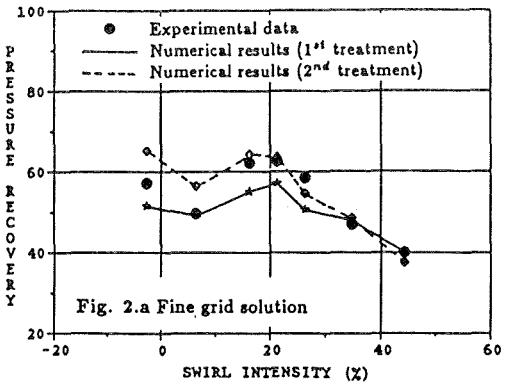

Fig. 2(*a*)

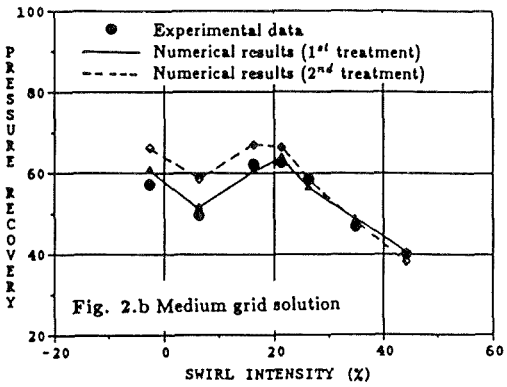

Fig. 2(*b*)

Fig. 2 Pressure recovery factor as function of the swirl intensity. Comparison between experimental data and computer prediction

sults and except otherwise stated, only its results are presented here.

The inlet turbulence level is specified as 5 percent of the kinetic energy at the inlet for all the cases. The grid size affects the accuracy of the solution and also the computation time. In order to assess the grid dependancy of numerical solution, flow analyses were performed with four different grid sizes. In general, for a coarse grid system ($7 \times 11 \times 31$ nodes) only about 20 minutes of CPU is required for obtaining a converged steady-state flow solution. The medium grid system ($11 \times 15 \times 45$ nodes) and the fine grid system ($15 \times 21 \times 61$ nodes) required respectively about 3 and 15 hours of CPU whereas the very fine grid ($21 \times 29 \times 81$ nodes) took about 40 hours of CPU for one flow solution. All the calculations were made with a VAX 8600 computer.

On each node at the inlet of the grid system, the three velocity components are specified by linear interpolation from pitot traverse measurements along the inlet diameter. Near the solid wall, all the grid velocity components are also linearly interpolated between zero (value for the wall) and the first value measured from pitot traverse.

The Reynolds number, which is based on the draft tube inlet diameter and the average axial velocity at the inlet, is considered in the flow analyses. For flow in water model test stand, the Reynolds number is about 10^6 whereas the Reynolds number is about 0.5×10^6 for all tests with the wind tunnel. With an inlet optimal solid body swirl and by varying the Reynolds number from model test to prototype operating conditions (from 10^6 to $2. \times 10^7$), the draft tube pressure recovery factor is improved by about 2.5 percent. The same trend is observed when we step up the turbine efficiency from model test to prototype.

4.1 Numerical Prediction of the Pressure Recovery Factor. The pressure recovery of the low head elbow draft tube tested

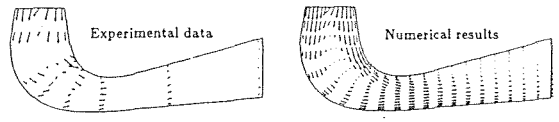

Fig. 3(*a*) Elevation view · velocity field near draft tube center

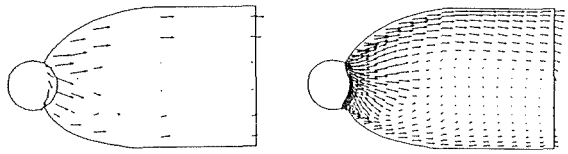

Fig. 3(*b*) Plan view · velocity field near the top of the draft tube

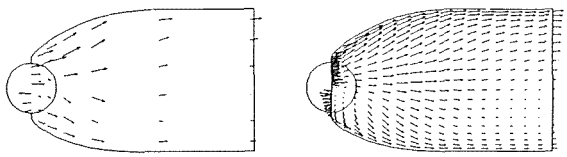

Fig. 3(*c*) Plan view · velocity field at the mid-height of the draft tube

Fig. 3 Flow behavior with inlet swirling flow

with the wind tunnel is shown in Fig. 2. For this particular case, the pressure recovery of the draft tube is decreased with the presence of a weak inlet swirling flow (distributor blades oriented at 5 deg), but quickly the draft tube finds its best efficiency at 22 percent swirl intensity. Beyond this point, the pressure recovery decreases with higher swirl intensities.

The flow analyses were performed with two different treatments for the velocity assigned at the solid wall. As the first treatment, the velocity components prescribed for the grid system at the inlet are linearly interpolated from pitot traverse measurements as explained earlier. The second treatment consists of calculating the velocity at the wall by linear extrapolation, instead of simply setting these values equal to zero. Then this set of data was used to specify the grid velocity components by interpolation. This manner of extrapolation for velocity values at solid wall improves very slightly the quality of the boundary layer, but it is enough to greatly influence the numerical result for inlet condition with low swirl intensity.

In Fig. 2(*a*), results from both treatments with the fine grid are shown. The solid line represents the computer prediction obtained with the first treatment whereas the dashed line represents the results obtained with the second treatment. Both curves agree very well with the experimental data, especially for high swirling flows where the centrifugal force is preponderant, therefore the uncertainty on the boundary layer is much less important. For low swirl intensities, the experimental data are bounded by the two curves indicating that more accurate experimental data near the wall is required for more precise prediction.

The comparison is also made with the medium grid system. The same behavior is observed, but the results obtained from the two treatments are less different. Excellent correlation with experimental data is also obtained with the medium grid system. Comparing the numerical results obtained from two different grid sizes, the pressure recovery factor obtained with coarser grid is consistently higher than with finer grid by about 3 percent due to larger numerical viscosity.

4.2 Numerical Prediction of the Flow Behavior With Swirling Flow at Inlet. The flow behavior in the elbow draft tube, with an optimal inlet swirling flow, was investigated in detail with pitot traverses taken from several cross sections (indicated in Fig. 1(*a*)). The experimental data are compared with numerical results obtained with four different grid sizes: coarse, medium, fine and very fine grid.

Fig. 4(*a*) Measurement section no. 3

Fig. 4(*b*) Measurement section no. 5

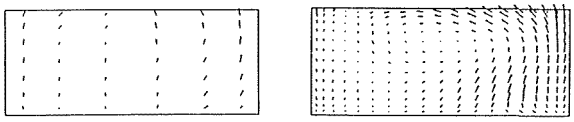

Fig. 4(*c*) Measurement section no. 8

Fig. 4 Flow behavior with inlet swirling flow - secondary flow (flow coming towards the reader)

The display of the velocity vectors in the main flow direction is shown in Fig. 3. The numerical result obtained with the fine grid system is presented. Observation at the velocity vector distribution at different elevation and plan views indicates clearly that a large recirculation zone occurs at the middle of the elbow section and further downstream, flow separation appears at the center and near the top of the draft tube. Also toward the outlet of the draft tube, the flow is somewhat shifted to one side wall. This tendency is more accentuated with a stronger inlet swirling flow. Excellent agreement is obtained between the measurement and the solution results from fine and very fine grid systems. The solution from medium grid predicted well the recirculation zone but not the flow separation near the draft tube outlet. The solution from coarse grid did not show any recirculation zone in the main flow direction.

Figure 4 shows the comparison of the secondary flow at different cross sections of the elbow draft tube. At the measurement section no. 3 which is located at the beginning of the elbow, both numerical result and experimental data show a strong swirl at the middle of the section, slightly to the left of the section center. This swirl is transported from the inlet swirl condition. At the measurement section no. 5, located near the end of the elbow, three distinctly swirling vortical flows are observed from the numerical result. The double swirls of opposite direction generated by the bend curvature are found at the two top corners. The third swirl, found at the left of the section center, is the existing swirl transported from the inlet. Observation from the experimental data shows clearly the main swirl at the left of the section center and only one swirl generated at the top left corner. The secondary flow at the draft tube outlet, which is represented by the measurement section no. 8, is much weaker (velocity vector of this section was magnified by three). The experimental data indicate that all the swirls are destroyed completely whereas a trace of the main swirl from the inlet is still preserved by the numerical simulation. This discrepancy is probably due to both the experimental uncertainty of the pitot measurement for recirculation flow and the shortcoming of the $k - \epsilon$ turbulence model.

A three-dimensional view of the simulated flow is represented in Fig. 1(*b*) (medium swirl intensity). The velocity vectors are shown at the inlet and outlet sections. All the solid lines starting from the center region of the inlet section and finishing at the outlet represent the streaklines of the mean velocity field. At the beginning of the elbow region, the randomly oscillating spiral streaklines indicate a recirculating zone. Also the streaklines are shifted to one side of the draft tube at the elbow region then shifted back to the opposite side near the outlet region. For higher swirl intensity, as shown in Fig.

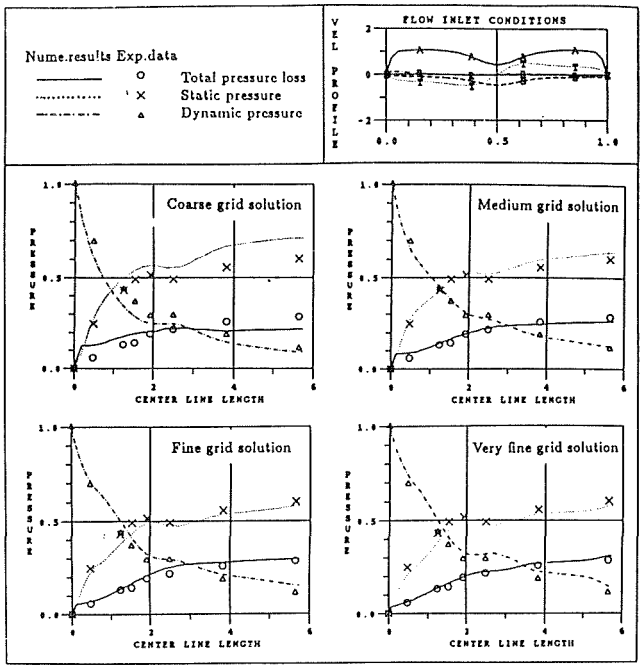

Fig. 5(*a*) Flow behavior with inlet swirling flow. Evolution of dynamic and static pressures and of total pressure loss - 2nd order scheme.

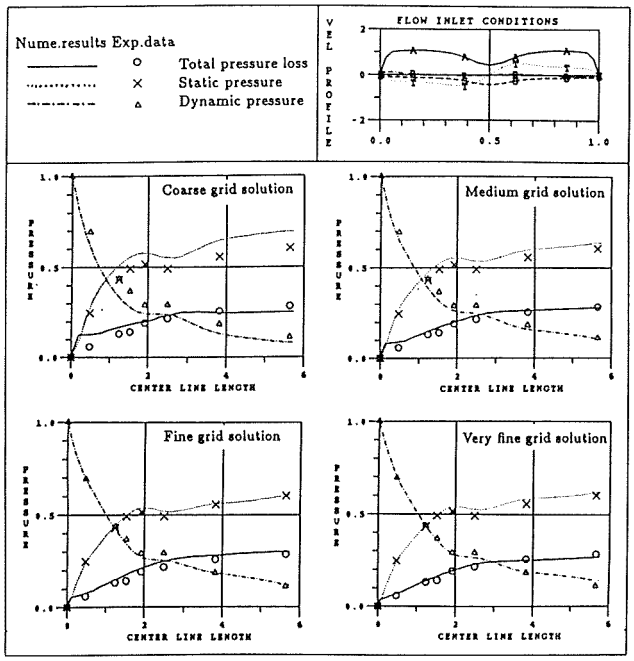

Fig. 5(*b*) Flow behavior with inlet swirling flow. Evolution of dynamic and static pressures and of total pressure loss - hybrid scheme.

1(*b*), the recirculation zone appears more important and the flow is shifted more to one side wall at the draft tube outlet. For low swirl intensity, the flow is shifted evenly to both side walls of the draft tube, and the mild spiral form of the streaklines indicates the existence of the double swirls generated by the bend curvature. In this case, the flow recirculation zone is not observed.

In order to study the evolution of the static and dynamic pressures along the main flow direction, massflow-weighted average values of these properties at each cross section are calculated. The numerical results are then compared with the experimental data in Fig. 5(*a*) and 5(*b*). At the ordinate, the pressures are normalized by the inlet dynamic pressure. At the abscissa the center line length is normalized by the draft tube

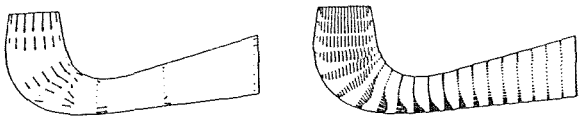

Fig. 6(*a*) Elevation view - velocity field near draft tube center

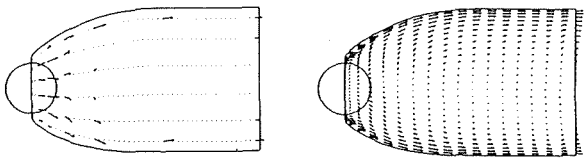

Fig. 6(*b*) Plan view - velocity field at the mid-height of the draft tube

Fig. 6 Flow behavior with inlet uniform flow

Fig. 7(*a*) Measurement section no. 3

Fig. 7(*b*) Measurement section no. 5

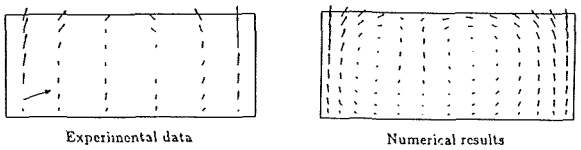

Fig. 7(*c*) Measurement section no. 8

Fig. 7 Flow behavior with inlet uniform flow - secondary flow (flow coming toward the reader)

inlet diameter. Results from the very fine and fine grid systems predict very well the variation of all the pressures, specially at the accelerating region at the end of the elbow section (Fig. 5(*a*) for the 2^{nd} order scheme). The result from the medium grid is acceptable but not for the coarse grid.

4.3 Numerical Prediction of the Flow Behavior With Uniform Flow at Inlet. The flow behavior in the draft tube was also investigated with a uniform flow (without swirl) at the inlet. As the previous case, the experimental data are compared with computer results obtained from four different grid sizes.

The display of the velocity vectors in the main flow direction is shown in Fig. 6. In this case, the numerical result obtained with the very fine grid system is presented. Contrary to the previous case, observation from experimental data and numerical results indicates that no recirculation is occurring at the elbow region whereas the flow separation appears very early from the elbow region and carried down to the draft tube outlet. All the solutions obtained from the four grid sizes predict the same flow behavior, but the experimental data shows a stronger flow separation zone than the prediction.

Figure 7 shows the comparison of the secondary flow at different cross sections of the elbow draft tube. At the measurement section no. 3 which is located at the beginning of the elbow, the numerical result shows that the double swirls generated by the bend curvature are already well defined whereas the experimental data do not show clearly the double swirls. At the measurement section no. 5, located near the end of the elbow, the double swirls are observed clearly at the two top corners from both experimental and numerical data. At the measurement cross section no. 8 which is at the outlet of the

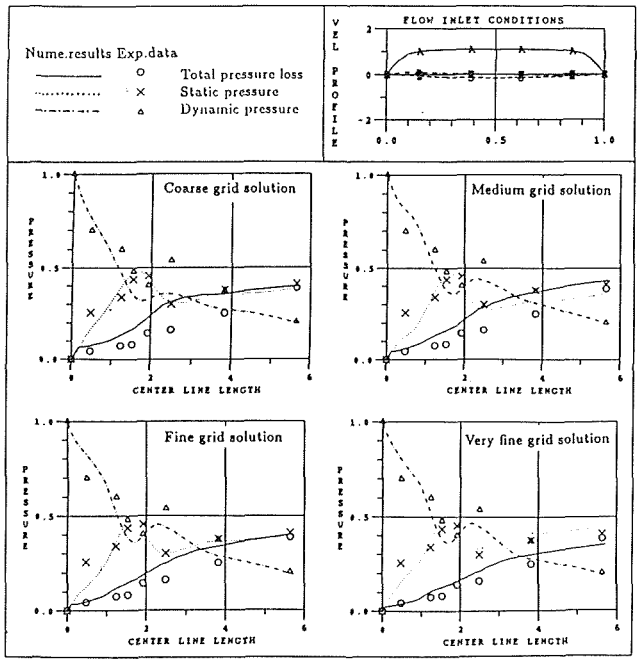

Fig. 8(*a*) Flow behavior with inlet uniform flow. Evolution of dynamic and static pressures and of total pressure loss - 2^{nd} order scheme.

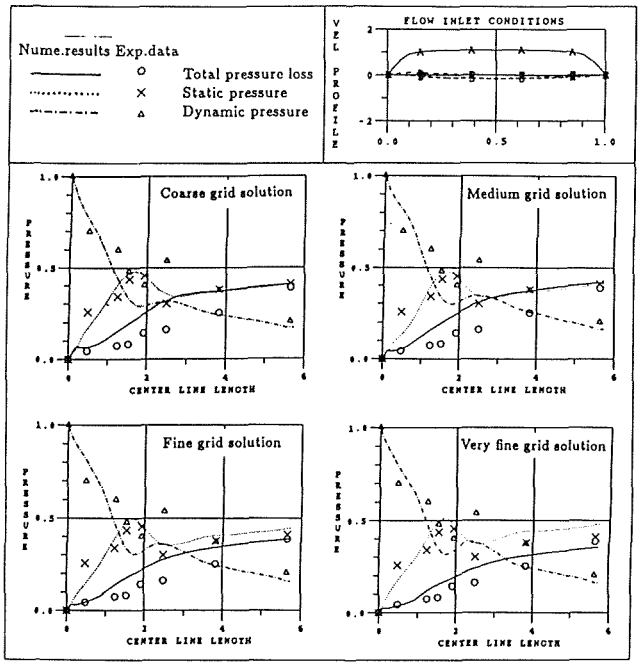

Fig. 8(*b*) Flow behavior with inlet uniform flow. Evolution of dynamic and static pressures and of total pressure loss - hybrid scheme.

draft tube, the secondary flow is much weaker (velocity vector of this section was magnified by three). But as in the previous case, the experimental data shows that all the swirling flows disappear completely at the outlet section whereas the numerical solution still preserve the trace of the double swirls generated from the elbow region. It is interesting to mention that all the solutions from four different grid sizes predict the same secondary flow behavior.

As in the previous case, the evolution in the main flow direction of the total pressure loss, the static and dynamic pressures obtained from the numerical solution is compared against the experimental data in Figs. 8(*a*) and 8(*b*). The variation of the pressures is more evident near the accelerating region. This tendency is well predicted by the 2^{nd} order upwind

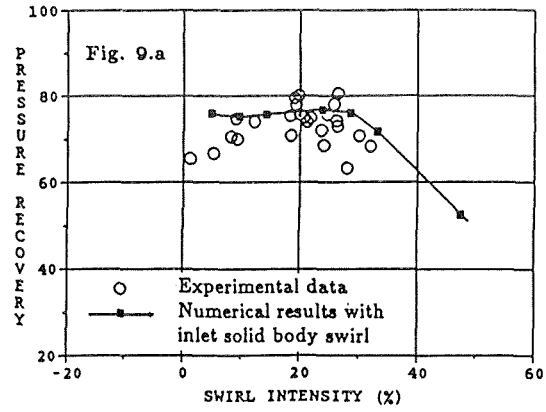

Fig. 9(*a*)

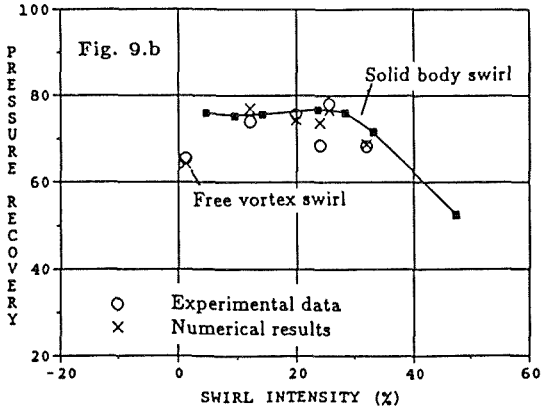

Fig. 9(*b*)

Fig. 9 Pressure recovery factor as function of inlet solid-body swirl. Comparison between experimental data and computer prediction

scheme solution (Fig. 8(*a*) whereas the hybrid scheme solution is less sensitive to the dynamic pressure variation. The numerical results obtained from fine and very fine grid systems agree quite well with measurements except for the dynamic pressure. But as we explained earlier, large flow separations taking place in the draft tube made the pitot measurement more difficult than usual.

4.4 Validation With Water Model Test Result. Figure 9(*a*) shows the variation of the pressure recovery factor of a medium head elbow draft tube functioning with various Francis runners at different operating conditions. Observation at the flow conditions at the draft tube inlet shows that the flow profile obtained has all the possible combinations, varied from a solid body swirl to a free vortex. The draft tube performs better with inlet swirling condition close to solid body swirl profile, shown by experimental data near the upper bound. As the inlet profile deviates from the solid body swirl, the draft tube efficiency decreases. This is the reason why there is a large variation of the draft tube pressure recovery factor for the same swirl intensity. But, if we consider only the upper bound of these experimental points, the draft tube efficiency is found to be optimal at swirl intensity from 20 to 25 percent. Prediction of the draft tube pressure recovery factor with solid body swirl specified as inlet conditions obtains the same optimal swirl intensity which is about 22 percent. Also, some of the measured inlet flow profiles, generated by Francis runners, were selected for flow analyses. Comparison between computer prediction and experimental data is satisfactory as shown in Fig. 9(*b*). It is worth noting that the draft tube pressure recovery is very bad with an inlet free vortex flow compared to an inlet solid body swirl condition. The difference in the flow behavior with the two inlet swirl conditions is shown in Fig. 10.

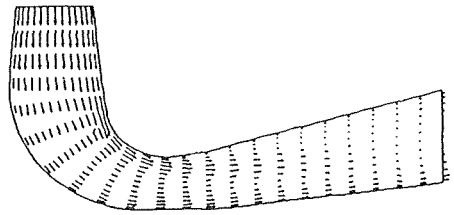

Fig. 10(*a*) Inlet solid body swirl condition

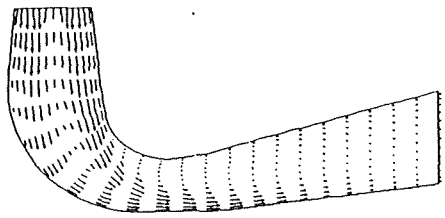

Fig. 10(*b*) Inlet free vortex flow condition

Fig. 10 Flow behavior with two different inlet swirling flows

5 Conclusions

This paper discusses the application of the three-dimensional Navier-Stokes flow analysis to hydraulic turbine draft tubes. The predicted pressure recovery factor and flow behavior in the draft tube with a wide range of swirling flows at the inlet agree well with experimental data. Particular attention was paid to the effect of grid size on the accuracy of the numerical result and the importance of accurately specifying the inlet flow condition. As future work, validation of the present Navier-Stokes flow computational algorithm will be applied to other hydraulic turbine components to continually improve the present design capacity.

Acknowledgments

The authors gratefully acknowledge the assistance and cooperation of Miss. L. Hénuset and the personnel of the Hydraulic Laboratory of Dominion Engineering Works during the experimental investigation. The softwares for grid generation and three-dimensional flow visualization were developed by the CASTOR project of Ecole Polytechnique de Montréal.

References

1 Shyy, W., Tong, S. S., and Correa, S. M., "Numerical Recirculating Flow Calculation Using a Body-fitted Coordinate System," *Numerical Heat Transfer*, Vol. 8, 1985, pp. 99-113.

2 Braaten, M. E., and Shyy, W., "A Study of Recirculating Flow Computation Using Body-fitted Coordinates: Consistency Aspects and Skewness," *Numerical Heat Transfer*, Vol. 9, 1985, pp. 559-574.

3 Shyy, W., and Vu, T. C., "A Numerical Study of Incompressible Navier-Stokes Flow Through Rectilinear and Radial Cascade of Turbine Blades," *Comp. Mech.*, Vol. 1, 1986, pp. 269-279.

4 Shyy, W., and Braaten, M. E., "Three-dimensional Analysis of the Flow in a Curved Hydraulic Turbine Draft Tube," *Int. J. Num. Meth. Fluids*, Vol. 6, 1986, pp. 861-882.

5 Shyy, W., "A Study of Finite Difference Approximations to Steady State, Convection Dominated Flow Problems," *J. Comp. Physics*, Vol. 57, 1985, pp. 415-438.

6 Launder, B. E., and Spalding, D. B., "The Numerical Calculation of Turbulence Flows," *Comp. Meth. Appl. Mech. Eng.*, Vol. 3, 1974, pp. 269-289.

7 Vu, T. C., and Shyy, W., "Navier-Stokes Computation of Radial Inflow Turbine Distributor," ASME JOURNAL OF FLUIDS ENGINEERING, Vol. 110, 1988, pp. 29-32.

8 Wilson, D. G., *The Design of High Efficiency Turbomachinery and Gas Turbines*, The MIT press, Cambridge, MA, 1984.

9 Ozell, B., and Camarero, R., "From Inlet to Outlet: The Complete Hydraulic Design of Turbomachines," *IAHR Symposium 1988*, Trondheim, Norway, 1988.

10 Shyy, W., "Effect of Open Boundary on Incompressible Navier-Stokes Flow Computation: Numerical Experiments," *Numerical Heat Transfer*, Vol. 12, 1987, pp. 157-178.

N. Hur

S. Thangam

Department of Mechanical Engineering,
Stevens Institute of Technology,
Hoboken, NJ 07030

C. G. Speziale[1]
Institute for Computer Applications in
Science and Engineering,
NASA Langley Research Center,
Hampton, VA 23665

Numerical Study of Turbulent Secondary Flows in Curved Ducts

The pressure driven, fully developed turbulent flow of an incompressible viscous fluid in curved ducts of square cross-section is studied numerically by making use of a finite volume method. A nonlinear K - l model is used to represent the turbulence. The results for both straight and curved ducts are presented. For the case of fully developed turbulent flow in straight ducts, the secondary flow is characterized by an eight-vortex structure for which the computed flowfield is shown to be in good agreement with available experimental data. The introduction of moderate curvature is shown to cause a substantial increase in the strength of the secondary flow and to change the secondary flow pattern to either a double-vortex or a four-vortex configuration.

1 Introduction

The study of viscous flow in curved or helically coiled ducts has been of fundamental interest to fluid dynamicists. There are numerous applications, which include the flow through turbomachinery blade passages, aircraft intakes, diffusers, and heat exchangers. Some of these problems of practical interest involve longitudinal curvature in the geometry for which the associated centrifugal forces can generate a secondary flow, which is normal to the main flow direction. Such secondary flows not only cause a reduction in the volumetric flow rate, but they can also cause the axial velocity field to be distorted with an outward shift of the contours of constant velocity. In addition, it is well known that the turbulent flow in straight noncircular ducts is characterized by the occurrence of secondary flows (see Gessner and Jones, 1965 and Nakayama et al., 1983). A clear understanding of the evolution and consequences of the turbulent secondary flows in curved and straight ducts is, therefore, quite important from the design standpoint. The present study is intended to address a facet of this issue, and involves the computational modeling of fully developed turbulent flow in square ducts with an emphasis on the prediction of secondary flows.

The results available in the literature on turbulent flow related to the work to be presented herein can be classified into two broad categories: fully developed flow in straight ducts and developing flow in curved ducts. The case of fully developed turbulent flow in straight ducts of square cross section was studied by Gessner and Jones (1965), Melling and Whitelaw (1976), and Nakayama et al. (1983), among others. Gessner and Jones (1965) conducted a series of experiments using hotwire anemometry to analyze fully developed turbulent flow in a square duct at a Reynolds number of 150,000. They also carried out computations by a finite difference method with an algebraic stress model to predict qualitatively the major feature of the flowfield, namely, the eight-vortex secondary flow structure. Melling and Whitelaw (1976) performed detailed experiments for fully developed flow using laser-doppler anemometry, and were the first to describe the axial velocity field and the Reynolds stress distribution in detail. Nakayama et al. (1983), on the other hand, analyzed the fully developed flowfield in ducts of rectangular and trapezoidal cross-sections computationally using a finite-difference method based on the algebraic turbulence stress model of Launder and Ying (1972). They were able to obtain a flowfield in good agreement with the available experimental measurements for a number of selected cross-sections. Improved calculations were conducted by Gessner and Po (1976) and DeMuren and Rodi (1984), using the nonlinear algebraic stress model of Rodi.

The computational analysis of developing turbulent flow in curved square ducts has been conducted by Pratap and Spalding (1975), Humphrey et al. (1981), and Choi et al. (1989). The work by Pratap and Spalding (1975) consisted of the solution of the three-dimensional time averaged Navier-Stokes equations incorporating a two-equation turbulence model based on a first order curvature ratio effect. Their study, which was conducted for a curvature ratio of 4.13 and a Reynolds number of 70,600, showed good agreement with the experimental results in the region near the entrance. However, in the fully developed region, they observed considerable discrepancies with the experimental results. Humphrey et al. (1981) also analyzed the developing turbulent flow in a square duct, but at a curvature ratio of 4.6 and a Reynolds number of 40,000. They solved the three-dimensional time-averaged Navier-Stokes equations with a two-equation turbulence model, by using a finite-difference method, and compared the results with their experimental findings obtained by laser-doppler anemometry. They concluded that in spite of the complex mean flow and Reynolds stress distributions, the centrifugal force and radial

[1]This research was supported by the National Aeronautics and Space Administration under NASA Contract No. NAS1-18605 and was carried out while the author was in residence at ICASE, NASA Langley Research Center, Hampton, VA 23665.

Contributed by the Fluids Engineering Division for publication in the JOURNAL OF FLUIDS ENGINEERING. Manuscript received by the Fluids Engineering Division April 20, 1989.

pressure gradient imbalance primarily controls the cross-stream flow. The calculated mean velocity results are therefore not strongly dependent on the turbulence model used. Choi et al. (1989) conducted computations for developing turbulent flow in a square-sectioned 180 deg bend.

The present study is motivated by the lack of a detailed analysis and prediction capability for turbulent secondary flows in curved ducts. Furthermore, several of the commonly used turbulence models (in particular, the standard $K - \epsilon$ model) are incapable of predicting the development of secondary flows in straight ducts of noncircular cross-section (see Speziale 1987). In the computational analysis to be presented, a finite-volume algorithm suitable for handling cylindrical geometry is implemented to analyze fully developed turbulent flows in straight as well as curved square ducts using a recently developed nonlinear $K - l$ turbulence model (Speziale, 1987) wherein K and l are specified empirically based on the experimental data of Laufer (1951). In the following sections the governing equations, the development of the turbulence model, and the numerical procedure will be described in detail followed by a discussion of the results and conclusions.

2 The Physical Problem and Method of Solution

The problem to be considered consists of the turbulent flow of an incompressible viscous fluid in a curved duct of square cross-section. Flow in helically coiled ducts may also be analyzed in the same manner so long as the ratio of torsion to curvature remains small. The physical configuration and the coordinate system used are shown in Fig. 1.

The flow is generated by a constant azimuthal pressure gradient, $G = -\frac{1}{r}\frac{\partial \overline{P}}{\partial \theta}$ (see Fig. 1). It is assumed that the flow is fully developed so that all flow variables are independent of the azimuthal coordinate θ. The fully developed mean velocity vector is three-dimensional, i.e., the mean (time-averaged) velocity vector $\overline{\mathbf{v}}$ in the cylindrical coordinate system employed is of the form $\overline{\mathbf{v}} = \overline{u}\,(r,z)\,\mathbf{e}_r + \overline{v}\,(r,z)\,\mathbf{e}_z + \overline{w}\,(r,z)\,\mathbf{e}_\theta$ where $\mathbf{e}_r$, $\mathbf{e}_z$, and $\mathbf{e}_\theta$ denote unit vectors in the r,z and θ directions, respectively. Here, $\overline{u}$ and $\overline{v}$ represent the secondary flow while $\overline{w}$ denotes the primary flow. The governing equations consist of the time-averaged equations for conservation of mass and momentum, and may be expressed in the following form

$$\frac{1}{r}\frac{\partial}{\partial r}(r\overline{u}) + \frac{\partial}{\partial z}(\overline{v}) = 0 \tag{1}$$

$$\frac{\partial \overline{u}}{\partial t} + \frac{1}{r}\frac{\partial}{\partial r}(r\overline{u}\,\overline{u}) + \frac{\partial}{\partial z}(\overline{v}\,\overline{u}) = \frac{1}{r}\frac{\partial}{\partial r}\left[r\nu\frac{\partial}{\partial r}(\overline{u})\right] + \frac{\partial}{\partial z}\left[\nu\frac{\partial}{\partial z}(\overline{u})\right] - \frac{1}{\rho}\frac{\partial \overline{P}}{\partial r} + \frac{\overline{w}^2}{r} - \nu\frac{\overline{u}}{r^2} + \frac{1}{r}\frac{\partial}{\partial r}\left[r\frac{\tau_{rr}}{\rho}\right] + \frac{\partial}{\partial z}\left[\frac{\tau_{rz}}{\rho}\right] - \frac{1}{r}\frac{\tau_{\theta\theta}}{\rho} \tag{2}$$

$$\frac{\partial \overline{v}}{\partial t} + \frac{1}{r}\frac{\partial}{\partial r}(r\overline{u}\,\overline{v}) + \frac{\partial}{\partial z}(\overline{v}\,\overline{v}) = \frac{1}{r}\frac{\partial}{\partial r}\left[r\nu\frac{\partial}{\partial r}(\overline{v})\right] + \frac{\partial}{\partial z}\left[\nu\frac{\partial}{\partial z}(\overline{v})\right] - \frac{1}{\rho}\frac{\partial \overline{P}}{\partial z} + \frac{1}{r}\frac{\partial}{\partial r}\left[r\frac{\tau_{rz}}{\rho}\right] + \frac{\partial}{\partial z}\left[\frac{\tau_{zz}}{\rho}\right] \tag{3}$$

$$\frac{\partial \overline{w}}{\partial t} + \frac{1}{r}\frac{\partial}{\partial r}(r\overline{u}\,\overline{w}) + \frac{\partial}{\partial z}(\overline{v}\,\overline{w}) = \frac{1}{r}\frac{\partial}{\partial r}\left[r\nu\frac{\partial}{\partial r}(\overline{w})\right] + \frac{\partial}{\partial z}\left[\nu\frac{\partial}{\partial z}(\overline{w})\right] + \frac{G}{\rho} - \frac{\overline{u}\,\overline{w}}{r} - \nu\frac{\overline{w}}{r^2} + \frac{1}{r}\frac{\partial}{\partial r}\left[r\frac{\tau_{r\theta}}{\rho}\right] + \frac{\partial}{\partial z}\left[\frac{\tau_{z\theta}}{\rho}\right] + \frac{1}{r}\frac{\tau_{r\theta}}{\rho} \tag{4}$$

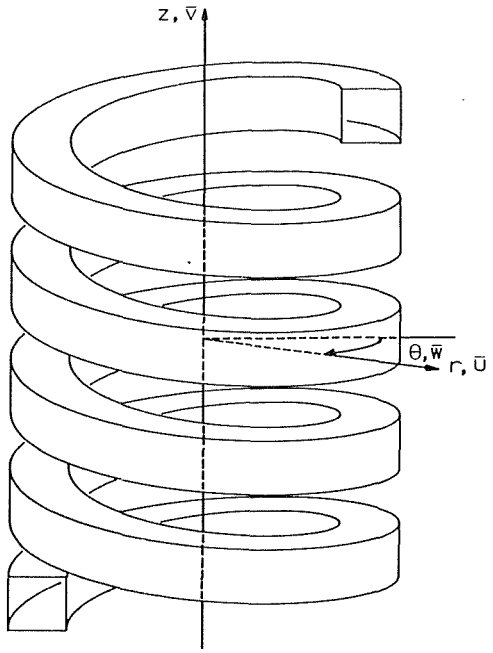

Fig. 1 Physical configuration and coordinate system of a helically coiled duct

where $G = -\frac{1}{r}\frac{\partial \overline{P}}{\partial \theta}$ is the azimuthal mean pressure gradient which is held constant, ρ is the fluid density, and ν is the kinematic viscosity of the fluid which can be neglected for high Reynolds number turbulent flows. The components of the Reynolds stress tensor τ_{ij} appearing in (2)–(4) can be obtained through various modeling techniques such as algebraic, one-equation, two-equation, and second-order closure models (Launder and Spalding 1972 and Lumley 1978). Recently, a nonlinear two-equation model of the $K - l$ and $K - \epsilon$ type was developed by Speziale (1987). This model yields more accurate predictions for normal Reynolds stress anisotropies allowing for the calculation of turbulent secondary flows in straight, non-circular ducts. The nonlinear $K - l$ model takes the form:

$$\tau_{ij} = -\frac{2}{3}\rho K\delta_{ij} + \rho K^{1/2} l \overline{S}_{ij} + C_D\rho l^2\left(\overline{S}_{im}\,\overline{S}_{mj} - \frac{1}{3}\overline{S}_{mn}\,\overline{S}_{mn}\,\delta_{ij}\right) + C_E\rho l^2\left(\overset{\circ}{\overline{S}}_{ij} - \frac{1}{3}\overset{\circ}{\overline{S}}_{mm}\,\delta_{ij}\right) \tag{5}$$

where

$$\overline{S}_{ij} = \frac{1}{2}\left(\frac{\partial \overline{v}_i}{\partial x_j} + \frac{\partial \overline{v}_j}{\partial x_i}\right) \tag{6}$$

$$\overset{\circ}{\overline{S}}_{ij} = \frac{\partial \overline{S}_{ij}}{\partial t} + \overline{\mathbf{v}}\cdot\nabla\overline{S}_{ij} - \frac{\partial \overline{v}_i}{\partial x_k}\overline{S}_{kj} - \frac{\partial \overline{v}_j}{\partial x_k}\overline{S}_{ki} \tag{7}$$

are the mean rate of strain tensor and its frame-indifferent Oldroyd derivative, respectively; K is the turbulent kinetic energy, and l is the turbulent length scale. C_D and C_E are dimensionless constants that each assume the value of 1.68 which was obtained by Speziale (1987) from correlations with turbulent channel flow data. The turbulent length scale l can be prescribed algebraically by empirical means, or can be tied to the turbulent kinetic energy K and dissipation rate ϵ through the relation

$$l = 2C_\mu\frac{K^{3/2}}{\epsilon} \tag{8}$$

where C_μ is a dimensionless constant which is typically taken to be 0.09. This forms the basis for the nonlinear $K - \epsilon$ model for which (5) - (7) are supplemented with modeled transport equations for K and ϵ that take the form

$$\frac{\partial K}{\partial t} + \bar{v}_i \frac{\partial K}{\partial x_i} = \frac{\partial}{\partial x_i}\left(\frac{C_\mu}{\sigma_k}\frac{K^2}{\epsilon}\frac{\partial K}{\partial x_i}\right) + \tau_{ij}\frac{\partial \bar{v}_i}{\partial x_j} - \epsilon \tag{9}$$

$$\frac{\partial \epsilon}{\partial t} + \bar{v}_i \frac{\partial \epsilon}{\partial x_i} = \frac{\partial}{\partial x_i}\left(\frac{C_\mu}{\sigma_\epsilon}\frac{K^2}{\epsilon}\frac{\partial \epsilon}{\partial x_i}\right) + C_{\epsilon 1}\frac{\epsilon}{K}\tau_{ij}\frac{\partial \bar{v}_i}{\partial x_j} - C_{\epsilon 2}\frac{\epsilon^2}{K} \tag{10}$$

where σ_k, σ_ϵ, $C_{\epsilon 1}$, and $C_{\epsilon 2}$ are dimensionless constants that are usually taken to be 1.0, 1.3, 1.44, and 1.92, respectively. The standard $K - \epsilon$ model is obtained in the limit as C_D, $C_E \to 0$.

Weaknesses in the performance of the modeled transport equations (9) - (10) for K and ϵ have been pointed out numerous times in the literature for problems involving swirl and streamline curvature (see Pope, 1978 and Reynolds, 1987). However, several attempts at developing improved versions of these modeled transport equations have not met with much success. It is a difficult problem that requires a substantial research effort to fully resolve. In this paper, we want to examine the efficacy of the nonlinear Reynolds stress correction to the $K - l$ and $K - \epsilon$ models given by equation (5), for problems involving secondary flows with streamline curvature. Hence, we will specify K and l empirically, based on experimental data for turbulent flow in rectangular channels, in order to determine the predictive capability of the nonlinear correction to the Reynolds stress independent of the deficiences in the modeled transport equations for K and ϵ.

For fully developed turbulent flow in a curved duct (using the cylindrical coordinate system shown in Fig. 1), the components of the Reynolds stress tensor corresponding to the nonlinear $K - l$ model (5) can be approximated as follows:

$$\tau_{rr} = -\frac{2}{3}\rho K + \rho K^{1/2} l \frac{\partial \bar{u}}{\partial r} + C_D \rho l^2 \left[\frac{1}{12}\left\{r\frac{\partial}{\partial r}\left(\frac{\bar{w}}{r}\right)\right\}^2 - \frac{1}{6}\left\{\frac{\partial \bar{w}}{\partial z}\right\}^2\right] + C_E \rho l^2 \left[\frac{1}{3r}\frac{\partial}{\partial r}(r^2 \bar{w})\frac{\partial}{\partial r}\left(\frac{\bar{w}}{r}\right) + \frac{1}{3}\left(\frac{\partial \bar{w}}{\partial z}\right)^2\right] \tag{11}$$

$$\tau_{zz} = -\frac{2}{3}\rho K + \rho K^{1/2} l \frac{\partial \bar{v}}{\partial z} + C_D \rho l^2 \left[-\frac{1}{6}\left\{r\frac{\partial}{\partial r}\left(\frac{\bar{w}}{r}\right)\right\}^2 + \frac{1}{12}\left\{\frac{\partial \bar{w}}{\partial z}\right\}^2\right] + C_E \rho l^2 \left[\frac{1}{3}\left\{r\frac{\partial}{\partial r}\left(\frac{\bar{w}}{r}\right)\right\}^2 + \frac{1}{3}\left(\frac{\partial \bar{w}}{\partial z}\right)^2\right] \tag{12}$$

$$\tau_{\theta\theta} = -\frac{2}{3}\rho K + \rho K^{1/2} l \frac{\bar{u}}{r} + C_D \rho l^2 \left[\frac{1}{12}\left\{r\frac{\partial}{\partial r}\left(\frac{\bar{w}}{r}\right)\right\}^2 + \frac{1}{12}\left\{\frac{\partial \bar{w}}{\partial z}\right\}^2\right] + C_E \rho l^2 \left[-\frac{2}{3}r^{1/2}\frac{\partial}{\partial r}\left\{r^{1/2}\bar{w}\right\}\frac{\partial}{\partial r}\left(\frac{\bar{w}}{r}\right) - \frac{2}{3}\left(\frac{\partial \bar{w}}{\partial z}\right)^2\right] \tag{13}$$

$$\tau_{r\theta} = \tau_{\theta r} = \rho K^{1/2}\frac{l}{2} r \frac{\partial}{\partial r}\left(\frac{\bar{w}}{r}\right) \tag{14}$$

$$\tau_{rz} = \tau_{zr} = \rho K^{1/2}\frac{l}{2}\left(\frac{\partial \bar{u}}{\partial z} + \frac{\partial \bar{v}}{\partial r}\right) + C_D \rho l^2 \left[\frac{1}{4} r \frac{\partial}{\partial r}\left(\frac{\bar{w}}{r}\right)\frac{\partial \bar{w}}{\partial z}\right] + C_E \rho l^2 \left[-\frac{1}{2}\frac{\bar{w}}{r}\frac{\partial \bar{w}}{\partial z}\right] \tag{15}$$

$$\tau_{z\theta} = \tau_{\theta z} = \rho K^{1/2}\frac{l}{2}\frac{\partial \bar{w}}{\partial z} \tag{16}$$

(see Hur, 1988 for more details). In deriving (11)-(16), terms that are quadratic in the secondary flow velocity components $\bar{u}$, $\bar{v}$ have been neglected since they are small (i.e., $||\bar{u}, \bar{v}||/||\bar{w}|| < 0.1$ for the computations to be presented herein where $||\cdot||$ denotes the maximum norm). As alluded to earlier, the turbulent kinetic energy K and length scale l will be specified empirically based on the experimental data of Laufer (1951) for turbulent channel flow (i.e., for turbulent flow in a large-aspect-ratio rectangular duct). It will now be shown that the data of Laufer can be represented by the power law

$$\frac{K^{1/2}}{U_0} = b_k\left(\frac{Sd}{U_0}\right)^{a_k} \tag{17}$$

$$\frac{l}{d} = b_l\left(\frac{Sd}{U_0}\right)^{a_l} \tag{18}$$

in the interior of the duct where U_0 is the centerline mean velocity, d is the half-width of the duct, and a_k, a_l, b_k, and b_l are dimensionless constants. In (17) - (18), S is the mean strain rate defined by

$$S = (S_{ij} S_{ij})^{1/2} \tag{19}$$

In Figs. 2-3, the turbulent kinetic energy and length scale are shown as a function of the mean strain rate for three different Reynolds numbers. For the following choice of empirical constants:

$$a_k = \begin{cases} 0, & Sd/U_0 < 0.06 \\ 0.43, & 0.06 \le Sd/U_0 < 0.3 \\ 0, & Sd/U_0 \ge 0.3 \end{cases} \tag{20}$$

$$b_k = \begin{cases} 0.032, & Sd/U_0 < 0.06 \\ 0.11, & 0.06 \le Sd/U_0 < 0.3 \\ 0.064, & Sd/U_0 \ge 0.3 \end{cases} \tag{21}$$

$$a_l = \begin{cases} 0, & Sd/U_0 < 0.04 \\ -0.33, & 0.04 \le Sd/U_0 < 0.25 \\ -0.90, & Sd/U_0 \ge 0.25 \end{cases} \tag{22}$$

$$b_l = \begin{cases} 0.18, & Sd/U_0 < 0.04 \\ 0.063, & 0.04 \le Sd/U_0 < 0.25 \\ 0.028, & Sd/U_0 \ge 0.25 \end{cases} \tag{23}$$

the power laws (17) - (18) do a reasonably good job in collapsing the experimental data for a variety of Reynolds numbers as shown in Figs. 2 - 3. These empirical constants are the values obtained based on a least-squares fit of the data. The results are relatively insensitive to mild changes in these constants. The power laws (17) - (18) are reminiscent of the ones used in viscoelastic flows; of course, the qualitative similarities between the mean turbulent flow of a Newtonian fluid and the laminar flow of a non-Newtonian fluid have long been recognized (see Lumley 1970). They have the advantage of allowing for a *substantial reduction in the level of computation* since separate transport equations for K and ϵ do not have to be solved. Furthermore, they provide a more accurate measure of K and l for straight ducts than that which can be obtained from modeled transport equations for K and ϵ (this allows for the study of the performance of the nonlinear Reynolds stress model in isolation from the complicating factor of defects in the K and ϵ modeled transport equations). Although these power laws become less accurate for curved duct flows, the errors introduced are moderately small for mild curvatures and are probably no worse than those that arise from the standard modeled transport equations for K and ϵ.

The boundary conditions for the secondary flow velocities

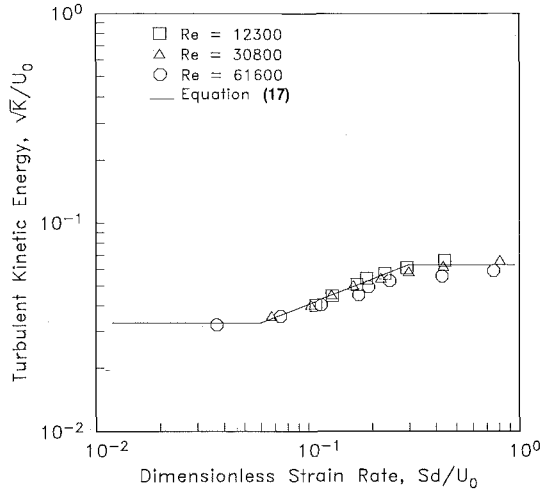

Fig. 2 Turbulent kinetic energy as a function of strain rate based on the data of Laufer (1951)

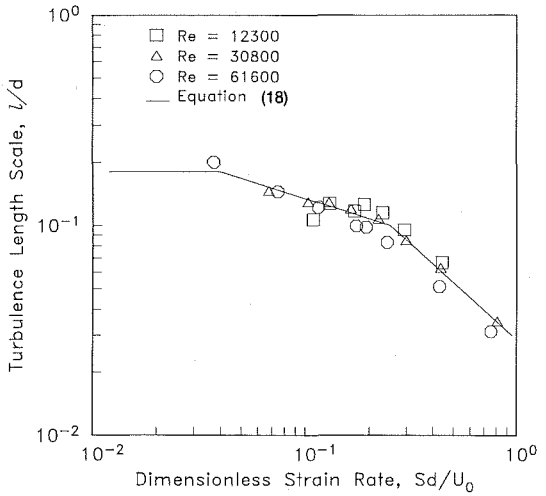

Fig. 3 Length scale of turbulence as a function of strain rate based on the data of Laufer (1951)

$\overline{u}$ and $\overline{v}$ are set equal to zero at the duct walls. In order to avoid resolving the very steep gradients of the azimuthal mean velocity $\overline{w}$ near the wall for turbulent flows, wall functions are used. These wall functions are based conventionally on a production equals dissipation equilibrium hypothesis and the law of the wall for the mean velocity profile (c.f., Amano 1984 for more details; in the present case, a single log wall layer starting at $y^+ = 30$ was used). The boundary conditions for the pressure are obtained in the usual fashion (c.f., Patankar 1980). The mean strain rate is approximated by

$$S = \left[\frac{1}{2}\left\{\frac{\partial}{\partial r}\left(\frac{\overline{w}}{r}\right)\right\}^2 + \frac{1}{2}\left(\frac{\partial \overline{w}}{\partial z}\right)^2\right]^{1/2} \tag{24}$$

which is obtained by neglecting quadratic terms in the mean secondary flow.

A finite volume scheme is used to solve the Reynolds equations (1) - (4), with the nonlinear $K - l$ model given by equations (11) - (16). The method of solution closely follows that outlined by Patankar (1980) as modified for the cylindrical coordinate system which is used in conjunction with the curved duct geometry. In this procedure, the physical domain is discretized into a finite number of computational cells (see Fig. 4). At the centroid of each (i.e., at point p), variables such as the pressure and azimuthal component of the mean velocity

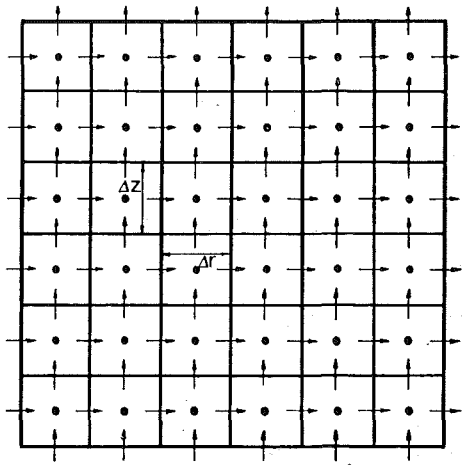

$\rightarrow \overline{u}$, $\uparrow \overline{v}$, $\bullet$ $\overline{w}, \overline{p}, K, l$

Fig. 4 Computational domain illustrating the staggered mesh system

are defined: the components of the mean velocity responsible for transport in the cross-sectional planes are defined at the cell boundaries. The difference equations for all of the variables are then obtained by integration over a control volume. A detailed description of the procedure used for obtaining these equations may be found in Hur (1988).

In the present work, the system of algebraic equations which result from the differencing procedure used for the governing equations (1) - (4) are solved by a successive line under relaxation (SLUR) procedure with the repeated use of the tridiagonal matrix algorithm (Isaacson and Keller, 1970). The details of the solution procedure and the algorithm development are given elsewhere (Hur, 1988). The following steps constitute only a brief summary of the technique:

(*a*) A set of pseudo-velocity components (for the secondary flow velocity) are obtained from the discretized momentum equations by assuming uniform pressure in the computational domain.

(*b*) These pseudo-velocities are then used to obtain the pressure by solving the discretized equation for the conservation of mass with the SLUR method.

(*c*) Based on the pressure obtained in (*b*), the secondary flow velocity components are obtained from the discretized momentum equations with the SLUR method.

(*d*) The correction for the velocity components are obtained by evaluating the correction for the mass flux in each cell.

(*e*) Using the corrected velocities from (*d*), the axial velocity is obtained by the SLUR method.

(*f*) The values of kinetic energy and length scale are then computed using the corrected velocity field.

(*g*) The procedure is repeated with the updated values of the variables until adequate convergence is obtained.

In addition, a time-averaged stream function $\overline{\psi}$ for the secondary flow can be defined in the following manner

$$\overline{u} = -\frac{1}{r}\frac{\partial \overline{\psi}}{\partial z} \tag{25}$$

$$\overline{v} = \frac{1}{r}\frac{\partial \overline{\psi}}{\partial r} \tag{26}$$

and can be obtained from the mean velocity field for analyzing the secondary flow field.

All the computations reported in this work, which are second-order accurate, were performed using a 32 × 32 uniform mesh. The choice of the uniform mesh was based primarily

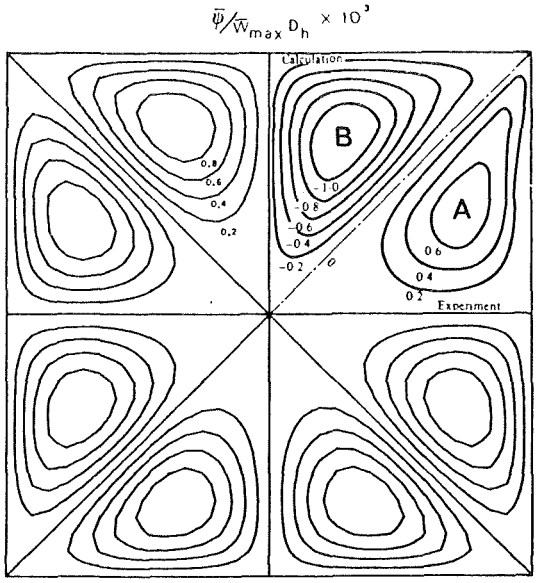

Fig. 5 Comparison of fully developed secondary flow streamlines based on the nonlinear K—l model in a straight duct at Re ≈ 42000 with the experiments of Gessner and Jones (Curve A: Re ≈ 15000) and the computations of Nakayama (Curve B: Re ≈ 83000)

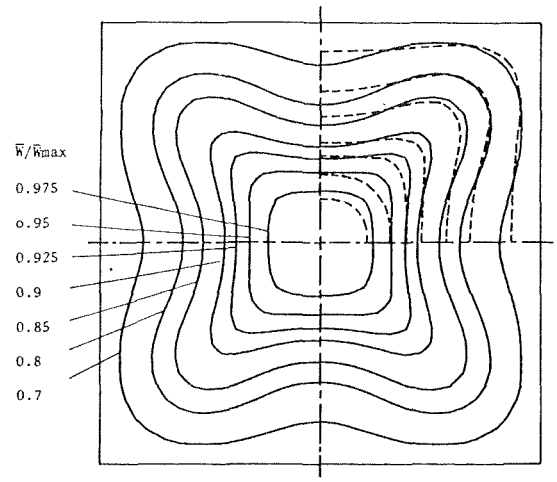

Fig. 6 Comparison of azimuthal velocity contours ($\bar{w}$) for straight duct at Re ≈ 42000: ——— nonlinear K—l model; · · · · · · experiments of Melling and Whitelaw

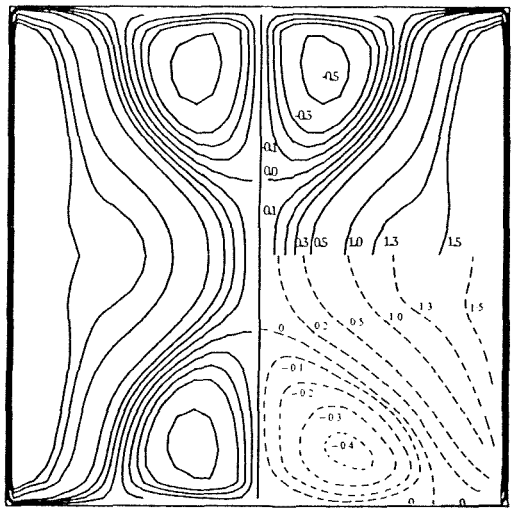

Fig. 7 Comparison of Reynolds stress (τ_{xz}) contours for straight duct at Re ≈ 42000: ——— nonlinear K—l model; · · · · · · experiments of Melling and Whitelaw

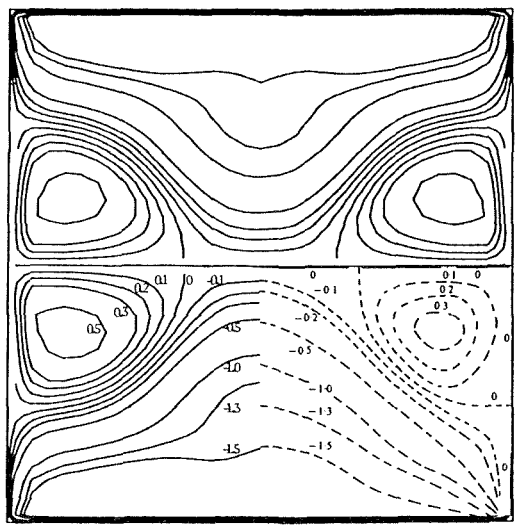

Fig. 8 Comparison of Reynolds stress (τ_{yz}) contours for straight duct at Re ≈ 42000: ——— nonlinear K—l model; · · · · · · experiments of Melling and Whitelaw

on the nature of secondary flow field encountered in the present study. The efficacy of the grid system to emulate the flow field was verified by carrying out computations with progressively finer grids and monitoring the volume flux, secondary flow strength, streamline patterns as well as the velocity profiles. For example, some cases were recomputed using a 48 × 48 mesh and the monitored quantities only differed from those obtained on the 32 × 32 mesh by 0.5 percent. The computed solution was assumed to have converged to its steady state when the root mean square of the average difference between successive iterations was less than 10^{-4} for the velocity components and pressure. This mesh size, for the analogous problem of rotating duct flows, has yielded results that were within 3 percent of results obtained from linear stability analyses (Speziale, 1985).

A DEC/VAX-8700 with a processing speed of 6 VUP (i.e., VAX Units of Performance wherein the VAX 11/780 is 1 VUP) was used for the calculations with 64 bit arithmetic. Each set of computations required approximately 35 minutes of CPU time corresponding to about 700 cycles consisting of four line iterations per each of the three velocity components and pressure. In the following section the results obtained by the computational technique outlined herein are discussed and compared with available experimental and computational findings.

3 Results and Discussion

The model predictions for turbulent flow in a straight duct will be analyzed first, followed by flow in curved ducts. The experimental investigations on turbulent duct flow include the works of Gessner and Jones (1965), Brundrett and Baines (1964), Launder and Ying (1972), and Melling and Whitelaw (1976) among others. In the present work, computations were performed at a Reynolds number of about 42,000 in ducts of square cross-section. This was done to facilitate comparison with the results of Melling and Whitelaw (1976), since their experiments were performed at the same Reynolds number and include laser anemometer measurements of the flow pattern with a detailed documentation of the Reynolds stress components. It should be noted here that Melling and Whitelaw

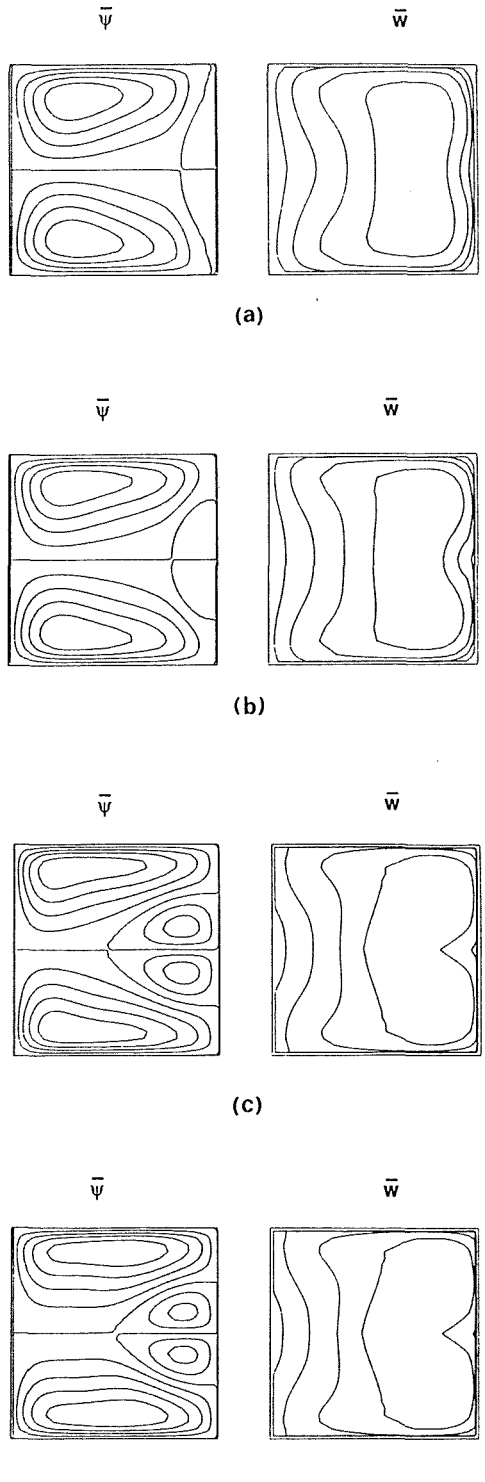

Fig. 9 Secondary flow streamlines ($\bar{\psi}$) and azimuthal velocity contours ($\bar{w}$) for turbulent flow in curved ducts at Re ≈ 42000 for different curvature ratios. (*a*) Cr = 125, (*b*) Cr = 62.5, (*c*) Cr = 31.25, (*d*) Cr = 15.63.

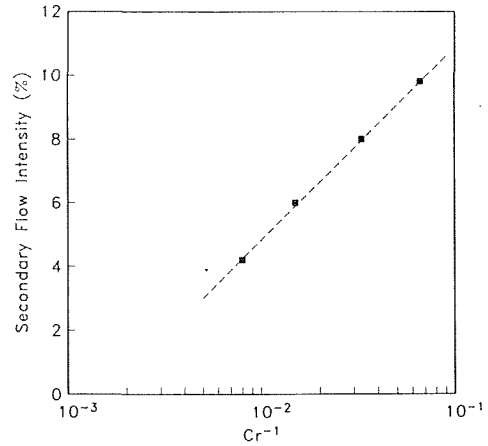

Fig. 10 Effect of curvature ratio on secondary flow intensity at Re ≈ 42000

(1976) did not evaluate the secondary flow stream function; these are obtained from other sources, although at different Reynolds numbers (e.g., Gessner and Jones, 1965; Nakayama et al., 1983).

The time-averaged secondary flow streamlines for the straight duct of square cross-section is shown in Fig. 5. It should be noted that the flow is outward toward the corner and returns to the center along the wall thus forming eight counter-rotating vortices. Qualitative comparisons with the experimental results of Gessner and Jones (1965) for a Reynolds number of 150,000 and the computational results of Nakayama et al. (1983) for a Reynolds number of 83,000 are possible as shown in Fig. 5. The computations by Nakayama et al. (1983) are based on the algebraic stress model developed by Launder and Ying (1972). It can be seen here that the present model agrees with the experimental results of Gessner and Jones (1965) in the sense that it also exhibits weaker secondary flow velocities near the center of the duct.

Due to the secondary flow associated with the turbulence, the axial velocity profile for $\bar{w}$ is distorted, as shown in Fig. 6. Comparison with the experiments of Melling and Whitelaw (1976) is also shown in Fig. 6 and the results indicate qualitatively good agreement. The computed values of the Reynolds shear stress will now be compared with the experiments. The results for the two shear stress components, τ_{xz} and τ_{yz} (where x and y are the horizontal and vertical coordinates in the plane of the secondary flow and z is the coordinate normal to this plane) are shown in Figs. 7 - 8. As can be seen from these results, the computed values of τ_{xz} and τ_{yz} are in good agreement with the experimental findings.

The computations were then extended to flow in curved ducts. Figures 9(*a*) - (*d*) show the evolution of the flow field as the curvature ratio Cr (i.e., the ratio of the radius of curvature to the duct width) increases for a Reynolds number of about 42,000. In the case of curved ducts, the interaction between the centrifugal force and the force induced by the normal Reynolds stress differences (due to the anisotropic turbulence) characterizes the secondary flow. However, as can be seen from Figs. 9(*a*) - (*b*), even for very loosely coiled ducts (i.e., ducts of large curvature ratio) the fully developed flow field is characterized by a predominately double vortex structure which is representative of a flow field dominated by centrifugal effects. There is, however, a pair of weak counter-rotating vortices near the outer wall of the duct. When the curvature ratio is decreased (i.e., as the duct is coiled tighter), the centrifugal effects gain further dominance, and the vortices near the outer wall and, hence, the secondary flow gain strength and assume a four-vortex structure as shown in Figs. 9(*c*) - (*d*). The effect of an increase in the secondary flow intensity on the azimuthal velocity profiles can also be observed in Figs. 9(*a*) - (*d*). As can be seen from the constant velocity lines, there is a substantial outward shift of the azimuthal velocity field with a decrease in the curvature ratio. In practice the secondary flow structure assumes an essentially eight vortex structure for extremely loosely coiled ducts with Cr > 1000.

Unfortunately, direct comparisons cannot be made with previously conducted experiments (e.g., Chang et al., 1983) since those experimental studies involve developing flow or large curvatures for which Cr = O(1).

In Fig. 10, the associated increase in the secondary flow intensity with a decrease in the curvature ratio (i.e., increase in duct curvature) is shown. From this figure, it is clear that curvature can increase the secondary flow intensity (defined as $|\bar{u}, \bar{v}, |_{max}/\bar{w}_{max}$) from 0.02 to 0.10.

4 Conclusion

A numerical study of turbulent secondary flows in straight and curved ducts of square cross section has been conducted using the nonlinear $K - l$ model of Speziale (1987). The results are shown to compare well with the detailed laser-Doppler anemometry measurements of Melling and Whitelaw (1976) for fully developed turbulent flow in straight ducts of square cross-section. Here, the model predicts an eight vortex secondary flow consistent with experimental observations. For curved ducts, the model predicts a double vortex secondary flow for mild to moderate curvature and a four-vortex secondary flow for moderate to strong curvature. These regimes are analogous to those that are observed in laminar curved duct flows (c.f., Cheng, Lin, and Ou 1976) with one major exception: for the laminar case there would be no secondary flows in straight ducts (i.e., in the limit as Cr $\rightarrow \infty$ the laminar flow is unidirectional).

In our opinion, the calculations presented in this study (as well as the more detailed results of Hur 1988) indicate that the nonlinear $K - l$ and $K - \epsilon$ model has the promise to yield more accurate predictions for curved turbulent flows than the standard eddy viscosity models. This is particularly true of curved turbulent flows with large Cr since, for this case, the centrifugally generated secondary flow will significantly interact with the weak eight vortex secondary flow that occurs in the absence of curvature — an effect which cannot be described by the standard $K - \epsilon$ model. The nonlinear two-equation model could provide a useful alternative to a second-order closure model for those applications where savings in computational expense is a high priority. Future research should be directed toward the generation of a full nonlinear $K - \epsilon$ model solution to the curved flow problem. Invariably, this will require a careful examination of the modeled dissipation rate transport equation to properly account for curvature effects. With such improvements, the nonlinear $K - \epsilon$ model could have a variety of important technological applications to turbulent flows involving streamline curvature.

References

Amano, R. S., 1984, "Development of a Turbulent Near-Wall Model and its Application to Separated and Reattached Flow," *Numerical Heat Transfer*, Vol. 7, pp. 59-75.

Brundrett, E., and Baines, W. D., 1964, "The Production and Diffusion of Vorticity in Duct Flow," *Journal of Fluid Mechanics*, Vol. 19, pp. 375-394.

Chang, S. M., Humphrey, J. A. C., and Modavi, A., 1983, "Turbulent Flow in a Strongley Curved U-Bend and Downstream Tangent of Square Cross-Sections," *Physico-Chemical Hydrodynamics*, Vol. 4, pp. 243-269.

Cheng, K. C., Lin, R. C., and Ou, J. W., 1976, "Fully-Developed Laminar flow in Curved Rectangular Channels," ASME JOURNAL OF FLUIDS ENGINEERING, Vol. 98, pp. 41-48.

Choi, Y. D., Iacovides, H., and Launder, B. E., 1989, "Numerical Computation of Turbulent Flow in a Square-Sectioned 180° Bend," ASME JOURNAL OF FLUIDS ENGINEERING, Vol. 111, pp. 59-68.

DeMuren, A., and Rodi, W., 1984, "Calculation of Turbulence-Driven Secondary Motion in Non-Circular Ducts," *J. Fluid Mech.*, Vol. 140, pp. 189-222.

Gessner, F. B., and Jones, J. B., 1965, "On Some Aspects of Fully-Developed Turbulent Flow in Rectangular Channels," *Journal of Fluid Mechanics*, Vol. 23, pp. 689-713.

Gessner, F. B., and Po, J. K., 1976, "A Reynolds Stress Model for Turbulent Corner Flows-Part II: Comparisons Between Theory and Experiment," ASME JOURNAL OF FLUIDS ENGINEERING, Vol. 98, pp. 269-277.

Humphrey, J. A. C., Whitelaw, J. H., and Yee, G., 1981, "Turbulent Flow in a Square Duct with Strong Curvature," *Journal of Fluid Mechanics*, Vol. 103, pp. 443-463.

Hur, N., 1988, "Numerical Study of Secondary Flows in Curved Ducts," Ph. D. thesis, Stevens Institute of Technology, April 1988.

Isaacson, E., and Keller, H. B., 1970, *Analysis of Numerical Methods*, Wiley.

Laufer, J., 1951, "Investigation of Turbulent Flow in a Two-Dimensional Channel," NACA TN 1053.

Launder, B. E., and Spalding, D. B., 1972, *Mathematical Models of Turbulence*, Academic Press.

Launder, B. E., and Ying, W. M., 1972, "Secondary Flows in Ducts of Square Cross-Section," *Journal of Fluid Mechanics*, Vol. 54, pp. 289-295.

Lumley, J. L., 1970, "Toward a Turbulent Constitutive Relation," *Journal of Fluid Mechanics*, Vol. 41, pp. 413-434.

Lumley, J. L., 1978, "Turbulence Modeling," *Adv. Appl. Mech.*, Vol. 18, pp. 123-176.

Majumdar, A. K., Pratap, V. S., and Spalding, D. B., 1977, "Numerical Computation of Flow in Rotating Ducts," ASME JOURNAL OF FLUIDS ENGINEERING, Vol. 99, pp. 148-153.

Melling, A., and Whitelaw, J. H., 1976, "Turbulent Flow in a Rectangular Duct," *Journal of Fluid Mechanics*, Vol. 78, pp. 289-315.

Nakayama, A., Chow, W. L., and Sharma, D., 1983, "Calculation of Fully Developed Turbulent Flows in Ducts of Arbitrary Cross-Section," *Journal of Fluid Mechanics*, Vol. 128, pp. 199-217.

Patankar, S. V., 1980, *Numerical Heat Transfer and Fluid Flow*, McGraw-Hill.

Pope, S. B., 1978, "An Explanation of the Turbulent Round-Jet/Plane-Jet Anomaly," *AIAA J.*, Vol. 16, pp. 279-281.

Pratap, V. S., and Spalding, D. B., 1975, "Numerical Computation of the Flow in Curved Ducts," *Aeronautical Quarterly*, Vol. 26, pp. 219-228.

Reynolds, W. C., 1987, "Fundamentals of Turbulence for Turbulence Modeling and Simulation," Lecture Notes for Von Karman Institute, AGARD Lecture Series No. 86, North Atlantic Treaty Organization.

Roache, P. J., 1972, *Computational Fluid Dynamics*, Hermosa.

Speziale, C. G., 1985, "Numerical Solution of Rotating Internal Flows," *Lectures in Applied Mathematics*, Vol. 22, pp. 261-288.

Speziale, C. G., 1987, "On Nonlinear $K - l$ and $K - \epsilon$ Models of Turbulence," *Journal of Fluid Mechanics*, Vol. 178, pp. 459-475.

A Reinterpretation of the Results of the Moby Dick Experiments in Terms of the Nonequilibrium Model

Z. Bilicki*

J. Kestin

M. M. Pratt

Brown University,
Providence, RI 02912

The topological pattern of the set of measured pressure distributions included in the Moby Dick series of experiments on critical flow through a slender channel provided with a throat does not agree with that expected on the basis of the rigorous mathematical theory which predicts the appearance of a singular point, most likely, of a saddle point at or near the throat. This is considered to be paradoxical. The paper provides an alternative interpretation of these results. The Moby Dick experiments have clearly demonstrated the profound influence of the existence of metastable conditions near the flash point. For this reason, among others, the paper undertakes a re-evaluation of some of the Moby Dick results in terms of the nonequilibrium model first suggested by L. J. F. Broer in 1958 for use in flows of chemically reacting gases. Since the Moby Dick data contain measurements of the distribution $\alpha(z)$ of void fractions, it becomes possible to calculate local relaxation times, $\theta[\alpha(z)]$, and so to close the system of differential equations of the model. Extensive numerical calculations reproduce the measured pressure distributions with an error of 6–10 percent at most. More importantly, the topological features of the calculated pressures, $P_{th}(z)$, turn out to be identical with the measured ones, $P_{ex}(z)$. The most important, and totally unexpected, result is that the flow in the Moby Dick channel remained subcritical everywhere. In particular, the channel was not choked at the throat. Since the mass-flow rates were independent of back-pressure, it is concluded that the flows were choked at or near the exit. The paper advances additional reasons for the feasibility of this alternative interpretation, but emphasizes and re-emphasizes its provisional nature.

1 Introduction

The classical measurements of critical flow-rates and of their dependence on the critical pressure and critical void fraction performed at the Centre d'Etudes Nucléaires in Grenoble (France), known as "Moby Dick," [1], have served as a basis for the understanding of critical two-phase, single-component flows ever since their publication. These experiments have clearly demonstrated the profound influence exerted on such flows by the time-lag introduced into the process of internal evaporation as the pressure drops. The time-lag is introduced into the flow by the system's failure to begin evaporation when saturation conditions are reached at the flash point introducing metastable conditions. This manifests itself by the fact that the process of homogeneous nucleation (flash point) occurs at a temperature which exceeds the saturation temperature by as much as 2–3°C.

The experiments were carried out in a channel consisting of a straight portion followed by a conical expander provided with a 7 deg included-angle divergence. The exit from the divergent cone was connected to the condenser by a considerable length of constant-area piping. The channel profile, reproduced from [1], is shown in Fig. 1, and the connections at both its ends are shown in Fig. 2.

The evaluation of these experiments assumed that critical conditions occurred at the throat, presumed to exist at the junction of the conical section to the upstream constant-area channel. Measurements of pressure and void fraction, as functions of longitudinal distance, were reported. The authors in Grenoble emphasized that the channel shape was carefully designed to secure that a one-dimensional mathematical description of the flows created in it should apply. A close examination of the published diagrams fails to reveal a topological-geometrical pattern of the curves expected in the

*Permanent address: Institute for Fluid Flow Machinery, Polish Academy of Sciences, 80-952 Gdansk, Poland.

Contributed by the Fluids Engineering Division and presented at the Winter Annual Meeting, Chicago, Ill., November 27–December 2, 1988, of THE AMERICAN SOCIETY OF MECHANICAL ENGINEERS. Manuscript received by the Fluids Engineering Division December 12, 1988.

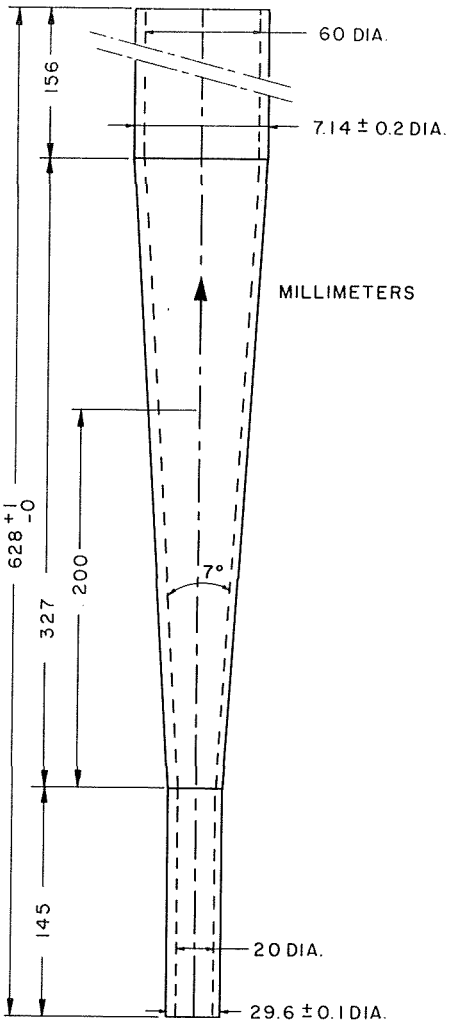

Fig. 1 The channel used in Moby Dick experiments

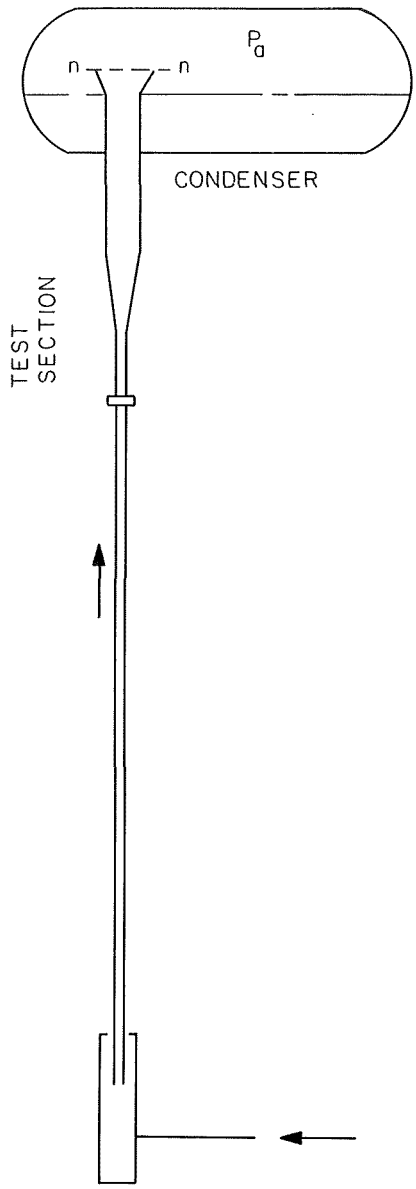

Fig. 2 Experimental arrangement

neighborhood of the cross-section in which critical flow is presumed to occur.

In a recent paper, [2], the authors have demonstrated that a transition from subcritical to supercritical flow need not occur at the narrowest cross-section (throat) and must be associated with the appearance of a singular point (saddle or nodal point) in the phase space of the relevant mathematical model which reliably describes the physical process. This conclusion is independent of the number of ordinary nonlinear differential equations (i.e., of the number of components in the vector of dependent variables) in the model, as long as a one-dimensional approximation is applicable.

A typical pressure profile is shown in Fig. 3 which represents six runs at the same upstream conditions and mass-flow rate, but at different back-pressures. The diagram also plots the variation of the void fraction, measured by gamma-ray absorption. It seems that the upstream branch cannot correspond

Nomenclature

B = function defined in equation (4g)
f = friction factor
G = specific mass flux
h = enthalpy
$\dot{m}$ = mass-flow rate
P = pressure
R = radius of cross-section
T = temperature
v = specific volume
w = velocity
x = dryness fraction
$\tilde{x}$ = equilibrium dryness
z = length coordinate
α = void fraction
γ = factors defined in (5b, c, d)
Δ = characteristic determinant of the system of equations (1a–d), see equation (4f)
ΔT = superheat at flash point
θ = relaxation time
ρ = density
σ = vector of dependent properties
τ = dummy independent variable

Subscripts

a = outside exit
crit = critical
e = at channel entrance
ex = experimental
f = at flash point
t = at throat
th = calculated by the model

Superscripts

$''$ = property of vapor on saturation line
L = pertains to nonequilibrium temperature of liquid
$*$ = critical state

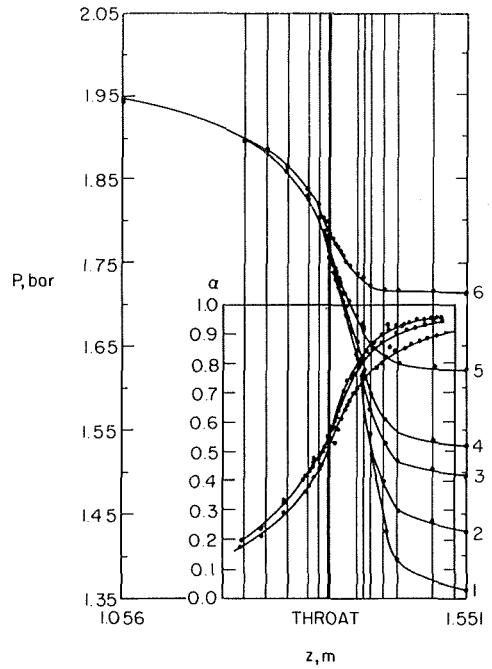

Fig. 3 Typical result. 1. run 423, G = 4383 kg/m²s, P_e = 1.359 bar, P_a = 1.381 bar, T = 121.9°C; 2. run 424, G = 4357 kg/m²s, P_e = 1.430 bar, P_a = 1.451 bar, T = 121.8°C; 3. run 425, G = 4355 kg/m²s, P_e = 1.494 bar, P_a = 1.512 bar, T = 121.7°C; 4. run 426, G = 4360 kg/m²s, P_e = 1.531 bar, P_a = 1.551 bar, T = 121.8°C; 5. run 427, G = 4345 kg/m²s, P_e = 1.619 bar, P_a = 1.636 bar, T = 121.8°C; 6. run 428, G = 4331 kg/m²s, P_e = 1.712 bar, P_a = 1.724 bar, T = 121.8°C.

to the usual saddle point through which a transition from subcritical to supercritical flow would be expected to occur, (nodal points are observed so rarely that we can ignore them for the time being), in spite of the fact that the mass-flow rate fixed by G = (4360 ± 0.6 percent) kg/m²s remained the same at all six back-pressures.

Thus the juxtaposition of this mathematical conclusion and the experimentally produced graphs, of which the above is a typical example, results in an apparent paradox. The present paper will explore the possibility of an interpretation of results which differs from the hitherto accepted one; it is based on the hypothesis that nonequilibrium phenomena are dominant and analyzes the results in terms of the nonequilibrium model first proposed by L. J. F. Broer [3] in 1958.

2 The Model

The homogeneous relaxation model consists of the usual three conservation laws which are supplemented with an evolution equation for the phase transition in terms of a relaxation time θ, which characterizes the vapor-generation rate. The governing equations are as follows:

$$\frac{dw}{dz} - G\frac{dv}{dz} = -2v\,GR'/R, \tag{1a}$$

$$\frac{dP}{dz} + G\frac{dw}{dz} = -fv\,G^2/R, \tag{1b}$$

$$\frac{dh}{dz} + w\frac{dw}{dz} = 0 \tag{1c}$$

$$\frac{dx}{dz} = -\frac{x-\bar{x}}{\theta w}. \tag{1d}$$

Here w denotes the barycentric velocity, v is the specific volume of the mixture, $G = w/v$ is the specific mass flux, $R(z)$ is the radius of a cross-section and $R'(z)$ is its derivative. Further, P denotes pressure, f is the friction factor, h the enthalpy, and x is the actual dryness fraction, whereas $\bar{x} = \bar{x}(P, h)$ denotes that dryness fraction which would exist in an equilibrium mixture at the local pressure and enthalpy. Finally, θ denotes the local relaxation time which characterizes the rate of mass transfer (caused by an existing temperature difference) between the phases.

To the preceding set there must be added the equation of state

$$h = h(v,P,x) = xh''(P) + (1-x)h^L[P,\ T^L(P,\ v)]. \tag{2}$$

The function $h''(P)$ represents the enthalpy of the vapor on the vapor-pressure line which corresponds to the local pressure P; T^L is the nonequilibrium temperature of the liquid. At the flashpoint $T^L > T(P)$ and the assumption underlying the equation of state (2) is that only the liquid exists in a metastable state, an assumption which seems to be consistent with experiment.

The preceding model neglects the slip between the phases since we found slip to be of secondary importance to nonequilibrium effects, $T^L \neq T(P)$. To complete the model, the superheat, ΔT, at flashing and the local relaxation times, $\theta(z)$, are needed. In the analysis that follows, ΔT was determined directly from the graphs included in [1]. In the Moby Dick series studied here ΔT ranged from 2.66 to 2.91°C.

Evidently, the relaxation time θ could not be measured and no theory exists which would make it possible to determine it. For this reason we have taken advantage of the availability of measured values of void fraction to calculate $\theta[\alpha(z)]$ and employed the model, together with the known value of flow-rate, to calculate a "predicted" pressure distribution. This was then compared with experiment. In this manner, we performed a test of validity of the model.

3 A Reservation

In view of the unanticipated result of our calculations, which will be presented later in Section 6, it is necessary to insert a word of caution at this point. We do not claim that the calculations represent more than a *possible interpretation* contained in the message suggested by the Moby Dick series of measurements; the importance of these calculations resides entirely in the fact that they satisfactorily resolve the paradox identified in the Introduction and seem to give us an insight which is unobtainable from the experiments directly.

4 The Working Equations

The system of equations (1) can be put in the following autonomous form

$$\frac{dz}{d\tau} = \Delta, \tag{4a}$$

$$\frac{dv}{d\tau} = 2v\Delta R'/R - B, \tag{4b}$$

$$\frac{dw}{d\tau} = -\rho wB, \tag{4c}$$

$$\frac{dP}{d\tau} = \rho^2 w^2(B - fv\Delta/R), \tag{4d}$$

$$\frac{dx}{d\tau} = -\Delta\frac{x-\bar{x}}{w\theta}, \tag{4e}$$

where

$$\Delta = \left(\frac{\partial h}{\partial v}\right)_{P,x} + \rho^2 w^2\left[v - \left(\frac{\partial h}{\partial P}\right)_{v,x}\right], \tag{4f}$$

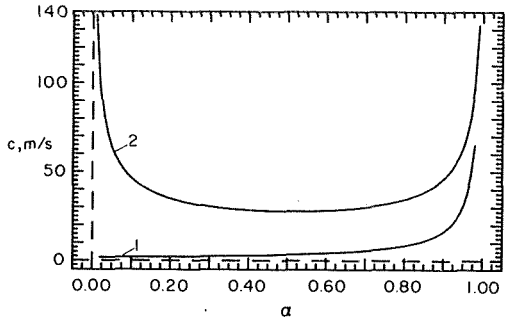

Fig. 4 Critical speeds as a function of void fraction for P = 1.7 bar. 1. Homogeneous equilibrium model; 2. Homogeneous relaxation model.

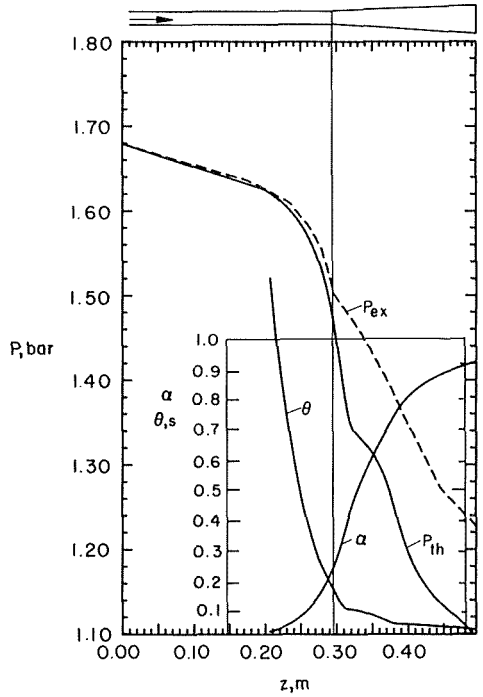

Fig. 5(*a*) Experimental results for run 400. G = 6526 kg/m²s, P_e = 1.227 bar, P_s = 1.232 bar, T = 116.7°C. P_{ex} - measured pressure distribution, in bar; P_{th} - pressure distribution calculated on the basis of the relaxation model, in bar; α_{ex} - measured void fraction; θ - relaxation time calculated on the basis of the relaxation model, in s.

$$B = \frac{v}{R}\left[2R'\left(\frac{\partial h}{\partial v}\right)_{P,x} - f\rho^2 w^2\left(\frac{\partial h}{\partial P}\right)_{v,x}\right] - \left(\frac{\partial h}{\partial x}\right)_{P,v} \cdot \frac{x-\bar{x}}{\theta w}, \quad (4g)$$

and τ is a dummy parameter.

The set of equations (4*a*-*g*) can be used to solve for the vector $\sigma\{z, v, w, P, x\}$ given initial conditions, provided θ is known. As stated earlier, we have applied an inverse procedure. Knowing the measured void fraction $\alpha(z)$, we can eliminate the dryness fraction $x = \alpha v/v''$ from the system of equations, and use equation (4*e*) to determine the relaxation time

$$\frac{1}{\theta} = -\frac{w}{\Delta(x-\bar{x})} \cdot \frac{dx}{d\tau} = -\frac{w}{\Delta(x-\bar{x})} \cdot \left(\Delta\gamma_1 \frac{d\alpha}{dz} + \gamma_2 \frac{dv}{d\tau} + \gamma_3 \frac{dP}{d\tau}\right), \quad (5a)$$

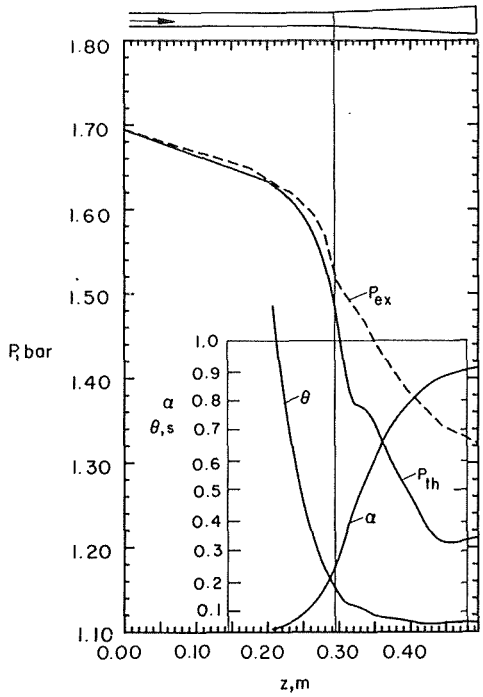

Fig. 5(*b*) Experimental results for run 401. G = 6465 kg/m²s, P_e = 1.323 bar, P_s = 1.337 bar, T = 116.6°C. P_{ex} - measured pressure distribution, in bar; P_{th} - pressure distribution calculated on the basis of the relaxation model, in bar; α_{ex} - measured void fraction; θ - relaxation time calculated on the basis of the relaxation model, in s.

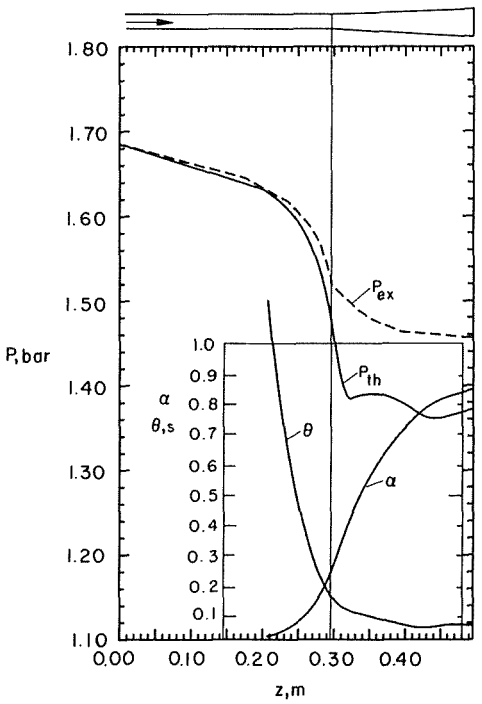

Fig. 5(*c*) Experimental results for run 402. G = 6496 kg/m²s, P_e = 1.456 bar, P_s = 1.469 bar, T = 116.7°C. P_{ex} - measured pressure distribution, in bar; P_{th} - pressure distribution calculated on the basis of the relaxation model, in bar; α_{ex} - measured void fraction; θ - relaxation time calculated on the basis of the relaxation model, in s.

where

$$\gamma_1 = \frac{v}{v''}, \quad \gamma_2 = \frac{\alpha}{v''}, \text{ and } \gamma_3 = -\frac{\alpha v}{(v'')^2} \cdot \frac{dv''}{dP}. \quad (5b,c,d)$$

Table 1 Experimental conditions and calculated results for runs 400, 401 and 402 of the Moby Dick series.

Run	400	401	402
Mass flow $\dot{m}$, kg/s (or 2.04 ± 0.5 percent)	2.05	2.03	2.04
Specific flow rate at inlet G, kg/m²s (or 6495 ± 0.5 percent)	6526	6465	6496
Back-pressure P_a, bar	1.232	1.337	1.469
Location of throat z_t, mm	295	295	295
Location of flash point z_f, mm (or 201 ± 3 percent)	194	206	204
Location of throat with respect to flash $z_t - z_f$, mm	101	89	91
Flow velocity at throat w_t, m/s	8.96	8.80	8.93
Mach number at throat Ma_t	0.256	0.250	0.255
Largest flow velocity w_{max}, m/s	18.9	14.9	10.6
Location of w_{max} with respect to flash point z, mm	301	243	239
Location of exit with respect to flash point z_e, mm	301	289	291

5 Analysis

It was emphasized in Section 2 that no reliable expression for the relaxation time is available.[1] Before applying the nonequilibrium model with the values $\theta(z)$ calculated by the procedure described in Section 4, we made calculations with the aid of the homogeneous model, [2], and the slip model, [5], and ascertained that each of these models failed in that both predicted a critical speed which was lower than the flow velocity at the flash point.

By contrast, the results of the procedure described here were generally acceptable, as will be detailed in the next section, and convinced us that the use of this model led to results which were consistent with the measurements.

The diagram in Fig. 4 represents the critical velocity as calculated by the homogeneous equilibrium model (curve 1) and the nonequilibrium model (curve 2) in terms of the void fraction α for an entrance pressure of $P_0 = 1.7$ bar. The former are much lower than the latter and than the velocities at the throat listed in Table 1, to be discussed in the next section.

6 Results

The preceding algorithm was programmed on a computer and calculations were performed on runs 400, 401, and 402 of the Moby Dick series [1]. The results are presented graphically in Figs. 5(*a*, *b*, *c*) under the conditions specified in the captions and in Table 1. The back-pressure P_a, set at the exit $n-n$ (Fig. 2), was adjusted by varying it in the condenser. It is, thus, important to note that the mass-flow rate $\dot{m}$ remained essentially constant, even though the back-pressure varied by about 20 percent. This suggests that the flow was choked in all three cases, and the only detail subject to interpretation is to decide whether it was choked at the throat, at some downstream cross-section or at the exit. Our calculations seem to favor the latter interpretation, because they also support the hypothesis that the flow was subcritical everywhere.

More specifically, at all points in our calculations the determinant was positive ($\Delta > 0$), indicating that the flow velocity was lower than the local sound speed.

> This was the most essential, and totally unexpected, result of our research.

The flow velocity at the throat and the value of the corresponding local Mach number are listed in Table 1; they are all lower than unity. We recall here that the variation of sound velocity with void fraction, illustrated in Fig. 4, reinforces these conclusions.

[1]The correlation given by E. G. Bauer et al. [4], apart from not being dimensionally homogeneous, failed to reproduce the measured pressure distributions, when used in our program. Frequently, the errors were of the order of 100 percent.

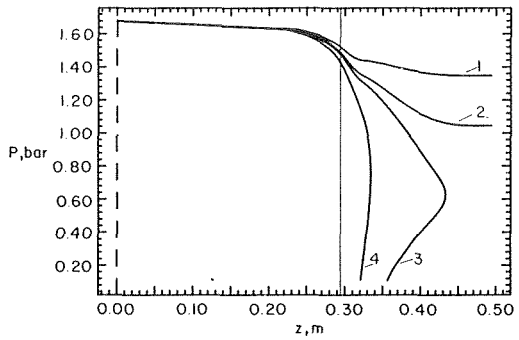

Fig. 6 Pressure distributions calculated along the Moby Dick channel with the inlet conditions and $\theta(\alpha)$ relation for run 400 obtained by the inverse method. 1. $\dot{m} = 0.964\ \dot{m}_{crit}$; 2. $\dot{m} = 0.997\ \dot{m}_{crit}$; 3. $\dot{m} = 1.003\ \dot{m}_{crit}$; 4. $\dot{m} = 1.018\ \dot{m}_{crit}$. Note the closeness of the mass-flow ratios of curves 2 and 3 which bracket the critical.

The calculated pressure distributions, P_{th}, in Figs. 5(*a–c*) appear to be significantly lower than the corresponding measured pressure distribution, P_{ex}, in the downstream section of the channel. However, the reader should notice the false zero in the diagrams. These differences are no more than of the order of 6–10 percent and can reasonably be attributed to the uncertainties in the measurement of void fraction. The essential feature from the point of view of the thesis represented in this paper is that their topological aspects agree completely.

The computer program made it possible to calculate the variation $\theta(z)$ of the relaxation time. The corresponding curves have been drawn in Figs. 5(*a*, *b*, *c*). The values thus obtained are of the order of 1s for small values of void fraction, decreasing monotonically as α increases. The curves change slope near $\theta = 0.1$s and at a point which corresponds to α between 0.3 and 0.35. Such values of void fraction are commonly associated with a transition in the flow regime from bubble to plug or froth flow. The change in regime results in a rapid increase in the interfacial area between the phases which seems to favor fast evaporation.

In further support of the claim that the throat was not the seat of critical conditions, we paid special attention to the velocities which result from the necessary condition, $\Delta = 0$, for choking. These yielded a minimum of $w^* = 26$ m/s at $\alpha = 0.5$ which should be compared with the maximum computer flow velocity, $w_{max} = 10.6$; 14.9; 18.9 m/s listed in Table 1. These maximum flow velocities, all lower than the predicted critical velocity w^*, always occurred downstream from the throat in a cross-section just upstream from the exit. It is difficult to escape the conclusion that the data suggest that the flow was choked either at or close to the junction with the condenser. In order to gain additional confidence in the suitability of the nonequilibrium model for the analysis of two-phase flows of a single substance, we have performed calculations on the Moby Dick channel with the data of run 400, Fig. 5(*a*). The $\theta(\alpha)$ relation which resulted from applying the inverse procedure was used as a closure for system (4*a–e*), and integrations were performed at two supercritical and two subcritical mass-flow rates. The resulting pressure curves are shown in Fig. 6. These curves demonstrate that the pattern of trajectories resulting from the nonequilibrium model is topologically equivalent to that presented in [2] for the homogeneous model, supporting our claim that the critical point must be a saddle-type singularity. In contrast to results obtained with the homogeneous model, however, the critical point is no longer near the throat as evidenced by the turning point in Fig. 6 at $z = 0.435$ m.

It would, of course, be possible to locate the saddle point from first principles, and to trace the critical trajectory by

reverse integration, but we have concluded that doing so in the present example would exceed the scope of this paper.

7 Interpretation

It is re-emphasized that the present paper has not created more than an alternative interpretation which can be put on the Moby Dick experiments. According to this, so far only very tentative view, the Moby Dick experiments did not produce critical and supercritical flow conditions, but only flows which remained subcritical everywhere. The principal reasons for such a possible point of view are:

(*a*) Absence of any evidence that the "portrait" of solutions in the P,z plane contains a singular point (saddle or node).

(*b*) Absence of any evidence that flow at the narrowest point (throat) was critical.

(*c*) Absence of a common segment in the pressure distribution in Fig. 3 (and similar) when the back-pressure is varied at a substantially constant flow-rate (4360 m/s $\pm$ 0.6 percent); such a pattern is suggested by all one-dimensional mathematical models.

(*d*) Absence of any evidence of the occurrence of normal or oblique shock waves which would be expected if critical flow was produced at the throat or closely downstream from it.

(*e*) Absence of flow velocities which are larger than the critical velocities calculated with the aid of the necessary condition $\Delta = 0$.

(*f*) Closeness of the location of the maximum velocity to the exit near the very wide tube leading to the condenser.

All preceding features are consistent with the view that the channel was choked, but that the critical cross-section was close to the condenser.

Conclusion

In conclusion, it must be emphasized once more that the line of reasoning, and the underlying analysis, are of a qualitative nature only. The tentative suggestions are advanced with the hope that other workers in the field will reopen the problem for further rigorous study.

Acknowledgments

The authors wish to acknowledge the financial support received from the Office of Energy Engineering Research of the U.S. Department of Energy under Grant DE-FG02-87ER-13687. Special thanks are due to Dr. O. P. Manley, the Project Manager, for his continuous interest and encouragement.

References

1 Réocreux, M., "Contribution a l'étude des debits critiques en écoulement diphasique eau-vapeur," Ph.D. thesis, Université Scientifique et Medicale de Grenoble, 1974.

2 Bilicki, Z., Dafermos, C., Kestin, J., Majda, G., and Zeng, D. L., "Trajectories and Singular Points in Steady-State Models of Two-Phase Flows," *Int. J. Multiphase Flow*, Vol. 13, 1987, pp. 511–533.

3 Broer, L. J. F., "Characteristics of the Equations of Motion of a Reacting Gas," *J. Fluid Mech.*, Vol. 4, 1958, pp. 276–282.

4 Bauer, E. G., Houdayer, G. R., and Sureau, H. M., "A Non-Equilibrium Axial Flow Model and Application to Loss-of-Coolant Accident Analysis: The CLYSTERE System Code," Paper presented at the OECD/NEA Specialists' Meeting on Transient Two-Phase Flow, Toronto, Canada, Aug. 1976.

5 Bilicki, Z., Kestin, J., and Pratt, M. M., "The Effect of Three Closures on Critical Conditions in Two-Phase Flow with Unequal Phase Velocities," *Int. J. Multiphase Flow* , Vol. 14, 1988, pp. 507–517.

Corrosion of Pure Copper in Flowing Seawater Under Cavitating and Noncavitating Flow Conditions

R. J. K. Wood
Department of Chemistry,
The University,
Southampton S09 5NH U.K.

S. A. Fry
Department of Mechanical Engineering,
Polytechnic South West,
Plymouth, Devon, U.K.

This paper investigates the corrosion of pure copper in flowing seawater under cavitating and non-cavitating flow conditions. Experiments were conducted in a 10 mm × 20 mm working section with a 60 deg symmetrical wedge cavitation source. A copper sidewall specimen was held under potentiostatic control and its average corrosion current was measured under different flow conditions. To facilitate a detailed investigation of the flow field upon the current distribution over the specimen surface, further tests were carried out using a sidewall incorporating 24 mini-electrodes. Apart from some indication of cavity shielding, corrosion currents were little affected by the presence of cavitation during the incubation period (when no material was being removed). However, under similar cavitation conditions (but with material removal under steady-state erosion conditions) the corrosion currents approximately doubled.

Introduction

Many components in marine environments are subjected to high velocity seawater flows which can also be cavitating. Examples of such components on board a ship include the propellers, pumps, valves, and some pipe fittings. It is known that when both corrosion and cavitation erosion act together on such components, the resultant damage rate is greater than the sum of the individual damage rates for erosion and corrosion. The accelerating mechanisms which produce this effect (a synergistic effect) are not understood. Therefore, a research program has become necessary to provide information to ship designers and maintenance engineers to keep through life costs of ships to a minimum.

An earlier paper [1] by the authors reports on pure erosion, pure corrosion and combined cavitation erosion and corrosion tests from the early stages of the program. From these tests a synergistic effect was found to be present on copper when both cavitation erosion and corrosion act together. From the depth of penetration measurements made, the synergistic effect was found to be most marked when cavitation erosion occurs in the presence of mild corrosion. Under these conditions the depth of penetration is double the sum of the expected pure erosion and pure corrosion depths. The mechanism of this synergistic effect was not made clear by such tests, thus requiring further investigations which are reported in this paper.

The synergistic mechanism could be either an enhancement of the corrosion or an enhancement of the cavitation erosion. In this paper the influence of cavitation on corrosion currents is investigated. The corrosion currents measured are converted to a depth of penetration and comparison made with the actual depths, obtained by profilometry measurements. If good agreement is found, corrosion currents could be used to measure depth of penetration. By monitoring the corrosion currents over the surface of a specimen subjected to various cavitation conditions it is hoped that a clearer indication to the mechanism of the synergistic effect would result.

Before investigating the synergistic mechanism in greater detail, it is necessary to understand the corrosion process. For pure copper corroding in natural seawater, the following reactions are likely. These reactions apply to flowing or static conditions and also apply whether the copper is freely corroding or under potentiostatic control.

Anodic dissolution of copper:

$$Cu \dashrightarrow Cu^+ + e^- \quad (1)$$

Further reactions depend on whether a passive film is present. Efird [2] concludes that on an unfilmed site, Cu_2O is formed by precipitation:

$$2Cu^+ + 4Cl^- \dashrightarrow 2CuCl_2^- \quad (2)$$

followed if conditions allow by

$$2CuCl_2^- + H_2O \dashrightarrow Cu_2O + 4Cl^- + 2H^+ \quad (3)$$

or

$$2CuCl_2^- + 2OH^- \dashrightarrow H_2O + Cu_2O + 4Cl^- \quad (4)$$

Equation (2) describes the formation of copper-chloro complex $CuCl_2^-$. The diffusion of this ion from the electrode/

Contributed by the Fluids Engineering Division for publication in the JOURNAL OF FLUIDS ENGINEERING. Manuscript received by the Fluids Engineering Division January 10, 1989.

seawater interface to the bulk solution is the step which controls the rate of dissolution.

The corresponding cathodic reaction to the above anodic reactions is the reduction of oxygen:

$$O_2 + 2H_2O + 4e^- \text{ ---> } 4OH^- \quad (5)$$

Lal and Thirsk [3] were the first to report that the anodic dissolution of copper in static NaCl solutions exhibit pure concentration polarization and predicted anodic Tafel slopes of 60 mV/decade. The effect of flow over the corroding surface is to increase the anodic Tafel slope because of the increased diffusion of $CuCl_2^-$ ions. The diffusion of the ions away from the surface will increase as the flow increases, the reaction becomes more activation controlled with a Tafel slope of 120 mV/decade. Although some research has reported Tafel slope values at differing velocities, only relatively low velocities (< 3 m/s) have been investigated. In some engineering applications, higher velocities are encountered such as components on-board ships (pumps, valves and pipework) and ships' propellers. Such components are also subjected to cavitation attack with a very much increased damage rate. Velocities up to 14.7 m/s in the test section upstream of the cavitation source (corresponding to approximately 30 m/s across the surface of the specimen) are investigated in this paper under both cavitating and non-cavitating conditions.

The effect of high flow rates on the anodic polarization branch of copper in seawater using a corrosion cell mounted in a cavitation flow tunnel is reported. Both noncavitating and cavitating conditions are established within the same corrosion cell. The influence of cavitation can therefore be investigated to determine whether its presence increases the corrosion current. This will allow the dependence of corrosion current on cavitation conditions to be made with the determination of its roll in the synergistic effect between cavitation erosion and corrosion [1].

Experimental Method and Apparatus

Initial work has concentrated on obtaining the corrosion currents from a complete specimen surface area (17 cm^2). The tunnel used for these experiments has been previously described in reference [1]. High conductivity copper (99.9 percent Cu) specimens were used which acted as the working electrode of a three electrode corrosion cell mounted in the cavitation tunnel under the control of a Hi-Tek potentiostat DT 2101. A similar sized piece of cupro-nickel (Cu/Ni 70/30) was mounted directly beneath the working electrode to act as the secondary electrode (see Fig. 1). As the required result of potentiostatic control is to hold the potential of the electrolyte as near to the working electrode surface as possible at a demanded potential, the position of the reference (Ag/AgCl type) electrode is critical. The potentiostat monitors the potential of the tip of the reference electrode capillary and therefore this must be positioned as near to the working electrode surface as possible. This has been achieved in the present work by inserting the capillary tube through a hole in the copper specimen thereby flush mounting the tip of the capillary with the specimen surface.

The copper specimen, freshly polished with 600 grade emery paper, was mounted into the tunnel and allowed to stand in static seawater for several minutes on open circuit. This allowed the initial rapid build up of oxidation to occur before polarization curves were obtained. It was then connected to the potentiostat and the potential adjusted until the cell current was zero. This potential is known as the corrosion potential (E_{corr}) and for copper in static seawater has a value of about − 220 mV re Ag/AgCl. Once a steady value has been obtained, the potential was adjusted by 10 mV in the cathodic direction allowing the cell current to settle for one minute before noting the cathodic current and proceeding to make the potential more cathodic by a further 10 mV. This procedure was repeated until a range of 200 mV had been covered. The potential was then set to the equilibrium (E_{corr}) and then the anodic branch of the polarization curve was measured in the same way, moving in 10 mV steps anodically each minute, i.e., a sweep rate (ν) of 10 mV/min, with the corresponding anodic current noted. Readings were obtained up to a potential of E = 0.100V (re. Ag/AgCl).

To avoid the influence of oxide layers (formed during the anodic branch) on the cathodic readings the cathodic branch was investigated first. Whether the cathodic branch was obtained before or after the anodic branch had no effect on the anodic curve.

Polarization curves were obtained under no flow (v=0 m/s) and flowing conditions (v = 2, 8, 14.7 m/s) in the cavitation flow tunnel. At v = 14.7 m/s both noncavitating and cavitating conditions were investigated. A fairly low cavitation intensity (λ = 3.0, σ = 6.00 where λ is the nondimensional cavity length as shown on Fig. 2) was chosen with a large erosion area giving a mass loss rate of 4.1 mg/hr. Polarization curves in the incubation period (no mass loss period) and steady-state erosion periods (linear period of cumulative mass loss versus time) were investigated.

The measurements of current in the earlier experiments reported in [1] are an integration of the current distribution over the whole specimen surface. It would be advantageous to be able to measure this current distribution to enable local current

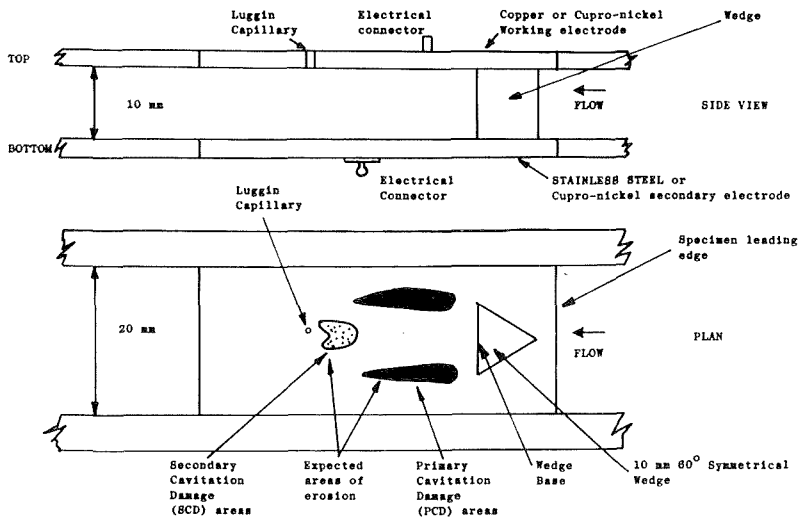

Fig. 1 Schematic diagram of the test section and corrosion cell

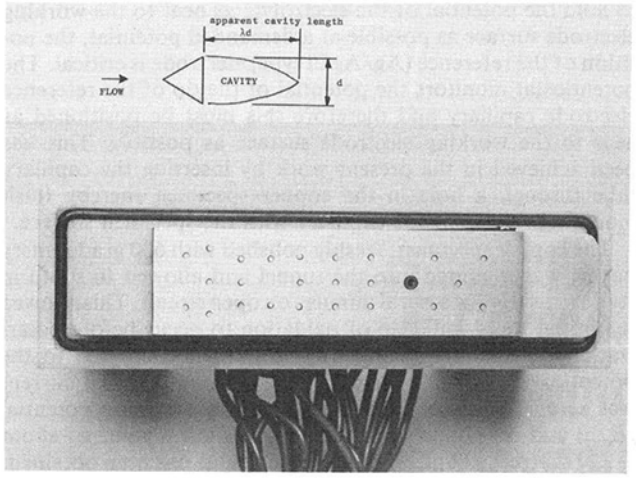

Fig. 2 Multi-electrode specimen

changes to be investigated. It is important that the influence of differing flow conditions on the current distribution is monitored. For example, the effect of a cavitating flow compared with a non-cavitating flow on the current distribution. Both cavitating and non-cavitating flow tests were carried out with the 60 deg symmetrical wedge in position; cavitation being suppressed by increasing the static pressure in the tunnel. The localized currents in the areas of combined cavitation erosion and corrosion are of particular interest.

In order to be able to measure the current distribution, the specimen surface must be split up into smaller individual electrically insulated electrode areas. These smaller or mini-electrodes must be flush mounted in the specimen surface to avoid affecting the hydrodynamic conditions. To be able to reproduce the current distributions of the above experiments, the mini-electrodes must be mounted into a similar specimen to that used previously. Mounting the mini-electrodes into the specimen ensures the electrodes monitor the local surface corrosion rates, the specimen being connected to the potentiostat as before with the potentiostat recording the corrosion current over the specimen surface area, referred to as the Main Electrode (M.E.) current. This does not include the mini-electrode surface areas. The individual mini-electrode currents are measured using a current follower circuit connected to each mini-electrode. Details of the circuit are given later.

The mini-electrodes were made from insulated copper transformer winding wire, the outside diameter of the wire chosen being 1.25 mm (insulation stripped). To enable the current distribution over the specimen surface to be measured, 24 mini-electrodes have been used. The arrangement of these electrodes over the specimen surface is illustrated on the photograph in Fig. 2. The mini-electrodes have been positioned such that, under high cavitation intensities ($\lambda = 1.6$, $\sigma = 6.22$, which corresponds to perceived peak noise in the laboratory). Four of the electrodes are in the primary cavitation damage area and two are in the secondary cavitation damage area, see Fig. 1. The remaining electrodes form three lines across the specimen width, spanning the specimen length. A standard copper specimen has been drilled and the winding wire glued into the holes with "Araldite." An electrical connection to the main copper electrode was made through a length of studding screwed into a tapped hole on the reverse side of the specimen. A special Delrin specimen holder was designed to seal the mini-electrode specimen in place in the Cavitation Erosion Corrosion Tunnel.

Figure 3 is a schematic of the data logging equipment used for the mini-electrode tests. For fast data acquisition, the current readings in micro-amps were logged by one of the Pet Computers (PET 1) and then stored on floppy disc. Further software plots out currents for a given mini-electrode against test duration for analysis of the longer duration experiments.

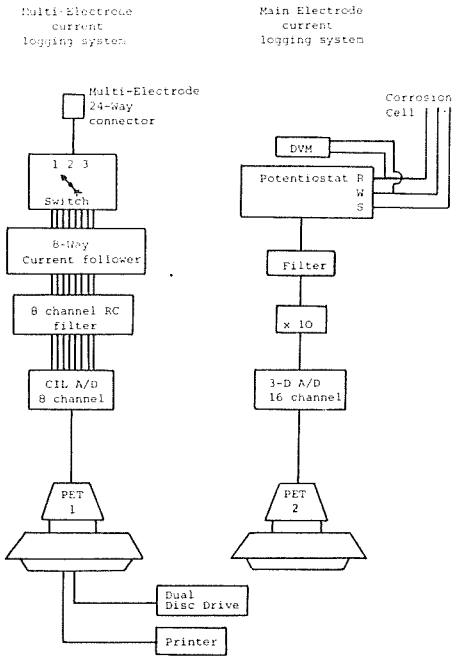

Fig. 3 Schematic of data logging equipment for multi-electrode experiments

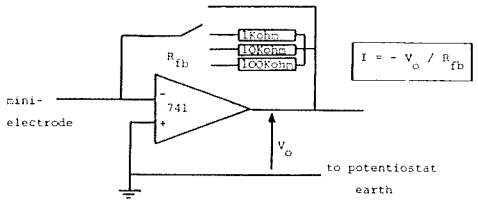

Fig. 4 Current follower circuit. Gain settings on current followers:
For R_{fb} = 1Kohm ..... 1μA = 1mV
= 10Kohm ..... 1μA = 10mV
= 100Kohm ..... 1μA = 100mV

As the Analogue to Digital (A/D) converter used in the experiments was limited to 8 channels, only 8 of the mini-electrodes could be logged at any one time. Hence, a switch was required to enable sets of 8 electrodes to be logged successfully. Once all the electrodes have been logged the current data is stored on floppy disc. From the switching box the signal travels to the current followers. A multi-way current follower was used. Care was taken to connect together the earths of the current follower box and of the potentiostat to eliminate floating earth problems. The circuit for each current follower is illustrated in Fig. 4.

As Fig. 4 shows, the current followers have several gain settings which can be used, depending on the magnitude of the current being measured. The outputs of the current followers are connected to an RC Low Pass Filter box which, in turn, is connected to the CIL type A/D converter under control of the PET 1 computer. The A/D converter has also three gain settings giving 0.1, 1 or 10 Volts full scale deflection. The gain settings selected on both current followers and the A/D converter are entered into the computer program before each experiment.

The second Pet Computer (PET 2) logs the main copper electrode current from the output of the potentiostat. Before the signal enters the 3-D type A/D converter it passes through an active 5 Hz Low Pass filter and is then amplified by 10. The signal requires amplification as the 3-D type A/D converter has only 8 bit resolution. The software for this data logging has no data storage facility and therefore requires the experimenter to note current readings from the computer monitor.

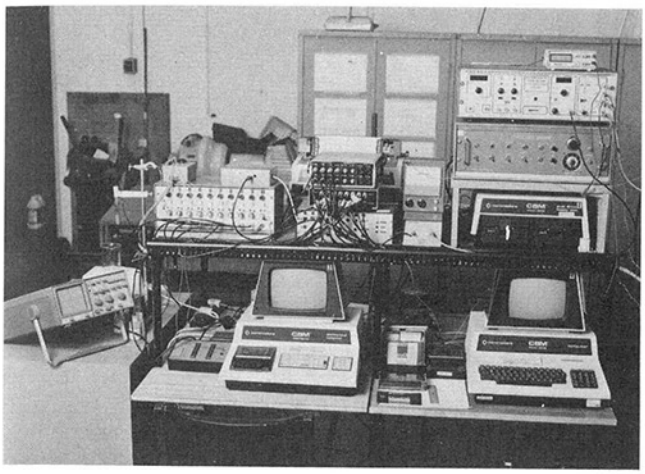

Fig. 5 Dual data logging system

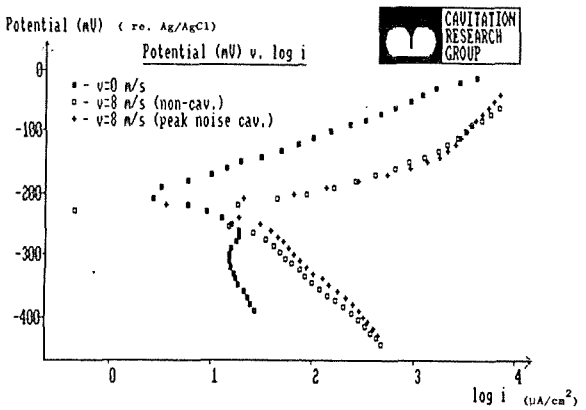

Fig. 6 Polarization curves for copper in seawater for $v = 0$ m/s and $v = 8$ m/s obtained from the C.E.C. tunnel corrosion cell

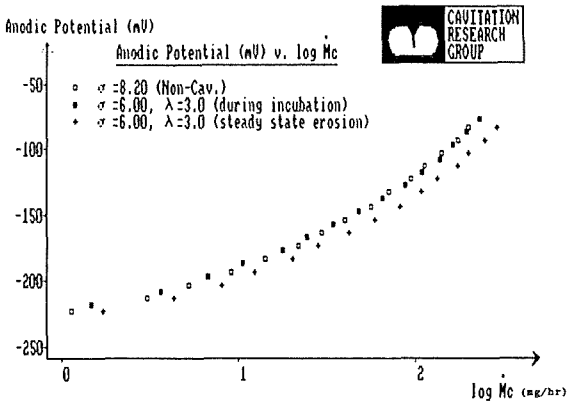

Fig. 7 Anodic polarization curves for copper in seawater at $v = 14.7$ m/s under various cavitation conditions

The photograph in Fig. 5 shows the dual data logging system used in these experiments. To ensure the CIL type A/D converter received a clean signal, care was taken to screen possible sources of noise. This included using screened cables where possible and encasing the computer monitors with earthed mild steel sheets.

Multi-Electrode Test Program. Two high values of η (where $\eta = E - E\text{corr}$) have been investigated using the multi-electrode specimen, $\eta = +50$ mV and $\eta = +100$ mV, under differing cavitation conditions (noncavitating, peak noise cavitation $\lambda = 1.6$, $\sigma = 6.22$ and $\lambda = 3.0$, $\sigma = 6.00$) at $v = 14.7$ m/s. The above tests are 5 minutes in duration to protect the specimen surface from cavitation damage. Damage to the surface might lead to the short circuiting of the mini-electrodes as the plastic deformation of the surface could break down the insulation around each electrode.

After the above tests were completed, a longer term test was carried out at $\eta = +50$mV under peak noise cavitation for a similar duration to that of the tests described in [1] (i.e., 4.5 hours). These tests allow currents from the mini-electrodes to be monitored throughout the test duration. Mini-electrodes positioned in the areas of bubble collapse are of particular interest as their effect on the local corrosion rate can be investigated.

Multi-Electrode Test Procedure. After polishing with 600 grade emery paper, a resistance check is performed on each electrode with a Digital Voltmeter to confirm that each electrode is insulated.

After the polished specimen and holder were clamped into position, the required cavitation and corrosion conditions were established and allowed to stabilize before readings were taken. The corrosion conditions were set up using the potentiostat to control the main electrode potential, as in the earlier experiments. The acquisition of the corrosion current from the mini-electrodes and the main electrode were under software control. For the short duration tests, three sets of current data were acquired for each electrode at one minute intervals. An average value of these three readings for each mini-electrode was used in subsequent analysis. In the case of the longer duration tests, a complete set of mini-electrode current readings were acquired at 5 minute intervals throughout the 4.5 hour test.

Discussion of the Results

Polarization Curve Results. Figure 6 illustrates a typical polarization curve (E versus log i) for copper in static seawater where i is current density. The anodic branch gives a straight line over a wide range of potentials. In contrast the cathodic branch is affected by diffusion of oxygen to the electrode surface and is therefore nonlinear. The influence of flow (i.e., $v = 8$ m/s) for both cavitating and noncavitating flow is also shown in Fig. 6. Imposing a flow over the specimen surface ensures the straightening of the cathodic branch curve and the shifting of the curves to the right on the E versus log i plot. The influence of cavitation is less easily seen with no visible effect on the anodic branch though some increase in current on the cathodic branch is seen. It should be noted that the cavitation conditions studied were set up for a very short period which meant that the specimen surface was only lightly damaged and remained within the incubation period.

A further experiment to look at the effect of cavitation on the anodic branch during steady state erosion (SSE) was also carried out. The results are presented in Fig. 7. A velocity of $v = 14.7$ m/s was studied. As seen in Fig. 7, the influence of cavitation during incubation is minimal when comparing the noncavitating curve with the cavitating curve during incubation. However, during SSE a measurable increase in the current occurs indicating that the synergistic effect is most likely to be measurable during SSE rather than during incubation.

Multi-Electrode Test Results

Short Duration Tests. The current readings obtained during the short term can be converted to depth of penetration values using Faraday's Law. For non-cavitating flow, the short term test values can be used to predict depth of penetration for longer test durations under similar potentiostatic and flow conditions. Figure 8 illustrates a typical plot of the projected depths of penetration for 4.5 hours test duration based on a short term test. The depths presented are for $\eta = +100$ mV under noncavitating conditions at $v = 14.7$ m/s, and are plot-

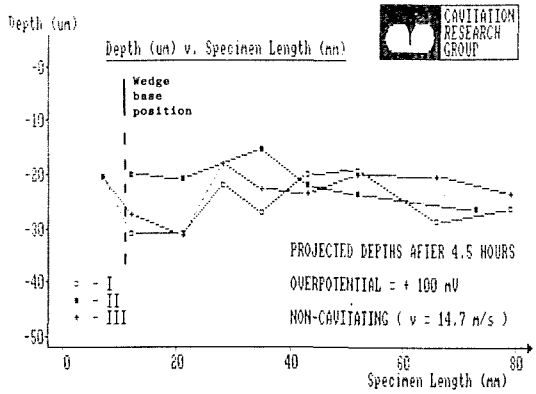

Fig. 8 Projected depths for 4.5 hours based on $\eta = +100$ mV short term tests (noncavitating)

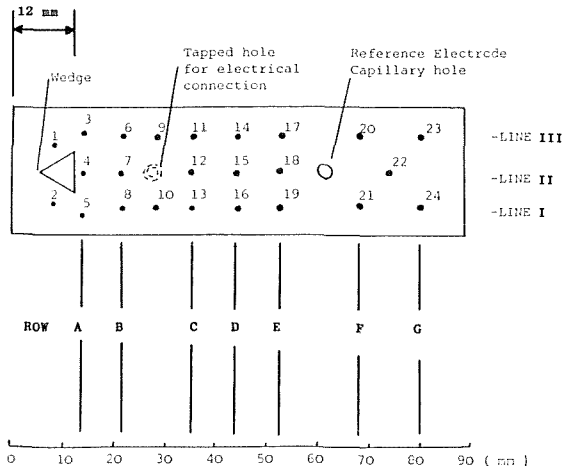

Fig. 9 Numbering of mini-electrodes. Electrodes in the primary cavitation damage area = 6, 8, 9, and 10. Electrodes in the secondary cavitation damage area = 15 and 18.

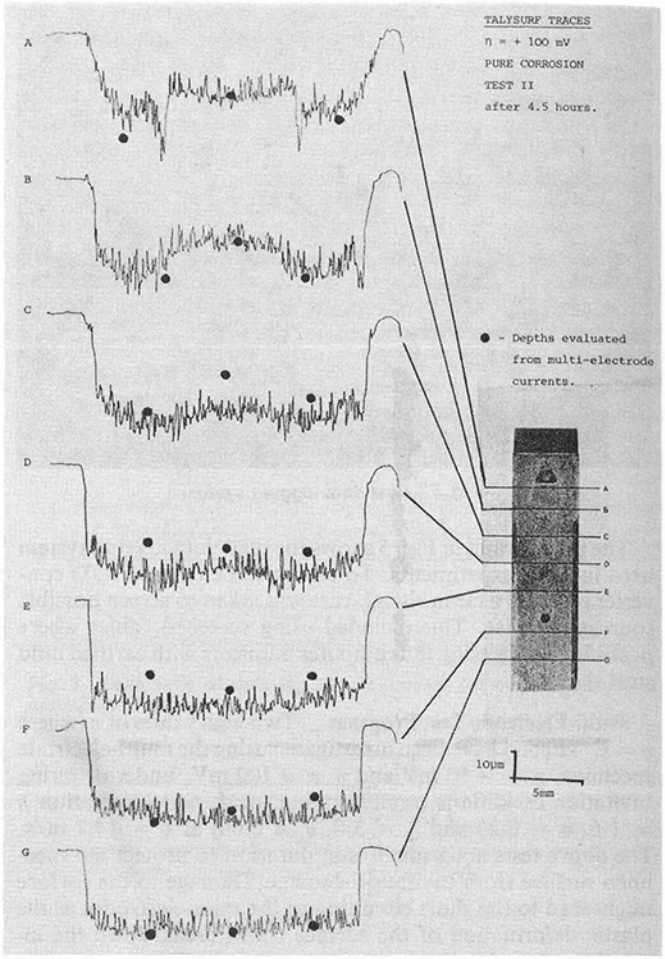

Fig. 10 Comparison of talysurf traces after 4.5 hours with projected depths evaluated from short duration (5 minutes) multi-electrode. $\eta = +100$mV (noncavitating)

ted against the distance along the specimen from the leading edge (Fig. 1). As the mini-electrodes lie in three lines across the specimen width, the values from them have been plotted out separately forming plots I, II, and III on Fig. 8, plot I being the bottom line of electrodes, as shown in Fig. 9, plot II the middle line and plot III the top line.

As expected, the maximum currents (penetration depths) occur in the areas of maximum shear flow (extreme turbulence), adjacent to high bulk fluid velocities (i.e., electrodes 3, 5, 6, and 8). For plots I and III this is seen to be the case. Moving further downstream from these electrodes the current decreases and then recovers slightly towards the trailing edge of the specimen. For Plot II, the center line of the specimen, the currents recorded in the wedge wake are much less than plots I and III until about 40 mm downstream from the leading edge. At this position on the specimen, and for positions further downstream, the currents have recovered to similar values to those of plots I and III. It is believed that the low current measured just downstream of the edge is due to the low flow velocity in that part of the wake. Further downstream the measured currents across the specimen (plots I, II, and III) become nearly equal because of turbulent mixing of the wake with the outer flow.

A useful check of the depth of penetration values can be made by comparing them with the actual depths from the Talysurf tests under non-cavitating flow at $v = 14.7$ m/s and $\eta = +100$ mV). Such a comparison is illustrated on Fig. 10. The Talysurf traces A to G were taken at positions on the specimen coinciding with certain rows of electrodes as shown in Fig. 11. Good agreement between the projected depths and actual depths can be seen. Therefore, for non-cavitating flows the mini-electrode currents from short term tests can be converted to depth values and used to predict depth of corrosion attack.

The effect of changing cavitation conditions can also be investigated by monitoring mini-electrode currents. Figure 11 shows mini-electrode currents versus specimen length for $\eta = +100$ mV, $v = 14.7$ m/s and three different cavitation conditions: noncavitating, peak noise cavitation ($\lambda = 1.6$, $\sigma = 6.22$) and cavitation with $\lambda = 3.0$, $\sigma = 6.00$. The effect of cavitation can be seen by comparing Figs. 11(*b*) and 11(*c*) with 11(*a*). The effect of peak noise cavitation on the current plots can only be seen in the region immediately downstream of the wedge base (compare Figs. 11(*a*) with 11(*b*)). Within this region, plots I and III have slightly increased current values while plot II has decreased values. The decrease in current seen in plot II could indicate shielding of the specimen by bubbles trapped in the dead water region.

The effect of $\lambda = 3.0$, $\sigma = 6.00$ cavitation conditions are seen when Figs. 11(*a*) and 11(*c*) are compared. The presence of a large apparent cavity length appears to have an effect upon the current plots similar to the shorter peak noise cavity length. Plots I and III appear unaffected in the cavitation damage areas (damage areas are indicated on Figs. 11(*b*) and 11(*c*)) which indicates that there is no additional corrosion due to the presence of cavitation.

The above current plots are obtained while the specimen is in the cavitation erosion incubation period (i.e., no mass loss). To investigate whether there is any additional corrosion due

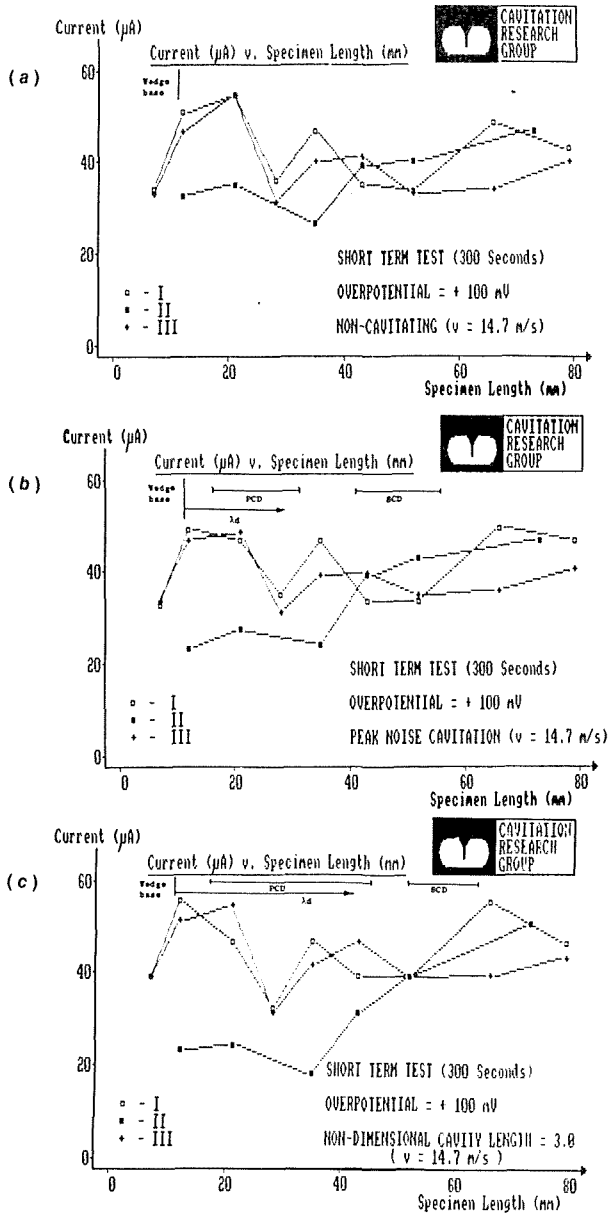

Fig. 11 The effect of cavitation conditions on the measured current distribution. Short term tests (300 seconds). η = + 100 mV. Flow velocity = 14.7 m/s

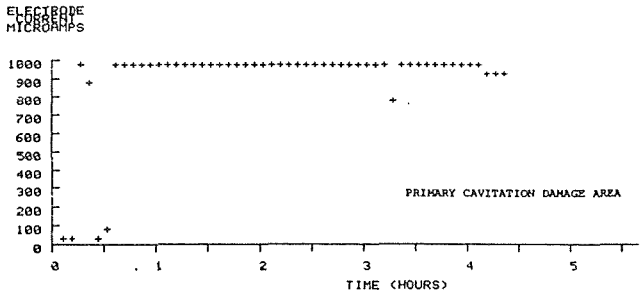

Fig. 12 Mini-electrode no. 8 current readings for 4.5 hour test under peak noise cavitation, η = +50 mV

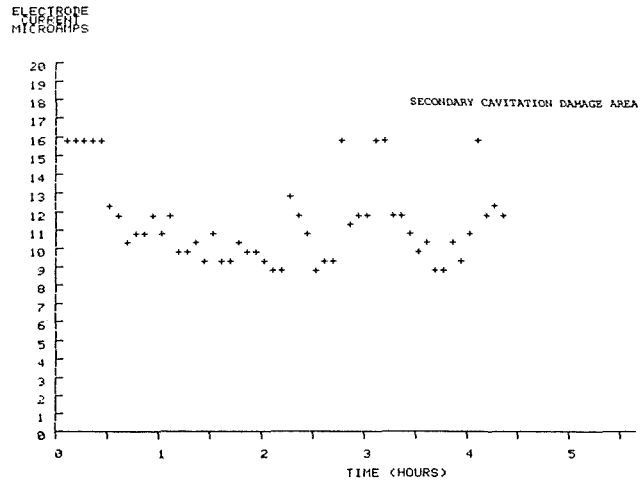

Fig. 13 Mini-electrode no. 15, current readings for 4.5 hour test under peak noise cavitation conditions, η = +50 mV

Table 1 Mini-electrode currents recorded within the primary cavitation damage areas on a copper specimen

λ = 1.6, v = 14.7 m/s, η = +50 mV, Temp = 26°C.
Mean main electrode current = 14.6mA

Electrode No.	Short duration Test 5 mins. (μA)	Long duration Test* (μA)	Duration before shorting (mins)
6	11.2	21.6	40
8	10.4	31.3	15
9	5.9	17.4	115
10	7.2	19.8	70
Average current	8.7	22.5	

*Long duration test currents averaged over the time before shorting.

to the presence of cavitation in the cavitation damage areas, requires a test of longer duration to include the steady state erosion period (i.e., constant mass loss rate). From the discussion on the polarization curves reported earlier in this paper, it was found that during the steady state erosion period an additional corrosion current was detected.

Long Duration Tests. The long duration test was conducted under peak noise cavitation conditions (λ = 1.6, σ = 6.22) at v = 14.7 m/s with η = +50 mV. It should be noted that the values for electrodes 8, 10, and 16 are not present on the long duration test plots as they shorted out during the test, the electrodes 8 and 10 being in the primary cavitation damage area (see Fig. 1) were expected to short out. Electrode 16 periodically shorted out during the test. Electrodes 14 and 17 were also corrupted by periodic shorting.

The mini-electrode currents of greatest interest are those from within the cavitation affected areas. Figures 12 and 13 show currents from electrodes 8 and 15 which are in the primary cavitation damage area and the secondary cavitation damage area respectively. It can be seen from Fig. 12 that in the primary cavitation damage area the mini-electrode No. 8 shorted out after 15 minutes test duration. The mini-electrode remained insulated for a short period before further damage caused permanent shorting. This was typical of the four mini-electrodes in the primary cavitation damage area. Prior to the shorting of these electrodes, their average current readings were 22 μA. This is double the average current reading for the equivalent 5 minute short duration test (9 μA, see Table 1).

A possible cause of this current increase recorded during long duration tests would be local or crevice corrosion occurring at the mini-electrode/main electrode interface. Optical investigations revealed no evidence of such corrosion.

Two other factors could account for this increase in current. First, it could be due to an increase in the local corrosion rate caused by roughening of the surface as a result of material

removal by cavitation since the corrosion rate is dependent upon the level of turbulence. Second, as the only difference between the short and long term tests is that material removal is occurring in the long duration test, a process which produces fresh (reactive) copper surfaces. This could increase the current. A further investigation using the multi-electrode technique is required to determine which of the above explanations is correct.

Conclusions

Multi-Electrode Experiments. A 24 mini-electrode specimen has been used to monitor the current distribution over a copper specimen surface. A test program consisting of short and long duration test has been completed to investigate the effect of changing cavitation conditions on the current distribution over the specimen surface.

Short Duration Tests. The mini-electrode currents have been converted into depth of penetration values to allow a comparison with the Talysurf profiles obtained in previous experiments [1]. Projected depths, evaluated from the short duration tests (5 minutes), were found to be in good agreement with the Talysurf profiles of a specimen subjected to similar corrosion conditions. Therefore, for the limited cases studied, current measurements over a short time period could be used to predict corrosion penetration depths.

The current distributions obtained using the multi-electrode specimen have been related to the flow conditions in the corrosion cell. The presence of cavitation in the corrosion cell affects the current distribution (i.e., penetration depths) downstream of the wedge. The main effect caused by cavitation is to lower the corrosion current in the dead water region directly behind the wedge. No evidence was found of any additional corrosion due to the presence of cavitation in the cavitation damage areas while the specimen was in the incubation period.

Long Duration Tests. As concluded in the last section, for a surface exposed to cavitation bubble collapse within the incubation period, no additional corrosion currents due to the presence of cavitation in the damage zones were measurable. The long duration tests enabled the comparison of these currents with currents obtained from the same electrodes but while mass loss was occurring. The electrode currents from the long duration tests within the primary cavitation damage areas showed, on average, a doubling of the short duration currents. This increase in current has already been noticed when comparisons between polarization curves obtained during the incubation period and the steady state erosion period were made. The doubling of the current is likely to be a result of fresh (highly reactive) surfaces being exposed to the seawater by material erosion.

An alternative reason to cause a doubling of the current is that of increased turbulence due to the increase in surface roughness. The turbulence level is likely to be a maximum during the steady state erosion period as the surface roughness is greatest during that period. A study of the dependence of the corrosion rate on the surface roughness is required to confirm this point.

Further tests are required, using the techniques described in this paper to determine the synergistic mechanism. Not enough information is available to say whether the mechanism is either one of enhanced corrosion or enhanced cavitation erosion.

Uncertainties at 20:1 odds

		Uncertainty
Sigma	σ	± 0.01
Nondimensional cavity length	λ	± 0.1
Mass loss rate	M	± 0.1 mg/hr
Overpotential	η	± 0.5 mV
Mini-electrode currents	I	Within range ± 0.5 μA to ± 5.0 nA
Main electrode currents	I	± 0.1 mA

References

1 Wood, R. J. K., and Fry, S. A., "The Synergistic Effect of Cavitation Erosion and Corrosion for Copper and CuNi in Seawater," ASME JOURNAL OF FLUIDS ENGINEERING, Vol. 111, Sept. 1989, pp. 271–277.

2 Efird, K. D., "Potential-pH Diagrams for 90/10 and 70/30 Cu-Ni in Seawater," *Corrosion-Nace*, Vol. 31, No. 3, Mar. 1975, pp. 77–83.

3 Lal, H., and Thirsk, H. R., "The Anodic Behaviour of Copper in Neutral and Alkaline Chloride Solutions," *J. Chem. Soc.*, 1953, pp. 2638–2644.

M. Hanif Chaudhry
Professor.

S. Murty Bhallamudi
Graduate Student.

Department of Civil and Environmental Engineering, Washington State University, Pullman, WA 99164

C. Samuel Martin
Professor.

M. Naghash
Graduate Student.

School of Civil Engineering, Georgia Institute of Technology, Atlanta, GA 30332

Analysis of Transient Pressures in Bubbly, Homogeneous, Gas-Liquid Mixtures

Flow of a gas-liquid mixture in a piping system may be treated as a pseudo-fluid flow if the mixture is homogeneous and the void fraction is small. The governing equations for such flows are a set of nonlinear partial differential equations with pressure dependent coefficients. Shocks may be produced during transient state conditions. For numerical integration of these equations, two second-order explicit finite-difference schemes are introduced. To verify validity of the computed results, they are compared with the experimental results.

Introduction

Two-component flows occur in piping systems in several industries, such as nuclear power plants, chemical processes, petroleum industries, geothermal power plants, and in sewage pipelines (Pearsall [12]). Gases may be entrained in other liquid-carrying pipelines due to cavitation (Wiggert and Sundquist [16]), gas release during low-pressure transients (Swaffield [15], Kranenburg [5], Papadakis [11]), liquid-column separation (Safwat [13], Safwat and Polder [14]), or by an hydraulic jump (Kalinkske and Robertson [4]). The flow in these cases is, therefore, a mixture of gases and liquids. Unlike in a pure liquid in which the pressure wave velocity is constant, the wave velocity in gas-liquid mixtures varies with the pressure. Thus, the coefficients of governing equations are pressure dependent and consequently the analysis of transients in the two-component flows is more complex and difficult than in single-component flows. In addition, shock waves may form due to the steepening of pressure waves limiting the use of method of characteristics, usually employed for solving the governing equations. The complexity of analysis increases if the individual components are moving with different velocities (separated flow model) as compared to if they have the same velocity (homogeneous model).

The gas-liquid mixture may be treated as a pseudo-fluid if the void fraction is small and the mixture is homogeneous. This assumption simplifies the analysis considerably and usually produces acceptable results for typical engineering applications. Transient flow of homogeneous gas-liquid mixtures are described by a set of nonlinear hyperbolic partial differential equations. A closed-form solution of these equations is not available. Therefore, numerical methods are used for their solution (Martin and Padmanabhan [6], Martin et al. [7], Padmanabhan et al [10]). The coefficients in these equations are pressure dependent, which causes difficulties in the numerical solution. Since shocks may be produced during the transient-state conditions, only those methods which can handle shocks without special treatment are more suitable for their application. The method of characteristics and a number of finite-difference schemes have been used for the analysis of transient, two-component flows. The method of characteristics requires isolation of the shock and most of the other methods are first-order accurate which smears the shocks. Wiggert et al. [17] and Martin and Naghash [8] have used implicit methods to obtain a solution without isolating the shock.

In this paper, two new second-order explicit finite-difference schemes are introduced for the analysis of transient two-component flows. These schemes have been used in computational fluid dynamics and have been applied recently to solve the transient problem with only liquid in the pipe (Chaudhry and Hussaini [2]). They are second-order accurate both in space and time. Higher-order methods require more computational effort per time step; however, fewer computational nodes may be used to obtain the same accuracy by using these methods. In addition, higher-order methods reproduce sharper shocks compared to the first-order methods. The computed results are compared with the experimental results to demonstrate validity of the simplified model and of the computational procedures.

Governing Equations

As clearly formulated by Yadigaroglu and Leahy [18], the one-dimensional equations of two-phase flow constitute a six-

Contributed by the Fluids Engineering Division for publication in the JOURNAL OF FLUIDS ENGINEERING. Manuscript received by the Fluids Engineering Division December 6, 1988.

equation set of mass, momentum, and energy conservation. In addition to two equations for each phase, constitutive relationships are necessary for mass, momentum, and heat transfer at the interfaces and other surfaces, as well as wall friction. In general, however, the six separated flow equations, whether drift flux or other form, are not commonly used in their entirety. Indeed, for many systems the gas and liquid phase equations are combined to yield a pseudo-fluid equation that does not allow slip. Such an assumption is certainly reasonable for systems with very low void fractions and finely distributed bubbles, which was the case with the experiments reported herein.

The separate unsteady one-dimensional mass conservation equations are

$$(\partial/\partial t)[\rho_g \alpha A] + (\partial/\partial x)[\rho_g \alpha A V_g] = \Gamma A \quad (1)$$

for the gaseous phase, and

$$(\partial/\partial t)\{[\rho_l(1-\alpha)]A\} + (\partial/\partial x)\{[\rho_l(1-\alpha)]AV_l\} = -\Gamma A \quad (2)$$

for the liquid phase, where P = absolute pressure, x = distance along the pipeline, A = the cross-sectional area of the conduit, ρ_s = mass density of the gaseous phase, ρ_l = mass density of the liquid phase, α = the void fraction, V_g = the average velocity of the gaseous phase, V_l = the average velocity of the liquid phase, t = time, and Γ is the mass transfer between phases.

For flows with little or no slip between phases ($V_g \approx V_l = V$) the summation of equations (1) and (2) results in

$$(\partial/\partial t)\{[\rho_g \alpha + \rho_l(1-\alpha)]A\} + (\partial/\partial x)\{[\rho_g \alpha + \rho_l(1-\alpha)]AV\} = 0 \quad (3)$$

Defining the mass density of the mixture as

$$\rho_m = \rho_g \alpha + \rho_l(1-\alpha) \quad (4)$$

the continuity equation becomes

$$(\partial/\partial t)[\rho_m A] + (\partial/\partial x)[\rho_m A V] = 0 \quad (5)$$

The combined momentum equation representing the two phases undergoing horizontal flow is

$$(\partial/\partial t)\{[\rho_g \alpha + \rho_l(1-\alpha)]AV\} + (\partial/\partial x)\{[\rho_g \alpha + \rho_l(1-\alpha)]AV^2\} + A(\partial P/\partial x) + \pi D \tau_w = 0 \quad (6)$$

where τ_w = the wall (boundary shear stress), and D = the internal diameter of the pipe. The absolute value of the mixture velocity V is invoked in order to allow for boundary shear reversal as the flow reverses. The boundary shear relationship is based upon

$$\tau_w = (f/8)\,\rho_l\,(1-\alpha)\,V_l^2 \quad (7)$$

where f = the Darcy-Weisbach resistance coefficient. For this quite small void fraction flow, for which $(1-\alpha) = 1$, the boundary shear is approximated by $(f/8)\,\rho_l V^2$.

As shown by Martin, Padmanabhan, and Wiggert [7] mathematical techniques can be applied to the above conservation equations to yield the wave speed of the mixture. Assuming the liquid to constitute a large heat sink, the speed of sound under isothermal conditions for this homogeneous mixture at very low void fractions can be reduced to

$$a_m = \{\rho_m [\alpha/P + 1/(\rho_l a_l^2)]\}^{-1/2} \quad (8)$$

where a_l = the wave speed for single phase liquid only. The above equations do not allow for any effects of surface tension. By comparing the computed and measured wave speeds, Martin and Padmanabhan [6] showed that equation (8) yields satisfactory results.

Using the definition of mixture density ρ_m and pseudo-fluid wave speed a_m the governing equations for a two-phase mixture having a very low void fraction and insignificant slip become

$$\frac{\partial P}{\partial t} + \rho_m a_m^2 \frac{\partial V}{\partial x} = 0 \quad (9)$$

$$\frac{\partial V}{\partial t} + \frac{1}{\rho_m}\frac{\partial P}{\partial x} + \frac{f}{2D} V|V| = 0 \quad (10)$$

As is true for single-phase liquid flows at quite low Mach numbers, the convective acceleration terms have been dropped from these equations. Although the speed of sound can be considerably lower for a gas-liquid mixture than for the single-phase liquid itself, in these experiments the Mach number is still quite low because of relatively small velocities of the flowing phases.

The equation of state for the gas constitutes the third equation needed to solve the three dependent variables V, P, and α. For isothermal conditions, this is given as

$$\alpha P = \alpha_0 P_0 \quad (11)$$

where subscript 0 indicates the values at the initial conditions.

Solution of Governing Equations

Two second-order accurate explicit finite-difference methods are presented in the following paragraphs. Although these schemes have been applied for analyzing a number of problems in computational fluid dynamics, they have not been used for computing the transient two-component flows. In the following presentation, an asterisk (*) denotes the predicted values; subscript i refers to the space node and the superscript j refers to the time level (Fig. 1). A pipe is divided into n equal-length reaches, with the first section numbered as 1 and the last section numbered as $n + 1$. Each section is called a node. The values

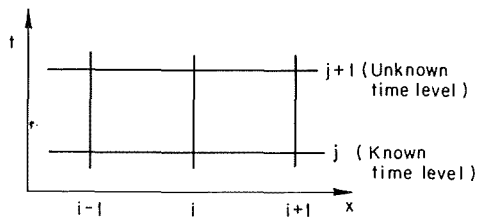

Fig. 1 Computational grid

Nomenclature

a = wave speed
D = pipe diameter
f = Darcy-Weisbach friction factor
G = air mass flow rate
g = subscript for the gas phase
i = subscript for the space node
j = superscript for the time node
l = subscript for the liquid phase
m = subscript for the gas-liquid mixture
n = number of reaches into which pipe is divided
P = absolute pressure
R = $f\Delta t/(2D)$
r = $\Delta x/\Delta t$
t = time
Δt = time interval
V = velocity
V = volume
x = distance
Δx = reach length
0 = subscript for the initial steady-state conditions
$*$ = superscript for indicating the predicted values
α = void fraction
ρ = density
η = unknown multiplier
λ = characteristic direction

of V, P, and α are assumed to be known at all nodes at j time level (referred to as the known time level) and their values are to be determined at the $j+1$ time level (referred to as the unknown time level). The known values at the known time level j may be the initial conditions or they may be computed during the previous time step.

MacCormack Scheme

The MacCormack scheme [9] is second-order accurate in both space and time. It is comprised of two steps: predictor and corrector. One-sided finite difference approximations are used for the spatial derivatives in each of these steps. For example, forward finite-difference may be used in the predictor part and backward finite differences in the corrector part. Another alternative would be to use the backward finite differences in the predictor part and forward finite differences in the corrector part. MacCormack recommends using these alternatives in a sequence, i.e., the first alternative at one time step, the second alternative during the next time step, followed by the first alternative again.

In the first alternative, the spatial derivatives are replaced as follows:

Predictor Part:

$$\frac{\partial F}{\partial x} = \frac{F_i^j - F_{i-1}^j}{\Delta x} \tag{12}$$

Corrector Part:

$$\frac{\partial F}{\partial x} = \frac{F_{i+1}^* - F_i^*}{\Delta x} \tag{13}$$

In these equations, F is used for brevity to represent both V and P. Substituting these approximations for $\partial P/\partial x$ and $\partial V/\partial x$ and simplifying the resulting equations, the following equations are obtained:

Predictor Part:

$$P_i^* = P_i^j - r(\rho_m a_m^2)_i^j (V_i^j - V_{i-1}^j) \tag{14}$$

$$V_i^* = V_i^j - r\left(\frac{1}{\rho_m}\right)_i^j (P_i^j - P_{i-1}^j) - RV_i^j|V_i^j| \tag{15}$$

in which $r = \Delta t/\Delta x$ and $R = f\Delta t/(2D)$.

Corrector Part:

$$\tilde{P}_i = P_i^* - r(\rho_m a_m^2)_i^* (V_{i+1}^* - V_i^*) \tag{16}$$

$$\tilde{V}_i = V_i^* - r\left(\frac{1}{\rho_m}\right)_i^* (P_{i+1}^* - P_i^*) - RV_i^*|V_i^*| \tag{17}$$

The values of V and P at the $j+1$ time level may be computed from the following equations:

$$P_i^{j+1} = \frac{1}{2}(P_i^j + \tilde{P}_i) \tag{18}$$

$$V_i^{j+1} = \frac{1}{2}(V_i^j + \tilde{V}_i) \tag{19}$$

In the second alternative, the above equations are:

Predictor Part:

$$P_i^* = P_i^j - r(\rho_m a_m^2)_i^j (V_{i+1}^j - V_i^j) \tag{20}$$

$$V_i^* = V_i^j - r\left(\frac{1}{\rho_m}\right)_i^j (P_{i+1}^j - P_i^j) - RV_i^j|V_i^j| \tag{21}$$

Corrector Part:

$$\tilde{P}_i = P_i^* - r(\rho_m a_m^2)_i^* (V_i^* - V_{i-1}^*) \tag{22}$$

$$\tilde{V}_i = V_i^* - r\left(\frac{1}{\rho_m}\right)_i^* (P_i^* - P_{i-1}^*) - RV_i^*|V_i^*| \tag{23}$$

The values of V_i^{j+1} and P_i^{j+1} may now be determined from equations (18) and (19) and then the value of α from the equation (11).

Note that these equations yield the values at the interior points only, i.e., at $i = 2,3, \ldots, n$; values at the boundary nodes are computed from the boundary conditions, as discussed later. This method is stable if $a_m\Delta t \leq \Delta x$.

Gabutti Scheme

In this scheme (Gabutti [3]), the governing equations are first transformed into the characteristic form and then the partial derivatives are replaced by the finite difference approximations. Like the MacCormack scheme, it is a predictor-corrector scheme. However, the predictor part is further subdivided into two parts.

By multiplying equation (10) by η and adding it to equation (9)

$$\left[\frac{\partial P}{\partial t} + \frac{\eta}{\rho_m}\frac{\partial P}{\partial x}\right] + \eta\left[\frac{\partial V}{\partial t} + \frac{\rho_m a_m^2}{\eta}\frac{\partial V}{\partial x}\right] + \eta\frac{f}{2D}V|V| = 0 \tag{24}$$

Let

$$\eta/\rho_m = dx/dt = \rho_m a_m^2/\eta \tag{25}$$

It follows from this equation that the characteristic directions, λ^+ and λ^-, are

$$\lambda^+ = dx/dt = a_m \tag{26}$$

$$\lambda^- = dx/dt = -a_m \tag{27}$$

By utilizing equations (25)-(27), equation (24) may be written as

$$\left[\frac{\partial P}{\partial t} + \lambda^+\frac{\partial P^+}{\partial x}\right] + \rho_m a_m\left[\frac{\partial V}{\partial t} + \lambda^+\frac{\partial V^+}{\partial x}\right] + \rho_m a_m\frac{f}{2D}V|V| = 0 \tag{28}$$

and

$$\left[\frac{\partial P}{\partial t} + \lambda^-\frac{\partial P^-}{\partial x}\right] - \rho_m a_m\left[\frac{\partial V}{\partial t} + \lambda^-\frac{\partial V^-}{\partial x}\right] - \rho_m a_m\frac{f}{2D}V|V| = 0 \tag{29}$$

By adding equations (28) and (29) and simplifying

$$\frac{\partial P}{\partial t} + 0.5\left[\lambda^+\frac{\partial P^+}{\partial x} + \lambda^-\frac{\partial P^-}{\partial x}\right] + 0.5\rho_m a_m\left[\lambda^+\frac{\partial V^+}{\partial x} - \lambda^-\frac{\partial V^-}{\partial x}\right] = 0 \tag{30}$$

By subtracting equation (28) from equation (29) and simplifying

$$\frac{\partial V}{\partial t} + 0.5\left[\lambda^+\frac{\partial V^+}{\partial x} + \lambda^-\frac{\partial V^-}{\partial x}\right] + \frac{0.5}{\rho_m a_m}\left[\lambda^+\frac{\partial P^+}{\partial x} - \lambda^-\frac{\partial P^-}{\partial x}\right] + \frac{f}{2D}V|V| = 0 \tag{31}$$

Equations (30) and (31) are referred to as the equations in λ-form. Note that the spatial derivatives are marked with superscripts + and − to indicate the characteristic directions along which these derivatives are approximated (Fig. 2). Substitution of finite-difference approximations for the time derivatives into equations (30) and (31) yields the predicted values of V_i^* and P_i^*:

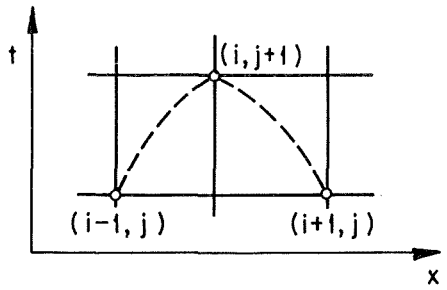

Fig. 2 Characteristic lines

$$P_i^* = P_i^j - 0.5\Delta t\left[\lambda^+\frac{\partial P^+}{\partial x} + \lambda^-\frac{\partial P^-}{\partial x}\right] - 0.5\rho_m a_m \Delta t\left[\lambda^+\frac{\partial V^+}{\partial x} - \lambda^-\frac{\partial V^-}{\partial x}\right] \quad (32)$$

$$V_i^* = V_i^j - 0.5\Delta t\left[\lambda^+\frac{\partial V^+}{\partial x} + \lambda^-\frac{\partial V^-}{\partial x}\right] - \frac{0.5\Delta t}{\rho_m a_m}\left[\lambda^+\frac{\partial P^+}{\partial x} - \lambda^-\frac{\partial P^-}{\partial x}\right] - RV_i^j|V_i^j| \quad (33)$$

The spatial derivatives in equations (26) and (27) are approximated as follows:

Predictor Part:

Part 1:

$$\frac{\partial F^+}{\partial x} = \frac{F_i^j - F_{i-1}^j}{\Delta x} \quad (34)$$

$$\frac{\partial F^-}{\partial x} = \frac{F_{i+1}^j - F_i^j}{\Delta x} \quad (35)$$

These finite-difference approximations are used to determine the predicted values of P_i^* and V_i^* from equations (32) and (33).

Part 2:

The following finite-difference approximations are used to determine the predicted values of time derivatives $\frac{\partial P^*}{\partial t}$ and $\frac{\partial V^*}{\partial t}$ from equations (30) and (31):

$$\frac{\partial F^+}{\partial x} = \frac{2F_i^j - 3F_{i-1}^j + F_{i-2}^j}{\Delta x} \quad (36)$$

$$\frac{\partial F^-}{\partial x} = \frac{-2F_i^j + 3F_{i+1}^j - F_{i+2}^j}{\Delta x} \quad (37)$$

Corrector Part:

By using the following finite-difference approximations and using V^* and P^* instead of V and P in equations (30) and (31), the corrected values of time derivatives $\frac{\partial P}{\partial t}$ and $\frac{\partial V}{\partial t}$ are:

$$\frac{\partial F^+}{\partial x} = \frac{F_i^* - F_{i-1}^*}{\Delta x} \quad (38)$$

$$\frac{\partial F^-}{\partial x} = \frac{F_{i+1}^* - F_i^*}{\Delta x} \quad (39)$$

Then the values of V and P at the unknown time level are determined from the following equations:

$$P_i^{j+1} = P_i^j + 0.5\Delta t\left(\frac{\partial P^*}{\partial t} + \frac{\partial P}{\partial t}\right) \quad (40)$$

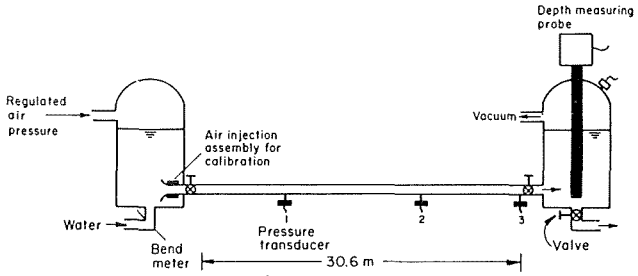

Fig. 3 Schematic of experiment

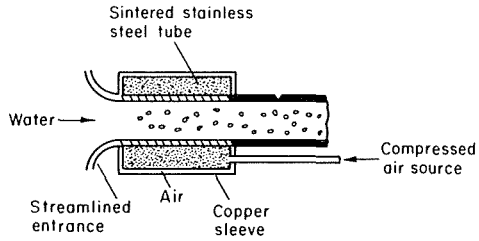

Fig. 4 Air injection assembly

$$V_i^{j+1} = V_i^j + 0.5\Delta t\left(\frac{\partial V^*}{\partial t} + \frac{\partial V}{\partial t}\right) \quad (41)$$

Note that the above discretization is possible only at nodes 3,4, ..., $n-1$ during the part 2 of the predictor part. One sided differences are used at nodes 2 and $n-1$. Also, special treatment is needed at the boundary nodes, which is discussed next.

Boundary Conditions

The computational procedures discussed in the previous sections are for the interior nodes; boundary nodes require special treatment. For this purpose, several procedures have been proposed. In the writers' opinion, the characteristic boundaries yield better results and are used herein.

It follows from equation (25) that

$$\eta = \pm\rho_m a_m \quad (42)$$

If $\eta = \rho_m a_m$, then equation (24) may be written as

$$\frac{dV}{dt} + \frac{1}{\rho_m a_m}\frac{dP}{dt} + \frac{f}{2D}V|V| = 0 \quad (43)$$

and, if $\eta = -\rho_m a_m$, then equation (24) may be written as

$$\frac{dV}{dt} - \frac{1}{\rho_m a_m}\frac{dP}{dt} + \frac{f}{2D}V|V| = 0 \quad (44)$$

Multiplying equations (43) and (44) by dt, integrating along the positive and negative characteristic lines (Fig. 2) and by using the values of coefficients at the known time level, the following equations are obtained

$$V_i^{j+1} - V_{i-1}^j + (1/\rho_m a_m)_{i-1}^j(P_i^{j+1} - P_{i-1}^j) + RV_{i-1}^j|V_{i-1}^j| = 0 \quad (45)$$

$$V_i^{j+1} - V_{i+1}^j - (1/\rho_m a_m)_{i+1}^j(P_i^{j+1} - P_{i+1}^j) + RV_{i+1}^j|V_{i+1}^j| = 0 \quad (46)$$

At the downstream end, equation (45) is solved simultaneously with the condition imposed by the boundary; and at the upstream end, equation (46) is solved simultaneously with the condition imposed by the boundary.

Experimental Investigations

To verify the validity of the above model and of the numerical schemes presented in the previous sections, experiments were conducted on a piping system in the hydraulics laboratory

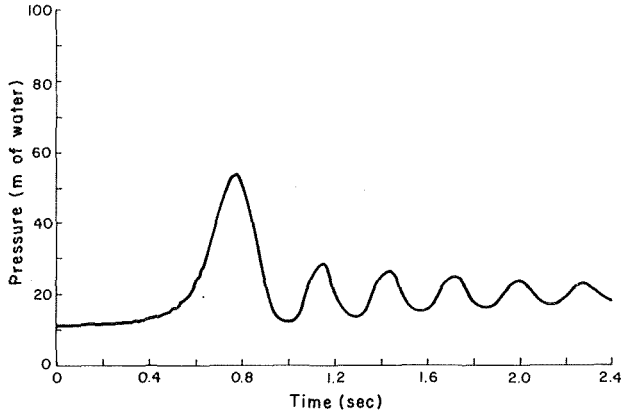

Fig. 5 Pressure variation at the downstream end for Test 1

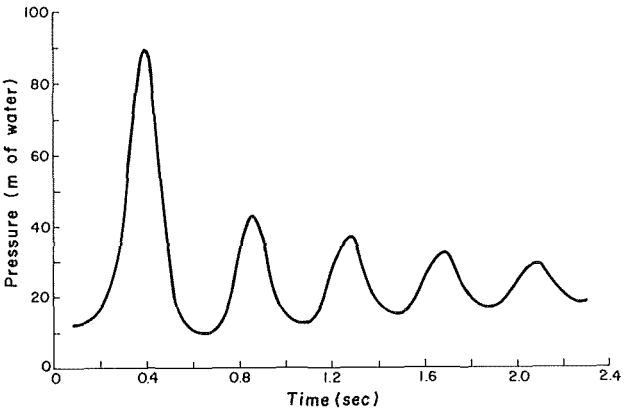

Fig. 6 Pressure variation at the downstream end for Test 2

of the Georgia Institute of Technology. A schematic of the test facility is shown in Fig. 3. The length of the pipe, L was equal to 30.6 m and its diameter was 0.026 m. The air pressure in the tank could be controlled by a pressure regulator. The rate of water inflow into the left tank was measured by means of a bend meter. Under equilibrium conditions, this flow rate corresponded to the mean flow rate through the pipe. Compressed air was injected into the test pipe through a porous wall portion of the entrance, as shown in Fig. 4. A micrometering valve with a fine adjustment was used to measure the rate of mass inflow of compressed air. Transient-state pressures were monitored by high-frequency-response pressure transducers at three locations, as shown in Fig. 3. The three stations are located at $x = 8.0\ m$, 21.1 m and 30.6 m, respectively, from the upstream end. These pressures were recorded on a four channel Hewlett Packard recorder with a carrie pre-amplifier unit.

Experimental uncertainty estimates were calculated from the respective calibrations of the micrometer air flow meter, the elbow meter and the pressure transducers. The orifice type air flow meter was calibrated volumetrically using water over the same Reynolds number range as employed in the transient test program with air, while the water flow elbow meter was calibrated gravimetrically. The four pressure transducers were calibrated *in situ* with reference to a test pressure gage. The uncertainty estimates are as follows:

Pressure: $\pm 9.8 \times 10^3\ Pa$;
Volumetric flow rate of water: $\pm 1.4 \times 10^{-5}\ m^3/s$;
Mass flow rate of air: $\pm 2.3 \times 10^{-7}\ kg/s$;
Wave speed: $\pm 15.0\ m/s$.

The test procedure was as follows: A steady-state flow of

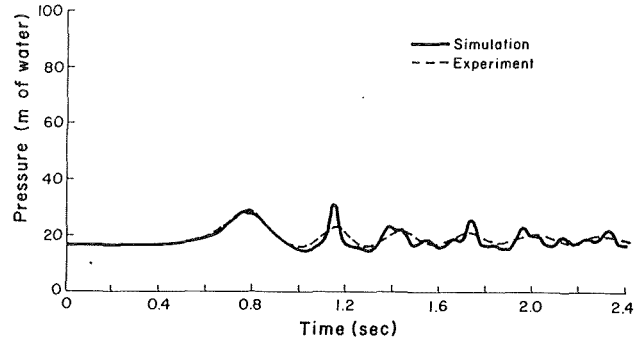

Fig. 7(a)

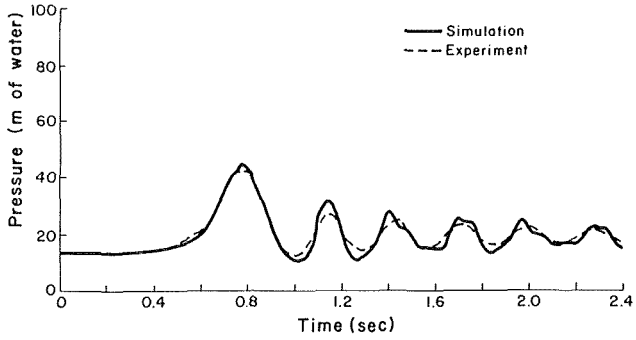

Fig. 7(b)

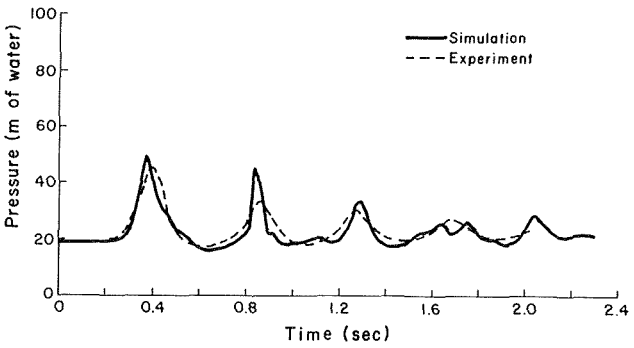

Fig. 7(c)

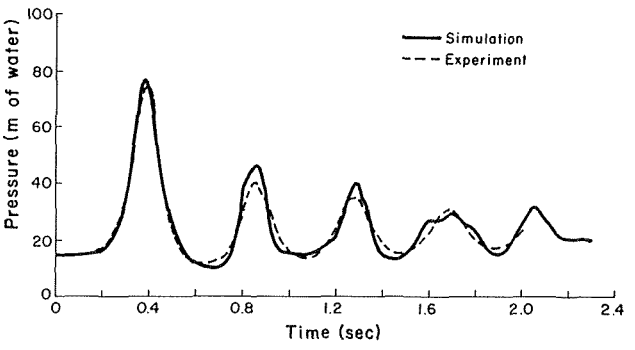

Fig. 7(d)

Fig. 7 Comparison of computed and experimental results: MacCormack method (*a*) at Station 1 for Test 1, (*b*) at Station 2 for Test 1, (*c*) at Station 1 for Test 2, (*d*) at Station 2 for Test 2

an air-water mixture was established in the test pipe by controlling the exit valves and the pressure of the injected air at the inlet. The flow velocity was maintained at a high enough rate so that slug flow could be avoided by limiting the rate of air injection. The steady-state readings of water-flow rate, mass

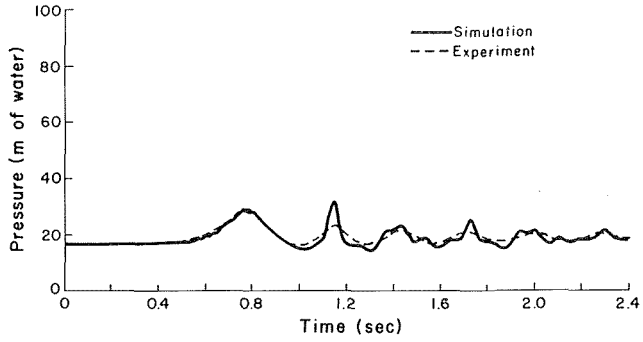

Fig. 8(a)

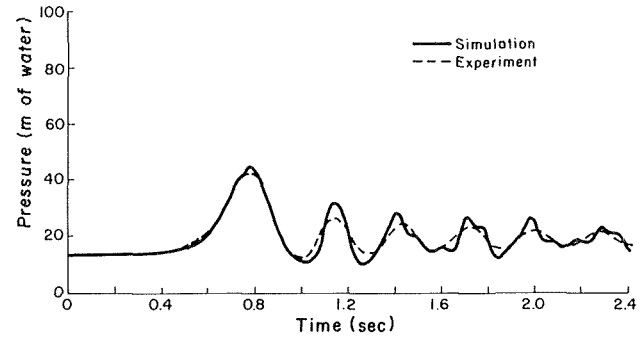

Fig. 8(b)

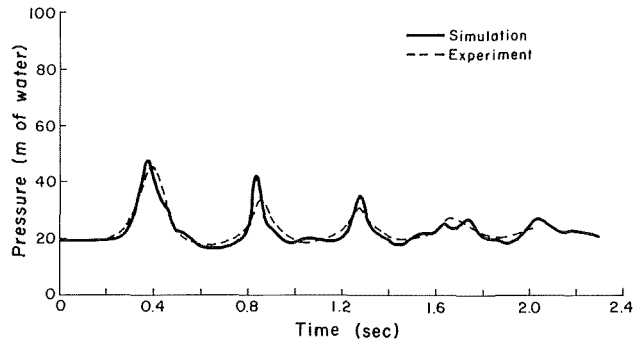

Fig. 8(c)

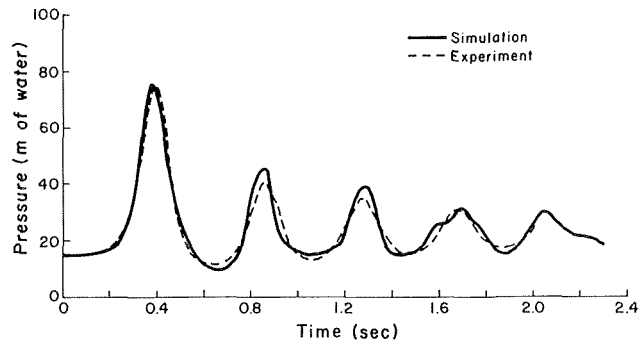

Fig. 8(d)

Fig. 8 Comparison of computed and experimental results: Gabutti method (*a*) at Station 1 for Test 1, (*b*) at Station 2 for Test 1, (*c*) at Station 1 for Test 2, (*d*) at Station 2 for Test 2

flow rate of injected air, air injection pressure, air pressure and water level in the upstream tank, and pressure at the selected locations were taken. The downstream valve was rapidly closed and the pressures at three locations were continuously recorded. These pressure records are used for verifying the above computational procedures.

Comparison of Computed and Measured Results

Both of the above two schemes were used to compute the transient-state pressures in the pipeline. The upstream boundary was a constant-level reservoir while the downstream boundary was the known pressure history at pressure transducer no. 3. A velocity boundary condition was not used at the downstream boundary because the measurement of the rate of closure of the exit valve and, consequently the measurement of velocity are very difficult. Characteristic boundaries were used in both the schemes. In the Gąbutti scheme, two-point finite difference approximations were used at the nodes adjacent to the boundaries if three points were not available in the desired direction. The computational time interval was selected such that the Courant stability condition was satisfied at all nodes with the computed values at the unknown time level. If necessary, the conditions were computed with a reduced time interval.

The computed and measured pressures were compared at stations 1 and 2 for two different test conditions. In test 1, the constant upstream reservoir pressure P_0 was 18.46 m of water absolute and the steady flow velocity V_0 was 2.42 m/s. Steady air mass flow rate G_0 was equal to 4.1×10^{-6} kg/s with a downstream void ratio α_0 of 0.0023. Steady flow friction factor f was computed from the measured data to be equal to 0.0205. The measured variation of pressure head at the downstream end, which is used as boundary condition is shown in Fig. 5. In test 2, $P_0 = 21.70$ m, $V_0 = 2.94$ m/s, $G_0 = 1.15 \times 10^{-5}$ kg/s, $\alpha_0 = 0.0053$ and $f = 0.0195$. Figure 6 shows the measured variation of transient state pressure at the downstream end. The wave speed with only water in the pipe was equal to 715 m/s. Typical comparisons for MacCormack scheme are shown in Fig. 7 and for Gabutti Scheme in Fig. 8. It is clear from these figures that transient pressures are satisfactorily simulated by the simplified model and the numerical schemes presented herein. However, it can be seen that the wave dissipated at a slower rate in the computations than that in the measured results. Similar behavior is usually observed during computations of transients in single component flows; the reasons for the difference are not clear at this point.

Summary and Conclusions

It is shown that the two-component gas-liquid flows in pipes may be treated as pseudo fluid flows for small void fractions and homogeneous mixtures. Two second-order explicit finite-difference techniques are used for solving the governing nonlinear partial differential equations. These techniques capture the shock without any special treatment and are therefore preferable to commonly used method of characteristics. Computed results compared satisfactorily with the experimental results demonstrating the validity of the model and the computational techniques.

References

1 Chaudhry, M. H., *Applied Hydraulic Transients* (second ed.), Van Nostrand Reinhold Company, 1987.

2 Chaudhry, M. H., and Hussaini, M. Y., "Second-Order Explicit Finite-Difference Schemes for Waterhammer Analysis," ASME JOURNAL OF FLUIDS ENGINEERING, Vol. 107, 1985, pp. 523-529.

3 Gabutti, B., "On Two Upwind Finite-Difference Schemes for Hyperbolic Equations in Non-Conservation Form," *Computers and Fluids*, Vol. 11, No. 3, 1983, pp. 207-230.

4 Kalinske, A. E., and Robertson, J. M., "Closed Conduit Flow," *Trans. ASCE*, Vol. 108, 1943, pp. 1435-1516.

5 Kranenburg, C., "Gas Release During Transient Cavitation in Pipes," *Jour. Hyd. Div.*, ASCE, Vol. 100, 1974, pp. 1383-1398.

6 Martin, C. S., and Padmanabhan, M., "The Effect of Free Gases on Pressure Transients," *L'Energia Elettrica*, No. 5, 1975, pp. 262-267.

7 Martin, C. S., Padmanabhan, M., and Wiggert, D. C., "Pressure Wave Propagation in Two-Phase Bubbly Air-Water Mixtures," Paper No. C1, Proc., Second International Conference on Pressure Surges, British Hydromechanics Assoc., 1976.

8 Martin, C. S., and Naghash, M., "Simulation of Two-Component Transient Flow Using Implicit Method," Unpublished Report, Georgia Tech., 1986.

9 MacCormack, R., "Numerical Solution of the Interaction of a Shock Wave with a Laminar Boundary Layer," *Lecture Notes in Physics*, Holt, M. ed., Vol. 8, Springer-Verlag, New York, N.Y., 1971, pp. 151-163.

10 Padmanabhan, M., Ames, W. F., and Martin, C. S., "Numerical Analysis of Pressure Transients in Bubbly Two-Phase Mixtures by Explicit-Implicit Methods," *Jour. of Engineering Mathematics*, Vol. 12, 1978, pp. 83-93.

11 Papadakis, C. N., and Hollingshead, D. F., "Air Release in the Transient Analysis of Condensers," Paper No. G1, *Proc. Second International Conference on Pressure Surges*, British Hydromechanics Assoc., 1976.

12 Pearsall, I. S., "The Velocity of Water Hammer Waves," Proc., Symp. on Surges in Pipelines, *Proc., Inst. of Mech. Engrs.*, London, 1965, Vol. 180, Part 3E.

13 Safwat, H. H., "Photographic Study of Water Column Separation," *Jour. Hyd. Div.*, ASCE, Vol. 98, 1972, pp. 739-746.

14 Safwat, H. H., and van der Polder, J., "Experimental and Analytical Data Correlation Study of Water Column Separation," ASME *Journal of Basic Engineering*, Vol. 95, 1973, pp. 91-97.

15 Swaffield, J. A., "A Study of the Influence of Air Release on Column Separation in an Aviation Kerosene Pipeline," *Proc., Inst. of Mech. Engrs.*, Vol. 186, 1972, pp. 693-703.

16 Wiggert, D. C., and Sundquist, M. J., "The Effect of Gaseous Cavitation on Fluid Transients," ASME JOURNAL OF FLUIDS ENGINEERING, Vol. 101, 1979, pp. 79-86.

17 Wiggert, D. C., Martin, C. S., Naghash, M., and Rao, P. V., "Modeling of Transient Two-Component Flow Using a Four-Point Implicit Method," *Proc. Numerical Methods for Fluid Transient Analysis*, C. S. Martin and M. H. Chaudhry (eds.), FED-4, ASME, Houston, TX, 1983, pp. 23-28.

18 Yadigaroglu, G., and Leahy, R. T., "On Various Forms of the Conservation Equations in Two-Phase Flows," *International Jour. of Multiphase Flow*, Vol. 2, 1976, pp. 477-494.

A. Crespo

F. Castro

F. Manuel

Cátedra de Mecánica de Fluidos,
E.T.S. Ingenieros Industriales, U.P.M.,
28006 Madrid, Spain

J. Hernández

Dept. Mecánica, E.T.S.I.I., U.N.E.D.,
Ciudad Universitaria, 28040 Madrid, Spain

Dynamics of an Elongated Bubble During Collapse

An analytical model is presented to describe the collapse of an elongated bubble, which appears in the core of a cavitating vortex. The flow field is assumed to be irrotational, due to a sink line. The kinematic and dynamic conditions are applied only at the tip and in the middle of the bubble surface. This simplified theory must retain losses of mechanical energy near the tips of the bubble, which are due to a microjet. In order to check the validity of this model, the irrotational flow equations have been solved numerically by using a panel method; the numerical results agree with the analytical ones and confirm the existence of the microjet at the tip. The agreement with experimental results is also good. For very slender bubbles the speed near the tips becomes very large, and this may be cause of cavitation damage. A simplified approach is proposed to explain the flow in the microjet.

1 Introduction

In this work a model is presented to describe the collapse of an elongated bubble which is formed in the nucleus of a vortex, and whose axial collapse velocities are very large and increase as the slenderness of the bubble increases.

In Fig. 1, taken from reference [1], it is shown that air injected in the liquid is attracted toward the core of a vortex shed from the tip of a blade. The wave-like shape of the interphase can be described with a model based on an analogy with the theory describing gravity waves in a water channel. Progressive linear waves and nonlinear hydraulic jumps and solitary waves are found to propagate along the interphase; good agreement is found between the theoretical predictions of the wave velocities and the experimental results (reference [1]).

In turbulent flows in general, and in particular in the turbulent boundary layers along the walls of turbomachine elements, there are multiple vortex filaments which may attract the gaseous products resulting from incipient cavitation. In Fig. 2 a scheme of the turbulence structure presented by Tennekes [2] is shown. If gaseous columns like those of Fig. 1 break into bubbles of a length of the order of magnitude of the radius of curvature of the filaments, it may be speculated that the resulting bubbles will be elongated, with a slenderness of an order of magnitude equal to the ratio of the Taylor and Kolmogorov lengths, which is proportional to $Re^{1/4}$, where Re is the Reynolds number of the mean flow. In turbulent boundary layers there will be secondary vortex lines perpendicular to the average vorticity due to the mean shear, and consequently normal to the wall. It is shown here that the resulting bubbles create very high velocities normal to the wall which may originate the cavitation damage.

Avellan and Karami [3] made some experiments which consisted in creating a vortex subjected alternately to underpressure and overpressure by periodically opening and closing a valve. During the underpressure period a cavity appeared in the vortex nucleus which subsequently collapsed against a wall normal to the vortex when the pressure was raised. In this wall a specimen was immersed and its erosion was observed. The side wall enclosing the vortex was transparent, and the diameter

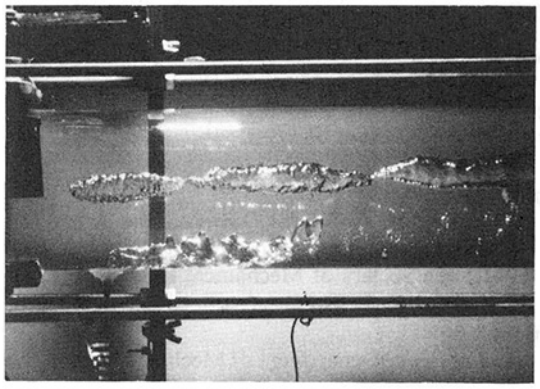

Fig. 1 Cavities along a tip vortex (reference [1])

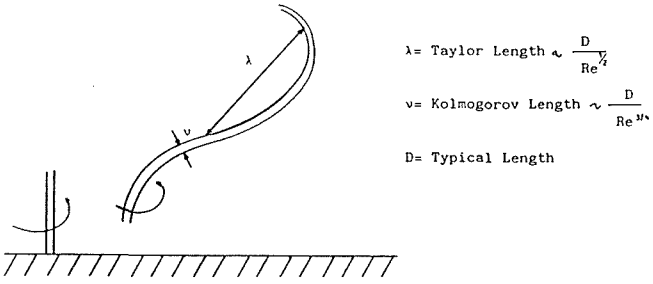

Fig. 2 Vortex filaments in turbulence

Contributed by the Fluids Engineering Division for publication in the JOURNAL OF FLUIDS ENGINEERING. Manuscript received by the Fluids Engineering Division September 22, 1988.

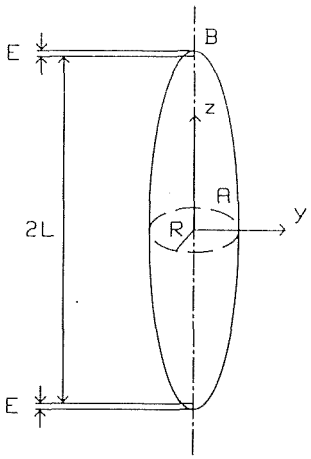

Fig. 3 Schematic showing bubble dimensions and coordinates

and length of the bubble were measured photographically as a function of time during the collapse; these results are used for comparison with the theory proposed in this paper. The collapse velocities and the damage to the specimen were substantially larger than those corresponding to the collapse of a spherical bubble.

In this paper we consider an elongated bubble, as it is represented in Fig. 3. The inverse of the initial slenderness ratio, ϵ, is assumed to be small. The presence of a wall normal to the bubble is taken into account by putting the wall at the middle of the bubble, so that the real bubble length will be half of that in Fig. 3. This relative position of the bubble with respect to the wall corresponds to the configuration of Avellan and Karami [3] experiments and to bubbles associated to the secondary vorticity of turbulent boundary layers.

Although the vortex causes the initial elongated shape of the bubble, the radial variation of pressure due to the centrifugal force is neglected in the model presented here. If this radial pressure variation is comparable to the driving pressure causing the collapse, this approximation is no longer valid, and the resulting flow field may be quite different. Chahine [4] has performed numerical calculations showing that for large enough azimuthal velocities a constriction appears in the middle of the bubble, whereas in our problem there is a microjet at the tip.

The effect of surface tension has not been considered either. This assumption may fail near the tip, where the radius of curvature is smallest, of the order of $L\epsilon^2$. On the other hand, the nondimensional velocity in that region is largest, of order $1/\epsilon$, so that both effects cancel when combined in a Weber number. Its order of magnitude turns out to be $\Delta pL/\sigma$, where Δp is the pressure difference between that at infinity and the saturated vapor pressure inside the bubble, and σ is the surface tension; in many situations of interest this number is large.

Viscous and turbulence effects are also neglected; however, a dissipative term is retained in Bernouilli's equation. This will be shown to be due to a microjet at the tip.

Prosperetti [5] suggests using distributions of sinks to describe the evolution of nonspherical bubbles during the collapse. Based on this idea, it is assumed here that there is a sink line of constant strength and length $2L$ along the axis of the bubble. During the collapse, the bubble has to be a fluid surface (kinematic condition), and the pressure on it has to be constant (mechanical condition) and equal to the vapor pressure. To satisfy initially the mechanical condition, it is necessary that the bubble surface is a surface of constant potential, which, in this case, is an ellipsoid of revolution, as shown by Milne-Thomson [6]. This means that the initial shape of the bubble is not arbitrary; nevertheless, it is expected to be representative of elongated bubbles. At later times, it turns out to be impossible to satisfy both the kinematic and mechanical conditions over all the surface of the bubble with a flow field given by a sink line. Consequently, the kinematic and mechanical conditions are applied only at the middle line (A in Fig. 3) and at the tips of the bubble. This results in a system of four ordinary differential equations for the three lengths indicated in Fig. 3 and for the sink intensity. When solving this system of equations, it is found that the distance E (Fig. 3) goes to zero in a very short time, while the bubble radius, R, and length, $2L$, remain almost equal to their initial values. This difficulty is solved if a dissipative term is retained in Bernouilli's equation at the tip of the bubble. It is shown that this dissipative process is due to a microjet. If there is a microjet, the velocity at the tip has both radial and axial components, and the dissipative term is the kinetic energy of the radial component. A simplified quasi-analytical solution is obtained to calculate the evolution of the bubble dimensions. Good agreement is obtained with the results of the quasi-analytical solution and the experiments of Avellan and Karami [3].

The simplification, which consists in satisfying the mechanical and kinematic conditions only at the tip and in the middle of the bubble, is strong and not very well justified. A similar simplification has also been made by Prosperetti [5], who obtained results which were in agreement with those of more exact methods; however, he studied the collapse of a slightly oblate bubble, which is very different from the one considered here. To check the validity of the model proposed here, a numerical panel method has been developed. The irrotational flow field is obtained by superimposing the flow fields of N sink rings, located in the inside normal of N points of the bubble surface, where the flow properties have to be calculated. For very small values of ϵ, this numerical procedure is very unstable, and diverges in a short time. Nevertheless, the calculations were carried out for sufficient time, and enough numerical data has been obtained to validate the analytical model.

The formation of the microjet in the regions of highest curvature of prolate bubbles has been observed by Blake and Kucera [7]. For oblate bubbles, an annular ring jet is formed (Blake and Kucera [7], Prosperetti [5]). The microjet appears typically in other situations, such as in the bubble collapse in the presence of boundaries, and in translating bubbles, as it is shown by Blake and Gibson [8] and Plesset and Prosperetti [9]. The microjet velocity may be expressed as

$$V = K(\Delta p/\rho)^{1/2}, \tag{1}$$

where ρ is the liquid density, and the factor K is a nondimensional value of the microjet velocity. It is shown in this paper that the microjet velocity is approximately twice the tip velocity, and the factor K is proportional to the initial slenderness ratio of the bubble, $1/\epsilon$, so that very elongated bubbles will produce very high microjet velocities.

A simple model is presented to describe the microjet, which is based on an interpretation proposed by Batchelor [10] for shaped charges. The predictions of this model are compared with the numerical results.

2 A Quasi-Analytical Model

The flow field is assumed to be due to a sink line of length L and intensity Q, whose velocity potential is given by

$$\phi = \frac{Q(t)}{4\pi} F(y,z,L(t)), \tag{2}$$

where

$$F(y,z,L(t)) = \ln \frac{z+L+[(z+L)^2+y^2]^{1/2}}{z-L+[(z-L)^2+y^2]^{1/2}}. \tag{3}$$

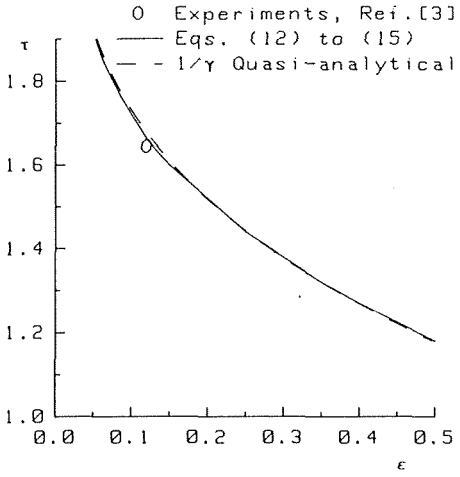

Fig. 4 Nondimensional collapse time

The kinematic condition is given by

$$d\mathbf{x}_B/dt = (\nabla\phi)_{x=x_B}, \tag{4}$$

and the mechanical condition is

$$\partial\phi/\partial t + 1/2(\nabla\phi)^2(1+\beta) = \Delta p/\rho, \text{ on } \mathbf{x} = \mathbf{x}_B, \tag{5}$$

where $\mathbf{x}_B$ is the position vector of the bubble surface, and β is a positive constant to take into account mechanical energy losses. If the velocity field derives from a potential, the flow is ideal and there should not be any losses; however, β is going to be different from zero only in a very small region near the tips of the bubble. The acceleration term in equation (5) is obtained from equation (2) in the form

$$\frac{\partial\phi}{\partial t} = \frac{1}{4\pi}\frac{dQ}{dt}F + \frac{Q}{4\pi}\frac{\partial F}{\partial L}\frac{dL}{dt}. \tag{6}$$

Initially, Q, dL/dt, and all the velocities are assumed to be zero, but dQ/dt may be different from zero; then, from equations (2), (5) and (6), it is obtained that $F=$const. at $t=0$ on the bubble surface. It may be shown that this is the equation of an ellipsoid of revolution, whose foci are at the end of the sink line. Initially, the semiaxes are R_0 and $L_0 + E_0$, and from equation (3) the following relation is obtained:

$$E_0 = L_0\{[1 + (R_0/L_0)^2]^{1/2} - 1\}. \tag{7}$$

The parameter ϵ, defined as

$$\epsilon = R_0/L_0, \tag{8}$$

is a small quantity. Then, equation (7) reduces to:

$$E_0 = \epsilon R_0/2 = \epsilon^2 L_0/2. \tag{7'}$$

Within this approximation, the curvature of the tip is $1/E_0$.

For $t>0$, it is not possible to satisfy the kinematic and mechanical conditions over all the surface of the bubble with the simple sink line model. The approximation is made of satisfying equations (4) and (5) only at the middle line (A in Fig. 3) and at the tips of the bubble (B in Fig. 3).

The following nondimensional variables are chosen:

$$r = R/R_0,\ l = L/L_0,\ e = E/E_0, \tag{9}$$

$$q = Q/[2\pi R_0(\Delta p/\rho)^{1/2}], \tag{10}$$

$$\tau = t(\Delta p/\rho)^{1/2}/R_0. \tag{11}$$

The kinematic condition at the middle line is

$$dr/d\tau = -q/r, \tag{12}$$

and at the tips

$$dl/d\tau = -q/e. \tag{13}$$

The mechanical condition at the middle line is

$$\ln\left(\frac{2l}{r\epsilon}\right)\frac{dq}{d\tau} + \frac{1}{2}\frac{q^2}{r^2}\left(1 + \beta_M - \frac{2r^2}{le}\right) = 1, \tag{14}$$

and at the tips

$$1/2\ln\left(\frac{4l}{e\epsilon^2}\right)\frac{dq}{d\tau} - \frac{q^2}{2}\left(\frac{1-\beta_T}{\epsilon^2 e^2} + \frac{1+\beta_T}{2le}\right) - \frac{q}{2e}\frac{de}{d\tau} = 1, \tag{15}$$

where β_M and β_T are the values of β at the middle and at the tip, respectively. In equations (12) to (15) terms of order ϵ^2 have been neglected.

The system of equations (12) to (15) has to be solved for the unknowns r, l, e, and q with the initial conditions:

$$r = l = e = 1 \text{ at } t = 0, \tag{16}$$

$$q = 0 \text{ at } t = 0. \tag{17}$$

Equations (12), (13), and (14) give explicitly the time derivatives of r, l, and q, respectively; and the time derivative of e is also obtained explicitly by eliminating $dq/d\tau$ between equations (14) and (15), obtaining the equation

$$\frac{q}{2e}\ln\left(\frac{2l}{r\epsilon}\right)\frac{de}{d\tau} = -\frac{q^2}{2}\left[\left(\frac{1-\beta_T}{e^2\epsilon^2} + \frac{1+\beta_T}{2le}\right)\ln\frac{2l}{r\epsilon} - \frac{1}{2r^2}\left(1+\beta_M - \frac{2r^2}{el}\right)\ln\frac{4l}{e\epsilon^2}\right] + 1/2\ln\frac{r^2}{le}, \tag{18}$$

which may be used instead of equation (15).

When solving numerically the previous system, if the dissipation coefficients β_M and β_T are zero, it turns out that, after a very short time, the distance e becomes zero, while r and l remain equal to their initial values of one. Crespo et al. [11] interpreted this phenomenon as a local collapse, and suggested that there were many consecutive local collapses whose energy dissipation would be taken into account by making $\beta_T = 1$. If in equation (18) we take the limit of ϵ going to zero, the only remaining term will be the first one on the right hand side, and β_T should be equal to one. In the last sections of this paper it will be shown that the fact that $\beta_T = 1$ is due to the existence of a microjet at the tip.

The collapse is studied by assuming that $\beta_T = 1$, and, since there are not any important mechanisms producing dissipation of energy at the middle of the bubble, it is assumed that $\beta_M = 0$. With these assumptions the system of equations (12), (13), (14), and (18), with the initial conditions (16) and (17), can be solved numerically. In Fig. 4 the nondimensional collapse time is given as a function of ϵ, and in Fig. 5 is given in dimensional variables the evolution with time of the length and diameter of a bubble. In both figures are also given the experimental results of Avellan and Karami [3]. The agreement of the numerical results and the experiments is good for the diameter and reasonable for the length.

A quasi-analytical solution is obtained if it can be assumed that the parameter

$$\gamma = [\ln(2/\epsilon)]^{-1/2} \tag{19}$$

is much smaller than one. For moderatelly small values of ϵ this is not true. Nevertheless, as it can be seen in Figs. 4 and 5, this analytical solution gives results which are very similar to those obtained by solving numerically the system of equations (12) to (18) for values of ϵ of the order 0.1. The variables q and τ are redefined as

$$\tilde{q} = q/\gamma, \tag{20}$$

$$\tilde{\tau} = \tau\gamma. \tag{21}$$

In the limit of small γ (and small ϵ), only the first and the last terms remain in equation (14), and its solution, with the initial condition, equation (17), is

$$\tilde{q} = \tilde{\tau}. \tag{22}$$

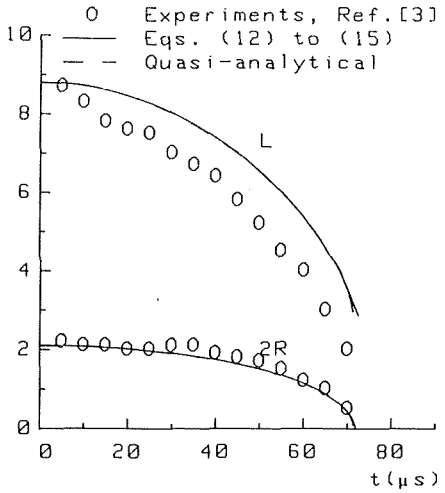

Fig. 5 Comparison with experiments

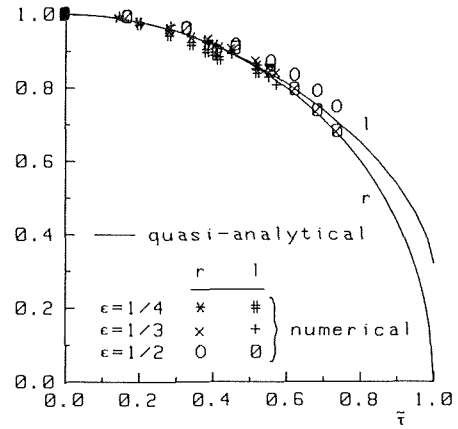

Fig. 6 Comparison of quasi-analytical and numerical results for the nondimensional bubble length and radius

By substituting this value of $\tilde{q}$ into equation (12) with the new variables, and using the initial condition, equation (16), it is obtained that

$$r = (1 - \tilde{\tau}^2)^{1/2}. \tag{23}$$

Equations (13) and (18) become in this limit

$$dl/d\tilde{\tau} = -\tilde{q}/e \tag{24}$$

$$\frac{\tilde{q}}{2e}\frac{de}{d\tilde{\tau}} = -\frac{\tilde{q}^2}{2r^2}\left(1 - \frac{r^2}{le}\right) + 1/2\ln\frac{r^2}{le}. \tag{25}$$

The corresponding values of l and r as functions of $\tilde{\tau}$ are given in Fig. 6. It should be emphasized that there are no parameters in equations (22) to (25) and in the corresponding initial conditions, so that the curves of Fig. 6 are universal. In this figure it can be observed that the bubble approximately retains its initial shape until almost the end of the process; then the slenderness of the bubble increases, because its radius goes to zero while its length goes to 32% of its initial value. In practice this limit may not be achieved because of surface instabilities.

The collapse time, expressed by the variable $\tilde{\tau}$, is one; and expressed by the variable τ is $1/\gamma$, which is represented in Fig. 4. The dimensional collapse time is

$$t_c = R_0\frac{[\ln(2/\epsilon)]^{1/2}}{(\Delta p/\rho)^{1/2}}. \tag{26}$$

3 Numerical Model

A numerical solution of the previous problem, applied to the whole surface of the bubble, has also been obtained. The method consists in solving Laplace's equation, with the kinematic condition, equation (4), and the mechanical condition, equation (5) (with $\beta = 0$). Equation (5), written in terms of the total derivative of ϕ at the fluid surface, becomes

$$d\phi/dt = 1/2(\nabla\phi)^2 + \Delta p/\rho, \text{ on } \mathbf{x} = \mathbf{x}_B. \tag{27}$$

To solve Laplace's equation N points are chosen along a meridian of the fluid surface; the values of ϕ are assumed to be known at these points. N sink rings are located inside the fluid surface in the normal to it through each one of the N points. The intensities of the N sink rings needed to give the values of ϕ are then calculated.

An implicit scheme of integration in time has been chosen. The values of the position and potential for each one of the N points are obtained from

$$\mathbf{x}(t+\Delta t) = \mathbf{x}(t) + [\mathbf{V}(t+\Delta t) + \mathbf{V}(t)]\Delta t/2, \tag{28}$$

$$\phi(t+\Delta t) = \phi(t) + \left[\left(\frac{d\phi}{dt}\right)_t + \left(\frac{d\phi}{dt}\right)_{t+\Delta t}\right]\Delta t/2. \tag{29}$$

where the time derivative of ϕ is given by equation (27). In a first iteration the values of the velocity components at the new time are supposed to be equal to those at time t. Then, with the values of ϕ at the new time obtained from equation (29), the sink intensities are calculated; from the intensities of the N sink rings the values of the velocity components at each point are obtained and compared with those of the previous iteration. The process is repeated until convergence is reached.

This numerical procedure has been tested by applying it to the well-known problem of the collapse of a spherical bubble; for $N = 40$, the resulting error is less than 0.2 percent.

4 Results of the Numerical Model

The numerical model is extremely unstable for very small values of ϵ. The smallest value of ϵ for which significative results were obtained was 0.25, and calculations for only half of the collapse time could be made. For larger values of ϵ, longer times can be reached.

In Fig. 7 the evolution of the profile of half a meridian of the bubble is given. In this figure the presence of the microjet at the tip is clearly shown. In Fig. 6 the evolution with time of the maximum length and radius of the bubble are given and compared with the values from the analytical solution; the agreement is good, even for values of ϵ as large as 0.5, for which the analytical theory previously presented is not valid.

The characteristics of the microjet will be examined in the next section, where a simplified model is proposed to interpret the flow at the tip.

5 Simple Model for the Microjet

Batchelor [10] proposes a simple model for shaped charges, which can be adapted to this problem in the form shown schematically in Fig. 8. A region near the tip, at distances from it of the order of ϵL, is considered. The flow is supposed to be steady in a reference frame moving along the z axis with the tip velocity, dL/dt. This assumption is justified by the fact that the second term in the right-hand side of equation (6), which corresponds to this translation effect, is larger than the first one. It may be shown that their ratio is of the order of ϵ^2. It is also assumed that the bubble surface (excluding the microjet and the tip) moves inwards with an absolute velocity V_n, which is decomposed as indicated in Fig. 8. The component $V_n\text{cosec}\alpha$ is the tip velocity, dL/dt, and has to be constant. The other component, $V_n\cot\alpha$, is the flow velocity in the mov-

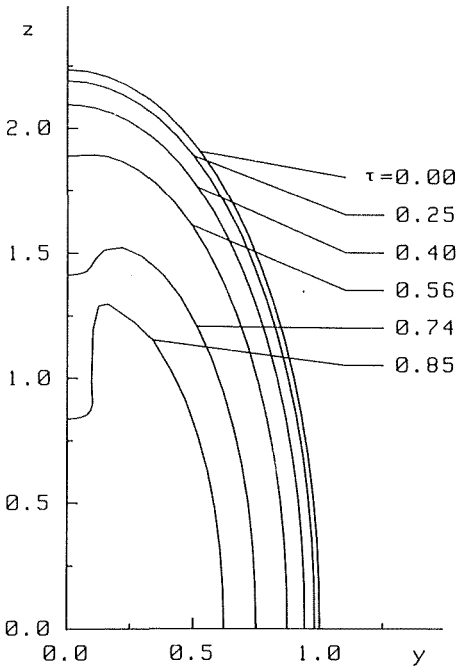

Fig. 7(*a*)

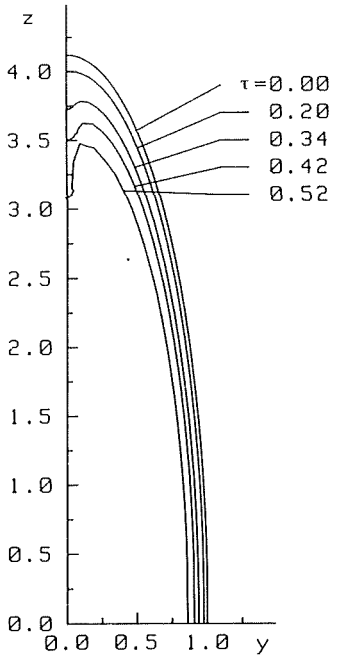

Fig. 7(*c*)

Fig. 7 Evolution of the bubble. (*a*) $\epsilon = 1/2$; (*b*) $\epsilon = 1/3$; (*c*) $\epsilon = 1/4$

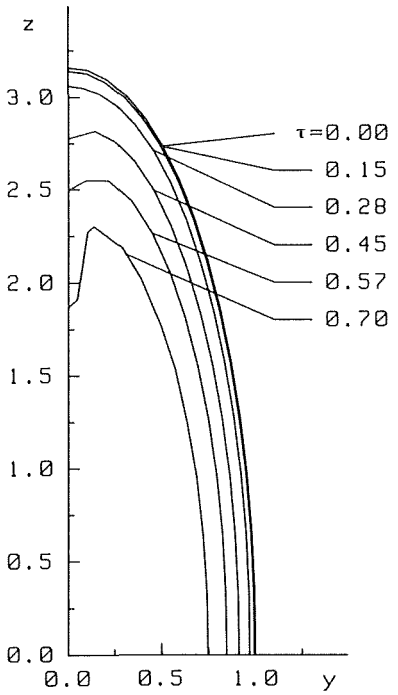

Fig. 7(*b*)

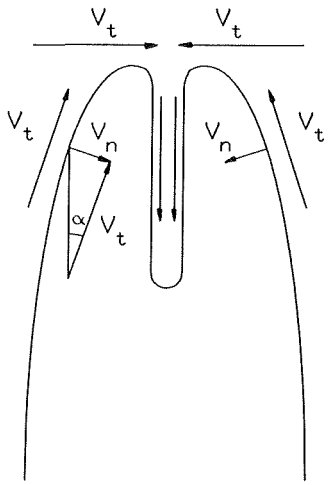

Fig. 8 Schematic showing the simple model for the microjet

ing frame, and has also to be constant because of Bernouilli's equation. If the bubble is slender and α is small, these two conditions can hold simultaneously, because $\cot\alpha$ and $\mathrm{cosec}\alpha$ are equal within an order of α^2. In the region located at a distance from the tip of the order of the minimum curvature radius, $\epsilon^2 L$, α has to be of order unity, and the absolute velocity is not normal to the bubble surface; obviously this also happens in the microjet.

The relative velocity along the interface will be equal to the axial tip velocity dL/dt, and the absolute microjet velocity will be $2dL/dt$. The dissipative term of equation (5) may then be interpreted as the kinetic energy of the radial velocity at the tip, which, according to the previous reasoning, is equal to the axial velocity at the tip.

To check this model, the values of the nondimensional microjet velocity divided by two and of the radial velocity at the tip, obtained from the numerical model, are respectively compared in Figs. 9 and 10 with the analytical value of $dl/d\bar{\tau}$. The agreement is reasonable even for values of ϵ as large as 0.5.

6 Conclusions

The results of the quasi analytical theory presented to describe the overall cavitation process of elongated bubbles are in good agreement with experimental results. The collapse time is given by equation (26). The axial velocity of collapse is of an order of magnitude

$$\frac{L}{t_c} \sim \frac{1}{\epsilon[\ln(2/\epsilon)]^{1/2}} (\Delta p/\rho)^{1/2}, \tag{30}$$

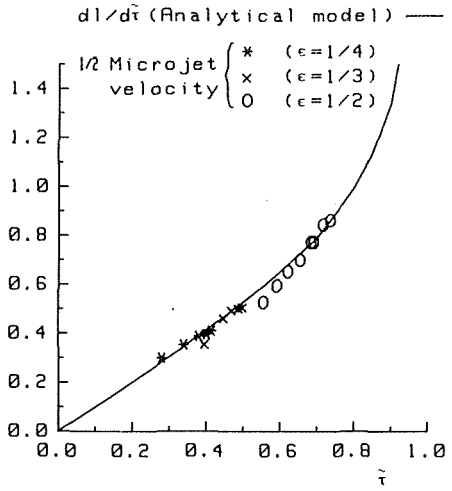

Fig. 9 Comparison of the nondimensional tip velocity and half of the nondimensional microjet velocity

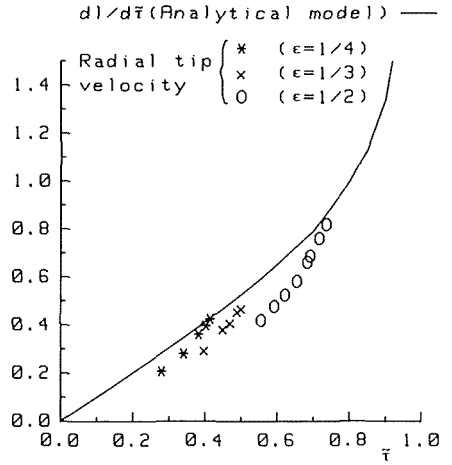

Fig. 10 Comparison of the radial and axial tip velocities

so that it is a decreasing function of ϵ, and the collapse will be intense if the bubble is very elongated.

The quasi-analytical model has been validated by comparison with a numerical model. The results of this numerical model show the existence of a microjet at the tip, which is taken into account in the analytical theory by means of a dissipation factor.

The nature of the microjet at the tip of the bubble has been examined, and a method to deal with it has been proposed. Simple relations are given to describe the flow magnitudes of the microjet.

It is of interest to improve the numerical methods of integration in the future so that they can be applied to more slender bubbles and times closer to the collapse could be reached.

References

1 Manuel, F., Crespo, A., and Castro, F., "Wave and Cavity Propagation Along a Tip Vortex Interphase," *Physico-Chemical Hydrodynamics*, Vol. 9, No. 3/4, 1987.

2 Tennekes, H., "Simple Model for the Small-Scale Structure of Turbulence," *Phys. Fluids*, Vol. 11, No. 3, 1968.

3 Avellan, F., and Karami, A., "Dynamics of Vortex Cavitation Involved in the Erosion of Hydraulic Machines," *Proc. VII International Conference on Erosion by Liquid and Solid Impact*, Cambridge, 1987.

4 Chahine, G. L., "A Numerical Model for Three-Dimensional Bubble Dynamics in Complex Flow Configurations," 22nd ATTC meeting, St John's, Newfoundland, Canada, 1989.

5 Prosperetti, A., "On the Dynamics of Nonspherical Bubbles," *Proc. of the First International Conference Cavitation and Inhomogeneities in Underwater Acoustics*, Göttingen, 1979.

6 Milne-Thomson, L. M., *Theoretical Hydrodynamics*, Macmillan, Ex. 7, Chapter XV, 1960.

7 Blake, J. R., and Kucera, A., "Elements of Bubble Dynamics Near Boundaries," Report from the University of Wollongong Australia, distributed at the Cavitation and Multiphase Flow Forum, Cincinatti, 1988.

8 Blake, J. R., and Gibson, D. C., "Cavitation Bubbles Near Boundaries," *Ann. Rev. of Fluids Mechanics*, Vol. 19, 1987, pp. 99-125.

9 Plesset, M. S., and Prosperetti, A., "Bubble Dynamics and Cavitation," *Ann. Rev. of Fluid Mechanics*, Vol. 9, 1977, pp. 145-185.

10 Batchelor, G. K., An Introduction to Fluid Dynamics, Cambridge University Press, Section 6.3, 1967.

11 Crespo, A., Castro, F., and Manuel, F., "Dynamics of an Elongated Bubble During Collapse," *Proceedings of the Cavitation and Multiphase Flow Forum*, Cincinatti, 1988, pp. 45-49.

Journal of Fluids Engineering

Technical Briefs

Turbulent Flow Separation Control Over a Backward-Facing Ramp Via Transverse and Swept Grooves

G. V. Selby[1], J. C. Lin,[2] and F. G. Howard[2]

Introduction

Flow separation control is a rich technology of long standing within the discipline of fluid mechanics. Momentum and energy losses due to flow separation are detrimental to airfoil and diffuser performance and result in increased body drag. For excessive separation, stalling may occur which can lead to catastrophic results. Controlling flow separation can result in an increase in system performance with consequent energy conservation, as well as weight and space savings.

One flow separation control technique of current interest is to impose a wall slip layer through the use of transverse grooves. The concept of using transverse surface grooves for delaying separation in diffusers evidently originated in the Soviet Union [1,2]. Research discussed in references [3, 4, and 5] also indicates that grooves aligned transverse to the direction of the flow are effective in controlling separation. Up to a 50 percent bluff-body drag reduction was reported in references [5 and 6] via small transverse shoulder grooves. References [1 and 2] suggest that the grooves function similar to a "roller bearing." In other words, the mechanism of the transverse groove separation control appears to be one of simply substituting several small regions of separation (which effectively provide a wall slip boundary condition) for a larger separated-flow region [6,7]. This approach has been studied thus far mainly in low Reynolds number flows and should be extended toward the more relevant, higher Reynolds number region. In the investigations cited, the Reynolds number based upon the distance between stagnation point and transverse grooves, Re_x, was less than 8×10^5, while Re_x for the present study was approximately 5.1×10^6. Improving the "roller bearing" effect by making the flow more three-dimensional through swept grooves should also be a subject for investigation.

An objective of the current research is to experimentally investigate the performance of transverse and swept grooves for controlling a two-dimensional, turbulent, separated flow at low speeds and moderate Reynolds numbers.

Apparatus and Tests

Separation control experiments were conducted in the NASA Langley 51×71 cm (20×28 in.) Shear-Flow Control Tunnel. This is a low-turbulence, subsonic, open-circuit wind tunnel. The speed range in the test section is from 2 to 46 m/s. In the current study, all experiments were conducted at a free-stream velocity of 40.2 m/s. (The uncertainty in free-stream velocity was ± 0.4 percent.) The flow separation ramp (model) was located approximately 1.93 m from the test section entrance. See Fig. 1 for the test configuration. A suction slot at the test section entrance was used to remove the converging section boundary layer to eliminate any influence of upstream history on the test boundary layer. The new laminar boundary layer that developed downstream of the suction device was artificially tripped with a 5-cm-wide strip of sandpaper (36 grit). The ceiling height of the test section was adjusted to obtain zero pressure gradient upstream of the ramp. The boundary layer on the centerline just ahead of the separation ramp was fully turbulent and approximately 3.25 cm in thickness. (The uncertainty in boundary-layer thickness was ± 1.7 percent.) At this same location, the momentum thickness (θ) was 0.34 cm and its spanwise variation across the test plate was within ± 2.5 percent. Values of θ were obtained from integration of streamwise velocity profiles from surveys conducted at intervals of 1.27 cm in the spanwise direction. The momentum thickness Reynolds number, R_θ, was approximately 9000.

The baseline (or reference) separation model was a two-dimensional 25 deg ramp with a 20.3 cm shoulder radius as shown in Fig. 1. The width of the model was 71 cm, which covered the entire test section in the spanwise direction. This model produced reasonably two-dimensional flow separation at approximately the midpoint of the ramp or about 2δ downstream of the horizontal (or first) tangent point. The transverse and swept grooves were located on the shoulder of the ramp model itself. The geometry of transverse and swept grooves tested in the present study is summarized in Fig. 2.

Static pressure orifices were located on the centerline of both

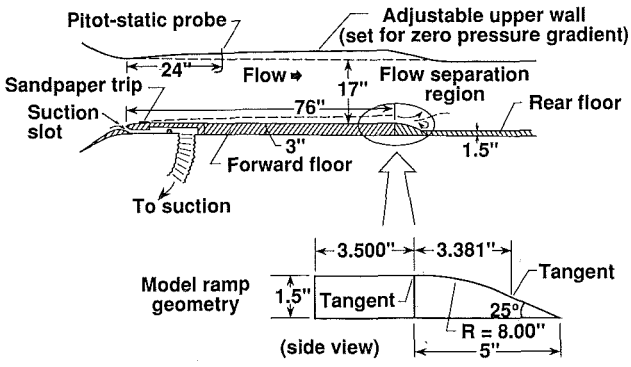

Fig. 1 Test configuration in tunnel

[1]Associate Professor, Mechanical Engineering and Mechanics Department, Old Dominion University, Norfolk, VA 23529-0247. Mem. ASME.

[2]Aerospace Engineer, Viscous Flow Branch, Fluid Mechanics Division, NASA Langley Research Center, Hampton, VA.

Contributed by the Fluids Engineering Division of The American Society of Mechanical Engineers. Manuscript received by the Fluids Engineering Division July 17, 1989.

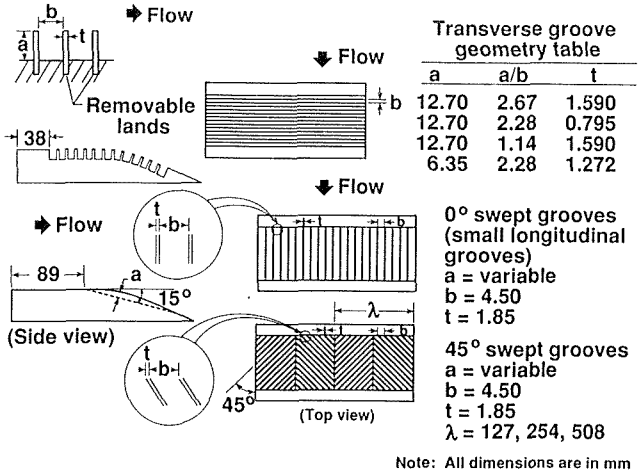

Transverse groove geometry table

a	a/b	t
12.70	2.67	1.590
12.70	2.28	0.795
12.70	1.14	1.590
6.35	2.28	1.272

Note: All dimensions are in mm

Fig. 2 Geometry of transverse and swept grooves

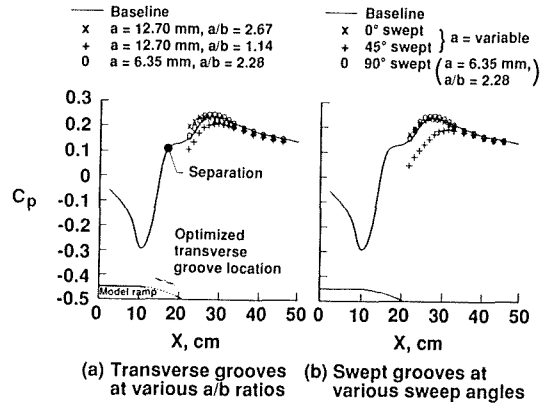

Fig. 3 Pressure distributions for transverse and swept grooves. (Uncertainty in C_p is ±0.005), (*a*) Transverse grooves at various *a/b* ratios; (*b*) Swept grooves at various sweep angles.

the reference separation ramp and the floor downstream of the ramp. The pressure tubes for the orifices were connected to a motor driven valve which sequentially connected each orifice to a single differential pressure gauge. All surface static pressure measurements were referenced to the freestream static pressure measurement located near the entrance of the test section. These pressure differences were nondimensionalized by the freestream dynamic pressure to obtain pressure coefficients (C_p). Because of physical constraints, pressure orifices could not be installed on the grooved ramp. However, pressure measurements were made on the floor downstream of the separation ramp to study reattachment and pressure recovery.

Results and Discussion

In the preliminary investigation of transverse grooves, the optimum transverse groove location was determined by systematically varying the beginning and end of the grooved section. Oil flow visualization of the flow downstream of the ramp with transverse grooves indicated that the optimum location for the beginning of the grooves was about one boundary-layer thickness (δ) upstream of the base model separation line (or baseline separation) with the grooved region extending to one δ downstream of the separation line. This optimum transverse groove configuration reduced the distance from the reference separation line to reattachment by almost 20 percent. This result was also verified by the pressure distribution measurements on the floor behind the separation ramp as shown in Fig. 3(*a*). When examining the baseline pressure distribution, it should be pointed out that the flow around a corner (or a

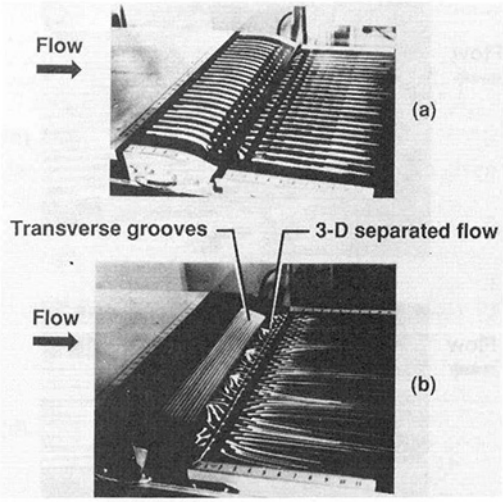

Fig. 4 Oil flow visualization of ramp models. (*a*) Reference model; (*b*) Model with transverse grooves.

shoulder) accelerates and decelerates symmetrically from the potential flow perspective, which is the reason for the pressure drop along the upstream portion of the shoulder. Baseline separation occurred just before the sharply increasing C_p distribution began to level off and reattachment occurred near the region of maximum C_p. The reattachment distance, therefore, was defined as the distance between the reference separation line and the streamwise location where maximum C_p occurred. Then, a reduction in the extent of the separation-flow region typically corresponded to the upstream movement of the location at which maximum C_p occurred (see Fig. 3(*a*)). Figure 3(*a*) also shows that the optimum transverse groove location is in the *maximum adverse pressure gradient region*. Of the configurations tested, the most effective groove configuration had a groove depth-to-width ratio (*a/b*) of 2.67. Doubling the groove width with constant groove depth moved reattachment back to the baseline case while the pressure recovery dropped below that of the baseline level (see Fig. 3(*a*)). One possible explanation for this adverse effect is that as *a/b* is reduced to 1.14, the critical aspect ratio for transition from an open to a closed cavity is approached. Associated with a closed cavity ($a/b < 1$) is an additional separated-flow region downstream of the cavity and increased drag. Although the optimum transverse groove location remained about the same after reducing both the groove depth and groove width by 50 percent, the effectiveness of the smaller transverse groove configuration in reducing the reattachment distance was also cut in half (down from approximately 20 to 10 percent). Varying the land (or rib) thickness from 1.6 mm to 0.8 mm did not change the effectiveness of the transverse grooves.

Flow visualization using surface tufts indicated high amplitude velocity fluctuations near the surface with transverse grooves. This result is in agreement with the findings of Stull [4], who reported pulsating free-shear layers and the formation of rollers over the grooved section which gave rise to large velocity fluctuations in the near-wall region. The present experiment also indicated that the transverse grooves generate three-dimensional flow, as shown in Fig. 4. The three-dimensional effects appeared when the transverse-grooved section extended downstream of the base model separation line. This three-dimensional flow suggests that properly designed swept grooves might enhance the performance of grooves for separation control.

The initial swept grooves investigated consisted of alternating +45 and −45 deg sweep angle (with respect to the flow direction) shoulder grooves with various widths (see Fig. 2).

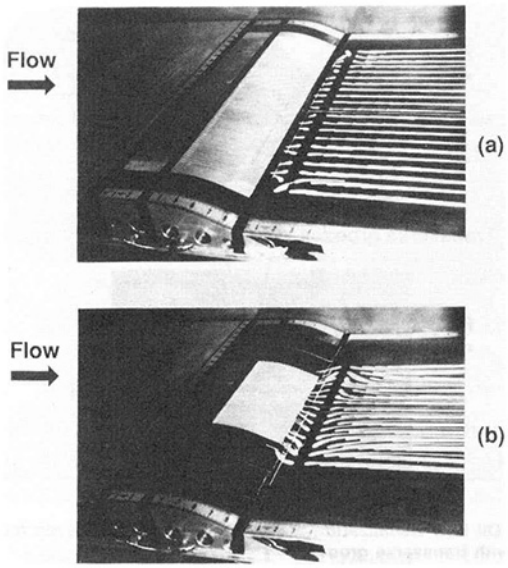

Fig. 5 Oil flow visualization of models with longitudinal and swept grooves. (*a*) 0 deg swept (longitudinal) grooves; (*b*) 45 deg (constant) swept grooves.

The swept grooves covered approximately the same streamwise adverse pressure gradient region as the optimized transverse grooves. Notice that the depth (*a*) for swept and longitudinal grooves is not constant. It varies from zero at the leading edge of a groove to a maximum of 0.64 cm near the midpoint of a groove. The results indicated that all alternating 45 deg swept grooves, regardless of spanwise width, increased the reattachment distance and reduced the pressure recovery when compared to the baseline case. Figure 3(*b*) shows the downstream floor pressure distribution comparison between the 45 deg constant (nonalternating) swept grooves, the 0 deg swept grooves (or small longitudinal grooves), and the 90 deg swept grooves (or small transverse grooves) of equivalent groove size. The results indicate that both 0 deg and 90 deg swept grooves showed a slight improvement over the baseline case as indicated by increased pressure recovery and reduced reattachment distance, while the 45 deg constant swept grooves performed very similar to the 45 deg alternating swept grooves, increasing the reattachment distance and reducing the pressure recovery. The adverse effects produced by the 45 deg swept grooves could be the same as that of the transverse grooves with $a/b = 1.14$, since the majority of grooves in the longitudinal plane have a/b less than one corresponding to a closed cavity. Figure 5 shows the oil flow visualization of longitudinal and swept grooves. It appears that the longitudinal grooves produce straighter surface streamlines downstream of the ramp than either the 45 deg swept grooves or the transverse grooves. Unlike the "roller bearing" mechanism associated with the transverse grooves, the separation control mechanism for the longitudinal grooves may be the local mitigation of the imposed adverse pressure gradient through the technique of partial "boattailing."

In summary, the present experimental investigation for controlling turbulent flow separation over a backward-facing ramp indicates that transverse grooves, located in the maximum $+dP/dx$ region with a height-to-width ratio greater than 2.5, reduced the reattachment distance by 20 percent over the baseline configuration. Unlike the transverse and longitudinal grooves of equivalent size, the 45 deg swept-groove configurations tested in the present study enhanced separation.

Acknowledgment

The work of the first author was supported by the National Science Foundation under grant MSM 8519116.

References

1 Migay, V. K., "The Efficiency of a Cross-Ribbed Curvilinear Diffuser," *Energomashinostroennie*, No. 1, 1962, pp. 45-46.

2 Migay, V. K., "A Study of Finned Diffusers," *Teploenergetika*, No. 10, 1962, pp. 55-59.

3 Chang, P. K., *Control of Flow Separation*, Hemisphere Publishing Corporation, McGraw-Hill, 1976.

4 Stull, F. D., and Velkoff, H. R., "Flow Regimes in Two-Dimensional Ribbed Diffusers," ASME JOURNAL OF FLUIDS ENGINEERING, Vol. 97, No. 1, Mar. 1975, pp. 87-96.

5 Stull, F. D., and Velkoff, H. R., "Effects of Transverse Ribs on Pressure Recovery in Two-Dimensional Subsonic Diffusers," AIAA Paper 72-1141, November-December 1972.

6 Howard, F. G., Goodman, W. L., and Walsh, M. J., "Axisymmetric Bluff-Body Drag Reduction Using Circumferential Grooves," AIAA Paper No. 83-1788, July 1983.

7 Howard, F. G., and Goodman, W. L., "Axisymmetric Bluff-Body Drag Reduction Through Geometrical Modification," *Journal of Aircraft*, Vol. 22, June 1985, pp. 516-522.

A Near-Wall Eddy Viscosity Formula for Turbulent Boundary Layers in Pressure Gradients Suitable for Momentum, Heat, or Mass Transfer

P. S. Granville[1]

An eddy viscosity formula is proposed for turbulent boundary layers in pressure gradients which is compatible with the slope and intercept of the log law. By having a "y^3" variation at the wall the formula is suitable for momentum, heat and mass transfer.

Introduction

Algebraic formulas for eddy viscosity or mixing length are the simplest and best known forms of turbulence modeling applied to predicting the development of turbulent boundary layers. They also have more-or-less stood the test of accuracy when compared to more complicated turbulence models [1, 2].

The problem to be addressed is an accurate formula for the eddy viscosity or mixing length in the region next to the wall for a turbulent boundary layer in a longitudinal pressure gradient on a smooth surface; said region encompassing the viscous sublayer, the buffer layer and the log layer.

The usual formula for the eddy viscosity or mixing length of the log layer is given by a Prandtl relation and of the viscous sublayer and buffer layer by a van Driest type damping function. A van Driest type damping function has an exponential form which asymptotically merges into the Prandtl relation for the log layer.

The van Driest damping function was originally proposed for mixing lengths in zero pressure gradients [3]. Various competing modifications had been proposed for pressure gradients and a final form [4] was proposed which correctly predicts the experimentally determined slope and intercept of the velocity log law [5, 6].

However there is another consideration which has been a subject of controversy for many years: namely, whether the eddy viscosity should vary as the third power or fourth power of the normal distance from the wall, "y^3" or "y^4". From the

[1]David Taylor Research Center, Bethesda, MD 20084-5000.

Contributed by the Fluids Engineering Division of THE AMERICAN SOCIETY OF MECHANICAL ENGINEERS and presented at the Applied Mechanics Conference, San Diego, Calif., July 1989. Manuscript received by the Fluids Engineering Division August 4, 1989.

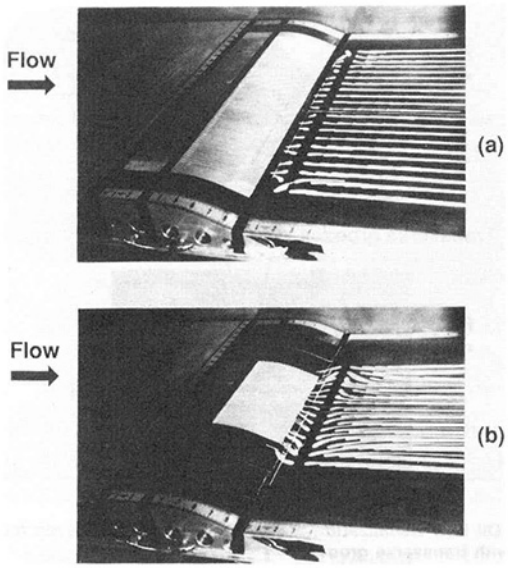

Fig. 5 Oil flow visualization of models with longitudinal and swept grooves. (*a*) 0 deg swept (longitudinal) grooves; (*b*) 45 deg (constant) swept grooves.

The swept grooves covered approximately the same streamwise adverse pressure gradient region as the optimized transverse grooves. Notice that the depth (*a*) for swept and longitudinal grooves is not constant. It varies from zero at the leading edge of a groove to a maximum of 0.64 cm near the midpoint of a groove. The results indicated that all alternating 45 deg swept grooves, regardless of spanwise width, increased the reattachment distance and reduced the pressure recovery when compared to the baseline case. Figure 3(*b*) shows the downstream floor pressure distribution comparison between the 45 deg constant (nonalternating) swept grooves, the 0 deg swept grooves (or small longitudinal grooves), and the 90 deg swept grooves (or small transverse grooves) of equivalent groove size. The results indicate that both 0 deg and 90 deg swept grooves showed a slight improvement over the baseline case as indicated by increased pressure recovery and reduced reattachment distance, while the 45 deg constant swept grooves performed very similar to the 45 deg alternating swept grooves, increasing the reattachment distance and reducing the pressure recovery. The adverse effects produced by the 45 deg swept grooves could be the same as that of the transverse grooves with $a/b = 1.14$, since the majority of grooves in the longitudinal plane have a/b less than one corresponding to a closed cavity. Figure 5 shows the oil flow visualization of longitudinal and swept grooves. It appears that the longitudinal grooves produce straighter surface streamlines downstream of the ramp than either the 45 deg swept grooves or the transverse grooves. Unlike the "roller bearing" mechanism associated with the transverse grooves, the separation control mechanism for the longitudinal grooves may be the local mitigation of the imposed adverse pressure gradient through the technique of partial "boattailing."

In summary, the present experimental investigation for controlling turbulent flow separation over a backward-facing ramp indicates that transverse grooves, located in the maximum $+dP/dx$ region with a height-to-width ratio greater than 2.5, reduced the reattachment distance by 20 percent over the baseline configuration. Unlike the transverse and longitudinal grooves of equivalent size, the 45 deg swept-groove configurations tested in the present study enhanced separation.

Acknowledgment

The work of the first author was supported by the National Science Foundation under grant MSM 8519116.

References

1 Migay, V. K., "The Efficiency of a Cross-Ribbed Curvilinear Diffuser," *Energomashinostroennie*, No. 1, 1962, pp. 45-46.

2 Migay, V. K., "A Study of Finned Diffusers," *Teploenergetika*, No. 10, 1962, pp. 55-59.

3 Chang, P. K., *Control of Flow Separation*, Hemisphere Publishing Corporation, McGraw-Hill, 1976.

4 Stull, F. D., and Velkoff, H. R., "Flow Regimes in Two-Dimensional Ribbed Diffusers," ASME JOURNAL OF FLUIDS ENGINEERING, Vol. 97, No. 1, Mar. 1975, pp. 87-96.

5 Stull, F. D., and Velkoff, H. R., "Effects of Transverse Ribs on Pressure Recovery in Two-Dimensional Subsonic Diffusers," AIAA Paper 72-1141, November-December 1972.

6 Howard, F. G., Goodman, W. L., and Walsh, M. J., "Axisymmetric Bluff-Body Drag Reduction Using Circumferential Grooves," AIAA Paper No. 83-1788, July 1983.

7 Howard, F. G., and Goodman, W. L., "Axisymmetric Bluff-Body Drag Reduction Through Geometrical Modification," *Journal of Aircraft*, Vol. 22, June 1985, pp. 516-522.

A Near-Wall Eddy Viscosity Formula for Turbulent Boundary Layers in Pressure Gradients Suitable for Momentum, Heat, or Mass Transfer

P. S. Granville[1]

An eddy viscosity formula is proposed for turbulent boundary layers in pressure gradients which is compatible with the slope and intercept of the log law. By having a "y^3" variation at the wall the formula is suitable for momentum, heat and mass transfer.

Introduction

Algebraic formulas for eddy viscosity or mixing length are the simplest and best known forms of turbulence modeling applied to predicting the development of turbulent boundary layers. They also have more-or-less stood the test of accuracy when compared to more complicated turbulence models [1, 2].

The problem to be addressed is an accurate formula for the eddy viscosity or mixing length in the region next to the wall for a turbulent boundary layer in a longitudinal pressure gradient on a smooth surface; said region encompassing the viscous sublayer, the buffer layer and the log layer.

The usual formula for the eddy viscosity or mixing length of the log layer is given by a Prandtl relation and of the viscous sublayer and buffer layer by a van Driest type damping function. A van Driest type damping function has an exponential form which asymptotically merges into the Prandtl relation for the log layer.

The van Driest damping function was originally proposed for mixing lengths in zero pressure gradients [3]. Various competing modifications had been proposed for pressure gradients and a final form [4] was proposed which correctly predicts the experimentally determined slope and intercept of the velocity log law [5, 6].

However there is another consideration which has been a subject of controversy for many years: namely, whether the eddy viscosity should vary as the third power or fourth power of the normal distance from the wall, "y^3" or "y^4". From the

[1]David Taylor Research Center, Bethesda, MD 20084-5000.

Contributed by the Fluids Engineering Division of THE AMERICAN SOCIETY OF MECHANICAL ENGINEERS and presented at the Applied Mechanics Conference, San Diego, Calif., July 1989. Manuscript received by the Fluids Engineering Division August 4, 1989.

viewpoint of overall momentum transfer in the boundary layer, this may be of little consequence owing to the thinness of the wall layer. For problems in heat or mass transfer at the wall involving turbulent Prandtl or Schmidt Numbers, this consideration, however, may be important.

In a comprehensive investigation and intensive analysis, Chapman and Kuhn [7] conclude that the "y^3" variation is more accurate than the "y^4" variation. Note the van Driest formula for mixing length gives a "y^4" variation even when modified for pressure gradient [4].

Chapman and Kuhn [7], accordingly, modified the van Driest formula for mixing length to provide a "y^3" variation for, however, only zero pressure gradient.

Johnson and King [8], on the other hand, have given a "y^3" variation to a formula for eddy viscosity with a modified van Driest type damping function which does apply to pressure gradients. However it is shown that this formula does not lead to the correct slope and intercept of the velocity log law.

Another consideration is the value of the y^3-coefficient at the wall. Chapman and Kuhn [7] show that their eddy viscosity formula gives a coefficient at great variance with a more accurate coefficient obtained from a Navier-Stokes analysis. It is shown here that the Johnson and King mixing length formula gives a coefficient also at great variance with the Navier-Stokes model.

Accordingly an eddy viscosity formula is now proposed which satisfies the following conditions:

1. the y^3-variation at the wall
2. the slope of the log law for pressure gradients
3. the intercept of the log law for pressure gradients
4. the proper y^3-coefficient at the wall
5. the dependence on molecular viscosity [9]

In addition it is shown the near-wall eddy viscosity may be analytically blended with an outer eddy viscosity such as that of Cebeci and Smith [10] to provide a continuous variation of eddy viscosity across the whole boundary layer. This eliminates an awkward intersection of the two eddy viscosities.

The proposed eddy viscosity formula is also applicable to the Baldwin-Lomax method [11] for solving the time-averaged Navier-Stokes (Reynolds) equations for turbulent flows.

General

Log Law. As shown experimentally by McDonald [5] and more recently by Salam [6], the inner logarithmic law (law of the wall) for the mean streamwise velocity (u) near a wall remains invariant in usual longitudinal pressure gradients, even close to separation such that

$$u^* = \frac{1}{\kappa} \ln y^* + B_1 \tag{1}$$

where $u^* = u/u_\tau$, $y^* = u_\tau y/\nu$, κ = von Kármán constant, $1/\kappa$ = slope of log law, B_1 = intercept (constant for smooth surfaces), u_τ = shear velocity = $\sqrt{\tau_w/\rho}$, τ_w = wall shear stress, ρ = density of fluid, ν = kinematic viscosity of fluid and y = normal distance from wall.

Mixing Length and Eddy Viscosity. The turbulent shear stress (τ_t) may be given by a Prandtl mixing length (l) or a Boussinesq kinematic eddy viscosity (ν_τ) ν_t as

$$\frac{\tau_t}{\rho} = l^2 \left(\frac{du}{dy}\right)^2 = \nu_t \left(\frac{du}{dy}\right) \tag{2}$$

or nondimensionally as

$$\frac{\tau_t}{\tau_w} = l^{*2} \left(\frac{du^*}{dy^*}\right)^2 = \frac{\nu_t}{\nu} \left(\frac{du^*}{dy^*}\right) \tag{3}$$

where $l^* = u_\tau l/\nu$.

The total shear stress (τ) has also a laminar contribution ($\nu\, du/dy$) near the wall so that

$$\tau^* = \frac{du^*}{dy^*} + l^{*2} \left(\frac{du^*}{dy^*}\right)^2 = \left(1+\frac{\nu_t}{\nu}\right) \left(\frac{du^*}{dy^*}\right) \tag{4}$$

where $\tau^* = \tau/\tau_w$.

Consequently the slope of the velocity profile is given nondimensionally by

$$\frac{du^*}{dy^*} = \frac{2\tau^*}{1+\sqrt{1+(2l^*)^2\tau^*}} = \frac{\tau^*}{1+(\nu_t/\nu)} \tag{5}$$

and the mixing length is related to the eddy viscosity by

$$\frac{\nu_t}{\nu} = \frac{1}{2}\left(\sqrt{1+(2l^*)^2\tau^*} - 1\right) \tag{6}$$

and

$$l^* = \sqrt{\frac{\frac{\nu_t}{\nu}\left(1+\frac{\nu_t}{\nu}\right)}{\tau^*}} \tag{7}$$

Also from the two-dimensional equation of motion the nondimensional shear stress (τ^*) for pressure gradients may be expressed [4] as

$$\tau^* = 1 + \hat{p}^+ y^* \tag{8}$$

where $p^+ = \nu/\rho u_\tau^3\, dp/dx$, a pressure-gradient parameter, p = pressure, x = streamwise coordinate, and $\hat{p}^+ = \alpha p^+$. Here α is an appropriate constant, somewhat less than one.

Slope of Log Law. The slope of the velocity profile is given by equation (5) which may be rewritten as

$$\kappa \frac{du^*}{d(\ln y^*)} = \frac{2\kappa\, \tau^* y^*}{1+\sqrt{1+(2l^*)^2\tau^*}} = \frac{\kappa\tau^*\, y^*}{1+(\nu_\tau/\nu)} \tag{9}$$

For the log law, $\kappa\, du^*/d\,(\ln y^*) = 1$, and for laminar flow, $\kappa\, du^*/d\,(\ln y^*) = \kappa\tau^*\, y^*$.

Intercept of Log Law. The mixing length formula and the eddy viscosity formula should also lead to the value of an intercept, B_1, which agrees with the log law. Equating the log law, equation (1), and the velocity profile obtained by integrating equation (5) results in

$$B_1 = \int_0^1 \frac{2\tau^*}{1+\sqrt{1+(2l^*)^2\tau^*}}\, dy^* + \int_0^{\ln \bar{y}^*} \left[\frac{2\tau^*\, y^*}{1+\sqrt{1+(2l^*)^2\tau^*}} - \frac{1}{\kappa}\right] d(\ln y^*) \tag{10}$$

or

$$B_1 = \int_0^1 \frac{\tau^*}{1+(\nu_t/\nu)}\, dy^* + \int_0^{\ln \bar{y}^*} \left[\frac{\tau^*\, y^*}{1+(\nu_t/\nu)} - \frac{1}{\kappa}\right] d(\ln y^*) \tag{11}$$

where $\bar{y}^*$ is a sufficiently large value of y^* in the log layer. The integrand of the second term becomes practically zero at the value of $\bar{y}^*$.

Mixing Length and Eddy Viscosity for Log Layer. The log layer is sufficiently far from the wall so that the laminar shear stress is negligible compared to the turbulent shear stress so that $\tau^* \cong \tau_t/\tau_w$. From equation (3) and differentiating equation (1) results in a mixing length $l^* = \sqrt{\tau^*}\, \kappa y^*$ and an eddy viscosity $\nu_t/\nu = \tau^*\kappa y^*$.

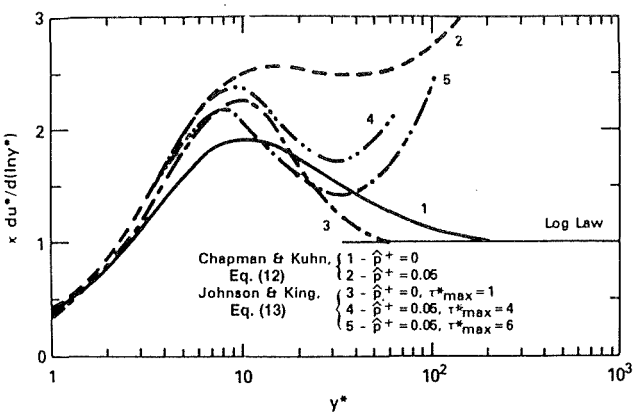

Fig. 1 Variation of slope κ du/d (ln y^*) with normal distance y^* for existing formulas

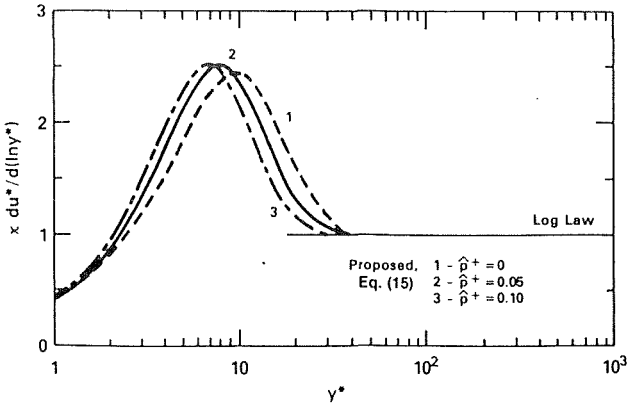

Fig. 2 Variation of slope κ du^*/d (ln y^*) with normal distance y^*

Existing "y^3" Formulas

Chapman and Kuhn Mixing Length Formula. After an intensive investigation which concluded that the eddy viscosity should vary as the cube of the normal distance, y^3, Chapman and Kuhn [7] propose a modified van Driest mixing length formula for zero pressure gradient as

$$l^* = \kappa y^* [1 - \exp(-y^*/\tilde{\lambda}_0^*)]^{1/2} \tag{12}$$

where $\tilde{\lambda}_0^*$ is the appropriate factor for zero pressure gradient. A value of $\lambda_0^* = 66$ corresponds to usual value of $\lambda_0^* = 26$ for the original van Driest formula if $\kappa = 0.4$. Here $B_1 = 5.23$.

Now, if the slope of the velocity profile as given by $\kappa\, du^*/d$ (ln y^*) in equation (9), is plotted in Fig. 1 for zero pressure gradient, the slope merges into the log law at higher values of y^*. If applied to an adverse pressure gradient, however, such as $\hat{p}^+ = 0.05$, it is seen there is no merger with the log law.

Johnson and King. An eddy viscosity formula for the near-wall region is proposed by Johnson and King [8] which has the y^3-variation and which may be rewritten as

$$\frac{\nu_t}{\nu} = \kappa y^* \sqrt{\tau^*_{max}}\, [1 - \exp(-y^*/\tilde{\lambda}_0^*)]^2 \tag{13}$$

Here τ^*_{max} is the maximum value of τ^* across the boundary layer. It should be noted that a maximum value in τ^* only occurs in adverse pressure gradients where $\partial\tau^*/\partial y^* > 0$ at the wall. A value of $\tilde{\lambda}_0^* = 17.4$ corresponds to the usual value of $\lambda_0^* = 26$ for the original van Driest formula.

Now, if the slope of the velocity profile as given by $\kappa\, du^*/d$ (ln y^*) in equation (9) is plotted in Fig. 1 for zero pressure gradient ($\tau^*_{max} = 1$), the slope merges into the log law at higher values of y^*. For an adverse pressure gradient such as $\hat{p}^+ = 0.05$ and say $\tau^*_{max} = 4$ or 6, it is seen there is no merger with the log law.

Proposed Formula

To ensure a more rapid convergence of the damping function, y^{*2} is used instead of y^* so that the eddy viscosity is proposed in the form

$$\frac{\nu_t}{\nu} = \kappa y^* \tau^* \{1 - \exp[-(y^*/\tilde{\lambda}^*)^2]\} \tag{14}$$

Loitsyanskii [12] used y^{*2} instead of y^* in the damping factor of the original van Driest formula. The combination $\kappa y^* \tau^*$ in the proposed formula is required to satisfy the slope of the log law.

To satisfy the requirement of an invariant intercept of the log law, equation (11) is numerically solved for B_1. For a constant value of $B_1 = 5.23$ and $\kappa = 0.4$, $\tilde{\lambda}^*$ becomes a function of $\hat{p}^+$. A numerical fit to $(24/\tilde{\lambda}^*)^2 = 1 + a\,\hat{p}^+$ results in $a = 14.5$ for $\hat{p}^+ > 0$ and $a = 18$ for $\hat{p}^+ < 0$. $\tilde{\lambda}_0^* = 24$. Finally the proposed formula is

$$\boxed{\frac{\nu_t}{\nu} = \kappa y^* \tau^* \{1 - \exp[-(y^* \sqrt{1 + a\hat{p}^+}/24)^2]\}} \tag{15}$$

A plot of the slopes is shown in Fig. 2 for various pressure gradients. It is seen that the lines in all cases rapidly converge to that for the log law.

Comparison of y^3-Coefficients

From Maclaurin series expansions of equations (12), (13) and (15), the y^3-coefficients are as follows:

Chapman and Kuhn:

$$\frac{\kappa^2}{\tilde{\lambda}_0^*} = \frac{(0.4)^2}{66} = 0.0024$$

Johnson and King:

$$\frac{\kappa\sqrt{\tau^*_{max}}}{(\tilde{\lambda}_0)^2} = \frac{0.4}{(17.4)^2} = 0.0013 \text{ for } \tau^*_{max} = 1$$

Proposed:

$$\frac{\kappa}{\tilde{\lambda}_0^{*2}} = \frac{0.4}{(24)^2} = 0.00069$$

Chapman and Kuhn obtain values of 0.0007 and 0.0005 from a Navier-Stokes analysis. The value of 0.00069 from the proposed model is hence very close to these values.

Applications

Blending of Inner and Outer Eddy Viscosities. An awkward intersection of the inner (near wall) and outer eddy viscosities may be avoided by using a blending relation such as

$$\frac{\nu_t}{\nu} = \left(\frac{\nu_t}{\nu}\right)_0 \tanh \frac{(\nu_t/\nu)_i}{(\nu_t/\nu)_0} \tag{16}$$

or

$$\frac{\nu_t}{\nu} = \left(\frac{\nu_t}{\nu}\right)_0 \left\{1 - \exp\left[-\frac{(\nu_t/\nu)_i}{(\nu_t/\nu)_0}\right]\right\} \tag{17}$$

where $(\nu_t/\nu)_i$ is the relation for the inner region such as equation (15) and $(\nu_t/\nu)_0$ is the relation for the outer region which may be that of Cebeci and Smith [10] or its variation [13].

The hyperbolic tangent relation is used in a less general way by Lam [14] for the case of zero pressure gradient and the exponential relation is used by Johnson and King [8].

Baldwin-Lomax Method. In general the Baldwin-Lomax method is based on the Cebeci-Smith eddy viscosity model for

the outer flow such that more readily determined factors are substituted for the boundary-layer and displacement thicknesses. Analytical statements [11] are given for these factors which apply to turbulent boundary layers in pressure gradients. The proposed formula for the inner region may be used without alteration and blended with the Baldwin-Lomax formula for the outer flow in a manner just presented.

References

1 Patel, V. C., Rodi, W., and Scheuerer, G., "Turbulence Models for near-Wall and Low Reynolds Numbers Flows: A Review," *AIAA Journal*, Vol. 23, No. 9, 1985, pp. 1308-1319.

2 Cebeci, T., Chang, K. C., Li, C., and Whitelaw, J. H., "Turbulence Models for Wall Boundary Layers," *AIAA Journal*, Vol. 24, No. 3, 1986, pp. 359-360.

3 van Driest, E. R., "On Turbulent Flow Near a Wall," *Journal of Aeronautical Sciences*, Vol. 23, 1956, pp. 1007-1011, 1036.

4 Granville, P. S., "A Modified van Driest Formula for the Mixing Length of Turbulent Boundary Layers in Pressure Gradients," ASME JOURNAL OF FLUIDS ENGINEERING, Vol. 111, Mar. 1989.

5 McDonald, H., "The Effect of Pressure Gradient on the Law of the Wall in Turbulent Flow," *Journal of Fluid Mechanics*, Vol. 35, Part 2, 1969, pp. 311-336.

6 Salam, M. Y., "Measurement of the Viscous Sublayer in Near-Separated Flows," *Applied Scientific Research*, Vol. 39, No. 4, 1982, pp. 337-347.

7 Chapman, D. R., and Kuhn, G. D., "The Limiting Behavior of Turbulence Near a Wall," *Journal of Fluid Mechanics*, Vol. 170, 1986, pp. 265-292.

8 Johnson, D. A., and King, L. S., "A Mathematically Simple Turbulence Closure Model for Attached and Separated Turbulent Boundary Layers," *AIAA Journal*, Vol. 23, No. 11, 1985, pp. 1684-1692.

9 Novozhilov, V. V., "Dependence of Turbulent Viscosity on Molecular Viscosity," *Soviet Physics Doklady*, Vol. 32, No. 6, 1987, pp. 451-453.

10 Cebeci, T., and Smith, A. M. O., *Analysis of Turbulent Boundary Layers*, Academic Press, New York, 1971.

11 Granville, P. S., "Baldwin-Lomax Factors for Turbulent Boundary Layers in Pressure Gradients," *AIAA Journal*, Vol. 25, No. 12, 1987, pp. 1624-1627.

12 Loitsyanskii, L. G., "Damping Factor to the Prandtl Equation for the Transition Portion of a Turbulent Boundary Layer," *Journal of Engineering Physics*, Vol. 45, No. 6, 1984, pp. 1381-1387.

13 Nituch, M. J., Sjolander, S., and Head, M. R., "An Improved Version of the Cebeci-Smith Eddy-Viscosity Model," *Aeronautical Quarterly*, Vol. 29, Part 3, 1978, pp. 207-225.

14 Lam, C. Y., "An Eddy Viscosity Turbulence Model," *International Communications in Heat and Mass Transfer*, Vol. 15, No. 3, 1988, pp. 356-363.

Velocity Measurements on the Forward Portion of a Cylinder

D. E. Paxson[1] and R. E. Mayle[1]

Velocity measurements in the laminar boundary layer around the forward portion of a circular cylinder are presented. These results are compared to Blasius' theory for laminar flow around a cylinder using a free-stream velocity distribution obtained from static pressure measurements on the cylinder. Even though the flow is periodically unsteady as a result of vortex shedding from the cylinder, it is found that the agreement is excellent.

Nomenclature

C_p = static pressure coefficient
D = cylinder diameter
n = frequency
R = cylinder radius
Re = Reynolds number
S = Strouhal number
u = velocity
u_i = coefficients in the series expansion of the free-stream velocity
U_ϕ = free-stream velocity
U_∞ = incident cross-flow velocity
y = coordinate normal to cylinder surface

Greek

ϕ = angular distance from stagnation
ν = kinematic viscosity

[1]Mechanical Engineering Department, Rensselaer Polytechnic Institute, Troy, New York, 12180.

Contributed by the Fluids Engineering Division of THE AMERICAN SOCIETY OF MECHANICAL ENGINEERS. Manuscript received by the Fluids Engineering Division March 7, 1989.

Introduction

In 1908, Blasius (or see Schlichting, 1979) obtained a series solution to the laminar boundary layer equations for steady flow around a circular cylinder; a solution which, in general, may be applied to any symmetrical, two-dimensional body. Later, it was developed further by Howarth (1935) and Görtler (1949). The solution, of course, requires the free-stream velocity distribution which is to be provided as a power series in ϕ, where ϕ denotes the angular distance (in radians) from stagnation. For flow around a symmetrical cylinder this has the general form

$$U_\phi U_\infty = u_1\phi + u_3\phi^3 + u_5\phi^5 + \ldots \quad (1)$$

where U_∞ is the incident cross-flow velocity. For potential flow around a circular cylinder, $u_1 = 2$, $u_3 = -2/3!$, $u_5 = 2/5!$, etc. In this case, the velocity profiles appear as shown in Fig. 9.6 in Schlichting and separation is found to occur at $\phi = 108.8$ deg (1.90 radians).

Comparisons between theory and experiments have generally involved calculating the separation position for a measured pressure distribution, from which the free-stream velocity distribution can be obtained, and comparing the result to the measured separation position. This work was initially conducted by Hiemenz (1911), who showed excellent agreement between his calculated and observed separation positions. For this case, however, the pressure distribution was not the same as that for potential flow and separation occurred at $\phi = 81$ deg (1.41 radians). Experiments and calculations were later made by Thom (1928) and Fage (1929) who, attempting to locate the position of separation, measured velocities profiles near separation ($50 \text{ deg} < \phi < 95$ deg) using a small total pressure tube. Their tests were conducted at virtually the same conditions of the present tests and although they admit that their data was somewhat affected by their traverse device, they obtained a reasonable agreement with their calculations.

Other experimental investigations include extensive measurements of drag (see Schlichting) and the unsteady shedding of the boundary layer from the cylinder. On the latter subject, Roshko (1954) presents the more recent results. In general, he shows that the shedding frequency n, expressed in a dimensionless form as a Strouhal number, $S = nD/U_\infty$, depends on the cylinder Reynolds number $\text{Re} = U_\infty D/\nu$. In these expressions, ν is the kinematic viscosity and D is the cylinder diameter. For $10^3 < \text{Re} < 10^5$, he found that the Strouhal number is nearly constant and equal to 0.21.

To the authors' knowledge, however, a complete set of velocity measurements in the laminar boundary layer and the forward portion of a cylinder have never been reported and compared to theory, and the effect of the unsteadiness in this region driven by the vortex shedding from the cylinder itself has never been mentioned. The results presented herein provide this information.

Experimental Apparatus and Procedure

The present tests were conducted in a low-speed, open-circuit

the outer flow such that more readily determined factors are substituted for the boundary-layer and displacement thicknesses. Analytical statements [11] are given for these factors which apply to turbulent boundary layers in pressure gradients. The proposed formula for the inner region may be used without alteration and blended with the Baldwin-Lomax formula for the outer flow in a manner just presented.

References

1 Patel, V. C., Rodi, W., and Scheuerer, G., "Turbulence Models for near-Wall and Low Reynolds Numbers Flows: A Review," *AIAA Journal*, Vol. 23, No. 9, 1985, pp. 1308-1319.

2 Cebeci, T., Chang, K. C., Li, C., and Whitelaw, J. H., "Turbulence Models for Wall Boundary Layers," *AIAA Journal*, Vol. 24, No. 3, 1986, pp. 359-360.

3 van Driest, E. R., "On Turbulent Flow Near a Wall," *Journal of Aeronautical Sciences*, Vol. 23, 1956, pp. 1007-1011, 1036.

4 Granville, P. S., "A Modified van Driest Formula for the Mixing Length of Turbulent Boundary Layers in Pressure Gradients," ASME JOURNAL OF FLUIDS ENGINEERING, Vol. 111, Mar. 1989.

5 McDonald, H., "The Effect of Pressure Gradient on the Law of the Wall in Turbulent Flow," *Journal of Fluid Mechanics*, Vol. 35, Part 2, 1969, pp. 311-336.

6 Salam, M. Y., "Measurement of the Viscous Sublayer in Near-Separated Flows," *Applied Scientific Research*, Vol. 39, No. 4, 1982, pp. 337-347.

7 Chapman, D. R., and Kuhn, G. D., "The Limiting Behavior of Turbulence Near a Wall," *Journal of Fluid Mechanics*, Vol. 170, 1986, pp. 265-292.

8 Johnson, D. A., and King, L. S., "A Mathematically Simple Turbulence Closure Model for Attached and Separated Turbulent Boundary Layers," *AIAA Journal*, Vol. 23, No. 11, 1985, pp. 1684-1692.

9 Novozhilov, V. V., "Dependence of Turbulent Viscosity on Molecular Viscosity," *Soviet Physics Doklady*, Vol. 32, No. 6, 1987, pp. 451-453.

10 Cebeci, T., and Smith, A. M. O., *Analysis of Turbulent Boundary Layers*, Academic Press, New York, 1971.

11 Granville, P. S., "Baldwin-Lomax Factors for Turbulent Boundary Layers in Pressure Gradients," *AIAA Journal*, Vol. 25, No. 12, 1987, pp. 1624-1627.

12 Loitsyanskii, L. G., "Damping Factor to the Prandtl Equation for the Transition Portion of a Turbulent Boundary Layer," *Journal of Engineering Physics*, Vol. 45, No. 6, 1984, pp. 1381-1387.

13 Nituch, M. J., Sjolander, S., and Head, M. R., "An Improved Version of the Cebeci-Smith Eddy-Viscosity Model," *Aeronautical Quarterly*, Vol. 29, Part 3, 1978, pp. 207-225.

14 Lam, C. Y., "An Eddy Viscosity Turbulence Model," *International Communications in Heat and Mass Transfer*, Vol. 15, No. 3, 1988, pp. 356-363.

Velocity Measurements on the Forward Portion of a Cylinder

D. E. Paxson[1] and R. E. Mayle[1]

Velocity measurements in the laminar boundary layer around the forward portion of a circular cylinder are presented. These results are compared to Blasius' theory for laminar flow around a cylinder using a free-stream velocity distribution obtained from static pressure measurements on the cylinder. Even though the flow is periodically unsteady as a result of vortex shedding from the cylinder, it is found that the agreement is excellent.

Nomenclature

C_p = static pressure coefficient
D = cylinder diameter
n = frequency
R = cylinder radius
Re = Reynolds number
S = Strouhal number
u = velocity
u_i = coefficients in the series expansion of the free-stream velocity
U_ϕ = free-stream velocity
U_∞ = incident cross-flow velocity
y = coordinate normal to cylinder surface

Greek

ϕ = angular distance from stagnation
ν = kinematic viscosity

[1]Mechanical Engineering Department, Rensselaer Polytechnic Institute, Troy, New York, 12180.

Contributed by the Fluids Engineering Division of THE AMERICAN SOCIETY OF MECHANICAL ENGINEERS. Manuscript received by the Fluids Engineering Division March 7, 1989.

Introduction

In 1908, Blasius (or see Schlichting, 1979) obtained a series solution to the laminar boundary layer equations for steady flow around a circular cylinder; a solution which, in general, may be applied to any symmetrical, two-dimensional body. Later, it was developed further by Howarth (1935) and Görtler (1949). The solution, of course, requires the free-stream velocity distribution which is to be provided as a power series in ϕ, where ϕ denotes the angular distance (in radians) from stagnation. For flow around a symmetrical cylinder this has the general form

$$U_\phi U_\infty = u_1\phi + u_3\phi^3 + u_5\phi^5 + \ldots \quad (1)$$

where U_∞ is the incident cross-flow velocity. For potential flow around a circular cylinder, $u_1 = 2$, $u_3 = -2/3!$, $u_5 = 2/5!$, etc. In this case, the velocity profiles appear as shown in Fig. 9.6 in Schlichting and separation is found to occur at $\phi = 108.8$ deg (1.90 radians).

Comparisons between theory and experiments have generally involved calculating the separation position for a measured pressure distribution, from which the free-stream velocity distribution can be obtained, and comparing the result to the measured separation position. This work was initially conducted by Hiemenz (1911), who showed excellent agreement between his calculated and observed separation positions. For this case, however, the pressure distribution was not the same as that for potential flow and separation occurred at $\phi = 81$ deg (1.41 radians). Experiments and calculations were later made by Thom (1928) and Fage (1929) who, attempting to locate the position of separation, measured velocities profiles near separation ($50 \text{ deg} < \phi < 95$ deg) using a small total pressure tube. Their tests were conducted at virtually the same conditions of the present tests and although they admit that their data was somewhat affected by their traverse device, they obtained a reasonable agreement with their calculations.

Other experimental investigations include extensive measurements of drag (see Schlichting) and the unsteady shedding of the boundary layer from the cylinder. On the latter subject, Roshko (1954) presents the more recent results. In general, he shows that the shedding frequency n, expressed in a dimensionless form as a Strouhal number, $S = nD/U_\infty$, depends on the cylinder Reynolds number $\text{Re} = U_\infty D/\nu$. In these expressions, ν is the kinematic viscosity and D is the cylinder diameter. For $10^3 < \text{Re} < 10^5$, he found that the Strouhal number is nearly constant and equal to 0.21.

To the authors' knowledge, however, a complete set of velocity measurements in the laminar boundary layer and the forward portion of a cylinder have never been reported and compared to theory, and the effect of the unsteadiness in this region driven by the vortex shedding from the cylinder itself has never been mentioned. The results presented herein provide this information.

Experimental Apparatus and Procedure

The present tests were conducted in a low-speed, open-circuit

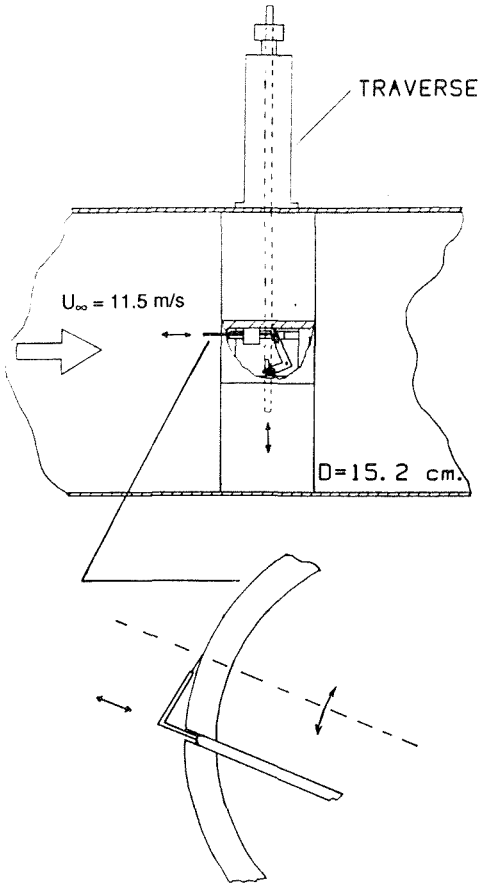

Fig. 1 Test cylinder and boundary layer probe arrangement

wind tunnel. The flow entering the test section had a steady velocity of 11.5 m/s, was uniform to within ±1 percent, and had a turbulent level of about 0.4 percent. The test section was a 46 cm high by 76 cm wide, 3 m long rectangular duct and contained the test cylinder positioned vertically in the center. This cylinder was a hollow metal cylinder with an outside diameter of 15.2 cm. Although the length-to-diameter ratio of the test cylinder is rather small, 3-to-1, Van Dresar and Mayle (1986) showed that the flow around the center 40 cm portion of the cylinder is two-dimensional.

Velocity measurements in the boundary layer of the test cylinder were made using a special miniature hot-wire probe as shown in Fig. 1. The sensor was a 5 micron Tungsten wire welded between two 6.4 mm long needles. These needles, the only nonsensor portion of the probe extending into the flow, tapered from a diameter of 0.38 mm to 0.076 mm at the sensor and were bent so that the probe would not interfere with the flow. The probe was inserted in a hole through the cylinder wall and attached to an external traverse device by a rod and bell-crank mechanism. The entire traverse mechanism except for the computer controlled traverse device and the probe head was contained within the cylinder. Even though the boundary layer traverses were always conducted in one direction, all of the linkages were very carefully designed and manufactured to keep backlash to a minimum and prevent the probe from rocking as it was moved in and out of the cylinder. Calibration tests showed that the relation between the probe and traverse device movement was linear within 2 cm from the surface of the cylinder. Measurements at different angular positions around the cylinder were obtained by rotating the entire test cylinder assembly.

The hot-wire was calibrated in a separate facility. A Pitot tube was used for calibrating the probe and was found adequate over most of the range of velocities measured. A method utilizing Roshko's results for vortex shedding from a cylinder was used to obtain the calibration at the very low velocities. A TSI 1052 linearizer was used to fit the calibration throughout the entire range. The resulting output signal from the wire showed a maximum deviation of 1.6 percent from the actual velocity. Near the wall, it was found that a "wall correction" had to be applied to the data. The correction according to Zemskaya (1979) was used. As a result, the reported dimensionless velocities, u/U_ϕ; are considered accurate to within 2 percent except for those nearest the wall where a correction of as much as $(u_{meas.} - u_{act.})/U_\phi = 0.06$ has been applied.

All of the tests were conducted at Reynolds number Re = 110,000. Velocity profiles in the boundary layer were measured at $\phi = 20$, 30, 40, 50, 60, and 70 deg. Separation was previously found to occur at $\phi = 79$ deg (Marziale and Mayle), which is only slightly different from Hiemenz' result. The difference is attributed to blockage.

Results and Discussion

Static pressure measurements were obtained from a small static pressure tap drilled into the test cylinder and the distribution of static pressure around the cylinder obtained by rotating the cylinder. The free-stream velocity distribution around the cylinder was determined from these measurements using Bernoulli's equation and was found to be symmetric about $\phi = 0$. This distribution is well represented by the series

$$U_\phi/U_\infty = 1.925\phi - 0427\phi^3 + 0.015\phi^5; \quad (\phi \le \pi/2 \text{ radians}). \tag{2}$$

The acceleration of the flow at stagnation, $u_1 = 1.925$ (which depends on wake and tunnel blockage) is only slightly less than for potential flow $u_1 = 2$. The coefficients in the above expression (corresponding to u_1, u_3, etc., in equation (1) were used in Blasius' theory to calculate the theoretical velocity profiles at each angular measurement position.

The measured velocity profiles are presented in Fig. 2. These are plotted as u/U_ϕ versus the Blasius coordinate $y\sqrt{U_\infty R/\nu}/R$. To avoid confusion, each profile has been shifted upward by 0.5 units. In addition, the theoretical profiles obtained by using equation (2) are shown as solid lines. In each case the comparison is excellent except for the data point nearest the wall where the wall correction becomes substantial. The dashed line for $\phi = 70$ deg corresponds to the theoretical profile using the potential free-stream velocity distribution. At $\phi = 20$ deg, the theoretical profiles obtained by using the potential free-stream velocity distribution and equation (2) are virtually identical. Since u_1 is nearly the same for both, this is to be expected.

The measurements presented in Fig. 2 are time-averaged velocity measurements. It was found, however, that the velocity everywhere in the boundary layer and in the free stream near the cylinder varied slight with time. The temporal variation of the free-stream velocity at $\phi = 30$ deg is presented in Fig. 3. The position corresponds to $y\sqrt{U_\infty R/\nu}/R = 2.4$ for $\phi = 30$ deg in Fig. 2 which is at the edge of the boundary layer. While the magnitude of the variation elsewhere in the flow depended on both y and ϕ, the frequency of the variation was independent of position and corresponded to a Strouhal number of 0.21. According to Roshko, for Re = 110,000, this is identical to the Strouhal number for vortex shedding from the cylinder and indicates that the periodic behavior was driven by the shedding. Later, it was found that by adding a 1 m long, 15.2 cm thick, parallel sided afterbody to the cylinder both the shedding and temporal variations were completely eliminated. This further substantiated that the unsteadiness

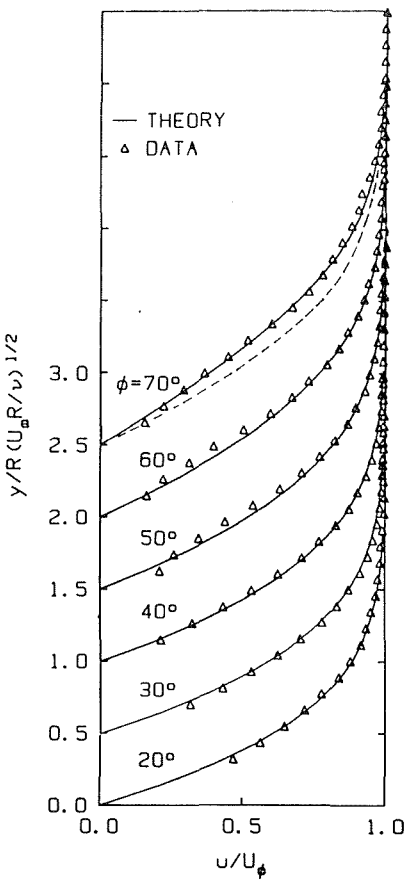

Fig. 2 Velocity profiles on the forward portion of the cylinder

was caused by vortex shedding and its effect on the overall flow field.

According to Lighthill (1954), the time-averaged solution to the unsteady, laminar boundary layer equations for a small periodically fluctuating free stream perturbation is identical to the steady-state solution provided

$$\frac{n\delta^2}{\nu} \ll 40$$

where n is the frequency of the fluctuation and δ is the boundary layer thickness. Upon substituting $\delta = 2.4R/\sqrt{U_\infty R/\nu}$, which is either found in Schlichting for the boundary layer thickness on a cylinder in crossflow or seen from Fig. 2, and using the definition of the Strouhal number this condition becomes $S \ll 14$. Since the Strouhal number for vortex shedding from a cylinder indeed satisfies this condition and the disturbance is indeed a small perturbation (about 0.1 U_ϕ, see Fig. 3), it can be expected that the time-averaged velocity profiles for flow around a cylinder with natural vortex shedding should be identical to the steady state profiles as was shown in Fig. 2. Furthermore, as shown by Lighthill, Childs, and Mayle

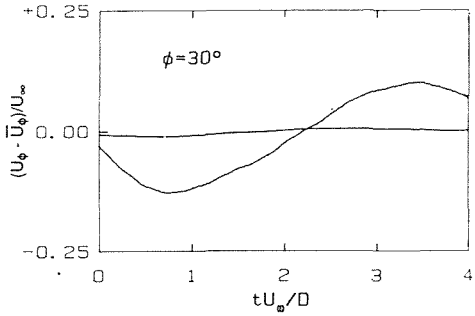

Fig. 3 Temporal variation of the free-stream velocity at $\phi = 30$ deg

(1984) and experimentally by Marziale and Mayle (1984), the same can be said about the heat and the mass transfer from the cylinder.

Conclusions

Time-averaged boundary layer velocity measurements were obtained on the forward portion of a cylinder and were found to be in excellent agreement with Blasius' theory for steady, laminar, boundary-layer flow on a cylinder.

A small unsteady component of velocity within the boundary layer was found to be driven at the Strouhal frequency by the unsteady vortex shedding from the cylinder. However, since both its magnitude and frequency were found to be small, its effect on the time-averaged velocity in the boundary layer according to Lighthill's theory, and as experimentally found, should be negligible.

References

Blasius, H., 1908, "Grenzschichten in Flüssigkeiten mit kleiner Reibung," *Z. Math. u. Phys.*, Vol. 56, No. 1. English translation: NACA TM 1256.

Childs, E. P., and Mayle, R. E., 1984, "Heat Transfer on a Rotationally Oscillating Cylinder in Crossflow," *International Journal of Heat and Mass Transfer*, Vol. 27, No. 1, pp. 85-94.

Fage, A., 1929, "The Airflow Around a Circular Cylinder in the Region Where the Boundary Layer Separates from the Surface," *Phil. Mag.*, Vol. 7, pp. 253-273.

Görtler, H., 1949, "Zur Approximation stationärer laminarer Grenzschichtströmungen mit Hilfe der abgebrochenen Blasiusschen Reihe," *Arch. d. Math.*, Vol. 1, No. 3, 235.

Hiemenz, K., "Die Grenzschicht an einem in den gliechförmigen Flüssigkeitsstrom eingetauchten geraden Kreiszylinder," Thesis Göttingen 1911, *Dingl. Polytechn. J.*, 326, 32.

Horwarth, L., 1935, "On the Calculation of Steady Flow in the Boundary Layer Near the Surface of a Cylinder in a Stream,"ARC R&M 1632.

Lighthill, M. J., 1954, "The Response of Laminar Skin Friction and Heat Transfer to Fluctuations in the Stream Velocity," *Proc. Roy. Soc.*, Series A 224, pp. 1-23.

Marziale, M. L., and Mayle, R. E., 1984, "Effect of an Oscillating Flow Direction on Leading Edge Heat Transfer," ASME *Journal of Engineering for Power*, Vol. 106, pp. 222-228.

Roshko, A., 1954, "On the Development of Turbulent Wakes from Vortex Streets," NACA Rep. 1191.

Thom, A., 1928, "The Laminar Boundary Layer of the Front Part of a Cylinder," ARC Rept. 1176 (or ARC Rept. 1194, 1929).

Schlichting, H., 1979, *Boundary Layer Theory*, McGraw-Hill.

Van Dresar, N., and Mayle, R. E., 1986, "Convection at the Base of a Cylinder with a Horseshoe Vortex," *Proceedings 8th International Heat Transfer Conference*, San Francisco.

Zemskaya, A. S., Levitskiy, V. N., Repik, YE. U., and Sosedko, YU. P., 1979, "Effect of the Proximity of the Wall on Hot-Wire Readings in Laminar and Turbulent Boundary Layers," *Fluid Mechanics-Soviet Reserach*, Vol. 8, No. 1, pp. 133-141.